

**CIRCUITS AND SYSTEMS FOR CW AND PULSED HIGH-
FIELD ELECTRON SPIN RESONANCE**

David Robert Bolton

**A Thesis Submitted for the Degree of PhD
at the
University of St Andrews**



2006

**Full metadata for this item is available in
Research@StAndrews:FullText
at:**

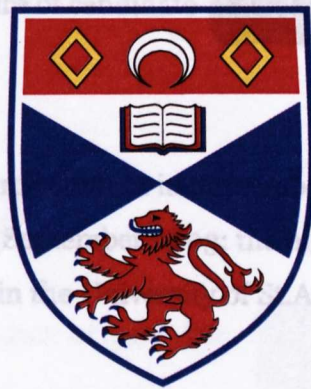
<http://research-repository.st-andrews.ac.uk/>

Please use this identifier to cite or link to this item:

<http://hdl.handle.net/10023/7104>

This item is protected by original copyright

Circuits And Systems For CW And Pulsed High-Field Electron Spin Resonance



A thesis presented by

David Robert Bolton BSc. MSc.

to the

University of St Andrews

in application for the degree of

Doctor of Philosophy

December 2005



Declaration

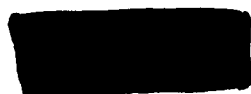
I, David Robert Bolton, hereby certify that this thesis, which is approximately 40,000 words in length, has been written by me, that is the record of work carried out by me, and that it has not been submitted in any previous application for a higher degree.

date 14/12/05 signature of candidate



I was admitted as a research student in September 2002 and as a candidate for the degree of Ph.D. in September 2003; the higher study for which this is a record was carried out in the University of St. Andrews between 2002 and 2005.

date 14/12/05 signature of candidate



I hereby certify that the candidate has fulfilled the conditions of the Resolution and Regulations appropriate for the degree of Ph.D. in the University of St. Andrews and that the candidate is qualified to submit this thesis in application for that degree.

date 14/12/05 signature of supervisor



Library Declaration

In submitting this thesis to the University of St. Andrews I understand that I am giving permission for it to be made available for use in accordance with the regulations of the University Library for the time being in force, subject to any copyright vested in the work not being affected thereby. I also understand that the title and abstract will be published, and that a copy of the work may be made and supplied to any bona fide library or research worker.

date 14/12/05

signature of candidate



Acknowledgements

“No man is an island” (John Donne 1572-1631) and this is certainly true of any attempt to complete a PhD thesis.

Firstly, I would like to thank Graham Smith, my supervisor in this endeavor, for being available at the drop of a hat to keep me on the straight and narrow and having the infinite patience to bring my knowledge of ESR to a something like a reasonable level. Duncan Robertson must also be thanked for his truly awful limericks, reading immense chunks of thesis and being a sounding board for some of my more hair brained schemes, some of them work! Paul Cruikshank, Dav MacFarlane and Robert Hunter were my partners in crime in the lab, only throwing things at me when the puns got too bad. Thanks to all of you for making the lab a fun place to be.

The workshop took big bits of metal and turned them into small bits of metal by following my very bad sketches, usually giving me something which worked better than my original idea. It would be impossible to undertake this type of work without your collective skills. Once again thanks.

Several companies were kind enough to lend me valuable equipment. Ag-

ilent loaned a very nice (very expensive) scope which allowed me to show that my pulses were even faster than I thought, Anritsu loaned me a network analyser so that I could measure filters and Trak Europe let me back on site to borrow their phase noise measurement kit for looking at 150MHz oscillators.

I would like to acknowledge the financial support of EPSRC and Dr. R. Wylde of Thomas Keating Ltd.

A special thankyou to Joan Ramsay who knew nothing about ESR but read an early draft of this to check the english. Joan still knows nothing about ESR, but the standard of english improved!

The support of Jane is impossible to estimate. She has listened to my ramblings about phase noise, multipliers, circuit design and difficult chapters and has been a constant source of support whilst producing this volume.

Finally, Mum and Dad. This is all thanks to you. Mum, for years you put up with piles of junk (actually valuable radio equipment) all over your nice tidy house. Dad, I never stood a chance! Thanks for giving me a kick start into physics and showing me one way forward.... mind you, I don't think that being a footballer was ever on the agenda! This is for both you, if you ever have a Ganglia, this will be a far more effective treatment than the family Bible.

Abstract

This thesis is concerned with the design and realisation of components for a new state of the art 94GHz Electron Spin Resonance (ESR) spectrometer capable of operating in both pulsed and CW modes. The complete spectrometer is designed to provide phase coherent 1kW peak power sub-nanosecond $\pi/2$ pulses having variable duration and repetition rate. The mm-wave response of a paramagnetic sample to these pulses is detected with a superheterodyne detector. Such a system would offer a step change in performance, promising unprecedented resolution and sensitivity. These aims should be compared with the performance of commercial (Bruker) instruments capable of delivering 200mW 30ns $\pi/2$ pulses.

For this type of system, both the long term (thermal) and short term (phase) stability of oscillators and sources employed are extremely important. Consideration of phase noise, frequency, tunability and power output shows that multiplied sources offer substantial benefits compared to fundamental sources. A delay line discriminator method of phase noise measurement, suitable for use with the low frequency oscillators is described and implemented. This is extended to 94GHz using a down convertor with a quasi-optically stabilised Gunn oscillator. These tools are used to select an optimum oscillator-multiplier combination to produce a low noise 94GHz source.

A new method of pulse generation, which has produced +23dBm peak power 250ps rectangular and 115ps Gaussian envelope phase coherent pulses, is described. These are believed to be the shortest phase coherent pulses at 94GHz available. This system will be used to provide ns pulses suitable for amplification to 1kW using a Klystron amplifier.

A heterodyne detector has been constructed which employs the same oscil-

lator/multiplier techniques identified above to produce the required local oscillator signal. It is demonstrated that by careful consideration of multiplication factors a system employing one variable and one fixed oscillator allows all the signals required in the spectrometer to maintain phase coherence. It is demonstrated that the complete demodulator responds to pulses on a ns time scale and has a noise temperature of 737K.

CONTENTS

Declaration	i
Library Declaration	ii
Acknowledgements	iii
Abstract	v
List of Figures	xiv
1 Introduction	1
1.1 Thesis Overview	4
2 A Theory of CW ESR	7
2.1 The electron in a magnetic field.	8
2.1.1 The electron in a constant magnetic field	8
2.1.2 The effect of an oscillating magnetic field	13
2.1.3 Single Electron Measurements	17

CONTENTS

2.2	ESR Spectra	17
2.2.1	The Landé g-factor	18
2.2.2	The Spin Hamiltonian	19
2.3	Thermal effects	20
2.3.1	A Simple Model of Relaxation	22
2.3.2	Relaxation Mechanisms	25
2.4	The Advantages of High Field ESR	27
3	The Measurement of Paramagnetic Changes	29
3.1	The cavity	30
3.2	Paramagnetic effects	32
3.2.1	Dispersive changes	33
3.2.2	Absorptive changes	34
3.2.3	Relative magnitudes	35
3.3	Coupling to cavities	35
3.3.1	The transmission cavity	36
3.3.2	The reflection cavity	38
3.4	Comparison of Cavities	39
3.5	Reflection cavity systems	43
3.5.1	Cavity locking.	44
3.6	Induction Measurements	46
3.6.1	The bimodal cavity	47
3.6.2	Polarisation and the induction mode.	49
3.7	Signal Detection	51
3.7.1	Direct detection	52
3.7.2	Other methods of detection	56
3.8	Spectrometer Sensitivity	58
3.8.1	Power detection	58

CONTENTS

3.8.2	Voltage detection	60
3.8.3	Field Modulation	62
3.8.4	Implementation Of A Homodyne Detector	65
4	Spectrometer Components	67
4.1	Spectrometer Outline	68
4.1.1	The Magnetic Fields	69
4.1.2	Temperature Control	72
4.2	Passive RF Components	72
4.2.1	Interconnections	73
4.2.2	The Coupling Structure	81
4.3	The Sample Holder	84
4.3.1	The rectangular cavity	84
4.3.2	The cylindrical cavity	86
4.3.3	The spherical cavity	87
4.3.4	Cavities and Sensitivity	88
4.3.5	Other types of cavity	90
4.4	Overview of a quasi-optical spectrometer	90
5	CW Sources	93
5.1	Early Microwave Sources	94
5.2	Oscillator Circuits	94
5.2.1	The Direct Generation of 94GHz	96
5.2.2	Oscillator Tuning	97
5.3	Oscillator Noise	99
5.3.1	Minimising Oscillator Phase Noise	100
5.4	Frequency Multiplied Sources	102
5.4.1	Frequency Multiplication	102

CONTENTS

5.4.2	Properties of Multiplied Sources	110
5.5	Chapter Summary	114
6	The Measurement of Source Phase Noise	115
6.1	The Measurement of Oscillator Phase Noise	116
6.1.1	Discriminator theory	117
6.1.2	Discriminator design	128
6.1.3	Realisation of the discriminator	128
6.1.4	Discriminator performance	132
6.1.5	Section Summary	137
6.2	Measuring Phase Noise at 94GHz	139
6.2.1	The Down Conversion Source	140
6.3	A Down Conversion Source	143
6.4	Cavity Q Measurement	146
6.5	A 94GHz Phase Noise Measurement System	150
7	The Design a 94GHz Source	152
7.1	Design Considerations	153
7.1.1	94GHz Gunn Oscillator Performance	153
7.2	Source Design	155
7.2.1	Oscillators	155
7.3	Phase Locked Sources	162
7.4	Multipliers	164
7.4.1	Multiplication using IMPATT Diodes	164
7.4.2	Schottky Diode Multiplier -1	166
7.4.3	Schottky Diode Multiplier -2	169
8	CW Source Performance	171
8.1	Measured oscillator Performance	172

CONTENTS

8.1.1	Measured DRO Performance	172
8.1.2	Measured PMYTO Performance	173
8.1.3	6 to 8GHz YTO performance	175
8.1.4	Oscillator Comparison	176
8.2	Measured Source Performance	179
8.2.1	IMPATT MULTIPLIER and YTO	180
8.2.2	IMPATT and DRO	183
8.2.3	Schottky Diode Multiplier -1	183
8.2.4	Schottky Diode Multiplier -2	187
8.3	Comparison of Sources	189
8.3.1	The Choice of Oscillator	189
8.3.2	The Effect of Multiplier Topology	192
8.4	Spectrometer Performance	193
8.5	Chapter Summary	195
9	HiPER	197
9.1	A Comparison of Pulse and CW Techniques	198
9.2	Pulse Requirements	200
9.3	Power Requirements	202
9.4	Cavity Requirements	203
9.4.1	Excitation Bandwidth	204
9.4.2	Cavity Ring Down	205
9.5	A 94GHz Pulse Spectrometer	206
9.6	Spectrometer Dead Time	208
9.6.1	The Effect of Low Cavity Q	208
9.6.2	Receiver Requirements	209
9.6.3	Standing waves	210
9.7	Chapter Summary	210

CONTENTS

10 Pulsed Sources	212
10.1 OOK Modulation	213
10.1.1 OOK Pulse Properties.	214
10.2 The use of diode ring mixers	218
10.2.1 DBM selection	221
10.3 Pulses and Multipliers	224
10.3.1 Varistor multipliers	225
10.3.2 Varactor multipliers	228
10.4 The Properties of Multiplied Pulses	230
10.4.1 DBM Attenuation Characteristics.	231
10.4.2 Pulse Parameters.	232
10.5 Chapter summary	234
11 A 94GHz Heterodyne Demodulator	237
11.1 The Heterodyne Demodulator	238
11.1.1 Choice of IF Frequency	239
11.2 Local Oscillator Generation	241
11.2.1 The Interpolation Mixer	243
11.2.2 Mixer saturation	244
11.2.3 The Interpolation Oscillator	246
11.2.4 Interpolation mixer output	259
11.2.5 Mixer output filter	263
11.2.6 Post filter amplification	269
11.3 94GHz to 1.8GHz Down Conversion	272
11.3.1 The down convertor circuit.	272
11.4 An 1800MHz Demodulator	279
11.4.1 The 1800MHz source	279
11.4.2 The homodyne stage	281

CONTENTS

11.5 The Complete Heterodyne Demodulator	288
12 Conclusions and Further Work	292
A Evaluation of Modified Bessel Functions	295
Bibliography	301

LIST OF FIGURES

2.1	Energy of an electron in a magnetic field	11
2.2	Parameters of an arbitrary orientation	11
2.3	Representation of a two level system	21
2.4	Excited state relaxations	24
3.1	Cavity equivalent circuit	30
3.2	The Relative values of χ' and χ''	34
3.3	Model of a coupled transmission cavity	36
3.4	Model of a coupled reflection cavity	38
3.5	Transmission cavity power transfer	40
3.6	Reflection cavity power transfer	41
3.7	A diagrammatic circulator	43
3.8	The final model of a reflection cavity used for simulation	44
3.9	Reflection cavity phase/amplitude response.	45
3.10	An absorption spectrometer	45
3.11	TE ₁₀₂ mode magnetic field distribution	48

LIST OF FIGURES

3.12	TE ₂₀₁ mode magnetic field distribution	48
3.13	A polarising spectrometer	50
3.14	Heterodyne outline	55
3.15	A homodyne spectrometer	65
4.1	Representation of an ESR Spectrometer	68
4.2	Attenuation of co-axial line	74
4.3	Attenuation of high frequency co-axial cable	75
4.4	Attenuation in waveguide	78
4.5	A magic T coupler	82
4.6	Quasi-optical isolator	83
4.7	Resonator dimensions	84
4.8	The TE ₁₀₂ mode of a rectangular cavity	85
4.9	The H ₀₁₁ mode of a cylindrical cavity	86
4.10	The H ₀₁₁ mode of a spherical cavity	88
4.11	A QO spectrometer	91
5.1	Negative resistance oscillator	98
5.2	Comparison of Oscillator Phase Noise	101
5.3	Comparison of harmonic generators.	105
5.4	Multiplier Amplifier Combinations	113
6.1	Delay Line Discriminator	117
6.2	The valid range of $\mathcal{L}(f)$ using a delay line discriminator . . .	126
6.3	Phase detector frequency response	127
6.4	Circuit of the discriminator	130
6.5	Realisation of the discriminator	131
6.6	Discriminator Noise Floor Measurement	135
6.7	Discriminator performance	138

LIST OF FIGURES

6.8	The down conversion process	139
6.9	87GHz Gunn oscillator phase noise	140
6.10	87GHz Hi Q Gunn oscillator phase noise	142
6.11	Circuit of a quasi-optical reaction mode cavity	144
6.12	Realisation of a reaction mode cavity	145
6.13	Normalised Q.O. cavity frequency responses	147
6.14	Curve fitted cavity frequency response	149
6.15	A mm-wave phase noise measurement system	150
7.1	Typical Gunn oscillator tuning parameters.	154
7.2	Calculated phase noise comparison	157
7.3	An FM coil driver	160
7.4	Outline PLL Source	162
7.5	The ELVA IMPATT x12 multiplier	165
7.6	Block diagram of a prototype Schottky Diode multiplier	167
7.7	Realisation of the prototype Schottky Diode multiplier.	168
7.8	The second Schottky Diode multiplier.	170
8.1	7.833GHz DRO phase noise	173
8.2	PMYTO parameters.	174
8.3	Oscillator test set.	176
8.4	YTO parameters.	177
8.5	The multiplier test set	180
8.6	IMPATT multiplied YTO performance	181
8.7	IMPATT multiplier phase noise	184
8.8	Performance of the second Schottky multiplier.	185
8.9	Performance of the first Schottky multiplier.	187
8.10	Performance of the second Schottky multiplier.	188

LIST OF FIGURES

8.11 Source comparison	190
8.12 Multiplier comparison	191
8.13 Spectrometer comparison.	194
9.1 A rectangular pulse and its Fourier dual.	201
10.1 OOK of a carrier using an output switch	213
10.2 Method of PIN switch testing.	215
10.3 PIN diode pulse envelopes.	216
10.4 The diode ring modulator.	219
10.5 DBM biphase modulator output	220
10.6 DBM switch output	221
10.7 Modified DBM switch	222
10.8 The use of a DBM based switch in a multiplier chain.	224
10.9 Diode current for various applied voltages.	225
10.10 Diode current for a Gaussian applied voltage.	226
10.11 Varactor response to a Gaussian envelope.	229
10.12 HMC220 attenuation characteristic	231
10.13 Multiplier power transfer characteristic	232
10.14 Realisation of a DBM based multiplier	233
10.15 DBM switch 94GHz pulse envelopes.	235
11.1 Outline Heterodyne detector	239
11.2 Spectrum of the conversion process.	240
11.3 Demodulator LO generation	242
11.4 94GHz spectrometer frequency plan.	244
11.5 Power distribution for the interpolation chain.	245
11.6 Interpolation mixer performance	246
11.7 150MHz crystal oscillator	249

LIST OF FIGURES

11.8 Crystal networks	253
11.9 Crystal oscillator performance	255
11.10 VCXO performance	258
11.11 Interpolation mixer output spectra.	261
11.12 YTO YTF tuning range comparison.	265
11.13 YTF frequency frequency response	266
11.14 Interpolation chain low level spectrum	268
11.15 Interpolation chain output spectra	270
11.16 Down convertor block diagram	272
11.17 Interpolation chain configurations	278
11.18 The 1800MHz multiplier chain.	280
11.19 1800MHz spectrum	282
11.20A two channel Homodyne demodulator.	283
11.21 Circuit diagram of the IQ demodulator.	286
11.22 The phase balance of the initial IQ demodulator	287
11.23 The complete Heterodyne Spectrometer	289
11.24 System pulse response	290

CHAPTER 1

Introduction

Spectroscopy is a window into the world of the atom and its constituent parts, and is probably one of the most important branches of practical physics. It has played a key role in confirming quantum mechanics - Newton's observation of dark lines in the solar spectrum remained something of a mystery until quantum mechanics explained spectra in terms of electron transitions within the atom. It has discovered new elements - spectroscopy of the Sun's Corona by Lockyer in 1868 revealed the existence of a previously unknown element, Helium.

When the spectrum of incandescent Sodium is viewed at optical wavelengths, two major spectral lines are observed. These are the 'D-Lines'. They lie in the orange part of the spectrum and have wavelengths of 5889\AA and 5895\AA [1]. These lines arise due to the interaction of an electron's orbit and its magnetic moment. When a sample of glowing Sodium is placed in a magnetic field and the spectrum observed, it is found that the D-Lines split into several

components, an effect first observed by Zeeman [2] and which is named after him.

The same spectrum may be observed if Sodium vapour is illuminated with white light. In this case however the spectrum is observed as dark lines imposed on a white light spectrum. This is an absorption spectrum and if the illuminated vapour is placed in a magnetic field the Zeeman effect is once again readily observed. If the illumination of the Sodium vapour (still in a magnetic field) is changed from light to an RF signal in the range MHz to THz depending upon the magnitude of the applied magnetic field, a new absorption spectrum is observed, these spectral lines correspond to transitions within the Zeeman system; and it is these transitions which form the Electron Spin Resonance (ESR) spectrum. There is also a nuclear Zeeman effect, and a corresponding RF spectrum; this is Nuclear Magnetic Resonance or NMR.

By varying the applied magnetic field, it is readily observed that the spacing between the lines of the Zeeman system varies with applied magnetic field, it is found that the frequency of ESR spectral line varies at a rate of 28GHz/T. The magnetic moments of neighbouring atoms will interact with the transitioning electron. The local magnetic field is the vector sum of the applied magnetic field and the effect of the interactions from the neighbours which gives rise to a potentially rich ESR spectrum from which the structure of the sample may be obtained.

ESR has become an important tool in the investigation of physical and biological systems. When tissue is exposed to radiation (both ionising and non-ionising) the level of exposure may be estimated by measuring changes in the ESR spectrum of bone and tooth material [3], a related measurement allows dating of archeological artifacts [4]. ESR has been used to determine

the structure of biologically important molecules such as the Heme complex [5] [6], chlorophyll [7], Rhodopsin [8] and to map structural changes during reactions [9].

Many biologically interesting molecules, such as DNA, are ESR quiet having either no or very low concentrations of paramagnetic centres within the molecule of interest, giving spectral signals which are either non existent or too small to be useful. However ESR may still be used as a spectroscopic tool by chemically substituting an ESR active species into the system of interest [10] [11]. This technique, known as Spin Labeling, is now finding wide application [12] [13] [14] and has also been employed by chemists in the study of polymers [15].

ESR has been employed to measure permeability directly in resonators for microwave circuits [16] and may be used to study phase transitions in low dimension systems [17] [18] [19].

Pulse ESR and NMR techniques directly manipulate the spin state of a system and these have been proposed as viable input and output devices in Quantum computers [20], [21].

This is not intended to be an extensive list of ESR applications- a search on the 'Web of Science' using 'Electron Spin Resonance' as the key word, produced over 5000 papers, published in the last five years with applications in all branches of the physical and biological sciences; it is intended to indicate the wide range of applications of ESR.

1.1 Thesis Overview

This thesis is concerned with the design of a 94GHz ESR spectrometer, employing low noise sources (both CW and pulsed) and a Heterodyne demodulator suitable for both CW and pulsed spectrometry. It gives a background in ESR theory, spectroscopy and instrumentation, followed by a detailed description of a new instrument.

Chapter 2 describes the interaction of electrons with magnetic fields. It is shown that by applying two orthogonal magnetic fields, a large static (or slowly sweeping) field and a small high frequency (RF/Microwave) field, to a suitable sample it is possible to obtain a signal which may form the basis of a spectroscopic technique. By considering relaxation mechanisms, it is also shown that the magnitude of the oscillating field cannot be usefully increased without limit. Chapter 3 considers how an ESR signal is produced by a paramagnetic sample placed in a resonant cavity. By considering the Noise Effective Powers (NEPs) of detectors, the concentration sensitivity (minimum detectable number of spins) of a spectrometer is obtained and a Homodyne detector is described.

Chapter 4 describes the essential components of a spectrometer, such as magnets and methods of propagating microwave signals within the spectrometer and which are not considered elsewhere in this thesis. It shows how consideration of these components leads to the design of the quasi-optical Homodyne spectrometer which is currently employed at St Andrews. Significant factors which limit spectrometer sensitivity are the phase noise and power produced by a 94GHz source, chapters 5 to 8 describe a low noise source capable of delivering in excess of 200mW (+23dBm) at 94GHz. Chapter 5 considers ways in which low noise mm-wave sources may be produced. Because phase noise is so important, methods of measuring phase

noise were investigated. Chapter 6 describes a phase noise measuring system for use at 94GHz based on a highly stabilised Gunn oscillator being used to down convert the mm-wave signal to a frequency at which phase noise measurement may be more easily performed. In this case the low frequency phase noise measurement was performed using a delay line discriminator optimised for use at 7GHz. Chapter 7 then describes sources based round various oscillators and multipliers.

Chapter 8 details the performance of these oscillator-multiplier combinations in terms of power output, phase noise and where applicable tuning range. It is demonstrated that a significant reduction in the spectrometer noise floor compared to that obtained using a Gunn oscillator can be obtained with the correct choice of oscillator-multiplier combination.

A problem with CW ESR spectrometry is the lack of resolution caused by overlapping signals. In the field of NMR, techniques which use pulses of RF energy to manipulate the nuclear spin system have been developed which permit the use of sophisticated correlation techniques which allow the contributions to be differentiated or resolved. Whilst such techniques have been employed in low field ESR, it would be of great advantage if these techniques could be brought to bear in high field ESR. Chapter 9 obtains the characteristics which pulses for use in a high field pulsed ESR spectrometer must ideally possess. It is demonstrated that it would be highly beneficial to generate pulses with $\sim 1\text{ns}$ duration and peak powers of 1kW. Whilst pulse spectrometry is performed using high field instruments, to date the available pulses have been sub-optimal. Chapter 10 describes a fast switch which when used in conjunction with the multipliers described in previous chapters is able to produce rectangular sub ns pulses at the +23dBm level and which are suitable for amplification to the kW level.

1.1. THESIS OVERVIEW

Finally, chapter 11, describes a complete Heterodyne spectrometer, operating at 94GHz and which is suitable for pulsed high field ESR spectrometry.

CHAPTER 2

Continuous Wave Electron Spin Resonance

Electron Spin Resonance (ESR) spectroscopy, which is also known as Electron Paramagnetic Resonance (EPR) spectroscopy, is a technique which measures the absorption of RF energy by a sample containing paramagnetic species when it is placed in a magnetic field. The results of this measurement may be used to elucidate the structure of the sample.

Conceptually, absorption from a continuous (CW) RF signal is the simplest ESR experiment which may be performed. However, there is often insufficient detail in the absorption spectrum for the structure to be resolved at a particular frequency, in which case a higher frequency CW measurement, a pulsed measurement or a double resonance experiment may help determine the structure of the sample.

In this chapter, the origin of the CW absorption spectrum and how this leads

2.1. THE ELECTRON IN A MAGNETIC FIELD.

to the design of a spectrometer are discussed.

2.1 The electron in a magnetic field.

In this section, the dynamics of a single electron in a magnetic field are used to explain the origin of the EPR spectrum. This is an attractive scheme for initial discussion because there are no complications of orbital or nuclear effects. Two cases are considered; in the first the electron is immersed in a uniform, constant magnetic field, whilst in the second an oscillating magnetic field perpendicular to the constant field is introduced.

2.1.1 The electron in a constant magnetic field

Due to its spin angular momentum \mathbf{S}^1 , an electron has a magnetic moment

$$\boldsymbol{\mu}_S = g\beta\mathbf{S} \quad (2.1)$$

where g is the Landé g -factor having a value close to 2, and β is the Bohr magneton defined by

$$\beta = \frac{e\hbar}{2m_e} \quad (2.2)$$

where e is the electronic charge, m_e is the mass of the electron and therefore $\beta \sim 9.274 \times 10^{-24} \text{JT}^{-1}$. By virtue of its magnetic moment, an electron placed in a magnetic field has a potential energy

$$H = -\boldsymbol{\mu}_S \cdot \mathbf{B} \quad (2.3)$$

$$= g\beta\mathbf{S} \cdot \mathbf{B} \quad (2.4)$$

¹Bold characters are use to denote vector quantities

2.1. THE ELECTRON IN A MAGNETIC FIELD.

Where, in equation 2.4, the minus sign is dropped to account for the negative electron charge. Equation 2.3 shows that, classically, the energy of the moment in the magnetic field has an infinite number of values depending upon its angle (θ) to the applied magnetic field. However, the energy is a minimum when the spin is parallel ($\theta = 0$) to the applied field, and a maximum when the spin vector is anti-parallel ($\theta = \pi$) to the applied magnetic field.

Naively, it is expected that no matter what the initial orientation of the magnetic moment, it will align its self in the lowest energy state; this statement is discussed further in section 2.3. Then, if energy is applied to the system, the electron may be re-orientated into the higher energy state, an absorption of energy which may be measured and which may form the basis of a spectroscopic technique. In fact, ESR involves measuring the energy required to re-orientate an electron spin vector in an applied magnetic field.

2.1.1.1 The electron aligned with the applied field

If an electron is immersed in a magnetic field, the Stern-Gerlach experiment shows that, contrary to the above classical expectations, the electron may assume only two orientations in the applied magnetic field; it may only be parallel or anti-parallel to the applied field. It is concluded that electron spin is quantised.

To account for this quantisation, it is convenient to redefine S in terms of the Pauli Spin Matrices as

$$S = \frac{1}{2}\hbar\sigma \quad (2.5)$$

2.1. THE ELECTRON IN A MAGNETIC FIELD.

where σ is the spin matrix having the three components [22]

$$\sigma_x = \begin{pmatrix} 0 & 1 \\ 1 & 0 \end{pmatrix} \quad \sigma_y = \begin{pmatrix} 0 & -i \\ i & 0 \end{pmatrix} \quad \sigma_z = \begin{pmatrix} 1 & 0 \\ 0 & -1 \end{pmatrix}$$

Which account for the three spatial components of S . Equation 2.4 becomes

$$H = g\beta\sigma \cdot \mathbf{B} \quad (2.6)$$

The magnetic field is applied along the z-axis and the potential energy represents the Hamiltonian of the electron in the applied magnetic field. The electron is an eigenstate of σ_z and thus

$$H = g\beta B_z \sigma_z \quad (2.7)$$

$$= \omega_o \frac{\hbar}{2} \begin{pmatrix} 1 & 0 \\ 0 & -1 \end{pmatrix} \quad (2.8)$$

where $\omega_o = g\beta B_z$. The permitted energies of the system are the eigenvalues of the Hamiltonian and because the Hamiltonian is diagonal they are the diagonal elements of the Hamiltonian; thus

$$E_+ = \frac{\hbar\omega_o}{2} \quad (2.9)$$

$$E_- = -\frac{\hbar\omega_o}{2} \quad (2.10)$$

Comparison with equation 2.4 shows E_+ to correspond to the case of the electron spin parallel to the applied field, whilst E_- corresponds to the anti-parallel case. An electron being re-oriented in the magnetic field must therefore either emit or absorb a photon of energy $E_+ - E_-$, which corresponds to a frequency (f Hz) of

$$f = g \frac{1}{2\pi} \frac{e}{2m_e} B_z \quad (2.11)$$

The exact frequency of this transition depends crucially upon the applied external magnetic field and the value of g , which is close to 2. Therefore the

2.1. THE ELECTRON IN A MAGNETIC FIELD.

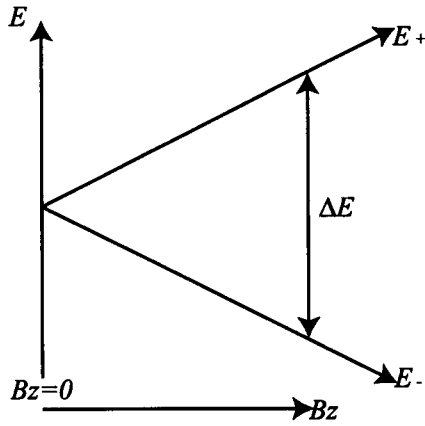


Figure 2.1: Energy of an electron in a magnetic field

frequency of the transition varies with B_z at a rate of order 28GHz/T. This is summarised in figure 2.1.

2.1.1.2 The arbitrarily aligned electron

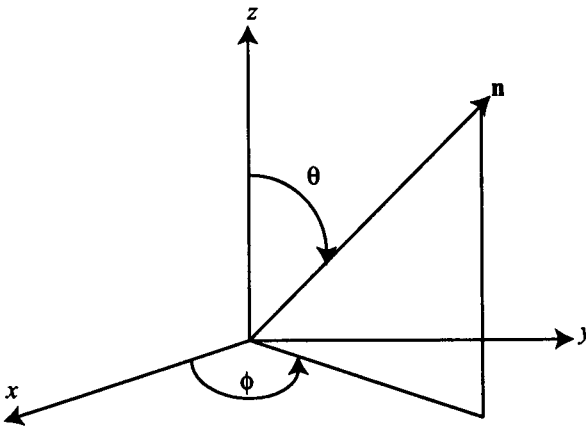


Figure 2.2: Parameters of an arbitrary orientation

Figure 2.2 shows a unit vector \hat{n} arbitrarily aligned in a cartesian co-

2.1. THE ELECTRON IN A MAGNETIC FIELD.

ordinate system. If \hat{i} , \hat{j} and \hat{k} are the usual cartesian unit vectors, it is a standard result [23] that

$$\hat{n} = \hat{i} \sin \theta \cos \phi + \hat{j} \sin \theta \sin \phi + \hat{k} \cos \theta \quad (2.12)$$

If an electron spin is aligned with \hat{n} , then the projection of this spin S_n onto the cartesian axis is

$$S_n = \mathbf{S} \cdot \hat{n} \quad (2.13)$$

$$= \sigma_x \sin \theta \cos \phi + \sigma_y \sin \theta \sin \phi + \sigma_z \cos \theta \quad (2.14)$$

and thus S_n may be represented as

$$S_n \doteq \frac{\hbar}{2} \begin{pmatrix} \cos \theta & \sin \theta e^{-i\phi} \\ \sin \theta e^{i\phi} & -\cos \theta \end{pmatrix} \quad (2.15)$$

The eigenvalues of equation 2.15 are $\lambda_+ = +\hbar/2$ and $\lambda_- = -\hbar/2$, giving eigenvectors of

$$|+\rangle_n = \begin{pmatrix} \cos \frac{\theta}{2} \\ e^{i\phi} \sin \frac{\theta}{2} \end{pmatrix} \text{ and } |-\rangle_n = \begin{pmatrix} \sin \frac{\theta}{2} \\ -e^{i\phi} \cos \frac{\theta}{2} \end{pmatrix}$$

respectively. Consider a magnetic field applied along the z-axis. The energy levels associated with an electron in this field are E_+ and E_- and are given in equations 2.9 and 2.10. Consider an electron in a 'spin up' state along \hat{n} , immersed in this magnetic field. Then the initial state of the electron is $|\psi(0)\rangle = |+\rangle$. Thus, the time evolved state of the electron $|\psi(t)\rangle$ may be represented as

$$|\psi(t)\rangle \doteq \begin{pmatrix} e^{-\frac{iE_+}{\hbar}t} \cos \frac{\theta}{2} \\ e^{-\frac{iE_-}{\hbar}t} e^{i\phi} \sin \frac{\theta}{2} \end{pmatrix} \quad (2.16)$$

which using equations 2.9 and 2.10 simplifies to

$$|\psi(t)\rangle \doteq e^{-\frac{i\omega_0 t}{2}} \begin{pmatrix} \cos \frac{\theta}{2} \\ e^{i(\phi - \omega_0 t)} \sin \frac{\theta}{2} \end{pmatrix} \quad (2.17)$$

2.1. THE ELECTRON IN A MAGNETIC FIELD.

The expectations of the three spin components ($\langle S_x \rangle$, $\langle S_y \rangle$ and $\langle S_z \rangle$) are therefore given by

$$\langle S_x \rangle = \langle \psi(t) | \sigma_x | \psi(t) \rangle = \frac{\hbar}{2} \sin\theta \cos(\omega_0 t + \phi) \quad (2.18)$$

$$\langle S_y \rangle = \langle \psi(t) | \sigma_y | \psi(t) \rangle = \frac{\hbar}{2} \sin\theta \sin(\omega_0 t + \phi) \quad (2.19)$$

$$\langle S_z \rangle = \langle \psi(t) | \sigma_z | \psi(t) \rangle = \frac{\hbar}{2} \cos\theta \quad (2.20)$$

Equation 2.20 shows the orientation of the electron to the z-axis to be time invariant. However, the motion of the electron in the x-y plane is the vector sum of $\langle S_x \rangle$ and $\langle S_y \rangle$; since equations 2.18 and 2.19 are the parametric equations of a circle, we conclude that the electron precesses about the applied magnetic field at a frequency of ω_0 rad/sec. This frequency of precession is known as the Larmor frequency.

2.1.2 The effect of an oscillating magnetic field

Ignoring the practicalities of producing a totally isolated electron and the problems of excited state life times, if a 1T magnetic field oscillating at 28GHz were applied to a single electron system, and the system temperature were to be reduced sufficiently, an absorption of energy would be observed. Even allowing the above simplifications, such a scheme is impractical; the inductance of the magnet (typically many Henrys) ensures that coupling high frequencies onto the magnetic field using the magnet coils is impossible.

However, consider an electron immersed in a constant (time independent) field B_z aligned with the z-axis, and an oscillating field $B_x \cos \omega t$ aligned with the x-axis. Equation 2.7 now reads

$$H = g\beta (B_z \sigma_z + B_x \sigma_x \cos \omega t) \quad (2.21)$$

2.1. THE ELECTRON IN A MAGNETIC FIELD.

The application of B_x causes a nutation of the Larmor precession, the frequency of which (the nutation frequency) is given by

$$\omega_x = g\beta B_x \quad (2.22)$$

Writing the Larmor and nutation frequencies explicitly, equation 2.21 may be represented as

$$H \doteq \frac{\hbar}{2} \begin{pmatrix} \omega_o & \omega_x \cos \omega t \\ \omega_x \cos \omega t & -\omega_o \end{pmatrix} \quad (2.23)$$

With a time dependant Hamiltonian, we require to solve the Schrödinger equation expressed in the form

$$i\hbar|\dot{\psi}(t)\rangle = H(t)|\psi(t)\rangle \quad (2.24)$$

where $\dot{\psi}$ denotes a time derivative. By writing² $|\psi(t)\rangle \doteq [a(t), b(t)]^T$, where $a(t)$ and $b(t)$ are the eigenfunctions of $\psi(t)$ and represent the time evolution of the electron spin states. The solution of 2.24 is set out in both [22] and [24].

Substituting this state vector and the Hamiltonian into equation 2.24 results in a pair of coupled differential equations

$$i\dot{a}(t) = \frac{a(t)}{2}\omega_o + \frac{b(t)}{2}\omega_x \cos \omega t \quad (2.25)$$

$$i\dot{b}(t) = -\frac{b(t)}{2}\omega_o + \frac{a(t)}{2}\omega_x \cos \omega t \quad (2.26)$$

The leading terms in this system of equations are due to rotation about the z-axis. The equations may be rendered approximately soluble, by transforming these equations from the laboratory frame, to a frame rotating about the z

²The wavefunction is written here as its transpose for typographic reasons, "T" indicating the transpose.

2.1. THE ELECTRON IN A MAGNETIC FIELD.

axis at the Larmor frequency; this is exactly the same as the ‘rotating frame’ introduced by Bloch [25] in the classical derivation of Bloch Equations.

In this rotating frame, the electron appears stationary, aligned with the applied magnetic field, and a field applied perpendicular to B_z will cause precession about the applied perpendicular field. The transformation to the rotating frame may be performed by writing

$$\begin{pmatrix} a(t) \\ b(t) \end{pmatrix} = \begin{pmatrix} \alpha(t)e^{-i\omega_0 t/2} \\ \beta(t)e^{i\omega_0 t/2} \end{pmatrix} \quad (2.27)$$

Now, using these expressions in equations 2.25 and 2.26, with the additional assumption that $\omega_0 \sim \omega$ and writing $\Delta = \omega_0 - \omega$ gives

$$i\dot{\alpha}(t) = \frac{1}{2}\omega_x\beta(t)e^{i\Delta t} \quad (2.28)$$

$$i\dot{\beta}(t) = \frac{1}{2}\omega_x\alpha(t)e^{-i\Delta t} \quad (2.29)$$

which, upon elimination of $\beta(t)$ produces the second order linear homogeneous differential equation

$$\ddot{\alpha}(t) - i\Delta\dot{\alpha}(t) + \frac{\omega_x^2}{4}\alpha(t) = 0 \quad (2.30)$$

which may be solved to obtain

$$\alpha(t) = \alpha_+e^{i\lambda_+t} + \alpha_-e^{i\lambda_-t} \quad (2.31)$$

$$\beta(t) = -\frac{2}{\omega_x}e^{-i\Delta t}(\lambda_+\alpha_+e^{i\lambda_+t} + \lambda_-\alpha_-e^{i\lambda_-t}) \quad (2.32)$$

in which λ_{\pm} are the roots of the auxiliary function of equation 2.30 and are given by

$$\lambda_{\pm} = \frac{1}{2} \left[\Delta \pm \sqrt{\Delta^2 + \omega_x^2} \right] \quad (2.33)$$

Use of equations 2.27, 2.31 and 2.32 now gives the original state vector $[a(t), b(t)]^T$. If, at $t = 0$, the electron is in an ‘up’ state such that $|\psi(0)\rangle =$

2.1. THE ELECTRON IN A MAGNETIC FIELD.

$[a(0), 0]^T$ we may calculate the probability of it being in a 'down' state $|\psi(t)\rangle = [0, b(t)]^T$. It is a standard result that

$$P(\downarrow) = |\langle - | \psi(t) \rangle|^2 \quad (2.34)$$

$$= \left| (0, b(t)) \begin{pmatrix} a(t) \\ b(t) \end{pmatrix} \right|^2 \quad (2.35)$$

$$= |b(t)|^2 \quad (2.36)$$

The initial conditions allow relationships to be found between λ_{\pm} and α_{\pm} , it is found that

$$|b(t)|^2 = \frac{1}{2} \frac{\omega_x^2}{\Delta^2 + \omega_x^2} \left[1 - \cos \left(\sqrt{\Delta^2 + \omega_x^2} t \right) \right] \quad (2.37)$$

Where as previously a resonance condition was defined as bringing the frequency of an oscillating field B_z to a point which matched the Larmor Frequency, in this case B_z is fixed and we define the resonance condition to be $\Delta = 0$ i.e. the frequency of the perpendicular field is made to equal the Larmor Frequency, in which case

$$|b(t)|^2 = \frac{1}{2} [1 - \cos \omega_x t] \quad (2.38)$$

Interestingly, this result is independent of the magnitude of B_x , which only determines the rate at which the spin is flipped from an up to a down state; the probability of a spin flip depends only upon the value of $\omega_x t$. When $\omega_x t = \pi$, $P(\downarrow) = 1$ and the electron is in the down state.

Thus we have a theoretical design for an ESR spectrometer. It consists of a fixed field which establishes the Larmor frequency, and a high frequency perpendicular field which is tuned to the Larmor frequency. Because the perpendicular field changes the spin state of the electron, energy is absorbed from this field and this energy absorption may be measured, and it is this

2.2. ESR SPECTRA

absorption which forms the basis of ESR measurements. Note that there is no particular requirement put on the magnitude of B_x , the magnitude is determined by other system requirements.

The implementation of this theoretical design is outlined in the following chapters. The remainder of this chapter is devoted to a discussion of the information which may gathered from a CW spectrometer of this type.

2.1.3 Single Electron Measurements

It may be thought that single electron systems are purely theoretical constructs, and even if they could be realised would show little of interest because the resonance has only one component. In fact there is a rich literature on the physics of the single electron in an ESR type measurement.

By isolating a single electron in a Penning Trap [26, 27] it has been possible to observe single electron resonances, measure the g factor of a free electron (and indeed the positron [28]); such systems appear to be sensitive methods of performing tests of some of the most fundamental aspects of modern physics.

2.2 ESR Spectra

Whilst the single electron allows a simple calculation to give an outline design of a spectrometer, the more interesting, and more important case is that of the spectrum obtained from a paramagnetic species when it interacts with its local environment. In this section the various contributions to an ESR spectrum are outlined.

2.2. ESR SPECTRA

2.2.1 The Landé g-factor

An electron in an orbital has an orbital angular momentum L , and therefore an orbital magnetic moment μ_L given by

$$\mu_L = g\beta L \quad (2.39)$$

A system having both spin and orbital angular momenta, has a total angular momentum J which is the vector sum of L and S . The overall magnetic moment associated with the total angular momentum is

$$\mu = g\beta J \quad (2.40)$$

By considering the magnitudes of the spin and orbital magnetic moments and applying the cosine rule [29], the Landé g-factor may be written as

$$g = 1 + \frac{J(J+1) + S(S+1) - L(L+1)}{2J(J+1)} \quad (2.41)$$

and therefore has a value ranging from 1 for a system having pure orbital angular momentum to 2 for a system having pure spin angular momentum. In many systems however, the motion of the electron in its orbital reduces the apparent orbital angular momentum, a process known as Quenching. The value of g is often found to be close to the value for completely free electron of $g \sim 2.0023$. However, other values are encountered, transition metal complexes in which high angular momenta are encountered produce g values in excess of 4 [30], whilst negative values may be found in semiconductor systems [31].

A system having a non zero total angular momentum has a permanent magnetic dipole moment and thus the local magnetic field is the vector sum of the applied (external) field and the local magnetic moment; and therefore in calculating the energy of the interaction of the magnetic moment with the

2.2. ESR SPECTRA

applied field it should be the effective field which is employed. The local field at any given location within a sample now depends crucially upon the environment -the number of and distance to neighboring moments at that point. Since we can have no apriori knowledge of this local environment, with a known external field when measuring the ESR spectrum we appear to have a varying g-factor.

This variation of g is often anisotropic, and in the general case is a Tensor with 6 independent components. It is this variation of g-factor which is responsible for the multiple line in an ESR spectrum, and which allows the structure of the ensemble to be determined.

2.2.2 The Spin Hamiltonian

The electron system considered in section 2.1, a two level system, is the simplest system which can be described. In more complicated systems, the Hamiltonian must be modified to account for interactions between the paramagnetic species with its environment. These interactions are described using the *spin Hamiltonian*, which may be written [32]

$$H = \mathcal{H}_{elec} + \mathcal{H}_{cf} + \mathcal{H}_{LS} + \mathcal{H}_{SS} + \mathcal{H}_{Zee} + \mathcal{H}_{hfs} + \mathcal{H}_Q + \mathcal{H}_N \quad (2.42)$$

in which

- \mathcal{H}_{elec} is the energy of the paramagnetic species in the free state
- \mathcal{H}_{cf} is the interaction energy of the ion with the crystalline field
- \mathcal{H}_{LS} is the spin-orbit interaction energy
- \mathcal{H}_{SS} is the spin-spin interaction energy
- \mathcal{H}_{Zee} is the Zeeman energy
- \mathcal{H}_{hfs} accounts for the hyperfine structure

2.3. THERMAL EFFECTS

\mathcal{H}_Q is the quadrupole energy

\mathcal{H}_N is the nuclear spin energy

Detailed descriptions of the importance and relative significance of the various components of the spin Hamiltonian may be found in [32, 33] and [34].

\mathcal{H}_{Zee} describes the energetics of the spectrum which would be observed in the absence of any other interactions, and is the Hamiltonian of the simple two level system described above. The terms \mathcal{H}_{elec} and \mathcal{H}_{cf} describe the g-factor variation, and therefore ESR spectrometry is the measurement of changes in the Zeeman term of the spin Hamiltonian due to the interaction of a paramagnetic species with its environment.

2.3 Thermal effects

It was stated above that the electron would assume a state of minimum energy; this is not strictly true. In an applied field of 1T, the energy of the 28GHz photon required to 'flip the electron spin' is approximately $1.856 \times 10^{-23} \text{ J}$ ($\sim 1.16 \times 10^{-4} \text{ eV}$), whilst at 300K thermal energy is of order $1/40 \text{ eV}$; thus thermal energy alone is sufficient to maintain the electron in a high (anti-parallel to the applied magnetic field) state.

Naturally, the physical environment could be changed to give a system in which the electron was in the lowest energy state. If the applied magnetic field is increased, the energy of the photon required to change the spin state of the electron will be increased. For the photon energy to exceed $1/40 \text{ eV}$, a frequency of order 6THz is required, which corresponds to a required magnetic field of some 214T. This field is a little excessive! The problems of generating a 40T continuous field are extreme [35], and include power sup-

2.3. THERMAL EFFECTS

ply and cooling issues. 65T 'long pulse' magnets are discussed by [36], whilst the destructive nature of producing fields in excess of 200T may be observed in some interesting footage at the Tokyo University web site ³. Naturally, the temperature could be reduced to bring kT to less than $1.16 \times 10^{-4} \text{eV}$; a temperature of less than approximately 1.4K is required.

For an ensemble of electrons the situation is rather different. In a two level

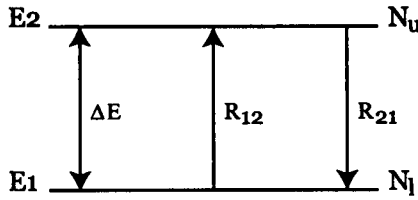


Figure 2.3: Representation of a two level system, showing the populations N_u and N_l of the two energy levels E_1 and E_2 spaced by ΔE and the rates of transition between these energy levels R_{12} and R_{21} .

system, the relative populations of the two energy levels is described by a Boltzman distribution

$$\frac{N_u}{N_l} = \exp \left[-\frac{\Delta E}{kT} \right] \quad (2.43)$$

where N_u and N_l are the populations of the upper and lower energy levels respectively. Taking the figures for a 28GHz system at 1T from above, at 300k the population is such that $N_u \sim 4.6 \times 10^{-2} N_l$ and this is an equilibrium state.

An ESR measurement proceeds by measuring energy absorption from the applied B_x field, which is proportional to the the difference between the populations of the energy levels. Let P_{abs} be the power absorbed and Φ be a

³www.issp.u-tokyo.ac.jp/labs/extreme/Megagauss/MGL/MGL-e.html -checked 6 August 2005.

2.3. THERMAL EFFECTS

constant of proportionality. Then

$$P_{abs} = \Phi (N_l - N_u) \quad (2.44)$$

$$= \Phi \Delta N \quad (2.45)$$

Which shows that power will only be absorbed by the system until $\Delta N = 0$ when the sample is said to be saturated.

However, using a Taylor expansion for equation 2.43, with the assumption that $\Delta E/kT \ll 1$ equation 2.43 becomes

$$P_{abs} = N_l \frac{\Phi}{kT} g\beta B_x \quad (2.46)$$

This would appear to suggest that the power absorbed increases indefinitely with the applied field B_x . Applying energy to the system effectively increases the spin temperature of the system, so that the spin system is no longer in thermal equilibrium with its environment and loses energy from the excited spin system to the local thermodynamic bath, a process known as relaxation. The relaxation of the excited state plays an important role in obtaining a good ESR spectrum.

2.3.1 A Simple Model of Relaxation

A description may be set out as follows [33]. For a sample containing N spins and having a population difference ΔN between the levels, considering figure 2.3 we may write

$$\left. \begin{array}{l} N = N_l + N_u \\ \Delta N = N_l - N_u \end{array} \right\} \Rightarrow \left. \begin{array}{l} \frac{1}{2} (N + \Delta N) = N_l \\ \frac{1}{2} (N - \Delta N) = N_u \end{array} \right\} \Rightarrow \begin{array}{l} \frac{d}{dt} N_l = \frac{1}{2} \frac{d}{dt} \Delta N \\ \frac{d}{dt} N_u = -\frac{1}{2} \frac{d}{dt} \Delta N \end{array} \quad (2.47)$$

Now, the rate at which electrons enter or leave a level is proportional to the population difference ΔN , and the constant of proportionality is the rate

2.3. THERMAL EFFECTS

of transition between levels. The rate of change in population of a level is therefore the sum of the rates at which electrons enter and leave a level.

Using equations 2.47 we may write

$$\frac{d}{dt}N_l = \Delta N R_{12} + \Delta N R_{21} \quad (2.48)$$

which gives rise to the rate equations

$$\begin{aligned} \frac{d}{dt}N_l &= -R_{12}N_l + R_{21}N_u \\ \frac{d}{dt}N_u &= R_{12}N_l - R_{21}N_u \end{aligned} \quad (2.49)$$

Then using equations 2.47 and 2.49 it may be shown that

$$\frac{d}{dt}\Delta N = 2 \left[N \frac{R_{21} - R_{12}}{R_{21} + R_{12}} - \Delta N \right] [R_{21} + R_{12}] \quad (2.50)$$

In the steady state $\Delta \dot{N} = 0$, and the steady state population difference (ΔN_{ss}) between the two levels is found to be

$$\Delta N_{ss} = N \frac{R_{21} - R_{12}}{R_{21} + R_{12}} \quad (2.51)$$

Noting that $(R_{21} + R_{12})^{-1}$ has the dimensions of time, equations 2.50 and 2.51 produce

$$\frac{d}{dt}\Delta N = \frac{2}{\tau} (\Delta N_{ss} - \Delta N) \quad (2.52)$$

where τ is the relaxation time given by $(R_{21} + R_{12})^{-1}$. Assuming that at $t = 0$, $\Delta N(0) = N_o$, this has the general solution

$$\Delta N(t) = \Delta N_{ss} + (N_o - \Delta N_{ss}) \exp \left[-\frac{2t}{\tau} \right] \quad (2.53)$$

Thus, the relaxation from the excited state follows an exponential law.

Whilst the probability of a spin flip is governed by ω_x , B_x (and hence ω_x) cannot be made arbitrarily large. Figure 2.4 is a representation of spin excitation and relaxation during one-and-a-half cycles of ω_x . Excitation occurs in the half cycle which includes the section of the curve O-A. Beyond A

2.3. THERMAL EFFECTS

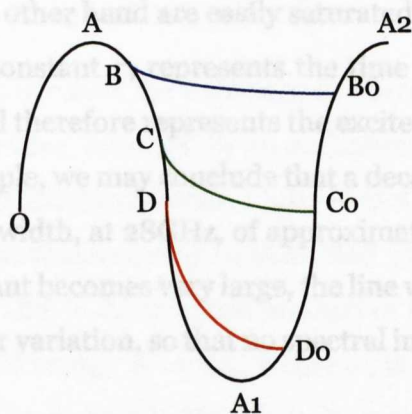


Figure 2.4: Spin flips during One-and-a-half cycles of ω_x applied to a paramagnetic sample. Excitation occurs during O-A, whilst relaxation occurs in the following period. A long relaxation time constant (blue), an intermediate relaxation time constant (green) and a short relaxation time constant (Red) are also shown.

relaxation takes place and three exponential decays of varying time constant τ are shown.

Relaxation A-D-Do represents a short time constant, relaxation A-B-Bo represents a long time constant, whilst A-C-Co is an intermediate case. Clearly the relaxation A-D-Do ensures that the maximum number of spins is available for excitation during the next (and each) cycle and represents a system of potentially high sensitivity, whilst the inverse is true for the A-B-Bo relaxation.

Because the probability of a spin flip follows ω_x and not the frequency (ω) of the applied B_x field which is tuned to the Larmor frequency due to B_z , it may be concluded that a short time constant implies that a large B_x may be applied to the system without saturation of the sample. Samples having long

2.3. THERMAL EFFECTS

time constants on the other hand are easily saturated.

The relaxation time constant τ , represents the time taken for the electron ensemble to relax, and therefore represents the excited state life time. Using the uncertainty principle, we may conclude that a decay time constant of 1ns corresponds to a line width, at 28GHz, of approximately 5.6mT. Thus if the relaxation time constant becomes very large, the line widths may well exceed spacing due to g-factor variation, so that no spectral information is obtained.

2.3.2 Relaxation Mechanisms

The above analysis introduced τ , the relaxation time constant. A more detailed analysis shows that there are two time constants involved in the relaxation process.

This detailed analysis was first performed by Bloch [25]. By recognising that time evolution of the expectation value of a single spin in a magnetic field exactly follows the classical equations of motion, Bloch was able to use a wholly classical analysis of the magnetisation vector to obtain the behavior of a spin ensemble.

The analysis requires the introduction of two time constants τ_1 and τ_2 . τ_1 relates to the loss of energy from the excited spin state to the crystal lattice which is sometimes known as longitudinal relaxation, whilst τ_2 relates to energy transfer within the spin system and is often known as transverse relaxation; the single time constant introduced above is an amalgamation of these processes.

2.3. THERMAL EFFECTS

2.3.2.1 Spin-lattice (longitudinal) relaxation

Spin-lattice relaxation involves the exchange of energy between the excited spin system and the lattice, followed by an exchange of energy between the lattice and the system thermodynamic bath; It is a two stage process for which three major contributions may be identified [34].

- *The direct process.* This is the simplest method of relaxation. The excited state emits a phonon of energy $E = \hbar\omega_p$, where ω_p is the phonon frequency. If this phonon is able to excite a lattice phonon, energy is lost to the lattice which may then be lost to the thermodynamic bath. At 'normal' temperatures, the lattice phonon density of states peaks at energies rather higher than E_p , and therefore the direct process is a low temperature relaxation mechanism.
- *The Raman process.* This is a two phonon process. Here, the spin system absorbs a phonon of energy ω_s and emits a phonon of energy $\omega_s \pm \omega_p$. This corresponds to a transition to a virtual energy level, and then a relaxation from this level to the ground state with a change of spin.
- *The resonant Raman (Orbach) process.* This relaxation mechanism is another two phonon process. In this case however, rather than a virtual energy level, the energy of the emitted phonon corresponds to an actual energy level; it is a rather more efficient process than the Raman process.

2.3.2.2 Spin-spin (transverse) relaxation

Whilst longitudinal relaxation requires a more or less direct energy transfer to the thermodynamic bath, in spin-spin relaxation direct energy transfer to the lattice is not required. Here, energy loss is by a dipole-dipole interaction between an excited and a neighboring unexcited site, the excited state in undergoing a relaxation (spin flip) transfers its energy to the unexcited state,

2.4. THE ADVANTAGES OF HIGH FIELD ESR

an exchange known as a two-spin flip flop process, and this constitutes spin-spin relaxation [34, 37, 38].

2.4 The Advantages of High Field ESR

ESR spectrometers are commercially available at frequencies ranging from 100s of MHz to 35GHz, although 94GHz instruments are becoming available.

The RF techniques required at the lower frequencies are reasonably straight forward, and become increasingly difficult as frequency increases. At low frequencies, standard electromagnets may be used to provide the B_z field. Such instruments, particularly at 10GHz, are becoming reasonably common. With the commercial availability of 10GHz and 35GHz ESR spectrometers, it is natural to enquire why it is desirable to use High Field ESR, with its attendant requirements for large and expensive superconducting magnets and technically challenging RF design requirements.

It will be shown later (section 3.8) that the minimum detectable number of spins (the spectrometer concentration sensitivity) is proportional to the applied field $1/B_z$, whilst equation 2.11 shows that the frequency of the resonance is directly proportional to the applied field B_z . Thus whilst increasing the magnetic field from 0.357T to 3.57T increases the concentration sensitivity by a factor of 10, it also increases the resonance frequency by a factor of 10, in this case from 10GHz to 100GHz. It may be shown [39] that the concentration sensitivity of the spectrometer varies as $f^{-7/2}$ and thus a change of frequency by a factor of 10 will improve the concentration sensitivity by a factor of 3100.

An additional advantage comes with the ability to resolve changes in the

2.4. THE ADVANTAGES OF HIGH FIELD ESR

g-factor. It may be shown [40] that two spectral lines occurring due to a difference in g-factor of Δg , will just be resolved if

$$B_z \frac{\Delta g}{g_{iso}} > \Delta B_{1/2} \quad (2.54)$$

where g_{iso} is the isotropic g-factor and $B_{1/2}$ is the resonance line half width, provided the line width does not increase with applied field. This inequality is known as the *high field condition*, and demonstrates that the resolution of a spectrometer is proportional to the applied field and therefore, to obtain high g-factor resolution, it is necessary to employ the highest possible frequency. It is also important to note that this condition is not met by many important systems until frequencies of 94GHz and above are employed [41].

CHAPTER 3

The Measurement of Paramagnetic Changes

Assuming that both a suitable signal source to provide the oscillating field (B_x) and a suitable magnet to provide the static field (B_z) are available, the required orthogonality of the static and oscillating fields may be obtained by placing the sample in a resonant structure called a cavity, as described in chapter 4.

The ESR experiment detects changes in the susceptibility of the paramagnetic sample, usually as a function of the applied magnetic field B_z . These changes alter the properties of the cavity in which the sample has been placed and therefore, an ESR spectrum is obtained by measuring the properties of the cavity as B_z varies.

This chapter describes how cavity parameters may be measured to obtain a spectrum and a simplistic spectrometer design is outlined. The sensitivity

3.1. THE CAVITY

of the spectrometer, in terms of the minimum number of detectable spins (concentration sensitivity) is evaluated and the outline of a Homodyne detector is presented.

3.1 The equivalent circuits of cavities

A microwave cavity may consist of a hollow box or cylinder constructed from a highly conductive metal, or be a piece of dielectric. In either case, in the vicinity of a resonance the cavity may be represented by an LCR circuit as shown in figure 3.1.

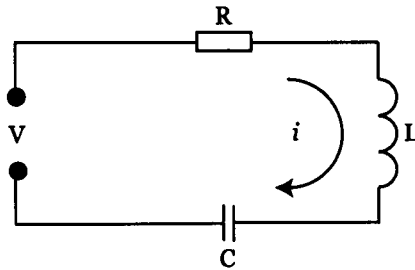


Figure 3.1: The equivalent circuit of a microwave cavity. A parallel circuit may also be used, in which case current excitation is employed and the voltage developed by the network is investigated.

Where L is the effective inductance of the cavity and accounts for the storage of magnetic energy in the cavity, C is the effective capacitance of the cavity and represents the electric field in the cavity and R represents the resistive losses of the cavity. The current i flows as a result of the application of voltage V .

3.1. THE CAVITY

$$\frac{dV}{dt} = L \left[\frac{d^2i}{dt^2} + \frac{R}{L} \frac{di}{dt} + \frac{1}{LC} i \right] \quad (3.1)$$

Equation 3.1 is the differential equation which describes the response of the series LCR circuit. It is the equation of a forced harmonic oscillator with damping; the harmonic oscillation arising from the exchange of energy between the inductor L and capacitor C and the damping being provided by the resistive element R .

Assuming that at $t = 0$, $i = 0$ and $V = 0$, taking the Laplace transform of equation 3.1 we have

$$sv(s) = L \left[s^2i(s) + \frac{R}{L}si(s) + \frac{1}{LC}i(s) \right] \quad (3.2)$$

where s is the Laplace operator, and therefore the transfer function $T(s)$ is given by

$$T(s) = \frac{i(s)}{v(s)} = \frac{s}{L s^2 + 2\zeta s + \omega_o^2} \quad (3.3)$$

in which $2\zeta = R/L$ and $\omega_o^2 = 1/LC$, the resonant frequency of a loss less ($R = 0$) cavity. The denominator of 3.3 may be factored as

$$s^2 + 2\zeta s + \omega_o^2 = [s + \zeta + j\omega_l][s + \zeta - j\omega_l] \quad (3.4)$$

where ω_l is the resonant frequency of the loaded (lossy) cavity, and is given by

$$\omega_l = \sqrt{\omega_o^2 - \zeta^2} \quad (3.5)$$

Thus, loading the cavity changes its resonant frequency. If the cavity is excited by a voltage step of amplitude V ($v(t) \iff V(s) = V/s$), then using equations 3.3 and 3.4 the current is given by

$$i(s) = \frac{V}{L} \left[\frac{1}{(s + \zeta + j\omega_l)(s + \zeta - j\omega_l)} \right] \quad (3.6)$$

3.2. PARAMAGNETIC EFFECTS

After a partial fraction expansion and the use of tables, the current is found to be

$$i(t) = \frac{V}{\omega_l L} e^{-\zeta t} \sin \omega_l t \quad (3.7)$$

Rather than using ζ to describe the circuit loss, it is more usual to use 'Q', the quality factor of the circuit, Following [42], and considering equation 3.1, Q is defined as

$$Q = \omega_o \frac{\text{coefficient of } i''}{\text{coefficient of } i'} \quad (3.8)$$

where primes denote differentiation. Therefore

$$Q = \omega_o \frac{L}{R} \quad (3.9)$$

and a low loss cavity has a high Q. Then the resonant frequency of a loaded cavity may be written

$$\omega_l = \omega_o \sqrt{1 - \frac{1}{4Q^2}} \quad (3.10)$$

whilst the response of a cavity to a step function may be written

$$i(t) = \frac{V}{\omega_l L} e^{-(\omega_o/2Q)t} \sin(\omega_l t) \quad (3.11)$$

The transfer function of the cavity equivalent circuit, given by equation 3.3, is simply the admittance of the cavity, and therefore the cavity impedance may be written, with the substitution $s = j\omega$, as

$$z(\omega) = R - j\omega_o L \left[\frac{\omega}{\omega_o} - \frac{\omega_o}{\omega} \right] \quad (3.12)$$

$$= R - j\omega_o L \delta f \quad (3.13)$$

3.2 Changes in cavity parameters

ESR is detected as a result of changes in the susceptibility of the sample in the cavity. Susceptibility may be represented as a complex number

$$\chi = \chi' + j\chi'' \quad (3.14)$$

3.2. PARAMAGNETIC EFFECTS

in which χ' is associated with *dispersion* of energy from the microwave field, and χ'' is associated with *absorption* of power from the microwave field. Dispersion results in a change of the cavity frequency due to a change in the cavity effective inductance (L), whilst absorption results in a change of the cavity loss parameter (R) [43]. In any ESR experiment both absorption and dispersion usually occur.

For a paramagnetic sample following Curie's law, the components of χ are given by [33]

$$\chi' = \chi_o \frac{\omega_B (\omega_B - \omega) \tau_2^2}{1 + (\omega_B - \omega)^2 \tau_2^2} \quad (3.15)$$

$$\chi'' = \chi_o \frac{\omega_B \tau_2}{1 + (\omega_B - \omega)^2 \tau_2^2} \quad (3.16)$$

in which χ_o is the static (DC) susceptibility of the sample, which is given by Curie's law, ω is the frequency of the applied microwave field ω_B is the resonance frequency and τ_2 is the spin relaxation time. After a change of variable and setting both χ_o and τ_2 to unity, the relative magnitudes of χ' and χ'' may be obtained and are shown in figure 3.2.

3.2.1 Dispersive changes

When the inductance of the cavity is changed, the change in resonant frequency for a change ΔL in inductance is

$$\begin{aligned} \Delta\omega &= -\frac{1}{2} (LC)^{-\frac{3}{2}} C \Delta L \\ \Delta f &= -\frac{1}{2} f_o \frac{\Delta L}{L} \end{aligned} \quad (3.17)$$

When a paramagnet is introduced into a resonant system, the change in inductance is [44] $\eta\chi'$, whence

$$\Delta f_d = -\frac{1}{2} f_o \frac{1}{L} \eta \chi'_m \quad (3.18)$$

3.2. PARAMAGNETIC EFFECTS

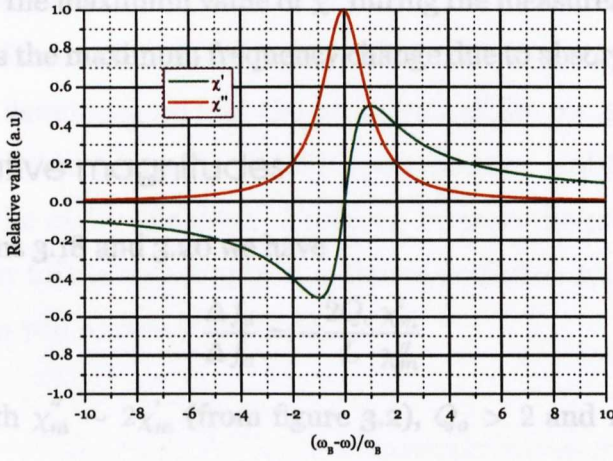


Figure 3.2: The Relative values of χ' and χ''

in which L is the unloaded cavity inductance, f_o is the unloaded cavity resonant frequency, η is the cavity filling factor [32], χ'_m is the maximum value of χ' obtained during the measurement, and therefore Δf_d is the maximum frequency change due to dispersion.

3.2.2 Absorptive changes

When a paramagnetic sample is placed in a cavity, the change in Q [39] is given by

$$\Delta Q = Q_o^2 \eta \chi'' \quad (3.19)$$

in which Q_o is the cavity Q without the paramagnetic sample. From equations 3.19 and 3.10, if $4Q^2 \gg 1$ we have

$$\begin{aligned} \Delta f_a &= \frac{f_o}{4Q_o^3} \left[1 - \frac{1}{4Q_o^2} \right]^{-1/2} \Delta Q \\ &\simeq \frac{f_o}{4Q_o} \eta \chi''_m \end{aligned} \quad (3.20)$$

3.3. COUPLING TO CAVITIES

in which χ_m'' is the maximum value of χ'' during the measurement, and thus Δf_a represents the maximum frequency change due to absorption.

3.2.3 Relative magnitudes

Using equations 3.18 and 3.20 we have

$$\frac{\Delta f_d}{\Delta f_a} = -\frac{2Q_o \chi_m'}{L \chi_m''} \quad (3.21)$$

Therefore, with $\chi_m'' \sim 2\chi_m'$ (from figure 3.2), $Q_o > 2$ and $L < 1$ we have $\Delta f_d > \Delta f_a$.

The change due to dispersive effects is greater than the change due to absorptive effects by orders of magnitude, and because both effects occur simultaneously, the result of a measurement will be an admixture of both dispersive and absorptive effects; the aim of any detection method should be to measure the changes due to either dispersion or absorption.

3.3 Coupling to cavities

When a cavity is used as a circuit element, it is necessary to couple the cavity to the rest of the circuit. For a hollow metallic waveguide this typically involves the use of apertures in the cavity wall to allow coupling to the fields in a waveguide.

The design of the aperture is an involved process (see for example [45]). However, for the purposes of this discussion, the aperture may be modeled as a perfect transformer with a 'turns ratio' of 1:n (primary:secondary) to provide the coupling between the cavity and any external circuitry with variation of the turns ratio allowing a variable coupling between the cavity and

3.3. COUPLING TO CAVITIES

the external circuit.

Two cases will be considered, the transmission cavity and the reflection cavity. It will be demonstrated that the properties of the transmission cavity make it undesirable for use in an ESR spectrometer, and that the reflection cavity is the cavity of choice. However, because the properties of the reflection cavity follow very simply from the transmission system, the transmission system will be considered first.

3.3.1 The transmission cavity

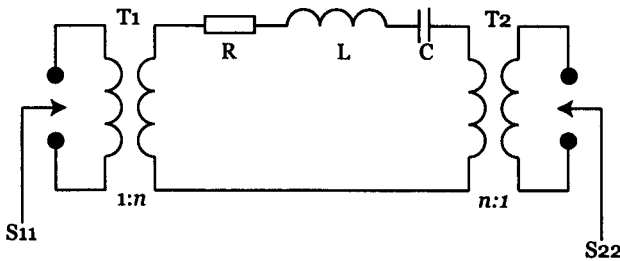


Figure 3.3: Model of a coupled transmission cavity

In the transmission cavity, shown in figure 3.3, power is coupled into the cavity through port 1 and out through port 2. There are two coupling coefficients, β_1 and β_2 , defined by

$$\beta_1 = n_1^2 \frac{Z_o}{R} \quad \beta_2 = n_2^2 \frac{Z_o}{R} \quad (3.22)$$

where subscripts define the port in question and Z_o is the characteristic impedance of the external components. The losses associated with the transmission cavity are the losses due to the cavity proper, described by

3.3. COUPLING TO CAVITIES

the unloaded cavity Q_o and losses due to radiation, described by the external cavity Q_x . We define

$$Q_{x1} = \frac{\omega_o L}{n_1^2 Z_o} \quad Q_{x2} = \frac{\omega_o L}{n_2^2 Z_o} \quad (3.23)$$

which allows the cavity loaded Q , Q_L to be defined as

$$\frac{1}{Q_L} = \frac{1}{Q_o} + \frac{1}{Q_{x1}} + \frac{1}{Q_{x2}} \quad (3.24)$$

3.3.1.1 Transmission cavity power transfer

The transfer of power through the transmission cavity is conveniently described using scattering (S) ¹ parameters, which may be easily calculated from the chain (ABCD) matrices of the various components [48]. Coupling power into port1 and out of port2, three matrices are involved

$$[A]_{T1} = \begin{bmatrix} 1/n_1 & 0 \\ 0 & n_1 \end{bmatrix} \quad [A]_z = \begin{bmatrix} 1 & z \\ 0 & 1 \end{bmatrix} \quad [A]_{T2} = \begin{bmatrix} n_2 & 0 \\ 0 & 1/n_2 \end{bmatrix} \quad (3.25)$$

where z is the impedance of the equivalent circuit of the cavity given in equation 3.13. The chain matrix for a transmission cavity is then simply

$$[A]_T = [A]_{T1} [A]_z [A]_{T2} \quad (3.26)$$

Which, using the coupling coefficients defined in equation 3.22 gives

$$[A]_T = \begin{bmatrix} \sqrt{\frac{\beta_2}{\beta_1}} & \frac{Z_o}{\sqrt{\beta_1 \beta_2}} [1 - jQ_o \delta f] \\ 0 & \sqrt{\frac{\beta_1}{\beta_2}} \end{bmatrix} \quad (3.27)$$

There are standard relationships between chain and scattering matrices [46].

Assuming the cavity to be terminated in Z_o at both ports we find

$$S_{11} = \frac{A + B/Z_o - CZ_o - D}{A + B/Z_o + CZ_o + D} \quad (3.28)$$

$$S_{21} = \frac{2}{A + B/Z_o + CZ_o + D} \quad (3.29)$$

¹A description of S parameters and their properties may be found in [46] or [47]

3.3. COUPLING TO CAVITIES

Substituting the requisite matrix elements from 3.27 into equations 3.28 and 3.29 we have

$$S_{11} = \frac{\beta_2 - \beta_1 + 1 - jQ_o\delta f}{\beta_2 + \beta_1 + 1 - jQ_o\delta f} \quad (3.30)$$

$$S_{21} = \frac{2\sqrt{\beta_1\beta_2}}{\beta_2 + \beta_1 + 1 - jQ_o\delta f} \quad (3.31)$$

Then, because scattering parameters are by definition *voltage* reflection coefficients, the power reflected from port 1 is $|S_{11}|^2$, whilst the power transferred to port 2 is $|S_{21}|^2$.

3.3.2 The reflection cavity

Figure 3.4 shows the equivalent circuit of a reflection cavity. Here, energy is coupled into and out of the cavity through the same aperture. The reflection

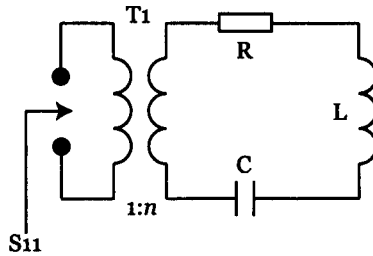


Figure 3.4: Model of a coupled reflection cavity

cavity has one coupling coefficient, given by

$$\beta = n_1^2 \frac{Z_o}{R} \quad (3.32)$$

where Z_o is the characteristic impedance of the external circuit and the port may be under, over or critically coupled, depending upon the value of β

3.4. COMPARISON OF CAVITIES

according to

$$\text{case1 : } \beta > 1 \text{ over coupled} \quad (3.33)$$

$$\text{case2 : } \beta = 1 \text{ critical coupling} \quad (3.34)$$

$$\text{case3 : } \beta < 1 \text{ under coupled} \quad (3.35)$$

The losses associated with the system are the losses due to the unloaded cavity (described by the unloaded cavity Q Q_o) and the losses due to radiation (described by the external Q Q_x) given by

$$Q_x = \frac{\omega_o L}{n^2 Z_o} \quad (3.36)$$

which combine to produce a cavity loaded Q Q_L given by

$$\frac{1}{Q_L} = \frac{1}{Q_o} + \frac{1}{Q_x} \quad (3.37)$$

3.3.2.1 Reflection cavity power transfer

The only S parameter of interest is S_{11} , which represents the power reflected from the cavity. This may be obtained from equation 3.30 by setting $\beta_2 = 0$, to obtain

$$S_{11} = \frac{1 - \beta - jQ_o \delta f}{1 + \beta - jQ_o \delta f} \quad (3.38)$$

and once again it is noted that the power reflected from the cavity is $|S_{11}|^2$.

3.4 Comparison of Cavities

The use of a cavity is intended to increase the sensitivity of the spectrometer. It may be shown [39] that the change in power from a cavity ΔP obeys

$$\Delta P \propto P_{inc} Q \quad (3.39)$$

3.4. COMPARISON OF CAVITIES

for either a transmission or reflection cavity, where P_{inc} is the power coupled to the cavity and Q is the cavity Q . Thus, for the same cavity Q , coupled power and filling factor, it should not make any difference whether a transmission or a reflection cavity is employed. However, as we shall see, the power transfer characteristics of the two cavities lead to a clear choice.

The power transfer function for a transmission cavity is given by equation 3.31 [49] as

$$T(f) = |S_{21}|^2 = \frac{4\beta_1\beta_2}{(1 + \beta_1 + \beta_2)^2 + Q_o^2 (\delta f)^2} \quad (3.40)$$

This is maximised at resonance, i.e. when $\delta f = 0$, in which case the transfer function becomes

$$T(f_o) = \frac{4\beta_1\beta_2}{(1 + \beta_1 + \beta_2)^2} \quad (3.41)$$

Whilst it is possible to employ independent coupling coefficients at the cavity

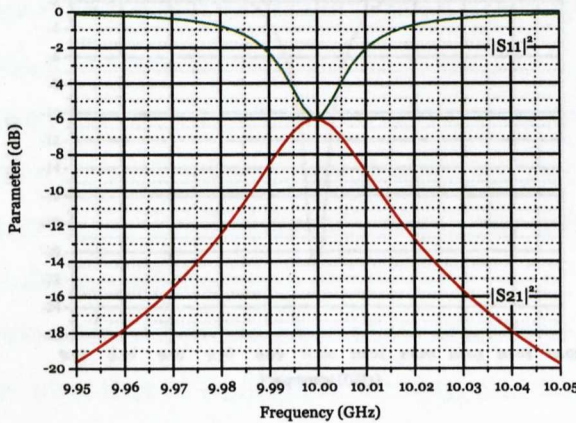


Figure 3.5: Power transfer through, and reflection of power from, a transmission cavity. It is assumed that the coupling coefficient to both ports is 0.5

which at resonance is zero when $\beta = 1$. Therefore no power is reflected by the cavity. The modeling of the cavity was undertaken using 'Eclipse Lite', a small signal RF simulator. The modeling is extremely sensitive and the adjustments are interactive.

3.4. COMPARISON OF CAVITIES

If it assumed that $\beta_1 = \beta_2$, then equation 3.41 becomes

$$T(f_o) = \frac{4\beta^2}{(1 + 2\beta_1)^2} \quad (3.42)$$

which is maximised when $\beta = 0.5$ and gives $|S_{21}| = 0.5$. Using this value of coupling coefficient in equation 3.30 gives $|S_{11}| = 0.5$. Only half the signal applied to the cavity is transmitted through the cavity, due to reflection at port 1.

Consider a cavity, resonant at 10GHz, for which $L = 15\text{nH}$, $C = 16.888\text{fF}$, $R=1\Omega$ (a cavity Q_o of 950) in a system having a characteristic impedance of 50Ω . The calculated² reflected power $|S_{11}|^2$ and the power transfer $|S_{21}|^2$ of the cavity are shown in figure 3.5.

The reflection coefficient of a reflection cavity is given by equation 3.38,

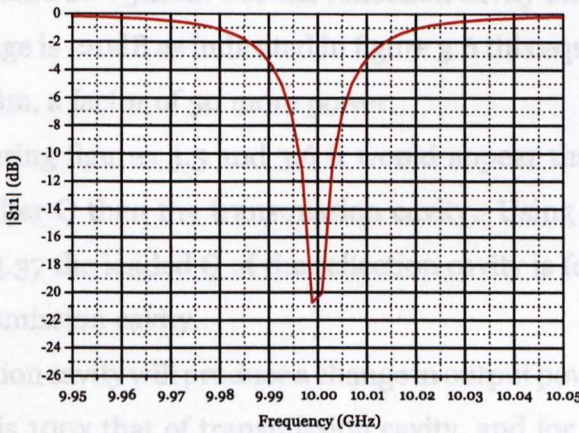


Figure 3.6: Power reflected by a reflection cavity. It is assumed that the port is critically coupled.

which at resonance is zero when $\beta = 1$. Therefore no power is reflected by

²The modeling of the cavity was undertaken using 'Eclipse Lite', a small signal RF simulation package which may be down loaded from www.ardentech.com

3.4. COMPARISON OF CAVITIES

a critically coupled reflection cavity at resonance, all the power is coupled into the cavity. This is shown in figure 3.6; note that the return loss is truncated by the finite frequency step of the simulation- it is infinite for this idealised simulation. The major differences between the two cavities are now apparent.

The power coupled into the transmission cavity is only 1/2 that coupled into the reflection cavity due to the 3dB reflection coefficient of port1.

Secondly, when perfectly aligned, potentially *all* the power coupling into the transmission cavity is applied to the detector, whereas the reflection cavity couples no power to the detector. It is now a question of detector dynamic range. If we assume that in both cases the same detector is used, and this is linear with 0dBm applied, then for the transmission cavity the maximum source power would be +3dBm. For the reflection cavity on the other hand, even if the leakage is -20dB as indicated in figure 3.6 this equates to a source power of +20dBm, a factor of 50 more power.

Finally, considering figures 3.5 and 3.6 it would appear that the reflection cavity has a higher Q than the transmission cavity. Using equations 3.23, 3.24, 3.36 and 3.37 the loaded Q of the reflection cavity is found to be twice that of the transmission cavity.

Thus, the reflection cavity will produce a change in output power which (using equation 3.39) is 100x that of transmission cavity, and for this reason, the reflection cavity is usually the cavity of choice. However, the transmission cavity has been used.

3.5 Reflection cavity systems

With both the applied and reflected signals on the same port, a method of isolating them is required. This task may be performed using a circulator. The operation of this device is unimportant here, we are only concerned with its function. The circulator (shown diagrammatically in figure 3.7) is a three

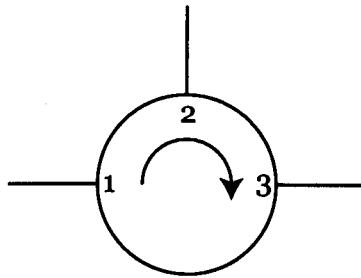


Figure 3.7: A diagrammatic circulator

port device which couples power between adjacent ports in the direction of the arrow; thus port 1 is coupled to port 2 port 2 to port 3 and port 3 to port 1. However, there is no coupling in the reverse direction, thus power will couple from port 1 to 2 but not from port 2 to port 1 and so on. The S parameters of an ideal circulator are [50]

$$\begin{bmatrix} 0\angle 0 & 0\angle 0 & 1\angle 0 \\ 1\angle 0 & 0\angle 0 & 0\angle 0 \\ 0\angle 0 & 1\angle 0 & 0\angle 0 \end{bmatrix} \tag{3.43}$$

In practice however, these devices have a finite bandwidth over which this circulation of power happens, there is both an insertion loss and a phase change associated with the coupling. The cavity and circulator may be combined, as shown in figure 3.8, to provide a system which isolates the signal applied to and the signal reflected from a cavity. In this combination, there

3.5. REFLECTION CAVITY SYSTEMS

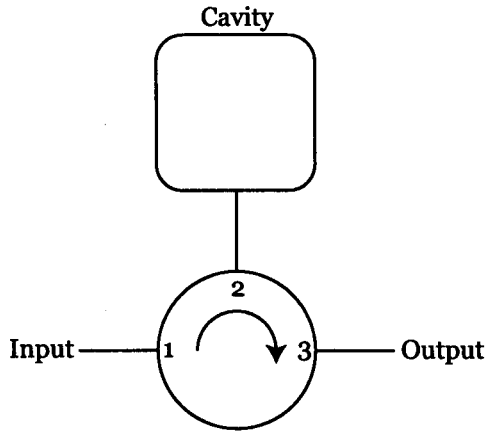


Figure 3.8: The final model of a reflection cavity used for simulation

can only be power at the output (port 3) if the cavity mis-matches port 2; the cavity has reduced the 3 port circulator to a 2 port network, and we are interested in the transfer of power from port 1 of the circulator to port 3 which is $|S_{21}|^2$. The power transfer, both phase and amplitude, is shown in figure 3.9.

3.5.1 Cavity locking.

Grambow [43] recognised that the phase shift of the cavity around resonance could be used to compensate the change in cavity resonant frequency due to dispersive changes in the scheme shown in figure 3.10. Here, the frequency of the source is controlled in a phase locked loop (PLL). The cavity output compared in phase to the source phase; and the PLL acts to keep the phase difference at zero. If the cavity resonant frequency changes from the zero reference point the phase comparator (which may be as simple as a double balanced mixer, see section 6.1) produces an output which brings the oscillator frequency to the new cavity resonant frequency.

3.5. REFLECTION CAVITY SYSTEMS

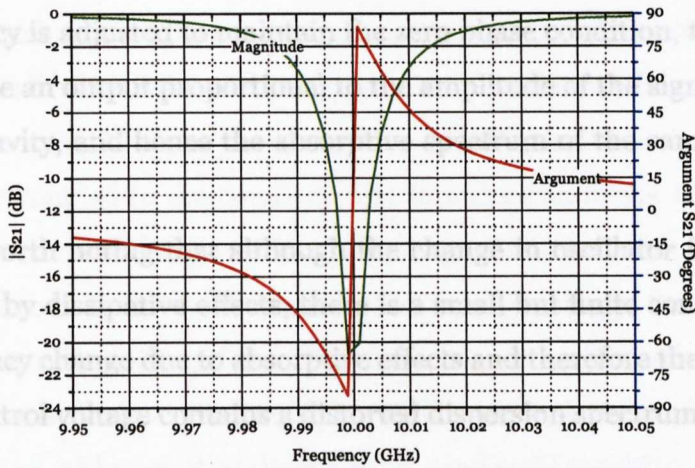


Figure 3.9: The amplitude and phase change of a signal being reflected from a cavity via a circulator.

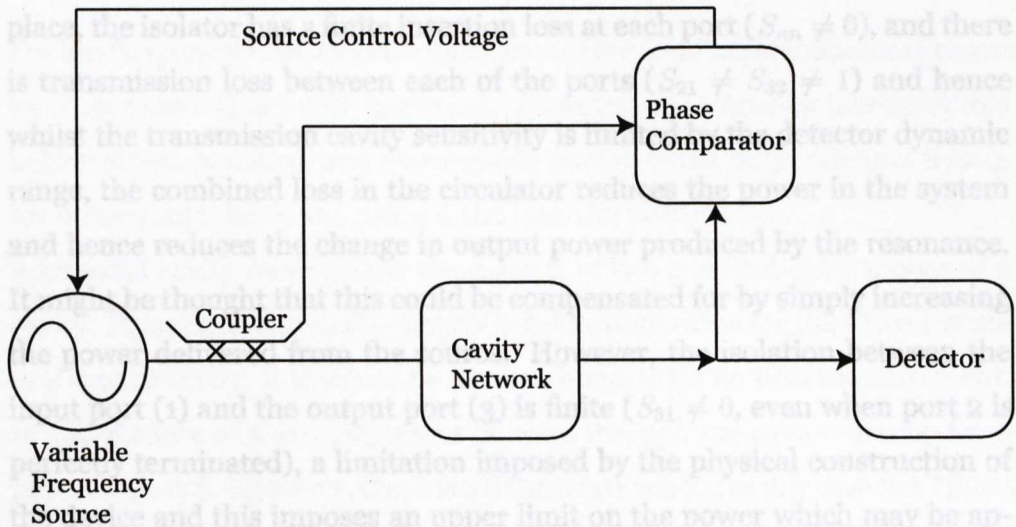


Figure 3.10: A method of eliminating dispersive effects from the ESR spectrum. Paraphrased from [43].

3.6. INDUCTION MEASUREMENTS

Then, provided the source amplitude does not change in the range over which its frequency is adjusted to maintain the zero phase condition, the detector will produce an output proportional to the amplitude of the signal reflected from the cavity, and hence the absorptive spectrum of the sample may be obtained.

It is also worth noting that although the change in oscillator frequency is dominated by dissipative effects, there is a small but finite contribution to the frequency change due to absorptive effects and therefore the source frequency control voltage contains a distorted dispersion spectrum.

3.6 Induction Measurements

Using circulators as described above to allow the separation of the power incident upon and reflected from the cavity has its disadvantages. In the first place, the isolator has a finite insertion loss at each port ($S_{nn} \neq 0$), and there is transmission loss between each of the ports ($S_{21} \neq S_{32} \neq 1$) and hence whilst the transmission cavity sensitivity is limited by the detector dynamic range, the combined loss in the circulator reduces the power in the system and hence reduces the change in output power produced by the resonance. It might be thought that this could be compensated for by simply increasing the power delivered from the source. However, the isolation between the input port (1) and the output port (3) is finite ($S_{31} \neq 0$, even when port 2 is perfectly terminated), a limitation imposed by the physical construction of the device and this imposes an upper limit on the power which may be applied to the system without saturating the detector. These problems become increasingly bothersome as frequency increases.

A technique which to some extent over comes this difficulty is borrowed from

3.6. INDUCTION MEASUREMENTS

the NMR community, the induction mode. Here, the sample is placed in an inductor which applies the excitation, and the spectral signal is detected in a coil perpendicular to the excitation [51]. In the absence of a sample, there can be no coupling between the excitation and detection coils and thus there is no power coupled to the detector. The introduction of the sample introduces a polarisation change to the applied signal at resonance, and hence a signal is *induced* in the detection coil. Not unsurprisingly, the exact alignment between the coils and the isolation between excitation and detector circuits becomes important [52, 53]. With care, isolations of 80dB have been obtained, although the adjustment is extremely sensitive and difficult to maintain [54].

3.6.1 The bimodal cavity

For low frequency ESR, resonators formed of perpendicular inductors ('crossed loop' resonators) are still employed. However as frequency increases this becomes less practical, and a waveguide analog of the perpendicular inductor is desirable. Such an analog is the bimodal cavity [55].

A bimodal cavity relies on the degeneracy of two perpendicular modes of a cavity. Figure 3.11 shows the magnetic field distribution for the TE₁₀₂ mode in a square cavity; this would be a suitable mode for an ESR measurement. In the absence of a sample, power couples through the cavity directly from port A to port B. However, there is a degenerate mode (in this case the TE₂₀₁ mode) which is orthogonal to the TE₁₀₂ mode. If a sample is introduced into the cavity, at resonance the sample induces a field orthogonal to the incident field which couples to port C (figure 3.12).

Thus, away from resonance there is no power coupled to port C with in-

3.6. INDUCTION MEASUREMENTS

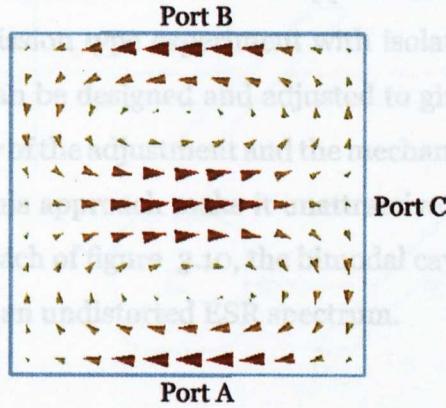


Figure 3.11: The Magnetic field distribution of the TE₁₀₂ mode in a square cavity. The height of the cavity is 1/4 the length of the side of the square face, which ensures that the cavity is 'cut off' in the third (not shown) dimension.

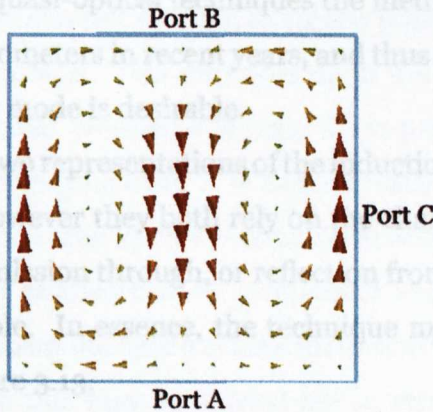


Figure 3.12: The magnetic field distribution of the TE₂₀₁ mode in a square cavity. Note the field distribution is orthogonal to that in figure 3.11. This mode is induced by the sample resonance.

3.6. INDUCTION MEASUREMENTS

creasing power coupled as the resonance is approached. The bimodal cavity is in effect a transmission type experiment with isolation. With care [56] the bimodal cavity can be designed and adjusted to give 80dB of isolation. However the stability of the adjustment and the mechanical difficulties in the implementation of this approach make it unattractive. Non-the-less, combined with the approach of figure 3.10, the bimodal cavity offers a potential method of obtaining an undistorted ESR spectrum.

3.6.2 Polarisation and the induction mode.

As frequency increases, the losses of circulators implemented in waveguide increase, whilst their isolation decreases³ Quasi optical techniques produce units which have isolations and insertion losses at W-band comparable with X-band waveguide devices [57]. The increased performance, and in general lower loss has made quasi-optical techniques the method of choice for high frequency ESR spectrometers in recent years, and thus a quasi optical equivalent of the induction mode is desirable.

There are essentially two representations of the induction mode quasi-optical spectrometer [58], however they both rely on the change of polarisation of a signal during transmission through, or reflection from, a cavity containing a paramagnetic sample. In essence, the technique may be reduced to the scheme shown in figure 3.13.

The incoming radiation, having both vertical and horizontal components,

³These parameters are highly bandwidth dependent. Typical figures for commercial units are at X-band insertion loss 0.15dB, isolation 28dB over a 5% bandwidth (KW Microwave) and at W-band insertion loss 0.4dB, isolation 25dB over a 1% bandwidth (EMS Technologies).

3.6. INDUCTION MEASUREMENTS

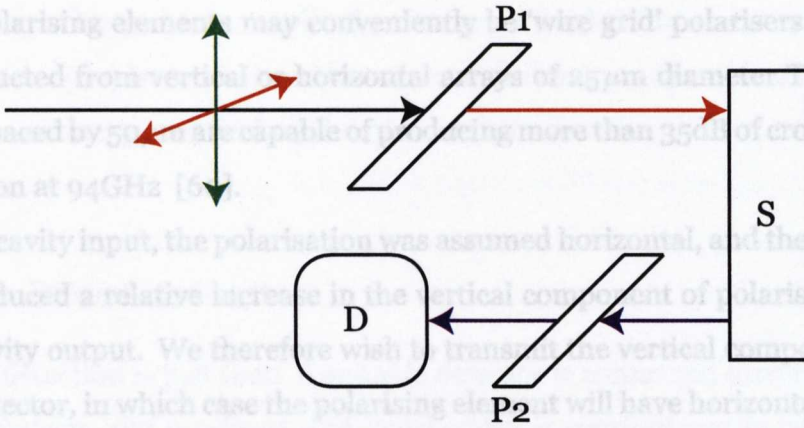


Figure 3.13: The outline of an induction mode spectrometer using polarisation changes to encode the required spectral information. Letters are referred to in the text.

is incident upon a polarising element (P1) which transmits, as shown here for example, the horizontal component. Now, a linear polarisation may be regarded as having two counter rotating circularly polarised components (P_r and P_l) of equal magnitude. This impinges upon the cavity/sample (S), in which one of the circular components (say P_r) is preferentially absorbed, and hence the signal emerging from 'S' is an elliptically polarised signal. The emerging radiation impinges upon a second polarising element (P2) which serves to remove any unabsorbed P_r component and if correctly aligned, pass the signal containing the spectral information to the detector (D).

The demonstration of this may be carried out in terms of Jones Matrices [59]. Based on the component model of the reflection cavity, the Jones matrix for a reflection cavity [48] is

$$\begin{bmatrix} R_V \\ R_H \end{bmatrix} = \frac{1}{1+\beta} \begin{bmatrix} (1-\beta) + j\beta\eta Q\chi & -j\beta\eta Q\chi \\ -j\beta\eta Q\chi & (\beta-1) - j\beta\eta Q\chi \end{bmatrix} \begin{bmatrix} I_V \\ I_H \end{bmatrix} \quad (3.44)$$

3.7. SIGNAL DETECTION

The polarising elements may conveniently be 'wire grid' polarisers. When constructed from vertical or horizontal arrays of $25\mu\text{m}$ diameter Tungsten wire spaced by $50\mu\text{m}$ are capable of producing more than 35dB of cross polar rejection at 94GHz [60].

At the cavity input, the polarisation was assumed horizontal, and the sample has induced a relative increase in the vertical component of polarisation at the cavity output. We therefore wish to transmit the vertical component to the detector, in which case the polarising element will have horizontal wires. The Jones Matrices of the reflected and transmitted components for such a polariser are [60]

$$M_r = \begin{bmatrix} 0 & 0 \\ 0 & 1 \end{bmatrix} \quad (3.45)$$

$$M_t = \begin{bmatrix} 1 & 0 \\ 0 & 0 \end{bmatrix} \quad (3.46)$$

Then, combining equations 3.44 and 3.46 with the signal transmitted by the second polariser is

$$T_v = -j\beta\eta Q\chi \quad (3.47)$$

which may be processed to obtain the desired spectrum using any of the methods to be described.

3.7 Signal Detection

So far, no use has been made of the magnetic field modulation, the spectrum has been obtained by sweeping the magnetic field, and the question of how the actual measurement is made has been left simply as a method of

3.7. SIGNAL DETECTION

detecting a change in the amplitude of a signal coupled from a cavity. In this section the problems of direct detection of the cavity output are discussed, and the advantages of field modulation are introduced.

3.7.1 Direct detection

Direct detection is just that! A suitable detector is connected directly to the cavity output, and produces a DC level which is proportional in some way to the power applied to the detector. The type of detector which might be considered depends upon the frequency of interest. For low frequencies, certainly to 10GHz, diode detectors might be considered, whilst at millimetric frequencies, Bolometric techniques are often encountered.

3.7.1.1 Bolometer detection

A Bolometer (also historically called a Barretter) is any device which detects radiation by using incident radiation to warm a sensing element. In older Bolometers this was a length of wire, where radiation coupled from the cavity changes the resistance of the wire which may be detected using, for example, a Wheatstone Bridge [61].

However, the thermal mass of the detection element gives this type of Bolometer a long response time, which limits the field modulation rate and makes them unsuitable for pulse measurements, although they have very wide operating bandwidths.

A more modern Bolometer, is the Hot Electron Bolometer. Constructed from a suitable semiconductor material, these devices rely on the incident radiation raising the temperature of conduction electrons above the background

3.7. SIGNAL DETECTION

lattice temperature, thus changing the conduction properties of the semiconductor. Depending upon the wavelength of interest, there are a number of suitable materials; Indium-Antimonide (InSb) has a wide frequency range and is suitable for use from low millimetric to infrared wavelengths. However at these wavelengths photons have a relatively low energy which means that to function the Bolometer must be cooled to liquid Helium temperatures.

The response time of the cooled InSb Bolometer is restricted by the rate at which the hot electrons may rethermalise [62]. By reducing the physical dimensions of the detector, the time required for electrons to rethermalise by diffusion may be reduced and high sensitivity high speed (10's of pS) may be produced [63].

Changing both the material and the size of the detection element can also assist the production of fast Bolometer detectors by introducing additional rethermalisation mechanisms. Improved electron-phonon coupling, which may be obtained in thin (10nm) Niobium (Nb) films is able to produce a detector capable of resolving pulses of a few pS duration; the disadvantage of this approach is a decrease in detector sensitivity [64].

3.7.1.2 Diode detection

Historically called crystal detection, this technique is another extremely simple method of detection; the diode is simply connected to the cavity output. The diode rectifies the incident radiation and diode current is in some way related to the applied power.

The relationship between applied power and output diode current is non linear, and gradually changes from being a square law device (device current proportional to applied power) at low powers, to a linear transfer character-

3.7. SIGNAL DETECTION

istic (diode current proportional to the square root of the applied power, in effect the applied voltage) at higher powers.

A complication of the diode detector over the Bolometric detector is that the diode requires a minimum applied power before the device current rises, which automatically imposes a minimum detectable signal on the diode detector, and therefore diodes with small turn on thresholds, Schottky and backward diodes, may be attractive. Backward diodes have been evaluated against point contact diodes at frequencies up to 115GHz, and have been shown to offer much improved detection properties [65]. Poole [32] reports work by Buckmaster which shows that spectrometer sensitivity may indeed be improved by the use of such diodes.

3.7.1.3 Homodyne-Heterodyne detection

As will be discussed in the next section, the sensitivity of a spectrometer employing direct detection is severely limited by excess $1/f$ noise introduced by the detector element.

The device excess noise shows a very rapid decrease in magnitude as the frequency of the detector output is increased away from 0Hz, the DC of direct detection. Therefore if the detector output were to be moved to a finite frequency, the sensitivity of the detector would be increased.

The Heterodyne and Homodyne are methods of demodulation are basically the same, and are shown in outline in figure 3.14. The signal from the cavity, at a frequency F_s is combined with a second signal F_{lo} in a circuit known as a mixer, which may be either a diode network or a Bolometer. The resultant output of the mixer is the Intermediate Frequency (IF) which is arranged to be the difference between F_s and F_{lo} .

3.7. SIGNAL DETECTION

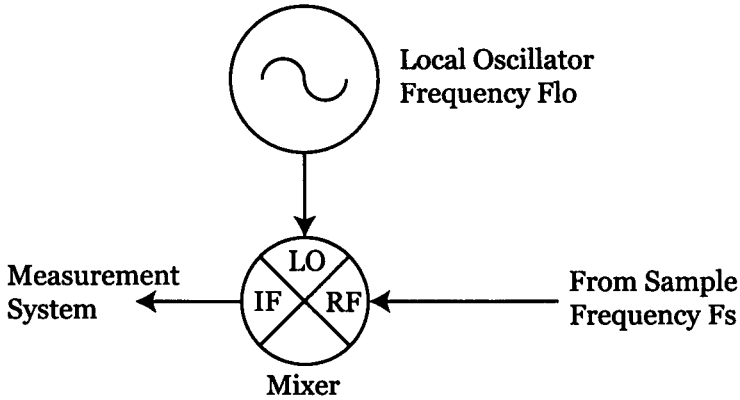


Figure 3.14: The essential components of the Homodyne and Heterodyne detection techniques.

If F_s and F_{lo} are equal, the Homodyne case, the IF frequency is 0Hz and we are apparently no better off than in the direct detection case. However, as we shall see, if field modulation is employed, the spectral information is contained in a modulation sideband which is converted to a signal at the field modulation frequency at the mixer output. Typically the field modulation frequency is of order 1kHz, which is sufficient to move the signal outside the region of high $1/f$ noise introduced by the mixer.

The Heterodyne scheme requires different F_s and F_{lo} values, in which case the IF frequency may be many MHz, and the spectral data is now well removed from the mixer $1/f$ noise. The problem now is the demodulation of the IF signal. This signal is now at a frequency which may be easily amplified to provide a signal for demodulation which easily exceeds any detector noise. Essentially then the Homodyne and Heterodyne detectors are the same, differing only in the mixer output frequency. It may be shown that in CW spectrometers employing field modulation there is no difference in terms of

3.7. SIGNAL DETECTION

sensitivity between Homodyne and Heterodyne detectors [39]. However in the case of pulsed spectrometers a Heterodyne scheme is very attractive. The outline of a Homodyne detector is given in section 3.8.4 of this chapter, and a detailed description of a Heterodyne demodulation system is given in chapter 11.

3.7.2 Other methods of detection

Whilst this chapter concentrates on measuring an ESR spectrum by measuring changes in the power (voltage) reflected by the cavity as the sample is taken through a resonance, there are other methods of detection. The following is by no means an exclusive list [66, 67].

3.7.2.1 Cavity resonant frequency

It was shown in section 3.2 that changes in the susceptance of the sample cause a change in cavity frequency. Therefore, an ESR spectrum may be obtained by measuring the change in cavity resonant frequency as the magnetic field is swept to satisfy the resonance condition. If the cavity were to be the frequency determining element of an oscillator, then the change in susceptibility would change the oscillator frequency, making the measurement of the spectrum a simple matter of frequency measurement.

The change in cavity frequency is dominated by the dispersive changes in susceptance component and therefore, the spectrum measured will consist predominantly of the dispersion spectrum. In reality the spectrum obtained will be an admixture of both dispersive and absorptive components. Whilst it is desirable to measure only one component, measurements of this nature

3.7. SIGNAL DETECTION

were amongst the first ESR measurements to be performed [44, 68].

3.7.2.2 The use of marginal oscillators

Although the change in cavity resonant frequency due to absorption is small in comparison to the change in cavity resonant frequency due to dispersion, it is possible to obtain a pure absorption spectrum by using the cavity containing the sample as the resonator in a marginal oscillator.

A marginal oscillator is an oscillator held on the very threshold of oscillation. Because the on set of oscillation depends crucially upon the cavity loss resistance, any change in the loss resistance can produce large (essentially no oscillation to full power) changes in the oscillator output, and because this effect depends only upon absorption, measuring the amplitude of the oscillator output provides a pure absorption spectrum of the sample. This technique has been much used in NMR experiments and has been successfully demonstrated in ESR applications [69, 70, 71].

3.7.2.3 Detection using the Hall effect

In this case the sample is placed on or very near to a semiconductor in which the Hall current is being measured. Changes in the magnetisation of the sample modify the local magnetisation of the sample and hence an ESR spectrum may be measured [66].

It is claimed that this approach may yield concentration sensitivities of 10^7 spins at room temperature and because of the small size ($50 \mu\text{m}^2$) of the Hall sensor, to be eminently suitable for use with biological samples [66].

3.8 Spectrometer Sensitivity

It was shown in section 3.4 that a spectrometer based upon a transmission cavity is fundamentally less sensitive than an instrument based upon a reflection cavity. In estimating the sensitivity of a spectrometer it is therefore only necessary to consider a reflection cavity.

To estimate the sensitivity of a given spectrometer, it is necessary to estimate the minimum change in the cavity output which can be detected and then relate this to the number of spins in the sample which produced the change. Detectors may respond to either changes in the power reflected from the cavity, or the change in the voltage of the reflected signal.

In this section, it is first demonstrated that the change in voltage produced by a cavity is greater than the change in power, and that therefore only voltage detection need be considered. The sensitivity of a direct detection scheme is estimated and having introduced the effect of field modulation the sensitivity of a Homodyne detector is estimated. Finally, an outline of a Homodyne demodulator, using a polarisation implementation of a reaction cavity is presented.

3.8.1 Power detection

Both diode and Bolometer detectors are power sensitive, and the power change at the cavity output is now estimated. When power is applied to the cavity, any power not reflected must have been absorbed by the cavity, and therefore any change in cavity absorption is mirrored in the power reflected from the cavity. It is a matter of definition [46] that

$$|S_{11}|^2 = \frac{P_r}{P_{av}} \quad (3.48)$$

3.8. SPECTROMETER SENSITIVITY

where P_r is the power reflected from the cavity and P_{av} is the power applied to the cavity. Then the power coupled into the cavity P_c is given by

$$P_c = P_{av} - P_R \quad (3.49)$$

Then, combining equations 3.48 and 3.49 gives

$$P_c = P_{av} [1 - |S_{11}|^2] \quad (3.50)$$

which in conjunction with equation 3.38 (at resonance) produces

$$P_c = P_{av} \frac{2\beta}{[1 + \beta]^2} \quad (3.51)$$

It is now assumed that the measurement is of an absorption spectrum, and the change in cavity loss resistance R produces a change in the power in the cavity

$$\Delta P_c = \frac{dP_c}{dR} \Delta R \quad (3.52)$$

which using equations 3.32 and 3.51 gives

$$\Delta P_c = 2P_{av} Z_o n^2 \frac{n^2 Z_o - R}{[n^2 Z_o + R]^3} \Delta R \quad (3.53)$$

$$\Delta P_c = 2P_{av} \frac{\beta [\beta - 1] \Delta R}{[\beta + 1]^3 R} \quad (3.54)$$

The change in cavity power may be maximised by allowing $d\Delta P_c/d\beta = 0$.

$$\frac{d}{d\beta} \Delta P_c = \frac{2[\beta + 1]^3 [2\beta - 1] - 6\beta [\beta - 1] [\beta + 1]^2}{[1 + \beta]^2} \quad (3.55)$$

which, upon equating the numerator to zero produces

$$\beta = 2 \pm \sqrt{3} \quad (3.56)$$

which is the result obtained in [39], and states that optimum sensitivity for a spectrometer employing a power sensitive detector and a reflection

3.8. SPECTROMETER SENSITIVITY

cavity, is obtained not when it is critically coupled ($\beta = 1$), but rather when it is either overcoupled (the positive case) or undercoupled. Then, using the above value of coupling coefficient, and equations 3.19 and 3.54, the change in cavity output power is

$$\frac{\Delta P_c}{P_{av}} = \pm 0.19245 \chi'' \eta Q_o \quad (3.57)$$

3.8.2 Voltage detection

The diode detector may also be voltage sensitive, and the change in voltage introduced by the sample may be estimated as follows. By definition

$$S_{11} = \frac{V_r}{V_{av}} \quad (3.58)$$

which using equation 3.30 (again at resonance) in conjunction with equation 3.32 gives

$$V_r = V_{av} \frac{1 - \beta}{1 + \beta} \quad (3.59)$$

$$= V_{av} \frac{R - n^2 Z_O}{R + n^2 Z_O} \quad (3.60)$$

Then differentiating and proceeding as above gives

$$\Delta V = \frac{2\beta}{[1 + \beta]^2} \frac{\Delta R}{R} V_{av} \quad (3.61)$$

$$= \frac{2\beta}{[1 + \beta]^2} \chi'' \eta Q V_{av} \quad (3.62)$$

Now, maximum energy is coupled into the reflection cavity when $\beta=1$, in which case

$$\Delta V = 0.5 \chi'' \eta Q V_{av} \quad (3.63)$$

Thus, comparing this result with that of equation 3.57, it is concluded that the most sensitive spectrometer will be produced by employing a critically

3.8. SPECTROMETER SENSITIVITY

coupled reflection cavity in conjunction with a voltage sensitive detector. The sensitivity of a spectrometer using this combination may be estimated by requiring the voltage produced by the detector due to the sample to exceed the noise voltage produced by the detector.

Now, the cavity resistance R , when terminated in a noiseless resistance R produces a noise voltage V_n

$$V_n = \sqrt{2kTR\Delta f} \quad (3.64)$$

Although T in this equation has been represented as the physical temperature of the cavity resistance, in reality the cavity is connected to a detector which will have it's own noise equivalent temperature, and this can be rather higher than the detector physical temperature. The cavity-detector noise voltages will therefore equilibrate at a noise temperature higher than the device physical temperature and lower than the detector noise temperature; the cavity noise temperature is written as T_{sys} . Then equating equations 3.63 (with this modification) and 3.64 gives the minimum detectable value of χ'' as

$$\chi''_{min} = \frac{4}{\eta Q} \sqrt{2kT_{sys}R} \quad (3.65)$$

in a 1Hz bandwidth. Equation 3.16 gives the variation of χ'' , and is a Lorentzian, which at resonance [72] may be written as

$$\chi'' = \frac{1}{2} \chi_o \frac{H_o}{\Gamma} \quad (3.66)$$

where χ_o is the DC susceptibility of the sample, H_o is the resonant field and Γ is the half width at half height of the resonance. Assuming the sample to be a Curie paramagnet, the static susceptibility of the sample is given by

$$\chi_o = \frac{\beta_m^2}{k(T - \theta)^2} \frac{N}{V_s} \quad (3.67)$$

3.8. SPECTROMETER SENSITIVITY

in which β_m is the Bohr Magneton, θ is the Curie temperature, N is number of paramagnetic centres in the sample and V_s is the sample volume. Then combining equations 3.65, 3.66 and 3.67 gives

$$N = \frac{4\sqrt{2}}{DQ} \sqrt{kT_{sys}} \sqrt{R} \frac{\Gamma}{H_o} \frac{k(T - \theta)^2}{\beta_m^2} V_c \quad (3.68)$$

where V_c is the cavity volume, and D is a factor from the definition of the filling factor $\eta = DV_s/V_c$ and N is now the number of detectable spins. Consider an X-Band (10GHz) system, with the following parameters; a rectangular TE₁₀₂ cavity for which $D=2$ [72], $Q=5000$, a volume of $9 \times 10^{-6} \text{ m}^3$, which is expected to have a loss resistance of order 0.2Ω . The sample has a line width of 2G (not untypical for DPPH⁴), and $T \gg \theta$. Because the resonance is at 10GHz H_o is $0.357T$. Both Bolometers and point contact diodes have very similar noise equivalent powers [73, 74] of approximately 10^{-10} W (in a 1Hz bandwidth) which gives $T_{sys} \sim 10^{11} \text{ K}$. Using these figures in equation 3.68 gives $N \sim 4 \times 10^{19}$ spins.

3.8.3 Field Modulation

Whilst this number of detectable spins would appear to be reasonable, it is clearly dominated by T_{sys} . The reason this is so high is that the detection is being performed directly using a variation in cavity output power. The noise from diode detectors falls rapidly as a small offset from the carrier is introduced, typically at a rate of between 6dB/octave and 12dB/octave. Thus, if a signal containing the required spectral information could be introduced as, say a 1kHz modulation of the original source signal, the detector introduced

⁴DPPH is the organic salt 2,2-diphenyl-1-picrylhydrazyl. It is noted for producing a large amplitude, single and narrow ESR spectral line.

3.8. SPECTROMETER SENSITIVITY

noise would fall by (assuming the noise to be flat below an offset of 1Hz) some 70dB, reducing the equivalent noise power to 10^{-17} W in a 1Hz bandwidth and giving $N \sim 10^{11}$. This rather desirable reduction in the number of spins which can be detected (increase in sensitivity) can be brought about by field modulation.

Consider equation 3.16 expressed in terms of magnetic fields. Let H_o be the resonant field, and $H + h \sin \omega_m t$ be the applied magnetic field consisting of a large slowly sweeping component H and a small modulated component of peak amplitude h and frequency ω_m . Then [72]

$$\chi''(t) = \chi_o \frac{1}{\sqrt{3}} \frac{H_o}{\Delta_o} \frac{\Gamma^2}{\Gamma^2 + (H - H_o + h \sin \omega_m t)^2} \quad (3.69)$$

in which Δ_o is the linewidth and all other terms have been previously defined.

Differentiating we have

$$\frac{d}{dt} \chi''(t) = \chi_o \frac{1}{\sqrt{3}} \frac{H_o}{\Delta_o} \frac{-2\Gamma^2 (H - H_o + h \sin \omega_m t)}{[\Gamma^2 + (H - H_o + h \sin \omega_m t)^2]^2} h \omega_m \cos \omega_m t \quad (3.70)$$

The modulation amplitude must not sweep the magnetic field through the resonance during a cycle of modulation, so it is required that $h \ll \Gamma$, which, because the line width is rather smaller than the applied field, reduces equation 3.70 to

$$\frac{d}{dt} \chi''(t) = \Lambda h \omega_m \cos \omega_m t \quad (3.71)$$

where Λ is the field derivative of χ'' in equation 3.70. Then

$$\Delta \chi''(t) = \Lambda h \omega_m \cos \omega_m t \Delta t \quad (3.72)$$

If Δt is associated with the rate of field sweep, it is possible to arrange $h \omega_m \Delta t \sim 1$ which requires that the rate of field sweep must be low in comparison to the modulation frequency; as an order of magnitude estimate with a line width of 2G say $h = 0.2G$, and a modulation frequency of 1kHz

3.8. SPECTROMETER SENSITIVITY

it follows that Δt is of order 8s, a sweep rate of 15G/minute. We then have the direct analogy of equation 3.63

$$\Delta V(t) \doteq \Lambda \cos \omega_m t * V_{av} \quad (3.73)$$

Now V_{av} , the signal applied to the reflection cavity, is of the form $V_o \cos \omega_c t$, which if substituted into equation 3.73, the use of a trigonometric relationship yields

$$\Delta V(t) \doteq \Lambda [\cos (\omega_c - \omega_m) t + \cos (\omega_c + \omega_m) t] \quad (3.74)$$

So, the signal variation at the output of the cavity is now two signals, removed from the actual signal used to illuminate the sample by the field modulation frequency, and whose amplitudes reflect the derivative of χ'' ; the cavity output is an RF carrier amplitude modulated at the field modulation frequency. The act of detection now requires a method of measuring the amplitude of either of these 'sidebands'.

Consider the effect of multiplying the cavity output by a signal of the form $\sin \omega_c t$, so that post multiplication we have

$$\Delta V_o(t) \doteq \Lambda [\cos (\omega_c - \omega_m) t + \cos (\omega_c + \omega_m) t] \sin \omega_c t \quad (3.75)$$

Where V_o is the result of the multiplication process. Expanding the trigonometric term and neglecting a high frequency term, the output of the multiplication stage is

$$V_o(t) \doteq \Lambda \sin \omega_m t \quad (3.76)$$

which is a signal at the field modulation frequency, the amplitude of which is proportional to the field derivative of χ'' . The act of multiplying an amplitude modulated carrier by the carrier frequency to produce a baseband signal in this way is, known as Homodyne demodulation. This baseband signal is removed from the high noise region of the diode encountered in the

3.8. SPECTROMETER SENSITIVITY

direct demodulation scheme calculated above and therefore an increase in sensitivity is obtained when Homodyne demodulation is employed instead of direct demodulation.

3.8.4 Implementation Of A Homodyne Detector

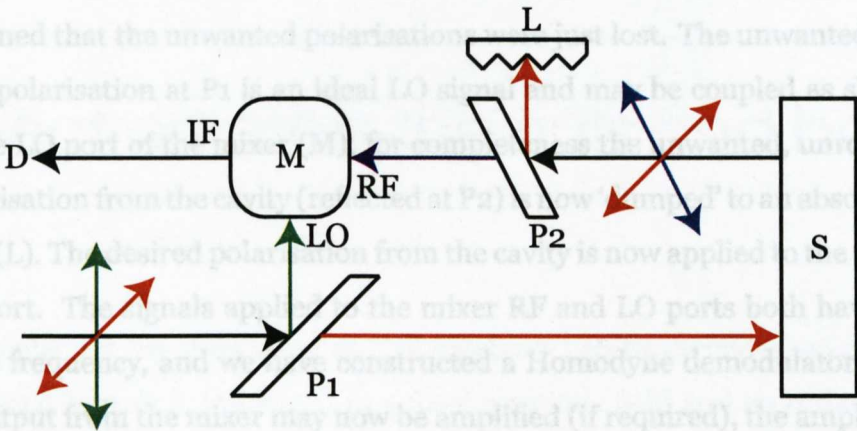


Figure 3.15: The outline of a Homodyne spectrometer. Letters are referred to in the text.

In RF engineering parlance, the multiplier employed above is known as a mixer. The mixer may be realised using Bipolar or FET devices [75] which using modern devices will certainly function to 10GHz [76]. However at high frequencies, diode mixers are encountered [77, 73], with the type and construction of diode becoming increasingly important as frequency increases [78]. The Bolometer may also be used with considerable advantage as a mixer at millimeter and submillimeter wavelengths [79]. No matter which construction is employed, all mixers have a port to which the signal (RF) is applied, an output (IF) port which contains the product of the RF signal and

3.8. SPECTROMETER SENSITIVITY

a second input to which the Local Oscillator or LO signal is applied. The mixer performance depends upon the level of the LO signal, which depends upon the type of mixer employed; the InSb bolometer may require a few 10's of μW whilst a simple diode mixer may require of order 10mW.

Independent of the mixer, the Homodyne receiver requires an LO signal at the same frequency as the RF signal and consideration of figure 3.15 shows how this might be achieved. In the polarising spectrometer of 3.13, it was assumed that the unwanted polarisations were just lost. The unwanted vertical polarisation at P1 is an ideal LO signal and may be coupled as shown to the LO port of the mixer (M); for completeness the unwanted, unrotated polarisation from the cavity (reflected at P2) is now 'dumped' to an absorbing load (L). The desired polarisation from the cavity is now applied to the mixer RF port. The signals applied to the mixer RF and LO ports both have the same frequency, and we have constructed a Homodyne demodulator. The IF output from the mixer may now be amplified (if required), the amplitude of the mixer output recorded on a suitable instrument (D), which will record will the derivative of the absorption spectrum of the sample in the cavity.

CHAPTER 4

Spectrometers-the nuts and bolts

In chapter 2 it was shown that an ESR spectrum may be excited when a paramagnetic sample is immersed in a fixed magnetic field and an orthogonal oscillating magnetic field applied. In this chapter the components required to measure the spectrum are discussed.

A general description of an ESR spectrometer is presented. Methods of obtaining and ensuring orthogonality between required magnetic fields are introduced, and methods of temperature control are alluded to.

The major part of this chapter is concerned with the realisation of low loss microwave inter-connection of all the microwave components, and the description of quasi-optical techniques which are employed in the realisation of modern high field ESR spectrometers.

4.1. SPECTROMETER OUTLINE

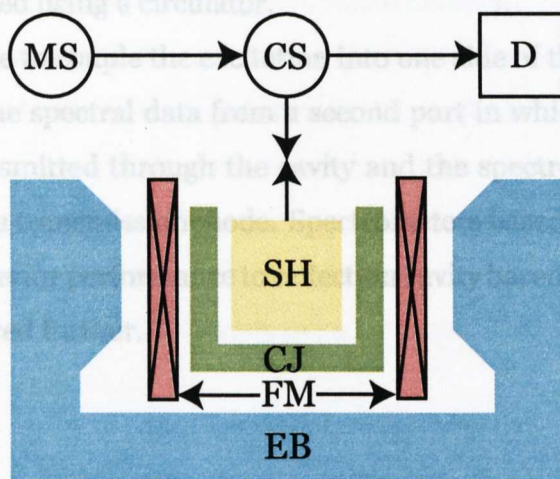


Figure 4.1: A diagrammatic representation of an ESR spectrometer. Labels are referred to in the text.

4.1 Spectrometer Outline

A block diagram of a typical reflection spectrometer is shown in figure 4.1. The required (potentially large) main magnetic field is supplied by a suitable electro- or superconducting magnet 'EB' and is applied to the sample in a sample holder 'SH' which is often a resonant cavity; this large magnetic field may be modulated at a low frequency (a few kHz) by a few Gauss by means of two small field modulation coils 'FM'. The sample may be contained in a temperature controlled environment provided by the cryogenic jacket 'CJ'. A source of RF/microwave energy, the oscillating field, is supplied by a microwave source 'MS' at the resonance frequency is coupled into the sample using a coupling structure 'CS'. The coupling structure must not only couple energy from the source to the sample, it must couple the signal returning from the sample into the detector 'D'. At microwave frequencies this function

4.1. SPECTROMETER OUTLINE

may be performed using a circulator.

It is also possible to couple the excitation into one side of the sample holder and to couple the spectral data from a second port in which case the spectral data is transmitted through the cavity and the spectrometer is said to be operating in a transmission mode. Spectrometers based on transmission cavities have inferior performance to reflection cavity based instruments and are not considered further.

4.1.1 The Magnetic Fields

There are two magnetic fields involved in obtaining an ESR spectrum, the main field which determines the frequency of the measurement, and a second (smaller) field, orthogonal to the main field, oscillating at the frequency of the measurement.

4.1.1.1 The main field

Although Gorter (1937) [68] observed a paramagnetic effect at 2MHz in a magnetic field of 4kOe (40mT), it is Zavoisky (1946) ¹ who is credited with recording the first ESR spectrum at a frequency of 130MHz from a sample of $\text{CuCl}_2 \cdot 2\text{H}_2\text{O}$, requiring a field of 4.6mT, whilst later in the same year an ESR spectrum at 2.93GHz was reported [80].

The fields for these measurements were obtained from small electromagnets. Modern commercially available instruments (Bruker) employing 'standard' electromagnets having a field capability of 2T, making them suitable for use

¹This paper apparently appeared in J. Phys. USSR, 9, p211 1946. It has not been possible to obtain a copy.

4.1. SPECTROMETER OUTLINE

in X-Band (10GHz) and Q-Band (35GHz) instruments.

The St. Andrews high field instrument [81] employs a super conducting magnet capable of 12T for work between 75GHz and 300GHz. Fields of 33T [35, 82]² are produced at European and American national High Field facilities using resistive (Bitters) magnets, and these are used for ESR studies; both facilities were projecting fields of 45T from compound magnets which would in principal allow ESR spectra to be recorded at frequencies in excess of 1THz.

4.1.1.2 The oscillating field

The oscillating field is produced by the microwave source, details of which are discussed in chapter 5. As has been shown, it is necessary to ensure that the magnetic component of the EM-wave coupled into the Sample Holder is orthogonal to the external field, which is the purpose of the sample holder. At microwave frequencies, the orthogonality of the fields may be ensured using a resonant cavity, of which the most common constructions are hollow rectangular boxes or cylinders. Cavities play a central role in the realisation of ESR spectrometers, and will be discussed in greater detail in section 4.3.

4.1.1.3 Field modulation

The required spectrum may be obtained by either holding the frequency of the RF field constant and varying the main field, or conversely, by varying the frequency of the RF field and holding the main field constant.

²The October 2003 Journal of Low Temperature Physics (Volume 133 No.1-2) was a special issue devoted to 'Physics and Technology at High Magnetic Fields'.

4.1. SPECTROMETER OUTLINE

The coupling of the RF into the sample holder is carefully adjusted to optimise the instrument sensitivity, and is intrinsically narrow band, and all components in the path are sources of reflection and hence standing waves. Thus maximum RF energy is only coupled into the sample holder over a narrow bandwidth and spectrometer sensitivity is therefore optimum over a narrow frequency range. Further, many sources have poor linearity and power stability over even moderate tuning ranges. Thus, it is not usual to modulate the microwave source.

Changing the main magnetic field is not at first glance easy. The magnets consist of large inductances and even with superconducting magnets it is necessary to change currents with magnitudes of 10's of Amps. This can only be done slowly, typical rates are 1T/min. Attempting to change the applied field in this way is known as field sweeping.

Small, ($\sim 10\text{G}$), linear, high frequency (of order kHz) field changes are referred to as field modulations, and are obtained using the field modulation coils shown in figure 4.1. The field produced by these coils either re-enforces or subtracts from the applied field, thus modulating the applied field; these coils are small, have a low inductance and therefore field modulation is viable.

In reality, the ESR spectrum is obtained by fixing the RF field frequency, and sweeping the main field whilst modulating it. It is however important not to modulate the field to amplitudes which are of the order of the spectral line under investigation, as this distorts the line shape [32].

4.1.2 Temperature Control

It was noted in section 2.3 that the relaxation time of the excited spin system defines the spectral line width. A fundamental problem arises when the relaxation time becomes of order the period of microwave radiation; the line becomes so broad that no spectral information is recorded. Short relaxation times, on the sub ns time scale may be found in transition metals [83]. Other processes which shorten relaxation times, for example damping effects in solution and collisions in gasses, are discussed in [34] [33]. Relaxation times can show a temperature dependence varying between $1/T$ and $1/T^9$ and therefore temperature reduction can allow a broadened line to be resolved; this is the primary use of the cryogenic jacket.

There are situations in which it is desirable to change the sample temperature. For example elevated temperatures are required to force conformation changes [84] in diamond, whilst low temperatures may be required to study conformation changes in organic systems [85].

Temperatures ranging from liquid Helium to a couple of hundred Kelvin may be obtained using conventional gas flow cryostats, which are commercially available. Specialist situations require specialist solutions; for example temperatures of 1000K [86] and the combination of low temperature and high vacuum [87] resulted in the development of in house solutions .

4.2 Passive RF Components

The spectrometer RF components not only consist of the source, the coupling structure and the detector, but includes the interconnection between the various components. In this section, the important properties of the

4.2. PASSIVE RF COMPONENTS

interconnection the coupler and the passive components, will be described.

4.2.1 Interconnections

The method used to connect the various front-end components together depends upon the frequency at which the spectrometer is to be operated.

Loss in the interconnect is undesirable for two reasons. Firstly, in the transmit path it reduces the power which can be applied to the sample. Considerable effort is expended in generating microwave power; at low microwave frequencies gain is reasonably cheap and readily available. However, as frequency increases gain becomes increasingly difficult to obtain and commensurately more expensive. Secondly, in the receive path the loss increases the noise temperature of the system, reducing the spectrometer sensitivity. An additional consideration is that in experiments removed from room temperature, thermal conduction by the interconnection can become a problem.

4.2.1.1 Co-axial cables

Figure 4.2 shows the loss of two common co-axial cables as a function of frequency. The construction of the co-axial cables determines their properties. The RG58³ has a braided outer sheath and a diameter of approximately 5mm, LDF6 (commonly known as Helix) on the other hand has a solid outer sheath and a diameter of 38mm⁴. Over the range of frequencies indicated, the major contributors to loss are radiation through the outer sheath (in the case of the RG58) and resistive ('copper') losses.

³Data obtained from www.rojone.com

⁴Data obtained from www.andrews.com

4.2. PASSIVE RF COMPONENTS

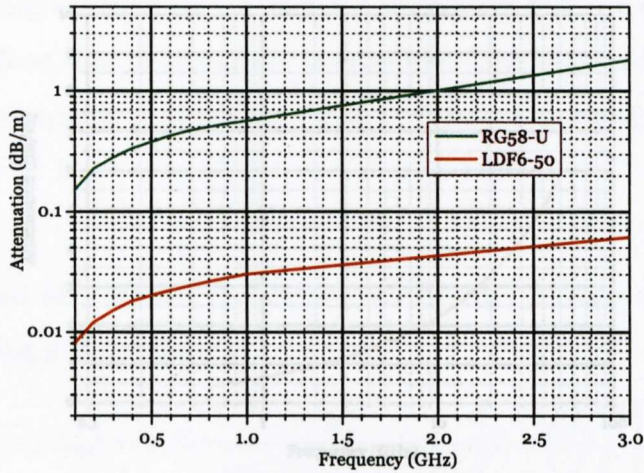


Figure 4.2: The loss (dB/m) of two commercially available types of co-axial line. Both have a characteristic impedance of 50Ω .

As frequency increases dielectric losses become increasingly important and copper losses increase, the combined effect of which is seen clearly in figure 4.3. This co-axial cable is specified for use to 50GHz and is 2.2mm diameter with a solid PTFE dielectric cable⁵. Extrapolating this curve to 100GHz shows that a loss of 9dB/m may be hoped for from this cable.

As frequency increases, the power handling capability of the cable falls. The SR086 discussed above has a maximum power handling capability of less than 200W at 100GHz and approximately 400W at 1GHz. Power handling capability depends upon the construction employed. SR250 is a 6mm cable which will handle 1.6kW at 1GHz, although its upper frequency limit is only 20GHz. As will be seen later, this power handling capability would impose severe limitations on an X-band pulsed spectrometer.

Even a moderate length of co-axial cable begins to look unattractive as a

⁵Data obtained from www.megaphase.com

4.2. PASSIVE RF COMPONENTS

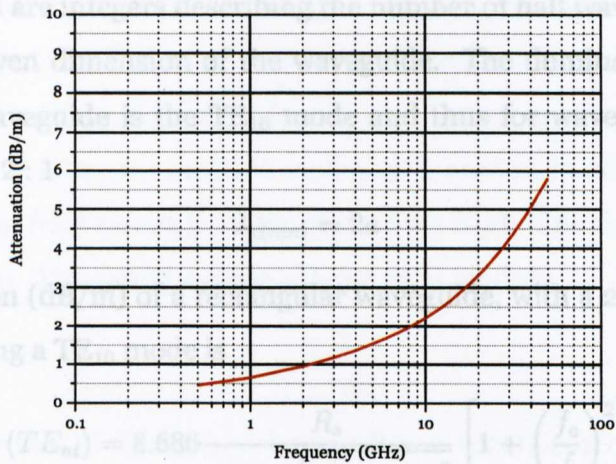


Figure 4.3: Loss of a 2.2mm semi rigid co-axial cable type SR086 suitable for use to 50GHz, obtainable from Megaphase Inc.

method of interconnection at high frequencies and an alternative method of interconnection becomes essential as frequency increases. Such an alternative is waveguide, which is simply a hollow pipe.

4.2.1.2 Rectangular waveguide

Rectangular waveguide is simply a hollow pipe of rectangular cross section. If figure 4.7 represents a waveguide of length d , the cut-off wavelength $\lambda_{c(mn)}$ (the wavelength below which the waveguide will not propagate a wave without considerable attenuation) is given by ⁶

$$\lambda_{c(mn)} = \frac{2ab}{\sqrt{m^2b^2 + n^2a^2}} \quad (4.1)$$

⁶All the required equations, and their derivations may be found in, for example [88].

4.2. PASSIVE RF COMPONENTS

where n and m are integers describing the number of half wavelengths supported in a given dimension of the waveguide. The dominant mode in a rectangular waveguide is the TE_{10} mode and thus for waveguide with an aspect ratio of 2 : 1

$$\lambda_{c(mn)} = 2a \quad (4.2)$$

The attenuation (dB/m) of a rectangular waveguide, with a 2:1 aspect ratio and propagating a TE_{10} mode is

$$\alpha(TE_{nl}) = 8.686 \frac{R_s}{120\pi b \sqrt{1 - (f_c/f)^2}} \left[1 + \left(\frac{f_c}{f} \right)^2 \right] \quad (4.3)$$

In which f_c is the cut off frequency, f is the propagating frequency, and the factor 8.686 is the conversion from Np/m to dB/m. R_s is the waveguide wall resistance at the frequency of propagation, and if μ is the permeability of free space and σ is the conductivity of the waveguide this may be calculated using

$$R_s = \sqrt{\frac{\pi f \mu}{\sigma}} \quad (4.4)$$

The standard waveguide for propagating a 10GHz TE_{10} mode is WR90 which has dimensions of 2.286cm x 1.143cm; this produces an f_c of approximately 6.56GHz, and assuming copper walls ($\sigma = 5.8 \times 10^{-7} \text{U/m}$) for the waveguide, an attenuation of approximately 0.1dB/m which is a considerable improvement over coaxial interconnection, and demonstrates clearly the attraction of waveguide for interconnection.

4.2.1.3 Circular waveguide

Waveguide may also be circular, and modes are denoted by TE_{nl} or TM_{nl} . n and l are integers; n describing the number of half wavelengths supported

4.2. PASSIVE RF COMPONENTS

on the waveguide radius and l the number of half wavelengths supported on a circumference. To differentiate modes in a circular waveguide from those in a rectangular waveguide, for modes in a circular waveguide TE modes will be referred to as H modes and TM modes as E modes, in effect describing the propagating field rather than the transverse field. The dominant mode is the H_{11} mode. The cutoff wavelength for an H mode is

$$\lambda_{c(nl)} = \frac{2\pi a}{p'_{nl}} \quad (4.5)$$

where p'_{nl} is the root of $J'_n(x)$, $J_n(x)$ being a Bessel function of order n and the prime denoting the derivative function. The attenuation of a propagating H wave is

$$\alpha(H_{nl}) = 8.686 \frac{R_s}{120\pi a \sqrt{1 - (f_c/f)^2}} \left[\frac{n^2}{p'^2_{nl} - n^2} + \left(\frac{f_c}{f} \right)^2 \right] \quad (4.6)$$

It is important to note that for $n = 0$ equation 4.6 shows that the attenuation of an H_{0l} mode will have an attenuation which falls indefinitely with frequency, making all H_{0l} modes attractive for low loss applications.

Consider a circular pipe propagating a 10GHz wave. The cut-off wavelength for the H_{01} mode is set to 6.56GHz. The pipe radius a is calculated using equation 4.5 with $p'_{01}=3.8317$ [89] to be 27.89mm. Then using equation 4.6, the attenuation of this circular pipe at 10GHz is found to be approximately 0.02dB/m, which offers considerable advantage over rectangular waveguide.

4.2.1.4 Waveguide at 94GHz

Waveguide WR10 (for which $a = 2.54\text{mm}$ and $b = 1.27\text{mm}$) is the preferred (rectangular) waveguide for use at 94GHz, and has a $f_{c(1,0)}$ of 59GHz. A circular waveguide with the same cut-off frequency has a radius of 3.1mm. The

4.2. PASSIVE RF COMPONENTS

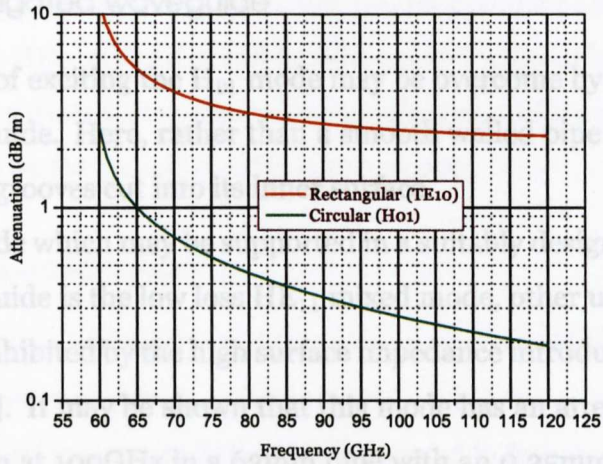


Figure 4.4: The attenuation of wave in rectangular and circular waveguide.

Both waveguides have a cut-off frequency of 59GHz.

attenuation of these waveguides is compared in figure 4.4. It is thus clear that a circular waveguide supporting an H_{01} mode is, from an attenuation point of view, the most attractive method of interconnection considered so far.

However, the H_{01} is not the mode with the lowest cut-off frequency and therefore any waveguide supporting H_{01} mode is able to support a number of other modes. In the case of the H_{01} mode, it is degenerate with the E_{11} mode and 3 modes with lower cut off frequencies are supported by this waveguide [88]. Exciting a pure H_{01} mode is therefore difficult, and once excited difficult to preserve as the guided wave propagates.

4.2. PASSIVE RF COMPONENTS

4.2.1.5 Corrugated waveguide

The problems of exciting the H_{01} mode may be overcome by the use of corrugated waveguide. Here, rather than a smooth walled pipe the waveguide has a series of grooves cut into its inner surface.

The lowest mode which may be supported in a suitably designed corrugated circular waveguide is the low loss HE_{11} mixed mode, other undesired lower modes being inhibited by the high surface impedance introduced by the corrugations [88]. It may be shown that this mode has an attenuation of less than 0.02dB/m at 100GHz in a 63mm pipe with an 0.25mm depth 0.5mm pitch corrugation [90] which is rather better than the H_{01} mode of the simple circular pipe.

Additional advantages are accrued in using this mode of the corrugated waveguide. Firstly it is polarisation preserving, a vertically polarised wave entering the waveguide in the HE_{11} mode is transmitted down the waveguide with minimal cross polar distortion and secondly, it is well matched to a free space Gaussian beam with waist of approximately 64% of the waveguide radius.

Waveguide power handling:

The power handling capability of waveguide is primarily restricted by the breakdown of air within the waveguide.

Between the broad faces of rectangular waveguide there are high electric fields which cause the breakdown; even so rectangular waveguide has multi kW power handling capabilities. WR-650L will handle 12MW at L-Band, WR-90 will handle 200kW at X-Band, whilst even the relatively narrow WR-10 employed at 95GHz will handle 3kW.

Circular waveguide having approximately the same dimensions as WR-10 will handle roughly the same power. Corrugated waveguide however, be-

4.2. PASSIVE RF COMPONENTS

cause it is being over-moded, has a rather greater diameter and a 63mm pipe propagating an HE_{11} at 89GHz will handle 400kW without breakdown. As will be demonstrated later, this power handling capability does not impose any limitations on the pulsed 94GHz spectrometer.

4.2.1.6 Quasi-optical systems

The ultimately low loss method of interconnection would be one in which no waveguides were required, and this is achieved in Quasi-optical systems. Essentially, the microwave radiation is propagated in free space using lenses and/or mirrors to focus and direct the radiation.

Using conical corrugated horns [91] it is relatively easy to launch a high purity fundamental mode Gaussian profile beam, the divergence of which is easily calculated. The design of a Quasi-optical system may then be reduced to using matrix transformations to obtain a set of optical elements which reform the beam in some desired way [92, 93].

Such a system is intrinsically low loss, for the beam forming elements are a small fraction of the total path length. However, the beam launched from a conical horn is not a pure Gaussian beam, and has energy contained in side lobes, and the energy contained in these lobes must be propagated without distortion to avoid truncation loss. This imposes a minimum size on the optical elements, and thus the required elements may be large.

For a Quasi-optical transmission mode spectrometer, Freed quotes a loss of 2dB through a series of lenses with a 54 inch path length. This instrument was of the same dimensions as a rectangular waveguide system in which the losses, it is claimed, would have been 16dB, a very attractive reduction in losses [94].

The St Andrews reflection mode quasi-optical spectrometer uses mirrors as

4.2. PASSIVE RF COMPONENTS

the beam forming elements and a short (approximately 1m) length of corrugated waveguide to couple into the cavity, and has a loss of less than 0.25dB. Thus, the method of interconnection changes with frequency. At low frequencies co-axial cable is viable, however as the frequency of operation increases co-axial cable losses increase and power handling capability falls until at microwave frequencies waveguide becomes the interconnection of choice, whilst at millimetric frequencies (and higher) quasi-optical schemes have become prominent.

4.2.2 The Coupling Structure

The type of coupling structure employed depends upon the method of construction employed in constructing the spectrometer. The coupling structure is required to 'disentangle' the power applied to, and the power reflected from the cavity, whilst isolating the source from the detector; the use of a circulator to achieve this end has been described. Circulators may be realised as co-axially connectorised components, in waveguide and quasi-optically (QO), the QO isolator will be described shortly. One of the earliest (and possibly the simplest) devices to be employed to perform the coupling function is a waveguide component known as the 'Magic T'.

4.2.2.1 The Magic T

The operation of the magic T is described in [77, 95]. If the cavity is placed at port 2, and power is applied to port 1, then port 4 will contain power reflected from the cavity and port 3 and therefore, if a suitable detector is placed at port 4 a spectrum may be recorded. Feher has used a magic T coupler in a

4.2. PASSIVE RF COMPONENTS

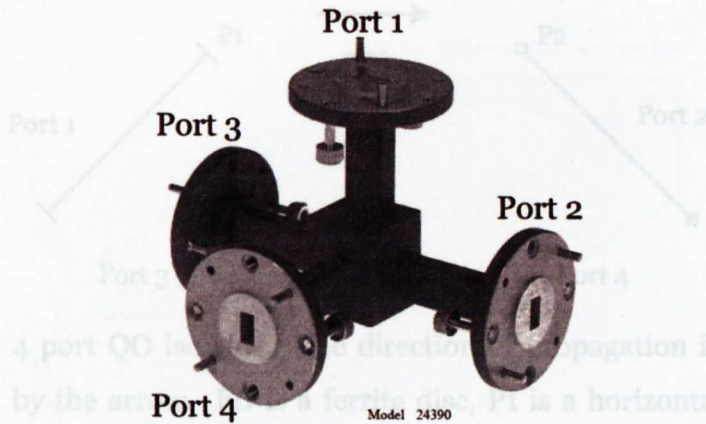


Figure 4.5: A magic T coupler, shown is the Flann Microwave model 24390 40GHz component. Ports are referred to in the text.

The Electric field vector of this wave is now perpendicular to the wires of superheterodyne demodulator at X-band [39], whilst electrical analogues have been used to allow measurements below 1GHz [43].

Whilst the inter-port isolation between ports 1 and 4⁷ of a magic T are comparable with those of a circulator, the magic T has the disadvantage that power is divided equally between ports 2 and 3, which immediately reduces the spectrometer sensitivity for a given power input. The circulator is therefore preferred.

4.2.2.2 The Quasi-Optical Circulator

The 'circuit' of a 4 port QO circulator is shown in figure 4.6. A vertically polarised wave at port1 is transmitted with minimal loss by polariser P1, and on passage through the ferrite disc undergoes a Faraday rotation of $+45^\circ$.

⁷Isolation figure obtained for a complete range products from www.mictotech-inc.com, June 2005.

4.3. THE SAMPLE HOLDER

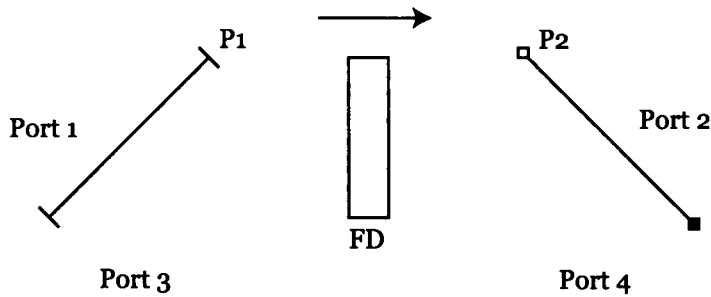


Figure 4.6: 4 port QO isolator. The direction of propagation is indicated by the arrow. FD is a ferrite disc, P1 is a horizontal wire grid polariser whilst P2 is a wiregrid polariser with wires at -45° to the vertical.

The Electric field vector of this wave is now perpendicular to the wires of P2 and is therefore transmitted to port2. In this way port1 is coupled in the forward direction to port2. Exactly similar arguments show that port2 is coupled to port3. In this implementation, wide bandwidths (20GHz), low insertion loss 0.49dB and isolations (S_{41} and S_{31}) of 30dB ; the operation of this component is described in [96], whilst over narrow bandwidths, similar insertion losses with spot isolations of order 60dB are attainable [97].

Thus, with the availability of low loss components, and the concept of an induction mode we are able to construct a spectrometer at 94GHz using QO techniques which will form the basis of a CW/Pulse ESR spectrometer, the source and detector of which are reported and discussed in the remaining chapters of this thesis.

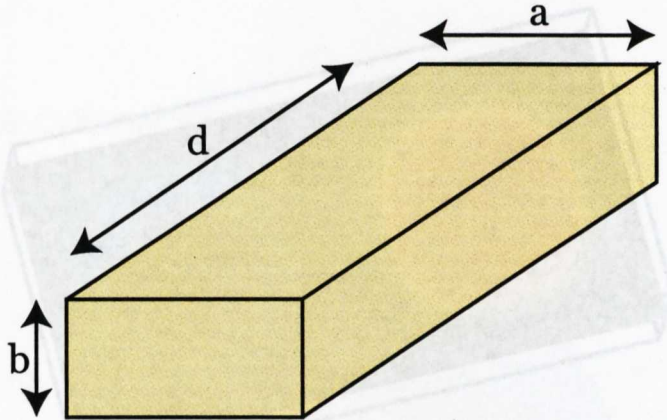


Figure 4.7: Rectangular resonator dimensions

4.3 The Sample Holder

At microwave frequencies, orthogonality may be ensured by placing the sample in a resonant cavity. This may take the form of a hollow rectangular box, a hollow cylinder or a hollow sphere with metallic walls. As the frequency of operation increases and the physical dimensions of closed resonators decreases, the Fabry-Perot resonator becomes attractive.

4.3.1 The rectangular cavity

The resonant frequencies of a rectangular box may be calculated from [88]

$$f = \frac{c}{2} \sqrt{\left(\frac{m}{a}\right)^2 + \left(\frac{n}{b}\right)^2 + \left(\frac{p}{d}\right)^2} \quad (4.7)$$

where c is the velocity of light, m , n and p are integers describing the number of half wavelengths in the box dimension a , b or c respectively. These dimensions are shown in figure 4.7.

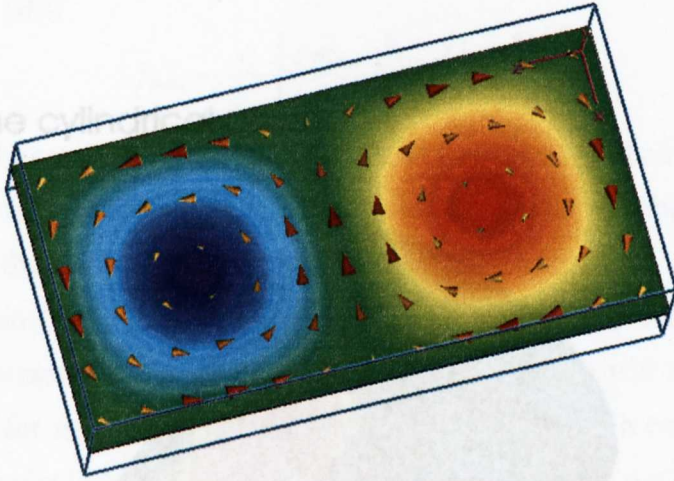


Figure 4.8: The E and H Fields of the TE_{102} mode in a rectangular cavity.

A simple cavity may be constructed by requiring $m = 1$, $n = 0$ and $p = 2$ in a cavity having $a = a$, $b = a/2$ and $d = 2a$; with $a = 2,25\text{mm}$, equation 4.7 gives a resonant frequency of approximately 94GHz. The resonant frequencies are known as modes and are identified as either TE_{mnp} or TM_{mnp} , depending upon which axis is taken as the axis of propagation. The mode evaluated here is a TE_{102} mode.

The field distribution for this mode may be calculated, and is shown in figure 4.8 which was obtained using the commercial EM simulation package 'CST'. The 'globules' of colour indicate the E-field distribution, whilst the arrow heads indicate the H-field distribution. It is clear that in the centre of the cavity there is a region of magnetic field parallel to the 'a' dimension wall, and that in this region there is no electric field. Then, if the cavity is placed in an external field perpendicular to the broad face of the cavity, and a sample is placed in the centre of the cavity we will have the two required orthogonal fields.

4.3. THE SAMPLE HOLDER

lated from [88]

$$f_{\text{max}} = \frac{c}{2\pi} \left[\left(\frac{\mu'_{\text{max}}}{a} \right)^2 + \left(\frac{l\pi}{d} \right)^2 \right]^{1/2} \quad (4.8)$$

4.3.2 The cylindrical cavity

where a is the cavity radius, d is the length of the cavity, μ'_{max} the root of a Bessel function derivative and the indices m , n and l denote the number of half wave lengths on the radius, circumference and length respectively. Following the same nomenclature that was used between rectangular and circular waveguides, the modes of a cylindrical cavity will satisfy the requirement for an axial magnetic field. In this case $\mu'_{\text{max}}=3.832$ and for a cavity having a radius of $a=2.1\text{mm}$ and a length of $d=2.1\text{mm}$ the resonant frequency is $f_{\text{max}}=9.4\text{GHz}$. The field distribution, obtained using 'CST', is shown in Figure 4.9. The sample placed on the axis of the cylinder, in the case of a cylindrical cavity, is correctly placed to be in the required orthogonal fields. The electric field is applied radially.

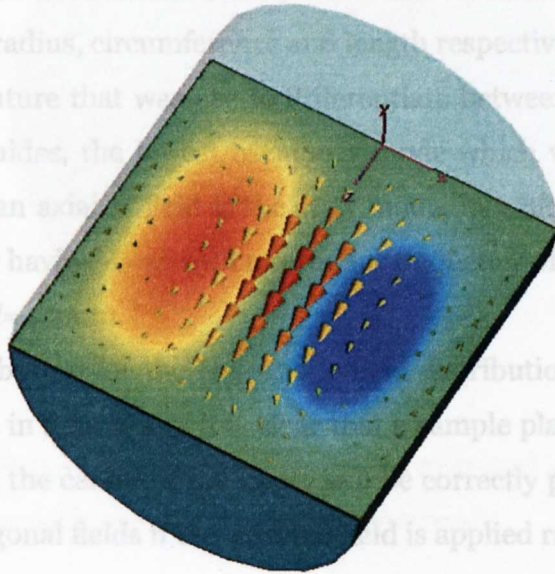


Figure 4.9: The H_{011} mode of a cylindrical cavity. Arrow heads represent magnetic field whilst 'globules' of colour represent electric field.

This time the external field can only be applied radially, and therefore any resonance must supply an axial magnetic field. The required mode is therefore the H_{011} mode. The required mode number is the lowest mode number. The modes of a spherical resonator may be calculated using the zeroes of the Bessel function (using

Defining the axis of the cavity along a co-ordinate system z -axis, the mode required is an H mode and the frequencies of resonant modes may be calcu-

4.3. THE SAMPLE HOLDER

lated from [88]

$$f_{mnl} = \frac{c}{2\pi} \left[\left(\frac{p'_{mn}}{a} \right)^2 + \left(\frac{l\pi}{d} \right)^2 \right]^{1/2} \quad (4.8)$$

where a is the cavity radius, d is the length of the cavity, p'_{mn} the root of a Bessel function derivative and the indices m , n and l denote the number of half wave lengths on the radius, circumference and length respectively. Following the same nomenclature that was use to differentiate between rectangular and circular waveguides, the lowest frequency mode which will satisfy the requirement for an axial H field is the H_{011} mode, in which case $p'_{mn}=3.832$ and for a cavity having $d=2a$ with a resonant frequency of 94GHz we obtain $a=2.1\text{mm}$ and $d=4.2\text{mm}$.

The field distribution for the H_{011} mode field distribution, obtained using 'CST', is shown in figure 4.9; it is clear that a sample placed on the axis of the cylinder, in the centre of the cavity will be correctly placed to be in the required orthogonal fields if the external field is applied radially.

4.3.3 The spherical cavity

This time the external field can only be applied radially, and therefore any resonance must supply an axial magnetic field. The required mode is therefore a TE_{mnl} (or an H_{mnl}) mode, where m is the radial mode number, n is the circumferal mode number and l the azimuthal mode number. The lowest mode which will satisfy the field condition is the H_{011} mode.

The modes of a spherical resonator may be calculated using the zeroes of associated Legendrè polynomials using

$$\frac{2\pi f_{mnl}}{c} = \xi_{nl} \quad (4.9)$$

4.3. THE SAMPLE HOLDER

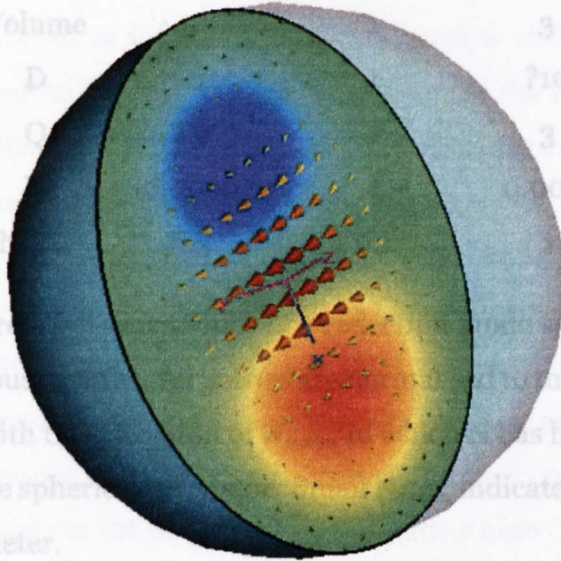


Figure 4.10: The H_{011} in a spherical cavity. Arrows and 'globules' represent magnetic and electric fields respectively.

where ξ_{nl} is the required zero of the polynomial, and for $n = 1$ has a value of 4.94 [98]. For 94GHz we require a sphere radius of 2.27mm.

The field pattern for the H_{011} mode in a sphere, obtained using 'CST', is shown in figure 4.10. The field pattern is thus confirmed as being suitable to ensure the orthogonality of the magnetic fields required by the spectrometer.

4.3.4 Cavities and Sensitivity

From equation 3.68 the concentration sensitivity of an ESR spectrometer may be written in the form

$$N \propto \frac{1}{D} \frac{1}{Q} V_c \quad (4.10)$$

4.3. THE SAMPLE HOLDER

	Cylindrical	Rectangular	Spherical
Volume	5	1	3
D	10	1	?10
Q	2.9	1	3
N	0.0069	1	0.0011
N_{norm}	6.3	9.1	1

Table 4.1: The relative sensitivities of a reflection mode spectrometer using various cavities. All entries are normalised to the rectangular cavity with the exception of N_{norm} in which N has been renormalised to the spherical resonator. Small N_{norm} indicates a sensitive spectrometer.

where D is a factor relating to the cavity filling factor given in [72]. Thus to maximise the instrument sensitivity (minimise N) it is desirable to maximise D and Q and minimise the cavity volume.

Table 4.1 compares estimated spectrometer sensitivities; it must be noted that D for the spherical cavity is an estimate based on visualising the volume of the magnetic field in the cavity relative to the total cavity volume, which appears to be approximately the same as the cylindrical cavity. Despite the small volume of the rectangular cavity, it produces the worst sensitivity due to it having the lowest Q and worst filling factor. As a hollow cavity, the sphere is probably not viable due to machining difficulties, which leaves the cylindrical cavity as the optimum cavity.

4.4. OVERVIEW OF A QUASI-OPTICAL SPECTROMETER

4.3.5 Other types of cavity

As was noted above, as frequency increases, hollow cavities become very small and difficult to handle. In such circumstances the Fabry-Perot cavity becomes attractive [99], [100]. However such resonators fail to realise their maximum Q due to finite mirror losses and have a very poor filling factor.

An interesting variation on the metallic cavity is the the Non-Radiative cavity [101]. Here, a solid (save for an axial hole to carry the sample) dielectric resonator is held between two metal plates. If the plate spacing is such that the gap between the plates is cut off, the cavity cannot loose energy by radiation and a high Q resonator is produced. In fact, the dielectric is not required and simple cut outs in the plates will also provide a high Q resonator [102]. There are many other types of resonator and type and design of resonator depends upon the the frequency and sample type being employed.

4.4 Overview of a quasi-optical spectrometer

A description of a Homodyne spectrometer was given in section 3.8.4 and the remainder of this chapter is an overview of the quasi-optical implementation of this concept which demonstrates the use of the low loss components described above.

This implementation is that of the 94GHz induction mode spectrometer, employing a reflection mode cavity and a homodyne demodulator as employed at St Andrews. The source and detector are major components of the spectrometer and are considered in subsequent chapters.

The 'circuit' of a quasi-optical spectrometer [81] is shown in figure 4.11. The left hand side of the circuit consists of a four port circulator, with the

4.4. OVERVIEW OF A QUASI-OPTICAL SPECTROMETER

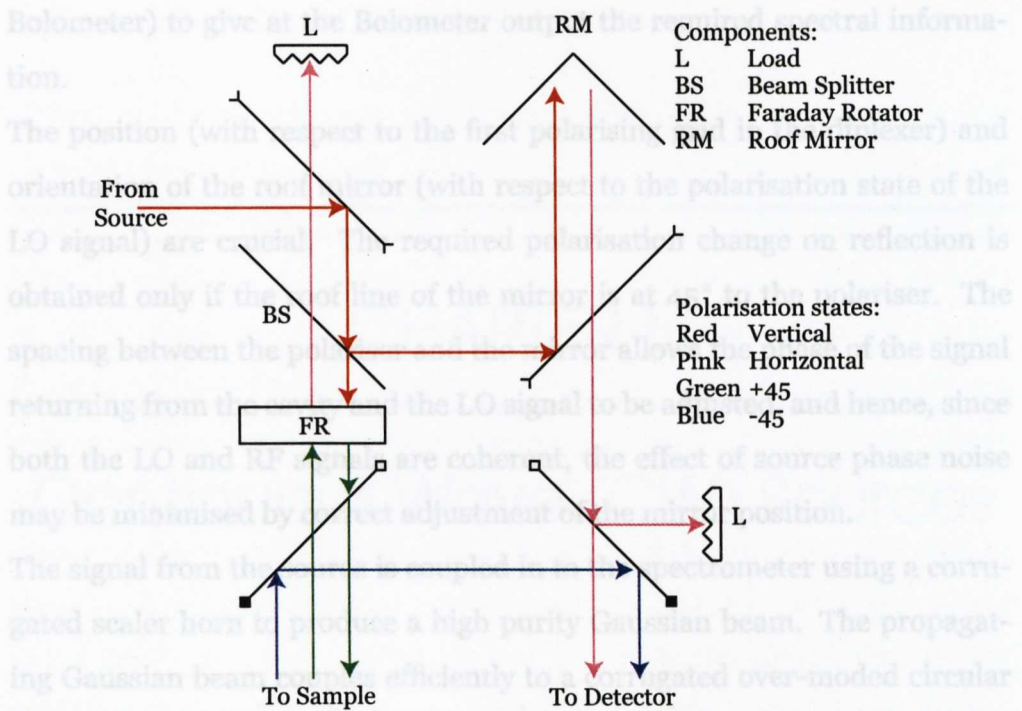


Figure 4.11: An implementation of a quasi-optical Homodyne ESR spectrometer, showing the polarisation states of the various propagating beams within the instrument.

addition of a beam splitter. The beam splitter is realised as a thin dielectric sheet which diverts a small portion of the signal from the source to act as the local oscillator for the homodyne detector. This differs from the description of section 3.8.4, where the unwanted polarisation from the source was employed; in this way a consistent local oscillator signal of known polarisation is obtained.

The right hand side of 4.11 is a diplexer [103], the purpose of which is to combine the LO and the signal from the cavity onto a common axis so that they may be mixed together by the detector (which in this case was an InSb

4.4. OVERVIEW OF A QUASI-OPTICAL SPECTROMETER

Bolometer) to give at the Bolometer output the required spectral information.

The position (with respect to the first polarising grid in the diplexer) and orientation of the roof mirror (with respect to the polarisation state of the LO signal) are crucial. The required polarisation change on reflection is obtained only if the roof line of the mirror is at 45° to the polariser. The spacing between the polariser and the mirror allows the phase of the signal returning from the cavity and the LO signal to be adjusted, and hence, since both the LO and RF signals are coherent, the effect of source phase noise may be minimised by correct adjustment of the mirror position.

The signal from the source is coupled in to the spectrometer using a corrugated scaler horn to produce a high purity Gaussian beam. The propagating Gaussian beam couples efficiently to a corrugated over-moded circular waveguide which supports an HE_{11} mode, which not only has a low attenuation, but preserves the polarisation of the coupled radiation as it propagates. The signal is coupled off the waveguide and into the cavity of choice [104] using an inverted scaler horn, and in this way a linearly polarised wave is coupled into the cavity.

CHAPTER 5

Continuous Wave (CW) Sources

The source, providing the energy to alter the electron spin vector orientation, is the heart of the spectrometer. It must provide the correct frequency, at a suitable power level. It must have a long term stability such that its frequency does not change during an experiment and a short term stability such that oscillator noise does not mask the signal of interest.

This chapter outlines methods of generating high frequency sources, with specific emphasis on obtaining a frequency of order 94GHz, using solid state devices. The Leeson model for estimating oscillator phase noise is introduced, and the minimisation of oscillator phase noise is discussed.

Having demonstrated that direct generation of 94GHz at even moderate powers using solid state techniques is not viable, methods of frequency multiplication are introduced and the properties of multiplied sources are considered.

5.1 Early Microwave Sources

The earliest RF generators were spark gaps. Spark gap transmitters are often thought of as low frequency devices, probably due to the LF nature of the Marconi Trans-Atlantic experiments. However, Hertz apparently demonstrated the validity of Maxwell's Equations at a frequency of order 100MHz in 1888 [105]. In 1897 Chandra Bose demonstrated experiments to the Royal Institution [106] at frequencies of 60GHz. Spark gaps are broadband noisy and have very poor stability; they are not recommended for use outside a Faraday cage!

Thus the generation of microwave radiation is as old as radio. The state of the art in direct generation is reviewed, and it is concluded that the low power and high phase noise of MMIC based solutions to the direct generation of 94GHz make such solutions unattractive.

As a result of the discussion of phase noise it is suggested that frequency multiplication offers a potential solution, and after discussing the properties of frequency multiplied sources the design of a multiplied source is presented.

5.2 Oscillator Circuits

An oscillator has two basic components, a gain block and a frequency determining block. It is the interaction of these two fundamental components which determine the upper frequency limit, and the phase noise content of the oscillator. An introduction to the design of oscillators, and a short modern bibliography, is provided by [107].

As the frequency of oscillation is increased, the type of active device and method of construction become increasingly important, difficult and critical.

5.2. OSCILLATOR CIRCUITS

The major problem encountered in attempting to produce a high frequency oscillator is parasitic components. These may be reduced by moving from packaged devices on PCBs, to chip and bond techniques which eliminates packaging parasitics. However, even very short lengths of bond wire can have surprisingly large inductances (0.5nH for a 1mm bond wire [108]), and eventually bond inductance sets an upper limit on the maximum attainable frequency. The ultimate in reducing the influence of parasitic components must be to integrate the oscillator onto a single chip. This technique has resulted in oscillators, albeit with low (<0dBm) output powers, at frequencies in excess of 100GHz [109].

An interesting approach to the generation of frequencies using active devices with cut off frequencies well below the required oscillator frequency is the push-push configuration, in which two devices are balanced 180° apart and are allowed to conduct for only half a cycle. If the outputs of the devices are summed, the result is a \sin^2 output, which, if the circuit is perfectly balanced produces no fundamental or odd harmonic components of the two basic devices, and a large output of the second harmonic [110, 109, 111]. A natural extension of the push-push technique is the triple-push [112, 113], in which three devices are phased 120° apart producing odd harmonics of the basic frequency. The point here is that each device is operating at a subharmonic of the desired output frequency, and therefore although the cited papers use MMIC techniques, it becomes viable to produce 18GHz oscillators using standard components [114].

Even with the advantages of integration, the active element must have a high transition frequency, and this can only be achieved with physically small devices, which means low current low voltage devices, and therefore low output powers.

5.2. OSCILLATOR CIRCUITS

For simplicity, the Gunn oscillator is a source which is often encountered in high field spectrometers [115, 81], whilst if powers of more than a few 100mW are required, the klystron still finds a place [116]. Whilst in many applications these sources are adequate, they have the disadvantages that they have relatively high phase noise contents and that short pulses (1ns) are difficult to produce from them. Pulse generation will be considered in chapter 10. In the following sections methods of producing low noise CW sources are considered.

5.2.1 The Direct Generation of 94GHz

Gunn oscillators are an attractive source of microwave energy. These oscillators employ a diode which, under the correct bias conditions, exhibit a negative dynamic resistance by virtue of their band structure [117]. Although GaAs diodes are limited to an upper frequency of approximately 60GHz, by deliberately matching at the second harmonic considerable power may be generated up to 120GHz with powers of 10 to 20mW [118]. InP based diodes on the other hand are able to generate considerable power in the fundamental mode at frequencies in excess of 100GHz and output powers in excess of 80mW [119]. GaN based diodes appear to offer an interesting future, being *simulated* to be capable of producing in excess of 5W at 88GHz [120].

Ignoring the fact that 94GHz MMIC oscillators are not readily available and that therefore access to a foundry is required, if a suitable signal for use in a spectrometer is to be generated by a means other than a Gunn oscillator, it must offer some advantage in terms of power output and/or phase noise.

State of the art MMIC oscillators (2004) [121] are able to produce of order -10dBm with a phase noise of -102dBc/Hz at 1MHz offset from the carrier.

5.2. OSCILLATOR CIRCUITS

A typical Gunn oscillator is able to produce +20dBm with a phase noise of order -110dBc/Hz [122] at a 1MHz offset frequency. Although, as will be demonstrated later, direct generation of a 94GHz signal for a pulsed spectrometer has problems, for CW applications the oscillator output may be amplified using commercially available modules based on either FET (the Farran Technologies FPA-109418 for example¹) to +18dBm, or using an IM-PATT amplifier (Elva ILLA series amplifier²) to +23dBm.

Clearly, direct generation of a suitable 94GHz signal is viable. However, phase noise is an issue and there are relatively few amplifiers which will raise the available power to suitable levels, although the number is increasing.

5.2.2 Oscillator Tuning

An oscillator may be modeled [47], as shown in figure 5.1. A negative resistance provides gain, and has associated with it a reactance. The reactance of the negative resistance is opposed by a second reactance provided by passive components known as the resonator.

A common type of oscillator is the varactor tuned oscillator (VTO) in which the capacitance of the resonator is implemented as a reverse biased diode [123] -the varactor. If the varactor has a minimum capacitance C_{Rmin} and a maximum capacitance C_{Rmax} , the maximum frequency change which can be obtained is

$$\frac{f_{max}}{f_{min}} = \sqrt{\frac{C_n + C_{Rmax}}{C_n + C_{Rmin}}} \quad (5.1)$$

¹www.farran.com

²www.elva-1.com

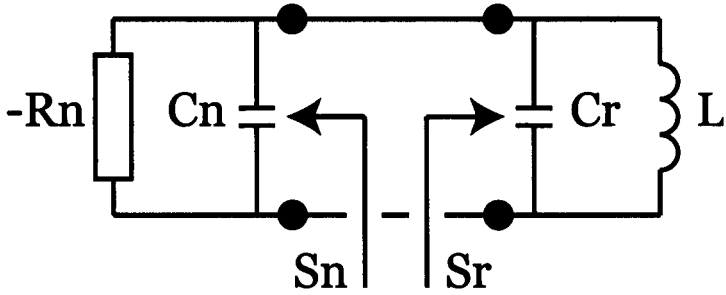


Figure 5.1: The negative resistance representation of an oscillator.

Even if C_n is zero and the varactor has a capacitance ratio of 10:1, the maximum frequency ratio which could be obtained would be approximately 3.16:1, and it is difficult to obtain a frequency ratio of 2:1. VTO's tend to have a non linear tuning curve (frequency against voltage) due to the capacitance-voltage law of the varactor diode [124] unless a great deal of design effort is expended [125]. Further, and because the resonator has a relatively low Q imposed by the varactor diode resistance, they also have a poor phase noise performance.

An interesting solution to these problems is to replace the varactor and its associated inductor with a YIG (Yttrium Iron Garnet) sphere, in which case the oscillator is known as a YTO. YIG is a low loss ferrite material whose electrons, when placed in a magnetic field, perform a Larmor precession about the applied magnetic field at a frequency of 28GHz/T. By coupling into this precession using a small loop, a very high Q oscillator [126] with tuning ranges in excess of an octave [127] and even a decade may be constructed [128, 129]. YIG oscillators have extremely linear tuning curves because of the simple linear relationship between applied magnetic field and the electron precession frequency. The *unloaded* Q of a highly polished YIG

Sphere can be in excess of 5000 at 10GHz [130], and whilst the loaded Q of the resonator depends upon the dimensions of the coupling loop and sphere, very high Q resonators and hence low phase noise, tunable oscillators may be realised.

5.3 Oscillator Noise

When the only available technologies were Silicon BJTs or GaAs FETs, it was accepted that oscillators based upon bipolar devices, which would function to approximately 4GHz, had a rather better noise performance than oscillators, albeit at higher frequencies, based upon GaAs devices. However modern oscillators based upon GeSi technology mean that this is no longer the case. Noise in oscillators arises when low frequency device noise is up converted [131] to the oscillator output frequency (the carrier). The extent (in terms of frequency offset from the carrier) and the shape [132] of the noise spectrum are crucially dependant upon the type of device (BJT or FET) [133] and the device material [134, 135].

The Leeson [136] model of oscillator phase noise is

$$\mathcal{L}(f_m) = 10 \log \left[\frac{1}{2} \frac{FkT}{P_s} \left(\frac{1}{4} \frac{1}{Q_l^2} \frac{f_o^2}{f_m^2} + 1 \right) \left(\frac{f_c}{f_m} + 1 \right) \right] \quad (5.2)$$

in which

- $\mathcal{L}(f_m)$ is the phase noise spectral density (dBcHz⁻¹)
- Q_l is the resonator loaded Q
- f_o is the oscillator carrier frequency (Hz)
- f_m is the offset frequency from the carrier (Hz)

5.3. OSCILLATOR NOISE

f_c	is the device flicker ($1/f$) noise corner frequency (Hz)
P_s	is the amplifier saturated output power (W)
F	is the device noise factor
k	is Boltzmann's constant
T	is the absolute temperature

This result is based on a linear feedback model of an oscillator and allows the phase noise content of any oscillator to be estimated. This model must, however, be applied with care. For example, whilst the model accounts for $1/f$ noise, close to the carrier other distributions are encountered and these must be accounted for by adding additional terms to the model [137, 138]. Despite this, when used with care, the Leeson model allows various options for a low noise source to be evaluated.

5.3.1 Minimising Oscillator Phase Noise

For a low noise source, it may be observed that a low noise factor, high power device is required. Unfortunately these are conflicting device requirements, low noise devices require small physical dimensions, the best that can be done is to maximise the available power from a given device.

It might be expected that to minimise phase noise Q_l must be as high as possible, and indeed this is the case. However, raising the loaded Q_l changes the active device termination and therefore changes the device noise factor. This may be taken into account [139], however even allowing for any change in F , simply maximising the resonator loaded Q_l may not produce the expected reduction in phase noise. The offset frequency at which the phase noise

5.3. OSCILLATOR NOISE

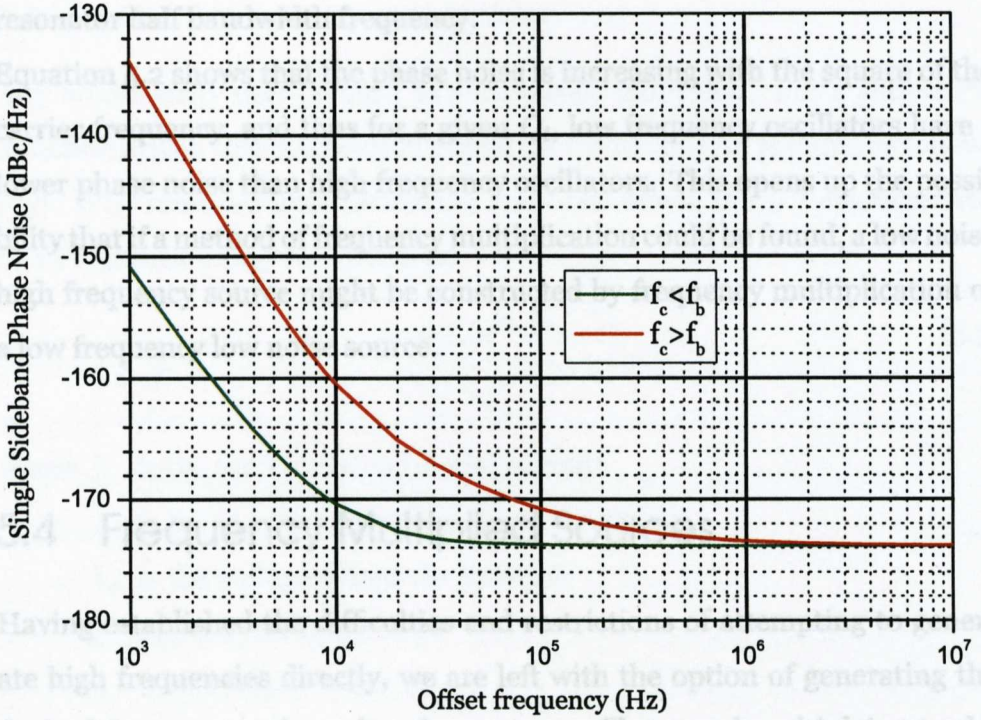


Figure 5.2: Hypothetical oscillator phase calculated using the Leeson model. In both cases f_b was set to 10kHz, whilst f_c was set to either 1kHz or 100kHz.

rises from the noise floor is determined by the resonator half bandwidth f_b .

Defining

$$f_b = \frac{1}{2} \frac{f_o}{Q_i} \tag{5.3}$$

equation 5.2 may be restated as

$$\mathcal{L}(f_m) = 10 \log \left[\frac{1}{2} \frac{FkT}{P_s} \left(\frac{f_b^2}{f_m^2} + 1 \right) \left(\frac{f_c}{f_m} + 1 \right) \right] \tag{5.4}$$

Figure 5.2 shows that the phase noise spectrum depends crucially upon the relationship between the flicker and resonator half bandwidth frequencies. It is desirable to ensure that the flicker corner frequency is less than the

resonator half bandwidth frequency.

Equation 5.2 shows that the phase noise is increasing with the square of the carrier frequency, and thus for a given Q_i , low frequency oscillators have a lower phase noise than high frequency oscillators. This opens up the possibility that if a method of frequency multiplication could be found, a low noise high frequency source might be constructed by frequency multiplication of a low frequency low noise source.

5.4 Frequency Multiplied Sources

Having established the difficulties and restrictions of attempting to generate high frequencies directly, we are left with the option of generating the desired frequency using a low frequency oscillator and multiplying to the desired output frequency. In this section the concept of frequency multiplication and its advantages and disadvantages are discussed.

5.4.1 Frequency Multiplication

Any amplifier driven into, or close to, saturation produces harmonic distortion, an effect which is usually avoided. Harmonics of the input frequency arise because when driven into saturation the amplifier becomes non-linear. However, if frequency multiplication is desired then a non-linear circuit or device is driven to produce harmonics, at the highest possible amplitude, and then the required harmonic of the input signal is selected by filtering.

5.4. FREQUENCY MULTIPLIED SOURCES

5.4.1.1 Variable resistance multipliers

Any nonlinearity may be used as a frequency multiplier. For a simple PN Junction driven with a sinusoidal signal the device current is found as follows [75]. Well removed from saturation and breakdown, the I/V characteristic of a PN junction may be written as

$$I_j = I_s(e^{V_d \frac{q}{\gamma k T}} - 1) \quad (5.5)$$

where I_j is the total junction (diode) current

I_s is the junction reverse saturation current

V_d is the voltage across the junction

q is the electronic charge

k is Boltzmann's constant

T is the junction's absolute temperature

γ is the junction ideality factor

The quantity kT/q is known as the thermal voltage (V_T) and has a value of approximately 26mV at room temperature. The across the junction voltage combines the junction 'built in' voltage ($\sim 600\text{mV}$ for Silicon) and an applied voltage (V_i). If the applied voltage is a sinusoid with a DC offset of V_{DC} and an amplitude V_{AC}

$$V_i = V_{DC} + V_{AC} \cos \omega t \quad (5.6)$$

and if the saturation current is small, the junction current may be written as

$$I_j = I_q e^{\frac{V_{AC}}{\gamma V_T} \cos \omega t} \quad (5.7)$$

where I_q is the diode quiescent current due to the DC component of the applied voltage. The exponential in equation 5.7 has a standard expansion

5.4. FREQUENCY MULTIPLIED SOURCES

in terms of modified Bessel functions [89]

$$e^{x \cos \theta} = I_0(x) + 2 \sum_{n=1}^{\infty} I_n(x) \cos(n\theta) \quad (5.8)$$

Combining equations 5.7 and 5.8 gives the harmonic content of the junction current to be

$$I_j = I_q I_0(x) \left[1 + 2 \sum_{n=1}^{\infty} \frac{I_n(x)}{I_0(x)} \cos(n\omega t) \right] \quad (5.9)$$

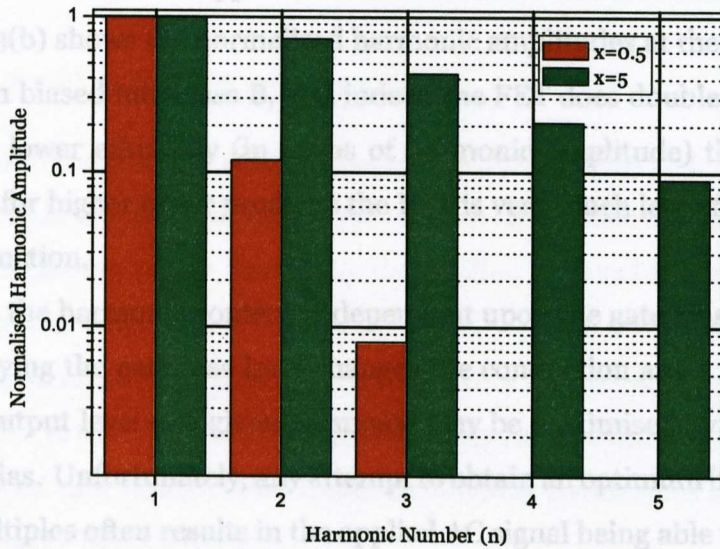
where $x = V_{AC}/\gamma V_T$ and $I_n(x)/I_0(x)$ is the amplitude of the n^{th} harmonic normalised to the amplitude of the DC component $I_0(x)$. Whilst values of $I_n(x)$ are tabulated in [89], such tables usually fail to contain the required coefficients, and for such cases a procedure for obtaining the coefficients based on Gaussian Quadrature is contained in Appendix A.

The coefficients $I_n(x)/I_0(x)$ in equation 5.9 are the amplitudes of the harmonics of the applied sinusoid produced by the non-linear I/V characteristic of a PN junction. Figure 5.3(a) shows the first 5 harmonics (normalised to the amplitude of the fundamental output) for two drive levels and demonstrates that for appreciable harmonic power to be generated, there is a threshold input power which must be exceeded.

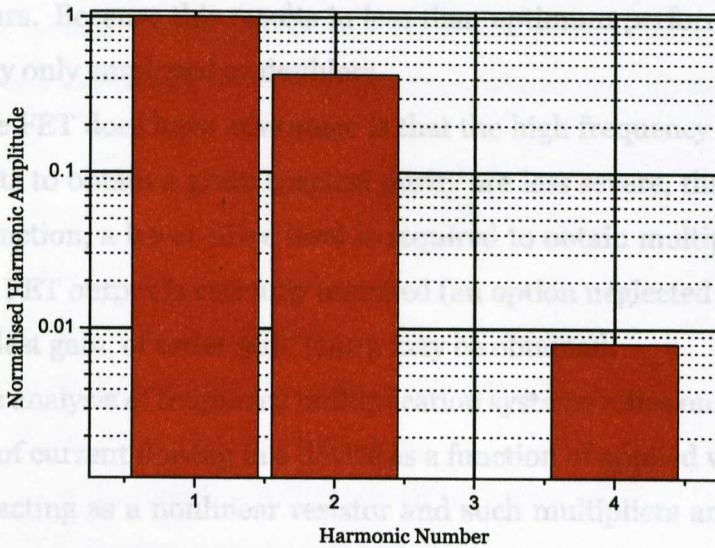
Another common non-linearity is the square law, which is encountered as the transfer characteristic of an FET. Analysis of the FET as a multiplier is complicated by the need to include a description of drain saturation effects. By assuming that the FET is biased into class B i.e. conducts for exactly 50% of the input cycle, and neglecting saturation effects, a half-wave rectified sinusoid waveform at the drain of the FET [140] is obtained. The Fourier coefficients A_n of a half wave rectified sine function are

$$A_n = \begin{cases} \frac{1}{2} & n = 1 \\ \frac{2}{\pi} \frac{1}{n^2 - 1} & n > 1 \quad n \text{ even} \\ 0 & n > 1 \quad n \text{ odd} \end{cases} \quad (5.10)$$

5.4. FREQUENCY MULTIPLIED SOURCES



(a) Harmonics generated by a PN junction.



(b) FET generated harmonic amplitudes

Figure 5.3: A comparison of the harmonics produced by a simple PN junction and a Class B biased FET when driven with a sin source.

5.4. FREQUENCY MULTIPLIED SOURCES

and thus the FET would appear to be an efficient even harmonic generator. Figure 5.3(b) shows the normalised harmonic amplitudes at the drain of an FET when biased into class B, and indeed the FET does double, but shows a slightly lower efficiency (in terms of harmonic amplitude) than the PN junction; for higher order products the FET is very much less efficient than the PN junction.

However, the harmonic content is dependant upon the gate bias level [140, 141]. Varying the gate bias level changes the conduction angle of the FET, and the output level of a given harmonic may be maximised by controlling the gate bias. Unfortunately, any attempt to obtain an optimum bias for high order multiples often results in the applied AC signal being able to drive the gate to a point at which drain-source breakdown, and hence damage to the FET, occurs. Because this results in less than optimum performance FETs are usually only employed as doublers.

Where the FET does have advantage is that the high frequency filtering requirements to obtain a given spectral purity are less severe, than those for the PN junction, a lower drive level is required to obtain multiplier action, and if the FET output is carefully matched (an option neglected in equation 5.10) modest gain, of order 3dB [140], may be obtained.

The above analysis of frequency multiplication systems relies on a nonlinear variation of current flowing in a device as a function of applied voltage. The device is acting as a nonlinear resistor and such multipliers are known as varistor multipliers. Varistor multipliers are able to offer operation over considerable bandwidths, although the amplitude of the harmonic output decreases as $1/n^2$ [142] and they may only be suitable for use in low power applications because even moderate drive levels can result in device currents sufficient to destroy the device.

5.4. FREQUENCY MULTIPLIED SOURCES

5.4.1.2 Variable reactance multipliers

An alternative method of using a semiconductor junction as a multiplier is to reverse bias the junction and employ the variation of charge, stored in the junction depletion region formed by the applied reverse bias, as a function of drive level. Here multiplication occurs as a result of a variation in the device impedance. Multipliers operating in this way are known as varactor multipliers. It should be noted that whilst any reverse biased junction may be employed as a varactor multiplier, the highest frequencies are obtained using Schottky Barrier devices.

Provided that a junction is operated in a region which is well removed from the device reverse breakdown voltage (thus preventing damage) and does not become forward biased, the capacitance of the reverse biased junction is given by

$$C(V) = C_{j0} \left[1 - \frac{V}{V_b} \right]^{-\gamma} \quad (5.11)$$

where $C(V)$ is the reverse biased junction capacitance

C_{j0} is the junction capacitance at zero bias

V is the applied reverse bias

V_b is the junction contact (built in) potential

γ is the junction ideality factor

γ defines the doping profile of the junction; for an efficient varactor multiplier an abrupt junction is desirable, in which case $\gamma = 1/2$ [143]. Now

$$Q(V) = \int C(V) dV \quad (5.12)$$

5.4. FREQUENCY MULTIPLIED SOURCES

which, provided $V/V_b < 1$ (i.e. the junction does not become forward biased) gives

$$Q(V) = Q_o \left[1 - \frac{V}{V_b} \right]^{1/2} \quad (5.13)$$

where $Q_o = -2C_{j_o}V_b$ is the charge stored at zero bias. The voltage developed due to a stored charge Q is therefore

$$V = V_b \left[1 - \left(\frac{Q(V)}{Q_o} \right)^2 \right] \quad (5.14)$$

If, due to an applied sinusoidal voltage, the charge variation is of the form

$$Q(V) = Q_o (\sin \omega_o t + \sin n\omega_o t) \quad (5.15)$$

where n is an harmonic number, the voltage developed by the diode as a result of this charge variation is of the form

$$V = 1 - \frac{1}{2} (\cos 2\omega_o t + \cos 2n\omega_o t) + \cos (n-1)\omega_o t - \cos (n+1)\omega_o t \quad (5.16)$$

If the diode is excited by a single tone ($n = 0$ or $n = 1$) the voltage developed can only contain second harmonic components; the varactor diode is only able to produce a doubling action.

If however $Q(V)$ is allowed to contain a second harmonic component, the diode develops a voltage containing terms in $4\omega, 3\omega, 2\omega$ and ω , and a 3^{rd} harmonic component may be extracted. The 3^{rd} harmonic is produced by allowing the 2^{nd} harmonic component to mix with the fundamental component using the charge nonlinearity. When used in this way, the 2^{nd} harmonic component is referred to as an *idler* frequency. By allowing various idler frequencies to mix together high order varactor multipliers may be produced, however the design of high order varactor multipliers becomes increasingly complicated as the harmonic number increases [144], and the bandwidth over which satisfactory operation may be obtained becomes restricted by the

5.4. FREQUENCY MULTIPLIED SOURCES

bandwidth of the idler circuits.

The efficiency of a varactor multiplier is obtained using the Manley-Rowe equations [145] which describe power conversion in any system having a nonlinear capacitor. For a varactor system with two excitation signals f_1 and f_2 the Manley-Rowe equations are

$$\begin{aligned} \sum_{m=0}^{\infty} \sum_{n=-\infty}^{\infty} \frac{mP_{m,n}}{mf_1 - nf_2} &= 0 \\ \sum_{n=0}^{\infty} \sum_{m=-\infty}^{\infty} \frac{nP_{m,n}}{mf_1 - nf_2} &= 0 \end{aligned} \quad (5.17)$$

where $P_{m,n}$ is the power at the frequency $|mf_1 - nf_2|$. In a multiplier application there is only a single excitation frequency, f_1 for example, in which case equation 5.17 reduces to

$$\sum_{m=0}^{\infty} P_m = 0 \quad (5.18)$$

where P_m is the power contained in the m^{th} harmonic. This suggests that all the applied power P_1 is converted with 100% efficiency to harmonic power, and in the case of a doubler all the applied power would be converted to power at the 2nd harmonic frequency.

This is an oversimplification. The above calculations are based on a model which treats the varactor diode as simply consisting of a capacitive element. A more realistic model includes a resistive element in series with the capacitor accounting for the bulk resistance of the semiconductor, which introduces a loss mechanism. A complete model of the varactor diode includes a number of additional components which not only limit conversion efficiency, they also introduce an upper frequency at which the diode will function [146].

Various configurations of diode and active device have been reported as methods of multiplying to 94GHz. MMIC realisations are low power options, require a foundry and need not be further considered.

5.4. FREQUENCY MULTIPLIED SOURCES

Because the reverse breakdown potential of a semiconductor junction is many volts, varactor multipliers are able to operate with considerably higher drive levels than varistor multipliers. This, and the high efficiency of varactor multipliers compared to varistor multipliers makes varactor circuits the preferred multiplier solution.

The major difficulty is that to obtain the best possible performance, parasitic components must be minimised. This leads to special diode geometries (planar diodes [147]), diode stacks [148] or arrays of diodes in Quasi-Optical systems (diode grids [149]). In either case the manufacture of multipliers able to generate significant power requires access to a suitable foundry and specialist assembly techniques [150, 151]. The multipliers employed in constructing the sources described in this thesis were commercially available varactor diode multipliers.

5.4.2 Properties of Multiplied Sources

In designing a multiplier chain, it is necessary to consider how the various components within the chain modify the phase noise spectrum of the initial oscillator. The effects of multiplication, and the inclusion of amplifiers in the multiplication chain are now considered.

5.4.2.1 Phase Noise and Multiplication

A carrier of unity amplitude, frequency ω and with a random phase modulation (noise) $\phi(t)$ may be represented as

$$V = \sin(\omega t + \phi(t)) \quad (5.19)$$

5.4. FREQUENCY MULTIPLIED SOURCES

At some frequency offset from the carrier (ω_m), let the peak phase modulation be β . Then the phase modulated carrier may be written as

$$V = \sin(\omega t + \beta \sin \omega_m t) \quad (5.20)$$

This may be expanded in terms of Bessel functions [152]. If the oscillator is low noise, the phase deviation is small and therefore with the approximations

$$\beta \ll 1 \begin{cases} J_0(\beta) = 1 \\ J_1(\beta) = \frac{\beta}{2} \\ J_n(\beta) = 0 \quad n > 1 \end{cases} \quad (5.21)$$

the phase modulated carrier may be expressed as

$$V = \frac{\beta}{2} \cos(\omega - \omega_m) t + \sin(\omega t) + \frac{\beta}{2} \sin(\omega + \omega_m) t \quad (5.22)$$

By definition ([153] equation 35), if the sideband amplitude is expressed in RMS terms, the phase noise Single Sideband spectral density at an offset f from the carrier ($\mathcal{L}(f)$) is

$$\mathcal{L}(f) = \left| \frac{V_{sb}}{V_c} \right|^2 \quad (5.23)$$

in which V_{sb} is the RMS sideband amplitude, and V_c is the carrier amplitude. Then from equations 5.22 and 5.23

$$\mathcal{L}(f) = \left| \frac{\beta}{\sqrt{2}} \right|^2 \Rightarrow 20 \log(\beta) - 3 \text{ (dBc/Hz)} \quad (5.24)$$

Now, if the above noisy signal is applied to a multiplier of factor n the multiplied output voltage may be written as

$$V_n = \sin[n(\omega t + \beta \sin \omega_m t)] \quad (5.25)$$

which using the same argument as above leads to

$$V_n = \frac{n\beta}{2} \cos(n\omega - \omega_m) t + \sin(n\omega t) + \frac{n\beta}{2} \sin(n\omega + \omega_m) t \quad (5.26)$$

5.4. FREQUENCY MULTIPLIED SOURCES

and hence

$$\mathcal{L}_n(f) = \left| \frac{n\beta}{\sqrt{2}} \right|^2 \Rightarrow 20 \log(\beta) + 20 \log(n) - 3 \text{ (dBc/Hz)} \quad (5.27)$$

Comparing equations 5.24 and 5.27, the act of multiplication has degraded the SSB phase noise by a factor of n^2 or $20 \log(n)$ dB. Thus if an oscillator can be found at a sub-harmonic of the desired output frequency, multiplication is only attractive if the low frequency oscillator phase noise is lower than the available high frequency oscillator by $20 \log(n)$ dB.

5.4.2.2 Amplifiers and Phase Noise

The above must be regarded as the absolute minimum degradation due to multiplication, it makes no allowance for the noise figure of the actual multiplier, nor does it allow for any amplifiers in the multiplier chain.

Figures 5.3(b) and 5.3(a) show that as the multiplication factor is increased the amplitude of the harmonic falls. Hence, at some point in the multiplier chain it is almost inevitable that amplification will be required.

Figure 5.4 shows ways in which amplifiers and multipliers may be combined. Consider case 'A'. Here it is assumed that the oscillator has insufficient power to adequately drive the multiplier. If the amplifier were noiseless, then since both the carrier and noise are amplified by the same factor the spectral power density is unchanged by amplification. However, if the amplifier has a noise factor F the spectral density at the amplifier output is

$$\mathcal{L}(f) = \mathcal{L}(f)_o + \frac{kTF}{P} \quad (5.28)$$

$$= \mathcal{L}(f)_o + \mathcal{L}(f)_A \quad (5.29)$$

5.4. FREQUENCY MULTIPLIED SOURCES

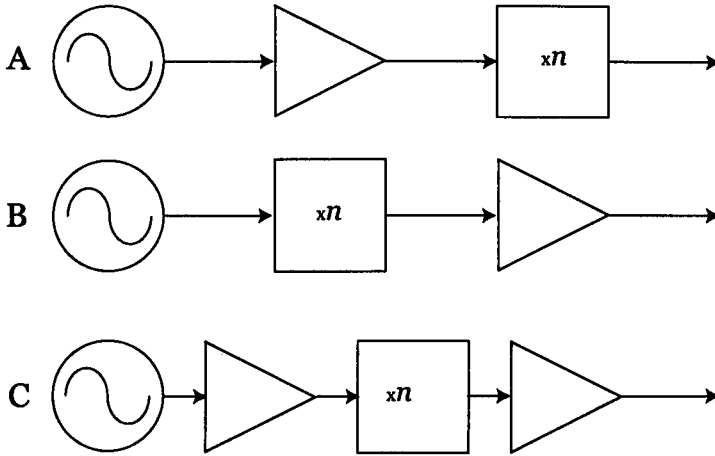


Figure 5.4: Ways in which an amplifier and multiplier may be combined.

where $\mathcal{L}f_o$ is the oscillator noise spectral density and P is the amplifier power output. Then at the multiplier output, the noise spectral density is

$$\mathcal{L}(f) = n^2 [\mathcal{L}(f)_o + \mathcal{L}(f)_A] \tag{5.30}$$

Following the same argument, the spectral density at the output of the multiplier chain shown as case 'B' will be

$$\mathcal{L}(f) = n^2 \mathcal{L}(f)_o + \mathcal{L}(f)_A \tag{5.31}$$

Thus if the amplifier in cases 'A' and 'B' have the same noise figure, case 'B' must have a lower noise density. However, this is often not the case as noise figure increases with frequency. Case 'C' is the logical extension of the previous cases, and will produce a noise content of

$$\mathcal{L}(f) = n^2 [\mathcal{L}(f)_o + \mathcal{L}(f)_{A1}] + \mathcal{L}(f)_{A2} \tag{5.32}$$

Thus, case 'B' would produce the optimum noise performance. The situation becomes even more complicated if the multiplication factor is split and

5.5. CHAPTER SUMMARY

amplification is used between multiplier stages, but is none-the-less a logical extension of all the above.

5.5 Chapter Summary

This chapter has covered the theory which is needed to design and construct a multiplier chain. It has been shown that oscillator noise depends upon both the active device used as the basic gain block, and the loaded Q of the frequency determining network. When it is not possible to obtain the required performance from a simple oscillator, multipliers may be employed and the properties of multiplied sources have been investigated.

CHAPTER 6

The Measurement of Source Phase Noise

Phase noise is a key parameter in obtaining a spectrometer with good performance. Whilst the phase noise of a source may be estimated using Leeson's equation (equation 5.2), it is often the case that parameters such as the device flicker noise corner frequency are not known and therefore a detailed analysis is not possible. In such cases, designers often make estimates of these parameters based on experience, add a nominal 3dB to 5dB to obtain an estimate of the oscillator phase noise and then measure the phase noise spectrum of a prototype.

Techniques for measuring phase noise at low frequencies are well established and may be broadly classified into two categories, single and multiple source, the relative merits of which are discussed in [154].

The relatively simple techniques of direct measurement using a spectrum

6.1. THE MEASUREMENT OF OSCILLATOR PHASE NOISE

analyser, a delay line discriminator or phase locking the oscillator under test to a low noise reference¹, which may be employed at low frequencies, become increasingly troublesome to implement as frequency increases.

The carrier null technique [156] was originally used at X-band, has been successfully extended to higher frequencies. The technique relies on being able to employ a high Q cavity at the oscillator carrier frequency to null the carrier and provide a significant phase delay in one arm of a balance mixer which then acts as an amplitude demodulator -a process described in section 6.1 in the context of the delay line discriminator. This method of phase noise measurement has been extended to 94GHz [157], and beyond [158], using Quasi-Optical techniques to produce a cavity with Q's of order 100,000.

However, such an approach to phase noise measurement at 94GHz is difficult to implement and a rather simpler solution solution was sought. This chapter describes such a measurement system, based upon a delay line discriminator operating at a nominal frequency of 7.8GHz and a down conversion system, using a low noise Gunn Oscillator operating at 86.2GHz.

6.1 The Measurement of Oscillator Phase Noise

The measurement of oscillator phase noise is both difficult and interesting. It requires the ability to measure a (hopefully) low level signal (the phase noise) within a kHz of a large (the carrier) signal. There are several methods of measuring oscillator phase noise [159], and commercial instruments capable of making the measurement are, at some considerable cost, readily available [160, 161].

Without ready access to commercial equipment, and because oscillator phase

¹an overview of these techniques may be found in [155]

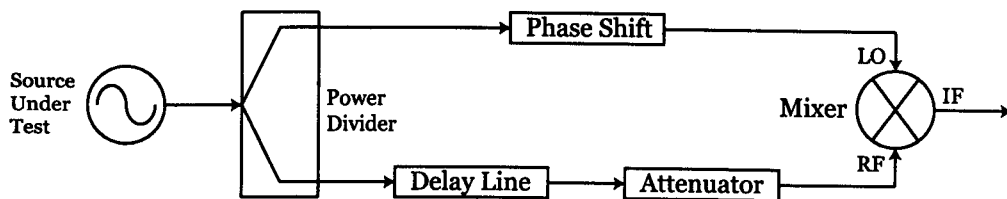


Figure 6.1: Delay Line Discriminator

noise is a key parameter within the spectrometer a simple delay line discriminator was implemented. This section covers the theory of the discriminator and confirmation of its performance.

6.1.1 Discriminator theory

A block diagram of a delay line based discriminator is shown in figure 6.1. The source under test is applied to a power divider. One output from the power divider has a phase shift applied to it and this phase shifted signal is applied to the local oscillator port of a double balanced mixer. The other output from the power divider is applied to a delay line, and via an attenuator to the RF port of the mixer; the attenuator is used to ensure that the RF port does not saturate. When the RF port and the LO port of the mixer are in quadrature (ensured by adjusting the phase shift introduced in the LO arm), the mixer output contains the source phase noise information. This may be measured on a spectrum analyser, and then converted into the Single Sideband phase noise of the source.

One advantage of this technique is that off the shelf components allow direct measurement to be made at frequencies in excess of 10GHz and a modification of this technique has been used to 94GHz [157] and 160GHz [158]. As

6.1. THE MEASUREMENT OF OSCILLATOR PHASE NOISE

will be shown, the delay line discriminator has a restricted range of carrier offset frequencies at which the SSB phase noise may be measured.

Let the various components of figure 6.1 have the following parameters

- A_o Oscillator (source) amplitude
- L_s Power divider loss
- L_ϕ Phase shift loss
- L_d Delay line loss
- L_a Attenuator value
- L_m Mixer conversion loss
- ω_C Source frequency
- τ Delay introduced by the delay line
- $\Delta\theta$ Phase shift introduced by the phase shift device

In this case, the oscillator amplitude and attenuations are in voltage terms. The oscillator output contains both amplitude and phase noise, and is described by

$$V_o(t) = A_o[1 + \alpha(t)] \cos(\omega_c t + \phi(t)) \quad (6.1)$$

where $\alpha(t)$ and $\phi(t)$ are random functions representing amplitude and phase noise respectively. Thus, the signals applied to the mixer LO and RF ports are

$$V_{LO}(t) = A_o[1 + \alpha(t)]L_sL_\phi \cos(\omega_c t + \phi(t) + \Delta\theta) \quad (6.2)$$

$$V_{RF}(t) = A_o[1 + \alpha(t - \tau)]L_sL_dL_a \cos(\omega_c(t - \tau) + \phi(t - \tau)) \quad (6.3)$$

The effect of the pre-multiplication terms in these expressions is to reduce the RF port signal amplitude to A_{RF} , and to reduce the LO port signal to an amplitude of A_{LO} where

6.1. THE MEASUREMENT OF OSCILLATOR PHASE NOISE

$$A_{RF} = A_o L_s L_d L_a \quad (6.4)$$

$$A_{LO} = A_o L_s L_\phi \quad (6.5)$$

The signals involved in the mixing process are therefore

$$V_{LO}(t) = A_{LO} \cos(\omega_c t + \phi(t) + \Delta\theta) \quad (6.6)$$

$$V_{RF}(t) = A_{RF}[1 + \alpha(t - \tau)] \cos(\omega_c(t - \tau) + \phi(t - \tau)) \quad (6.7)$$

The mixer consists of a diode ring, and the LO signal must switch the diodes from a conducting to a non-conducting state. The diode ring may be regarded as a multiplier, and being a passive network it has an overall attenuation between the RF and IF ports. This loss is dependent upon the LO drive level, and therefore the mixer may be regarded as having a unity amplitude LO signal with an RF LO port attenuation L_m , which is LO drive level dependent. The LO signal is amplitude limited by the mixer diodes so the actual LO signal has no amplitude variation and may be regarded as a unity amplitude waveform with only phase noise content. The mixer output voltage is therefore

$$V_{mo}(t) = L_m V_{RF}(t) V_{LO}(t) \quad (6.8)$$

Then

$$V_{mo}(t) = A_{RF} L_m [1 + \alpha(t - \tau)] [\cos(\omega_c t + \phi(t) + \Delta\theta)] [\cos(\omega_c(t - \tau) + \phi(t - \tau))] \quad (6.9)$$

Expansion of the product results in two terms

$$\begin{aligned} T1 &= \cos(\omega_c t + \phi(t) + \Delta\theta + \omega_c(t - \tau) + \phi(t - \tau)) \\ T2 &= \cos(\omega_c t + \phi(t) + \Delta\theta - (\omega_c(t - \tau) + \phi(t - \tau))) \end{aligned} \quad (6.10)$$

6.1. THE MEASUREMENT OF OSCILLATOR PHASE NOISE

T1 is a mixer output at twice the original oscillator frequency and is either deliberately filtered out, or filtered by the finite bandwidth of the IF port. It is important that this signal is reduced to a level at which it does not overload any subsequent amplifiers, or the measuring instrument. Neglecting the high frequency term, the mixer output is

$$V_{mo}(t) = A_{RF}L_m[1 + \alpha(t - \tau)] \cos(\phi(t) + \Delta\theta + \omega_c\tau - \phi(t - \tau)) \quad (6.11)$$

The oscillator noise spectrum may now be found by taking the Fourier transform of 6.11. Of the two terms involved, the Fourier transform of the first results in the phase noise spectrum, whilst the Fourier transform of the second involves the convolution of the phase and the amplitude spectra. Fortunately, the amplitude noise content of an oscillator is typically orders of magnitude smaller than the phase noise content, and may be neglected. Even if the oscillator amplitude noise content is rather higher than is desirable for the amplitude noise to be strictly negligible, it is now shown that correctly adjusted the delay line discriminator has good amplitude noise rejection.

6.1.1.1 Oscillator with only phase noise

Neglecting amplitude noise the mixer output is

$$V_{mo}(t) = A_{RF}L_m \cos(\phi(t) + \Delta\theta + \omega_c\tau - \phi(t - \tau)) \quad (6.12)$$

If the mixer inputs are arranged to be in quadrature i.e. $\Delta\theta + \omega_c\tau = \frac{\pi}{2}$, and if $\phi(t) - \phi(t - \tau) \ll 1$ the mixer output is found to be

$$V_{mo}(t) = A_{RF}L_m [\phi(t) - \phi(t - \tau)] \quad (6.13)$$

6.1. THE MEASUREMENT OF OSCILLATOR PHASE NOISE

whilst if the mixer inputs are arranged to be in phase and $\phi(t) - \phi(t - \tau) \ll 1$ the mixer output is found to be

$$V_{mo}(t) = A_{RF}L_m \quad (6.14)$$

In the first case, the mixer output contains the required phase noise information, whilst in the second case, the mixer output is a DC level.

6.1.1.2 Oscillator with only amplitude noise

The oscillator output is

$$V_o(t) = A_o[1 + \alpha(t)] \cos(\omega_c t) \quad (6.15)$$

and therefore, the LO and RF signals are given by

$$V_{LO}(t) = \cos(\omega_c t + \Delta\theta) \quad (6.16)$$

$$V_{RF}(t) = A_{RF}[1 + \alpha(t - \tau)] \cos(\omega_c(t - \tau)) \quad (6.17)$$

The mixer output voltage is defined as in equation 6.8, performing the same trigonometric operations and neglecting a high frequency term, the mixer output is found to be

$$V_{mo}(t) = A_{RF}L_m[1 + \alpha(t - \tau)] \cos(\omega_c \tau + \Delta\theta) \quad (6.18)$$

If the mixer inputs are arranged to be in quadrature the mixer output is zero, whilst if the mixer inputs are arranged to be in phase the mixer output is

$$V_{mo}(t) = A_{RF}L_m[1 + \alpha(t - \tau)] \quad (6.19)$$

which contains the required amplitude noise information. This is exactly the opposite to the pure phase noise case, and suggests that when the mixer inputs are set to quadrature the measurement system rejects amplitude noise

6.1. THE MEASUREMENT OF OSCILLATOR PHASE NOISE

making the phase noise measurement insensitive to amplitude noise. In reality, obtaining perfect quadrature is difficult, and the mixer is not a perfect multiplication circuit and it is suggested [162] that in the phase noise measurement an amplitude rejection of greater than 20dB is attainable.

6.1.1.3 The phase noise spectrum

Accepting that the oscillator amplitude noise may be neglected, the phase noise spectrum of the oscillator is obtained by taking the Fourier transform of 6.13. Let $\phi(t)$ have the Fourier transform $\varphi(\omega)$. The Fourier transform of $\phi(t - \tau)$ is found using the shift theorem and is $\varphi(\omega)e^{-j\omega\tau}$. Then the spectrum of the mixer output is

$$V_{mo}(\omega) = A_{RF}L_m (1 - e^{j\omega\tau}) \varphi(\omega) \quad (6.20)$$

If we assume that $\omega\tau \ll 1$ and employ a Taylor expansion for the exponential, the mixer output is

$$V_{mo}(\omega) = -j\omega\tau A_{RF}L_m\varphi(\omega) \quad (6.21)$$

The original phase modulation of the carrier has been down converted (the mixer acts as a *homodyne* demodulator) to baseband, and the Fourier frequency ω is therefore an offset frequency from the original carrier frequency, and at any frequency ω the amplitude of the mixer output is related to the magnitude of the original phase modulation. The spectrum of the mixer output is measured on an LF spectrum analyser which displays a power spectrum, which is simply $V_{mo}(\omega)V_{mo}^*(\omega)$, where * denotes the complex conjugate. Then the measured spectrum is

$$S(f) = \frac{1}{f^2} \frac{1}{(2\pi\tau)^2} \frac{1}{A_{RF}^2 L_m^2} V_{mo}^2(f) \quad (6.22)$$

6.1. THE MEASUREMENT OF OSCILLATOR PHASE NOISE

The units of this spectrum are WHz^{-1} and it is therefore the power spectral density. The phase spectral density is obtained by dividing the measured voltage by the phase comparator (mixer) phase gain k_ϕ . The result is

$$S_{\delta\phi}(f) = \frac{1}{f^2} \frac{1}{(2\pi\tau)^2} \frac{1}{A_{RF}^2 L_m^2} \left[\frac{V_{mo}(f)}{k_\phi} \right]^2 \quad (6.23)$$

At any frequency offset from the carrier, the phase modulation produced by the noise produces two modulation sidebands, one upper and one lower. The mixer converts both sidebands to exactly the same frequency at the mixer output. Thus the single sideband (SSB) phase noise is given by

$$\mathcal{L}(f) = \frac{1}{2} \frac{1}{f^2} \frac{1}{(2\pi\tau)^2} \frac{1}{A_{RF}^2 L_m^2} \left[\frac{V_{mo}(f)}{k_\phi} \right]^2 \quad (6.24)$$

A list of various definitions of phase noise and their inter-relationships is given in [163]. The final stage in obtaining the SSB phase noise spectrum is to note that the mixer must often be followed by a low noise amplifier to raise the mixer output above the spectrum analyser noise floor. If this amplifier has a voltage gain G , the actual SSB phase noise is given by

$$\mathcal{L}(f) = \frac{1}{2} \frac{1}{f^2} \frac{1}{(2\pi\tau)^2} \frac{1}{A_{RF}^2 L_m^2} \left[\frac{V_{mo}(f)}{k_\phi} \right]^2 \frac{1}{G^2} \quad (6.25)$$

6.1.1.4 The significance of approximations

In obtaining equation 6.25, only two approximations were made. Firstly it was assumed that the phase modulation was small (i.e. $\phi(t) \ll 1$) and secondly that $\omega\tau \ll 1$ which limits the maximum frequency offset from the carrier at which a measurement can be made. The implications of these assumptions are now briefly discussed.

6.1. THE MEASUREMENT OF OSCILLATOR PHASE NOISE

The significance of $\phi(t) \ll 1$

Let the phase modulation be given by

$$\phi(t) = \beta \cos \omega t \quad (6.26)$$

and the phase modulated carrier may be written as

$$V_o(t) = A_o \cos (\omega_c t + \beta \cos \omega t) \quad (6.27)$$

Which has a standard expansion²

$$V_o(t) = J_0(\beta) A_o \cos \omega_c t \quad (6.28)$$

$$+ 2A_o (J_2(\beta) \cos 2\omega t + J_4(\beta) \cos 4\omega t + \dots) \cos \omega_c t \quad (6.29)$$

$$+ 2A_o (J_1(\beta) \sin \omega t + J_3(\beta) \sin 3\omega t + \dots) \sin \omega_c t \quad (6.30)$$

where β is known as the modulation index, and defines the maximum phase modulation of the carrier, and where $J_n(\beta)$ is a Bessel function of the first kind of order n and argument β , which defines the amplitude of the n^{th} modulation sideband. It is seen that the spectrum of a phase modulated signal consists of an infinite number of sidebands spaced at harmonics of the phase modulation frequency. $J_n(\beta)$ may be expanded as a power series, and for the carrier ($J_0(\beta)$) and the first two sidebands ($J_1(\beta)$ and $J_2(\beta)$) we have

$$J_0(\beta) = 1 - \frac{\beta^2}{2^2} + \frac{\beta^4}{2^6} + \dots \quad (6.31)$$

$$J_1(\beta) = \frac{\beta}{2} - \frac{\beta^3}{2^4} + \frac{\beta^5}{2^7 \cdot 3} + \dots \quad (6.32)$$

$$J_2(\beta) = \frac{\beta^2}{2^3} - \frac{\beta^4}{2^5 \cdot 3} + \frac{\beta^6}{2^{10} \cdot 3} + \dots \quad (6.33)$$

The derivation of equation 6.25 requires that the only significant sideband is the first, and thus $\phi(t) \ll 1$ implies that β is sufficiently small that the

²All the required properties of Bessel's Functions are taken from [152]

6.1. THE MEASUREMENT OF OSCILLATOR PHASE NOISE

amplitude sidebands of $n > 1$ is small in comparison with the first sideband ($n = 1$). How small is arbitrary, however if we require that $J_1(\beta) = 10J_2(\beta)$ (i.e. the second sideband is 20dB down on the first) we find that $\beta \simeq 0.4$.

Now, the phase noise spectrum of the carrier is the spectrum of the modulation index, and it may be shown (equation (35) in [153]) that

$$\mathcal{L}(f) = 20 \log(\beta) - 10 \log(f) - 3 \quad (6.34)$$

where $\mathcal{L}(f)$ is in dBc/Hz and f is the offset from the carrier (phase modulation frequency) in Hz. Thus, the consequence of requiring that $\phi(t) \ll 1$ places an upper limit on the SSB phase noise which may be measured at any offset frequency from the carrier using a delay line discriminator; for $\beta = 0.4$ this is shown in figure 6.2.

The significance of $\omega\tau \ll 1$

The requirement that $\omega\tau \ll 1$ places an upper limit on the frequency offset from the carrier at which phase noise may be measured. Consider a 'perfect' noise free signal applied to the discriminator. Then after removal of the high frequency term, the mixer output, from equation 6.12 is

$$V_{mo}(t) = A_{RF}L_m \cos(\Delta\phi - \omega_c\tau) \quad (6.35)$$

Defining ω_o to be a frequency at which $\omega\tau + \Delta\phi = \pi/2$ and ω to be a frequency offset from ω_o , this reduces to

$$V_{mo}(t) = A_{RF}L_m \sin \omega\tau \quad (6.36)$$

6.1. THE MEASUREMENT OF OSCILLATOR PHASE NOISE

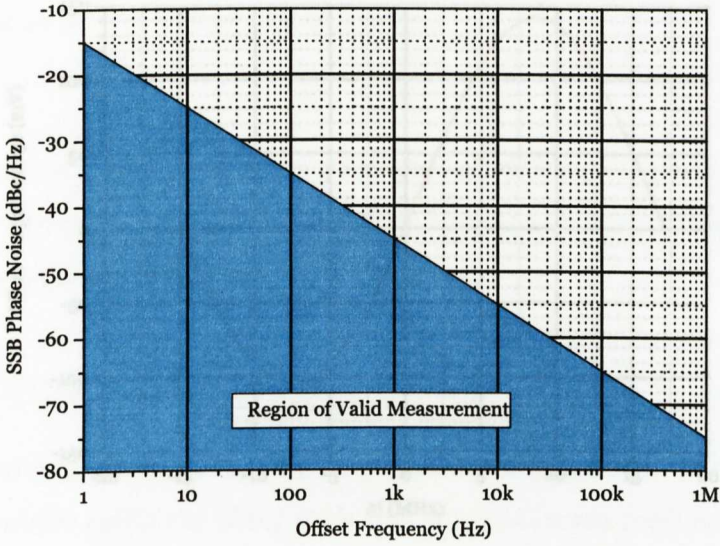


Figure 6.2: The valid range of $\mathcal{L}(f)$ using a delay line discriminator. In the shaded region, $\mathcal{L}(f)$ may be calculated as previously described without correction for a breakdown in the assumption that $\phi(t) \ll 1$.

With an HMC220³ used as a phase comparator and 28ns delay line, the port power levels were adjusted to be +10dBm at the LO port and -4.4dBm at the RF port. Figure 6.3 shows a typical transfer function for a nominal centre frequency of 7.8GHz. Then the requirement that $\omega\tau \ll 1$ ensures that the mixer output is linear. Writing $A_{RF}L_m = k$ and following [164], the deviation from linear is

$$E = k(\omega\tau - \sin \omega\tau) \quad (6.37)$$

³The HMC220 is a Double Balanced Mixer which is available from the Hittite Microwave Corporation. It has RF and LO ports with frequency responses extending from 5 to 12GHz and a DC coupled IF port with a bandwidth of 4GHz. Checked April 2006.

6.1. THE MEASUREMENT OF OSCILLATOR PHASE NOISE

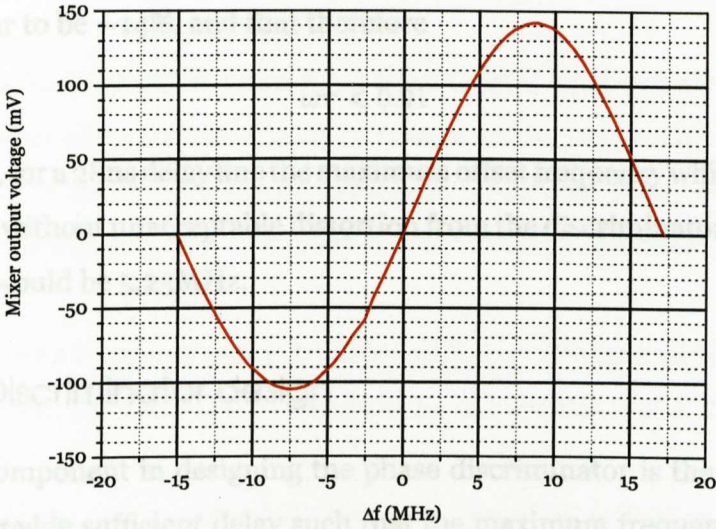


Figure 6.3: Phase detector frequency response

which results in a fractional error E_f of

$$E_f = 1 - \text{sinc } \omega\tau \quad (6.38)$$

which whilst elegant, is not too useful! A more useful result may be obtained by using a Taylor expansion of $\sin \omega\tau$ to give

$$E_f = \frac{(\omega\tau)^2}{3!} - \frac{(\omega\tau)^4}{5!} + \frac{(\omega\tau)^6}{7!} + \dots \quad (6.39)$$

If the maximum deviation from linear is $E_{\%}$ and this deviation is sufficiently small that only the first term of equation 6.39 need be retained, we have the final result

$$\omega\tau < \sqrt{\frac{6E_{\%}}{100}} \quad (6.40)$$

Once again the acceptable upper limit is somewhat arbitrary. However if we require that the second term in equation 6.39 is not to be greater than $\frac{1}{10}$ th of the quadratic term, we establish that the maximum acceptable deviation

6.1. THE MEASUREMENT OF OSCILLATOR PHASE NOISE

from linear to be $\sim 14\%$, and that therefore

$$\omega\tau < 0.91 \quad (6.41)$$

Therefore, for a 28ns delay line the maximum offset frequency which could be measured without unacceptable distortion from the discriminator frequency response would be 5.25MHz.

6.1.2 Discriminator design

The key component in designing the phase discriminator is the delay line. It must provide sufficient delay such that the maximum frequency of measurement satisfies the requirement that $\omega\tau \ll 1$, whilst not attenuating the signal to a point at which the system noise floor becomes significant.

There is therefore an optimum length of delay line, which for a power limited system (a system in which performance is limited by the power handling capabilities of the mixer) turns out to be the length at which the delay line has a loss of 1Np ($\sim 8.68\text{dB}$) [165]. Thus the lower the delay line loss, the longer the delay achievable, and the greater the frequency offset which can be measured whilst satisfying the requirements of section 6.1.1.4.

RG402 is a readily available low loss semi-rigid coaxial cable which has an attenuation of 1.2dBm^{-1} and a velocity factor of 0.695. Then the optimum length of cable for the delay line would be 7.23m, which would produce a delay of 34.67ns.

6.1.3 Realisation of the discriminator

The basic discriminator was constructed using readily available components; The circuit is shown in figure 6.4. A centre frequency of 7.833GHz was selected, because this is the starting frequency for the multiplication chain to

6.1. THE MEASUREMENT OF OSCILLATOR PHASE NOISE

94GHz.

The delay line was constructed from RG402 semi-rigid coaxial cable. The 6m of cable available in the laboratory is expected to produce a loss of 7.2dB and a delay of 28.8ns; measured values are 7.6dB and 28ns, which is reasonable agreement. Using this delay line the maximum offset frequency is 5.2MHz.

The mixer was a commercially available unit, the HMC220MS8 from Hitrite, which has RF and LO port bandwidths of 5-12GHz and a DC-4GHz IF bandwidth.

The IF amplifier was constructed using two Wenzel 'Blue Top' units and has a total cascade gain of 53dB with individual frequency responses of 10Hz-2MHz and a 50Ω input impedance which serves to correctly terminate the mixer IF port.

A disadvantage of using a diode ring mixer as the phase comparator is that the phase constant obtained depends upon the power levels at each port. With a wide range of oscillator powers to be measured, it becomes difficult to ensure that the LO port remains saturated, whilst the RF port remains below the 1dB compression point. To overcome this, an amplifier and attenuator are used to keep the power in the discriminator at known levels. As implemented in figure 6.4 the attenuator is adjusted to provide a +10dBm signal at the LO port, which allowing for losses in interconnecting cables and couplers, is a measured power of +2.2dBm at the power monitor point (PM). The input power divider has been realised as a 10dB directional coupler; this coupling factor in conjunction with the delay line loss gives a power of -4.4dBm at the mixer RF port with +10dBm at the LO port.

A consideration in selecting the amplifier G_1 is that when delivering these power levels to the discriminator its output must be well removed from its

6.1. THE MEASUREMENT OF OSCILLATOR PHASE NOISE

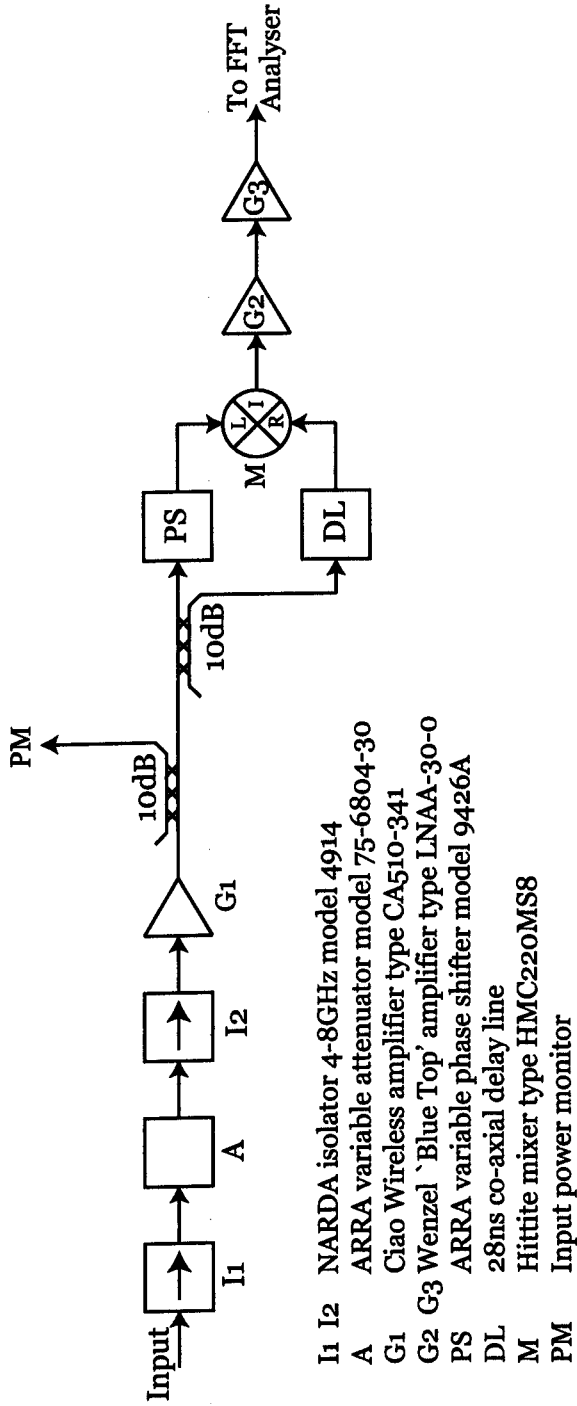


Figure 6.4: Circuit of the discriminator

6.1. THE MEASUREMENT OF OSCILLATOR PHASE NOISE

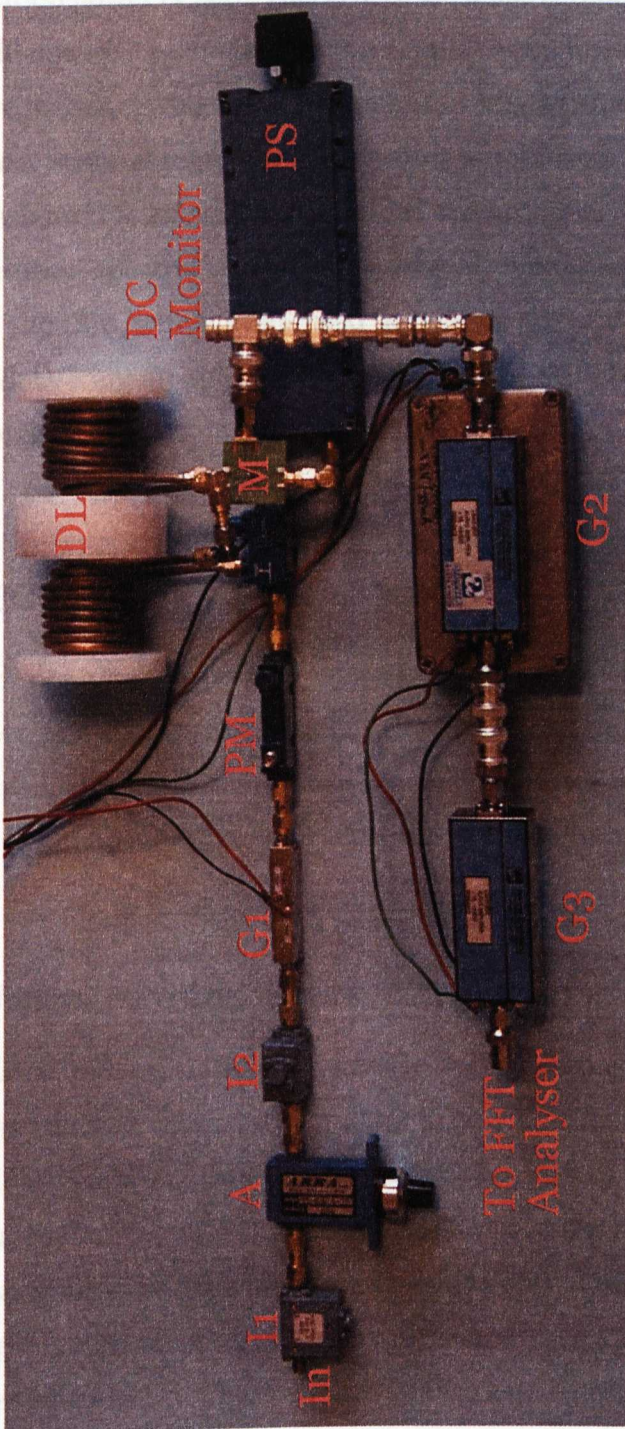


Figure 6.5: Realisation of the discriminator. The component identification follows the key in figure 6.4.

6.1. THE MEASUREMENT OF OSCILLATOR PHASE NOISE

1dB saturation power (P_{1dB}). This is because noise components from the oscillator will mix with each other on the amplifier non linearities and produce spectral regrowth, giving an erroneous (too high) value for the oscillator phase noise. Spectral regrowth in saturating amplifiers has been considered in [166], where it is shown that provided the amplifier is more than 10dB from saturation spectral regrowth is minimal. The specified amplifier has a P_{1dB} of +29dBm, which when used to provide the power levels indicated above, is delivering an output power of +14dBm, 15dB below the amplifier 1dB compression point.

6.1.4 Discriminator performance

The discriminator performance was established by measuring oscillators with known phase noise distributions. However, before any measurement could be made, it was necessary to calibrate the discriminator by finding the phase detector constant k_ϕ and establishing the discriminator noise floor.

6.1.4.1 Measurement Procedure

The oscillator under test was connected to the discriminator, and the power at 'PM' was adjusted using the attenuator to be +2.2dBm. The power at both the LO and RF ports was measured to be +10dBm and -4.4dBm respectively. A high impedance (10M Ω) DC meter was placed at the mixer output, prior to the IF amplifier, and the maximum positive and negative DC mixer output voltages (corresponding to relative phases of 0° and 180° between mixer inputs) recorded as the phase shifter was varied. These values were used to calculate k_ϕ and the DC offset, and the mixer DC output was set to the

6.1. THE MEASUREMENT OF OSCILLATOR PHASE NOISE

calculated DC offset voltage.

The mixer conversion loss was obtained from the manufacturers data sheet. On the grounds that the mixer was neither the worst or the best performing unit, the conversion loss was set at the mean of the quoted figures, a value for L_m of -6dB.

The spectra were measured and recorded on a Stanford Research Instruments FFT analyser type SR760; a word of caution is required here. The SRS analyser displays the mixer output voltage in terms of an RMS voltage, whilst in storing the data to disc or recovering the information over the GPIB interface, the voltage is stored as a peak value. A correction of 3dB must be applied to data stored to disc or recovered over the GPIB interface. Further, the SR760 corrects its display for any windowing function which may have been applied to the measurement. Whilst no correction is required in this case, not all analysers perform these corrections; the corrections required for various windows are tabulated in [167].

Measurement of the phase detector constant

One method of measuring the detector phase constant is to inject a signal with a known phase modulation at known modulation frequency, measure the oscillator spectrum using the discriminator and then calculate k_ϕ . This however requires the ability to measure the oscillator modulation spectrum at the carrier frequency.

In section (6.1.1.4) it was shown that the delay line based discriminator has a sinusoidal frequency response. An exactly analogous procedure leads to the conclusion that the discriminator has a sinusoidal phase response. This sinusoidal nature of the phase detector may be exploited to obtain the re-

6.1. THE MEASUREMENT OF OSCILLATOR PHASE NOISE

quired information. When adjusted to quadrature the mixer produces zero DC output, and the phase gain is simply the slope of the phase detector transfer characteristic about its zero point. Since the phase detector is sinusoidal, the slope about zero is simply the peak of the transfer function, which may be found by adjusting the phase shift in the LO arm of the mixer.

Considering figure 6.3, it is important to note the DC offset on the phase discriminator output. If the diode ring mixer is considered as a bridge system, for a perfect mixer there can be no DC offset. However due to imperfections in matching Balun transformers and diodes within the mixer, perfect balance is not obtained, and the DC output is rectified leakage of the LO signal to the IF port. Kurtz [164] has shown that this offset may be estimated from

$$V_{off} = 4.5 \cdot 10^\alpha \quad (6.42)$$

where $\alpha = (LO - IS - 30)/20$ and LO is the LO port drive level in dBm and IS is the LO-RF port isolation in dB. For the HMSC220 this results in an estimated offset of 30mV which is in reasonable agreement with the measured value of 20mV.

The phase detector constant is therefore measured by locating both the maximum and the minimum phase detector outputs by varying the phase shifter. The phase detector constant is the mean of these values, and to ensure symmetry of the phase detector output, the phase shift is set to the DC offset voltage which is half the difference between the two peak voltages.

When set up with the power levels described above typical values are (measured) $k_\phi = 120\text{mV}/\text{Rad}$ and a DC offset of 18mV. These values change with temperature, exact drive level and carrier frequency and must be established for every measurement.

6.1. THE MEASUREMENT OF OSCILLATOR PHASE NOISE

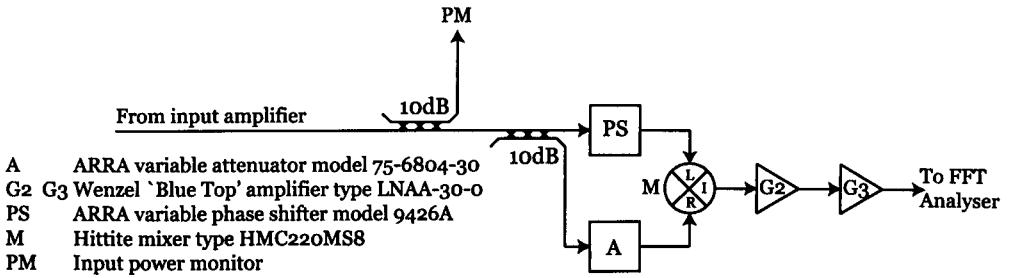


Figure 6.6: Discriminator Noise Floor Measurement

Instrument noise floor

The method of establishing the discriminator noise floor is described in [153]. Figure 6.6 shows the modified discriminator; the delay line is removed and replaced with an attenuator. The phase comparator must operate under the same conditions for a noise floor measurement as it does for a phase noise measurement. With the power from the source adjusted to give +2.2dBm at the power monitor point (ensuring +10dBm at the LO port) the attenuator 'A' is adjusted to give an RF port power of -4.4dBm.

The measurement now proceeds as normal; the phase detector constant and offset are determined, and the spectrum measured with the mixer ports in quadrature.

To obtain the noise floor we need to recalculate $\mathcal{L}(f)$; the starting point is equations 6.2 and 6.3, which with $\tau = 0$, a 90° phase difference between mixer inputs and assuming $\phi(t) \ll 1$ gives

$$V_{mo}(t) = A_{RF}L_m\phi(t) \quad (6.43)$$

The spectrum of the mixer output is

$$S(f)_{nf} = \frac{1}{(A_{RF}L_m)^2} V_{mo}^2(f) \quad (6.44)$$

6.1. THE MEASUREMENT OF OSCILLATOR PHASE NOISE

where 'nf' indicates a noise floor measurement value. Finally, we obtain the SSB phase noise density, including the IF amplifier gain, as

$$\mathcal{L}(f)_{nf} = \frac{1}{2} \frac{1}{(A_{RF}L_m)^2} \left[\frac{V_{mo}(f)}{k_\phi} \right]^2 \frac{1}{G^2} \quad (6.45)$$

which is used to calculate the instrument noise floor.

This figure is the 'ultimate' sensitivity of the measurement system, and represents the the noise of all the components referred to the instrument input. The *phase* noise floor of the instrument is obtained by multiplying the noise floor by the gain due to the delay line which is given by [159]

$$\mathcal{L}(f)_{pnf} = \mathcal{L}(f)_{nf} + 20 \log \left[\frac{1}{2\pi f\tau} \right] \quad (6.46)$$

where $\mathcal{L}(f)_{pnf}$ is the instrument phase noise floor and all other terms have been previously defined.

If the phase noise floor becomes too high the measured oscillator phase noise will contain a contribution due to the instrument phase noise floor. The result of the measurement will be too high and a correction is required. This correction is given by [155] and [153] to be

$$\Delta = 10 \log \left[1 + \text{antilog} \left\{ \frac{\mathcal{L}(f)_{pnf} - \mathcal{L}(f)}{10} \right\} \right] \quad (6.47)$$

which must be subtracted from the calculated oscillator phase noise.

6.1.4.2 Measured results

The oscillators employed to establish the discriminator performance were a permanent magnet biased YTO tuned using its FM coil to a frequency of 7.192GHz and having a power output of +20.5dBm, and a DRO with a nominal frequency of 7.192GHz and delivering +12dBm. The results of these

6.1. THE MEASUREMENT OF OSCILLATOR PHASE NOISE

measurements are shown in figures 6.7(a) and 6.7(b) respectively.

Whilst the agreement between the supplied data and the data obtained from the discriminator is not exact, the measured results are typically within 5dB of the supplied data which is held to be reasonable agreement.

The measured spectra are sufficiently below the limit derived in section 6.1.1.4 that the results are valid from the small angle point of view, and the upper frequency, although limited by the FFT analyser, is sufficiently within the upper frequency limit imposed by section 6.1.1.4 that no correction is required for the discriminator frequency response.

Finally, it is noted that the instrument phase noise floor is never less than 45dB below the measured oscillator noise floor. It is concluded that the measurements are sufficiently removed from the instrument noise floor that we may be sure that the measurements are not instrumentation limited.

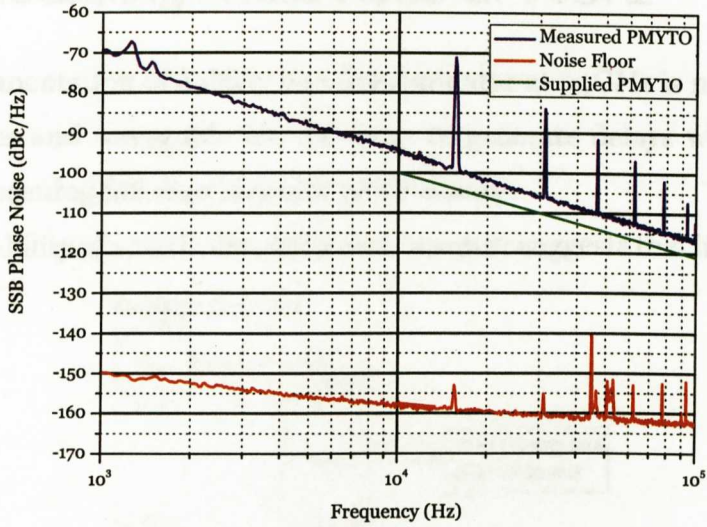
6.1.5 Section Summary

The theory behind a simple delay line discriminator used to measure oscillator phase noise has been described.

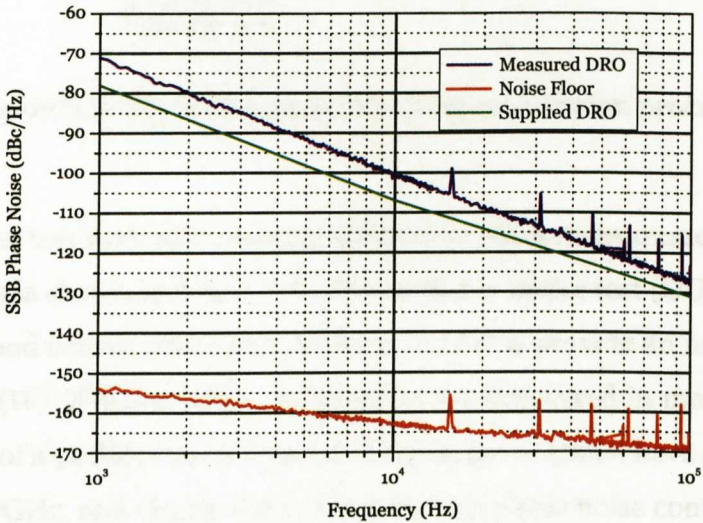
An instrument capable of measuring the phase noise of oscillators in the region of 7GHz has been constructed using a co-axial delay line and readily available components. The performance of this discriminator has been evaluated, using two oscillators of known phase noise performance, and found to be satisfactory.

This instrument has been used as the basis of an instrument for measuring the phase noise spectra of various 94GHz sources. This extension is discussed in the following sections.

6.1. THE MEASUREMENT OF OSCILLATOR PHASE NOISE



(a) Measured YTO Performance



(b) Measured DRO Performance

Figure 6.7: The comparison of manufacturers supplied test data and results obtained from the delay line discriminator used to confirm the performance of the discriminator

6.2 Measuring Phase Noise at 94GHz

The implementation of a delay line discriminator at 94GHz is not easy, coaxial cables and waveguide are too lossy to generate delays which would result in meaning full discriminator performance.

The availability of a 7GHz discriminator, however suggests that if the 94GHz

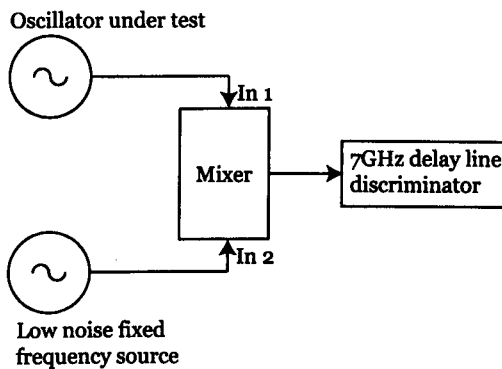


Figure 6.8: Block diagram of the down conversion process.

signal under test were to be down converted to 7GHz measurement could be made. This is shown in figure 6.8, The oscillator under test (OUT) is mixed with a second source (the local oscillator or LO) to provide an intermediate frequency (IF) of order 7GHz. Because we are interested in measuring the properties of a 94GHz source at an IF of 7GHz, the LO must have a frequency of order 87GHz, and clearly the LO must have a phase noise content significantly (at least an order of magnitude) better (lower) than the OUT.

Suitable mixers are reasonably readily available, and the Farran Technologies BMC10⁴ unit was selected, not least for its performance but also because there were a number available in the laboratory.

⁴The BMC10 data sheet may be obtained from www.farran.com

6.2.1 The Down Conversion Source

The key technical issue to be resolved, is the generation of a suitable LO. Since the OUT is to have a significantly better performance than a Gunn diode based source, it might be thought that a Gunn source would be precluded.

As a test of a quasi-optical phase noise measurement equipment, Smith

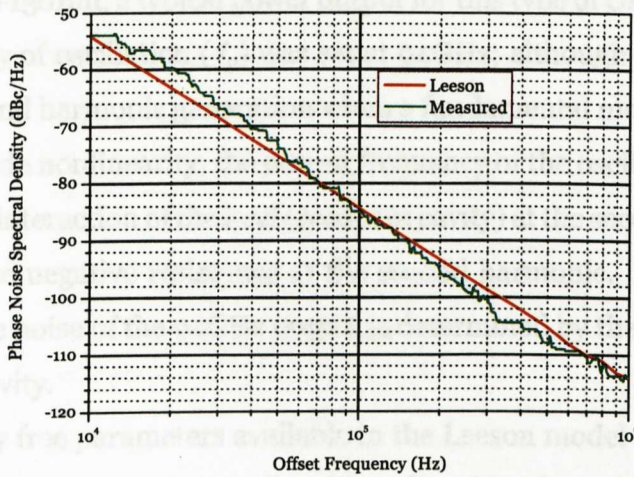


Figure 6.9: The phase noise of a second harmonic Gunn oscillator and the predicted noise distribution using Leeson's model. The parameters used in the Leeson model were $Q = 200$, $f_c = 4.8\text{MHz}$ and a device noise figure of 5dB; these parameters were used in figure 7.2

[157] measured the phase noise of a second harmonic free running 94GHz Gunn oscillator, the results of this measurement, are shown in figure 6.9,

6.2. MEASURING PHASE NOISE AT 94GHZ

the data for this plot having been extracted from [157] using 'Data Thief'⁵. The phase noise of the oscillator may also be calculated using the Leeson model (section 5.3.1). However, none of the device parameters were known. Therefore parameters in the Leeson equation were adjusted to give a reasonable agreement. The potential free parameters are the saturated power output (P_s), the device noise factor (F), the loaded Q of the resonant circuit (Q_l) and the flicker noise corner frequency (f_c).

P_s was set to +13dBm, a typical power output for this type of Gunn oscillator. The frequency of oscillation (f_o) was set at 94GHz; although this oscillator relies on second harmonic generation when a fundamental mode oscillation drives the diode nonlinearity, the output frequency of the oscillator is determined by the interaction of the load (resonant cavity) at the second harmonic and the device negative resistance at the second harmonic. It is assumed that the phase noise of the 94GHz output is determined by the properties of the 94GHz cavity.

Thus, the only free parameters available in the Leeson model are F , Q_l and f_c . These parameters were manually adjusted to give a best visual fit to the measured Gunn oscillator data.

The calculated phase noise is plotted in figure 6.9 for comparison with the measured data. This agreement is not excellent, however, errors have undoubtedly been introduced whilst extracting the data using 'Data Thief' and considering the simplicity of the Leeson model the agreement is adequate for this discussion.

Equation 5.4 indicates that the phase noise of an oscillator may be reduced by increasing the Q of the oscillator's resonator. The Q of a cavity is domi-

⁵Data Thief is a program which allows extraction of data points from a printed graph. It may be downloaded from www.datathief.org. Checked November 2005.

6.2. MEASURING PHASE NOISE AT 94GHZ

nated by the resistive losses in the cavity walls, and it has been demonstrated that quasi-optical open cavities may achieve Q's which are orders of magnitudes greater than metallic cavities. The agreement between measured and predicted oscillator phase noise demonstrated by figure 6.9 means that a good indication of the phase noise which might be expected from a Gunn oscillator using a quasi-optical cavity may be estimated using the Leeson model. Using the same device parameters as above, and increasing the cavity Q to 100,000 produces the phase noise spectrum shown in figure 6.10.

Comparison of this (predicted) phase noise distribution, with the predicted

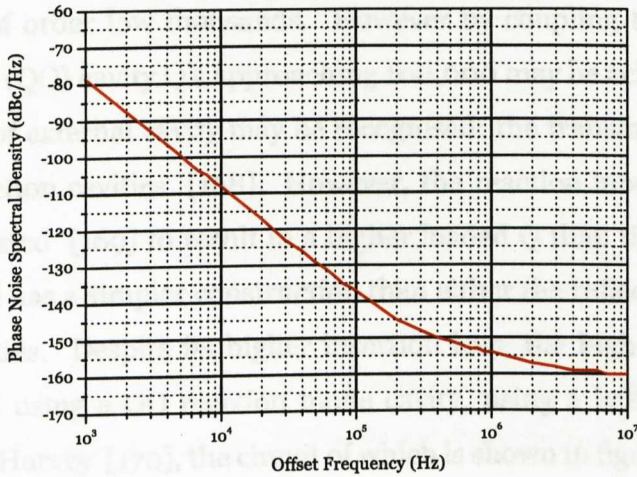


Figure 6.10: The predicted noise distribution of a Gunn oscillator at 94GHz using a quasi-optical cavity. The parameters used in the Leeson model were $Q = 10^5$, $f_c = 4.8\text{MHz}$ and a device noise figure of 5dB.

phase noise of the DRO based 94GHz source in figure 7.2 shows that this high Q oscillator has a phase noise which is at least an order of magnitude better

than the DRO based source down to frequency offsets of order 1kHz from the carrier. Thus, the Gunn oscillator with a high Q cavity can be expected to act as an adequate local oscillator for a down conversion measurement of oscillator phase noise.

6.3 Realisation of a Down Conversion Source

The Q of the cavity employed in a simple Gunn oscillator, is dominated by resistive losses in the cavity walls, and even gold plating will only result in a loaded Q of order low thousands. However by coupling to an external quasi-optical (QO) cavity Q's approaching 100,000 may be achieved.

Three types of external cavity may be recognised; the transmission, reflection and reaction cavities [168]. However, the reaction mode cavity may be demonstrated [169] to result in a higher loaded Q than the other types of cavity, and has a simpler construction than either the reflection or transmission cavities. Despite its higher insertion loss, the high Q cavity was implemented using a QO reaction mode cavity, using a half cube system described by Harvey [170], the circuit of which is shown in figure 6.11, and a photograph of which is shown in figure 6.12. The input, obtained from a 2nd harmonic Gunn oscillator with an 87GHz output, has its output waveguide aperture aligned to give a vertically polarised output, and is coupled into the cavity system using a standard corrugated horn. Any cross polar component produced by the horn is eliminated by the polariser (horizontal wire grid) P₁, which establishes the input vertical polarisation.

The cavity proper consists of the plane mirror M₁, the plano-concave mirror M₂ and the beam splitter BS. The roof mirror RM allows the cavity to be

6.3. A DOWN CONVERSION SOURCE

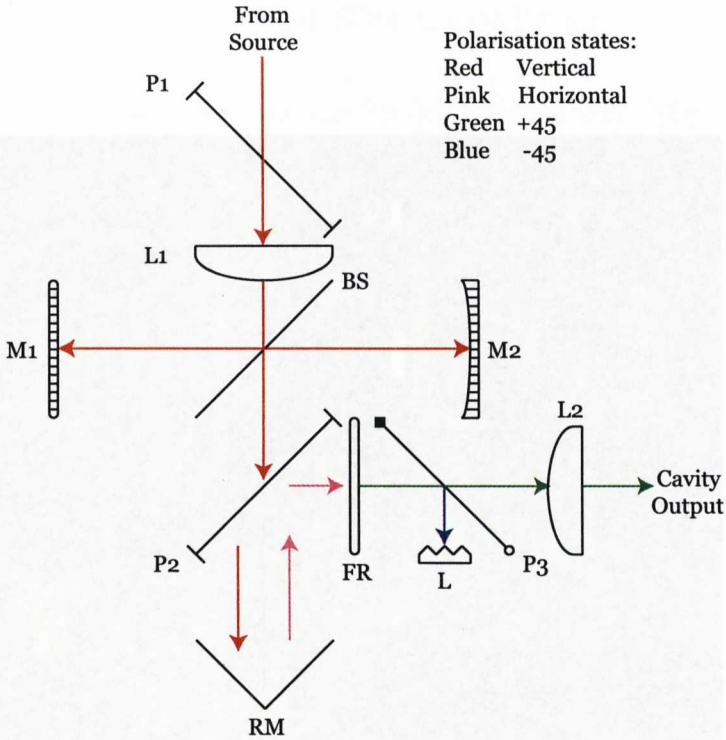


Figure 6.11: Circuit of a quasi-optical reaction mode cavity

matched to the Gunn oscillator, and is inclined at 45° . The combination of the Faraday rotator (FR) and the 45° polariser P3 forms an output isolator, which couples through lens L2 into a second corrugated horn which provides a waveguide output from the cavity. The waveguide output of the cavity is inclined at 45° and therefore any subsequent apparatus must account for this polarisation.

The interaction of this cavity with the Gunn diode non-linearity to produce a highly stable source is described in [171].

6.3. A DOWN CONVERSION SOURCE

6.4 Measurement of the Cavity Q

The cavity Q was measured using an 8 GHz Gunn source. The Gunn

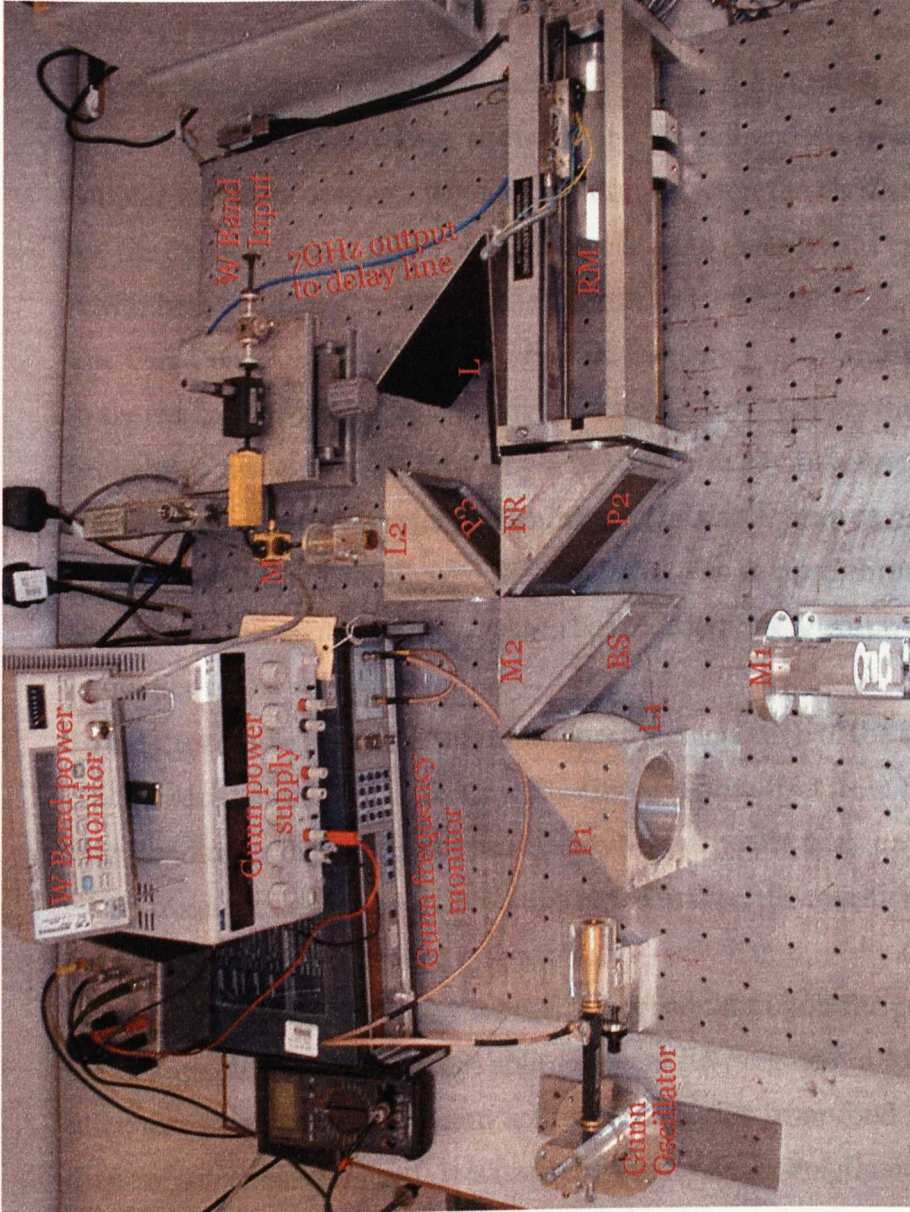


Figure 6.12: A quasi-optical reaction mode cavity labels are referred to in figure 6.11. The polariser P1, mirror M2, Faraday rotator FR and lens L2 are not visible in this projection. They are located as shown. M1 is the BMC10 down conversion mixer.

from two different sources and are defined by Γ_{11} and Γ_{22} .

The normalized results are shown in figure 6.13. Considering the frequency at half power and for the purposes of a quick Q estimation assuming the

6.4 Measurement of the Cavity Q

The cavity Q was measured using an 87GHz Gunn source. The Gunn Oscillator was coupled to the cavity using a standard corrugated horn. A single isolator between the horn and oscillator provided insufficient isolation to prevent the oscillator locking to the cavity. The directivity of a directional coupler was used to give adequate isolation between the oscillator and cavity, the dynamic range of the power meter used to measure the cavity output power being sufficient to handle the additional 10dB loss.

The Gunn oscillator was set to a nominal frequency of 87GHz and allowed to thermalise for 1 hour. Observing the cavity output power, the cavity was brought to resonance, indicated by a reduction in cavity output power, by adjusting the position of the plain mirror. The oscillator was phase locked to an EIP counter. This allowed the oscillator to be stepped through the resonance and the cavity power output to be recorded as a function of oscillator frequency under software control.

To aid the comparison of results and allow the calculation of the cavity Q, the results were normalised by subtracting any base line offset from the data and then dividing each point by the peak cavity output power to give a normalised cavity frequency response in interval 0 to 1. Further, the results were shifted to be symmetrical about zero frequency.

The performance of the cavity is crucially dependant upon the properties of the beam splitter. Three beam splitters were investigated, a Mylar film of thickness 0.1mm and two beam splitters fabricated from food grade Polythene of thickness 0.05mm. It is important to note that Polythene used came from two different sources and are denoted by BSa and BSb.

The normalised results are shown in figure 6.13. Considering the full width at half power and for the purposes of a quick Q estimation assuming the

6.4. CAVITY Q MEASUREMENT

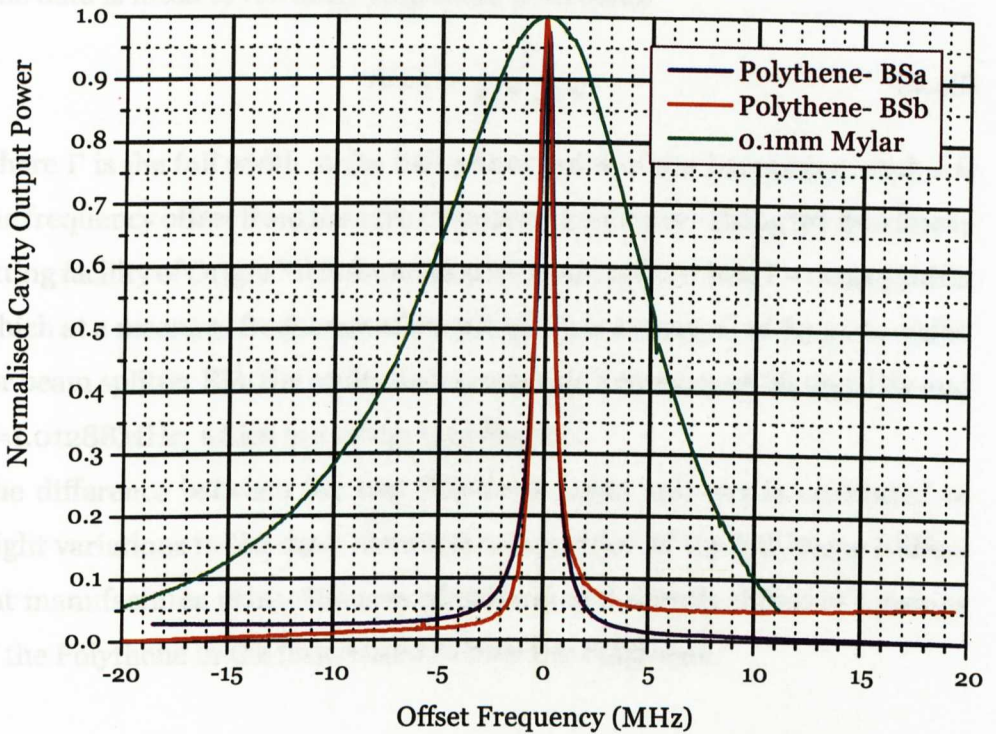


Figure 6.13: Normalised cavity frequency responses of a quasi-optical cavity at approximately 88GHz using 3 different beam splitters. Both Polythene beam splitters are 0.05mm thick.

cavity resonant frequencies to be 87GHz, approximate cavity Q values are 8700 for the 0.1mm Mylar beam splitter and 87,000 for both the Polythene beam splitters. The importance of the beam splitter is now clear. The 0.1mm Mylar beam splitter couples too much power into the cavity (is too reflective) whilst the Polythene beam splitters, being constructed of nominally identical food grade Polyethene, show very similar performance.

6.4. CAVITY Q MEASUREMENT

The data is fitted to the unity amplitude Lorentzian

$$A(\omega) = \frac{\Gamma}{4\omega^2 + \Gamma^2} \quad (6.48)$$

where Γ is the full width at the half power point of the Lorentzian, and ω is the frequency offset from the zero resonance frequency. Using the non linear fitting facility of Origin ⁶ it is found that for beam splitter BSa $\Gamma=1.02454\text{MHz}$ which at a resonant frequency of 86.9985GHz is a cavity Q of 84,900, whilst for beam splitter BSb the cavity had a resonant frequency of 86.995GHz and $\Gamma=1.01288\text{MHz}$, which is a cavity Q of 85,900.

The difference between the two Polythene beam splitters is attributed to slight variations in the exact chemical composition of the Polythene (different manufactures using different plastisers) and slightly different tensions of the Polythene in the frame used to hold the Polythene.

6.4.0.1 Validity of The Q values

The above calculation relies on the 'goodness of fit' of the Lorentzian to the data. Origin returns the *reduced* χ^2 value as a measure of the goodness of fit, which is defined as

$$\chi_r^2 = \frac{\chi^2}{N - V} \quad (6.49)$$

where χ^2 is the 'usual' estimate, N is the number of points and V is the number of variables. In all cases there is 1 variable, the curve width Γ .

For the BSa data there are 801 data points, and Origin returns $\chi_r^2=0.0003$, which gives $\chi^2=0.24$. From statistical tables for 95% confidence that a Lorentzian with $\Gamma=1.0245\text{MHz}$ represents the data, we require $\chi^2 < 3.841$, and we therefore conclude that the Lorentzian is a good fit.

⁶Origin is a commercial graphing package

6.4. CAVITY Q MEASUREMENT MEASUREMENT SYSTEM

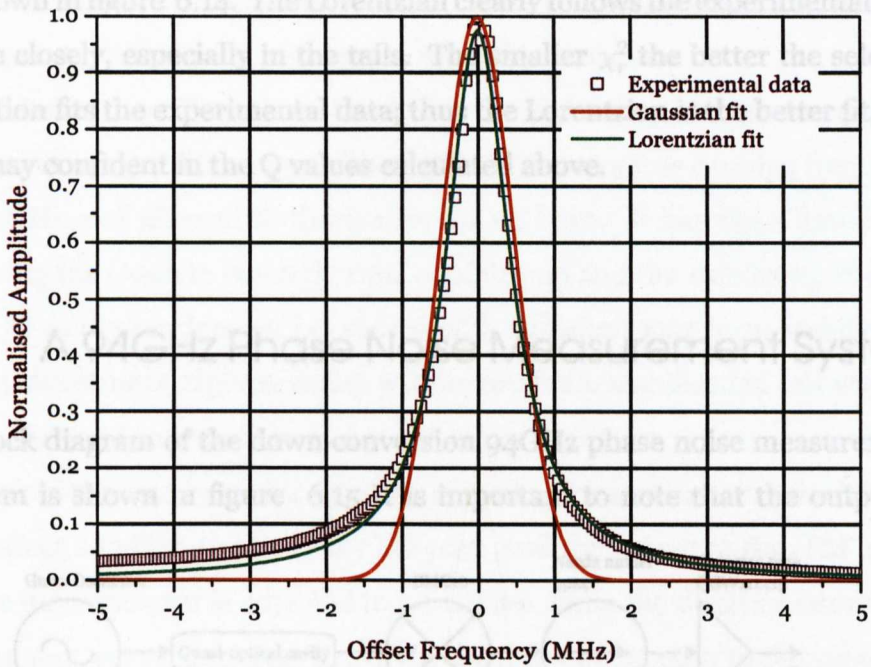


Figure 6.14: The comparison of measured data and both Gaussian and Lorentzian curves fitted to the measured data for the BSa beam splitter

For beam splitter BSb, there are 783 points and Origin returns $\chi_r^2=0.001$, which gives $\chi^2=0.782$, and we conclude that at the 95% level, the beam splitter is adequately represented by a Lorentzian with $\Gamma=1.01288\text{MHz}$.

Using Origin to fit the Gaussian

$$A(f) = \exp\left(-\frac{f^2}{2\sigma^2}\right) \quad (6.50)$$

to the data produces $\chi_r^2=0.0013$ and $\chi_r^2=0.002$ for BSa and BSb respectively, and it would appear that a Gaussian would also be a good fit. A comparison of the data and both a Lorentzian fit (using the above full width half power obtained above) and a Gaussian using $\sigma=0.48666$ returned by Origin

6.5. A 94GHZ PHASE NOISE MEASUREMENT SYSTEM

is shown in figure 6.14. The Lorentzian clearly follows the experimental data more closely, especially in the tails. The smaller χ_r^2 the better the selected function fits the experimental data; thus the Lorentzian is the better fit, and we may be confident in the Q values calculated above.

6.5 A 94GHz Phase Noise Measurement System

A block diagram of the down conversion 94GHz phase noise measurement system is shown in figure 6.15. It is important to note that the output of

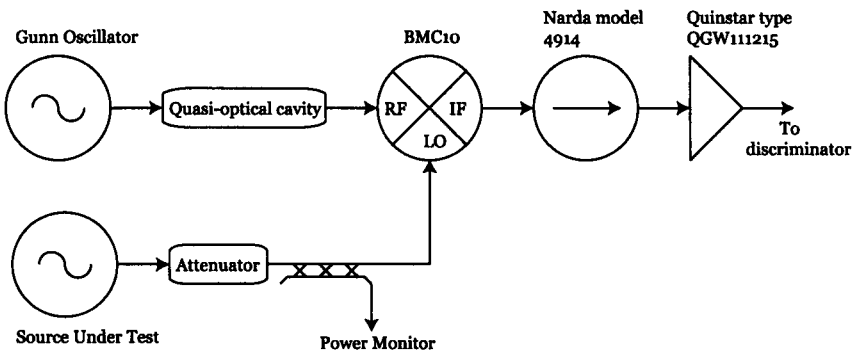


Figure 6.15: Realisation of a down conversion phase noise measurement system.

the cavity is connected to the mixer RF port and the source under test is connected to the mixer LO port. The 94GHz sources to be tested all produce enough power to drive the LO port to +13dBm as specified for the BMC10 mixer. The cavity output however is of order -10dBm when correctly adjusted to resonance which, while insufficient to drive the mixer LO port does not require any further processing for application to the mixer RF port. The

6.5. A 94GHZ PHASE NOISE MEASUREMENT SYSTEM

mixer IF output is insufficient to drive the delay line discriminator, and additional amplification is provided to solve this problem.

The LO Gunn oscillator is isolated from the QO cavity and assuming measurement of a 94GHz source with a 7GHz IF, set to a free running frequency of 87GHz and allowed to thermalise for an hour. It has been found that allowing the Gunn to reach thermal equilibrium and the stabilising effect of the QO cavity produce an LO source with sufficient long term stability for the measurement of phase noise- a Gunn oscillator stabilised in this way has been observed to remain locked to the cavity for hours.

The measurement system is set up by adjusting the attenuator in the LO arm to deliver +13dBm to the mixer LO port, and the power at the 'PM' point of the discriminator is adjusted to be +2dBm using the discriminator input attenuator, see section 6.1. The cavity may now be brought to resonance by moving the plain mirror M1 and observing the power at 'PM'. As the cavity is brought to resonance a sharp dip in power is observed, and careful adjustment of M1 and the position of the Gunn in front of P1 results in a very stable power reduction typically of more than 10dB. To perform a measurement, the power at 'PM' is brought back to +2dBm using the discriminator input attenuator, and measurement proceeds in the normal way as described in section 6.1.

CHAPTER 7

The Design a 94GHz Source

In this chapter, the design of a 94GHz source which is suitable for both pulsed and CW spectrometry, is discussed. The source consists of a low frequency oscillator and multiplier. The low frequency oscillator may be either a Dielectric Resonator Oscillator (DRO) for fixed frequency work, or a YTO (Yttrium Iron Garnet Tuned Oscillator) for variable frequency applications, whilst the multiplier employs either conventional or IMPATT diodes.

For all sources, key parameters are power output and phase noise, and a description of a down conversion measurement of phase noise at 94GHz will be presented. For the YTO based source an additional parameter is tuning range. The performance of a 94GHz Gunn source is presented for comparison.

7.1 Design Considerations

Prior to the development of the source to be described, the source used on the St Andrews ESR spectrometer was a Gunn oscillator locked to an EIP counter. In the current St Andrews spectrometer, the field modulation frequency is 1kHz and the phase noise of the oscillator at 1kHz is of paramount importance.

Extrapolating the measured Gunn oscillator phase noise of figure 6.9 from 10kHz to 1kHz indicates that at 1kHz a phase noise of order -25dBc/Hz might be expected for a free running Gunn oscillator. Phase locking the Gunn oscillator to an EIP counter in a 10kHz bandwidth introduces a 20dB suppression of the phase noise at 1kHz, giving a phase noise of -45dBc/Hz at a 1kHz offset from the carrier for an EIP locked Gunn oscillator.

Clearly any new source must provide an improvement in (i.e. a lower) the 1kHz phase noise performance and a lower phase noise in general is desirable. Other parameters which must be considered are power output and electronic tuning range.

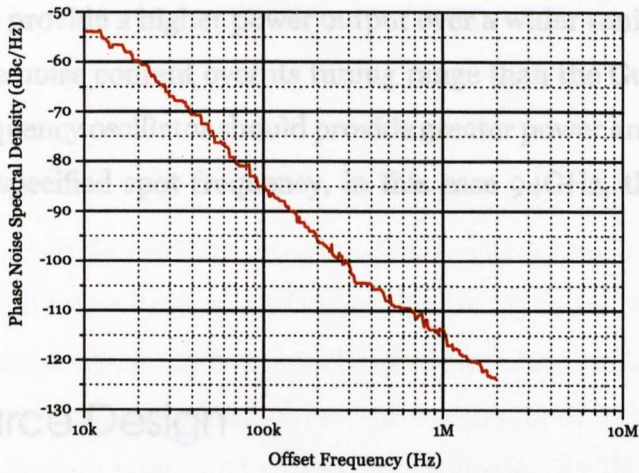
7.1.1 94GHz Gunn Oscillator Performance

In order to establish a performance base line, typical performance figures (tuning range, power output as a function of frequency and phase noise) of a second harmonic Gunn oscillator operating close to 94GHz were obtained¹. The phase noise curve is that given in [157]². These parameters are shown in figure 7.1, and establish the performance which must be bettered.

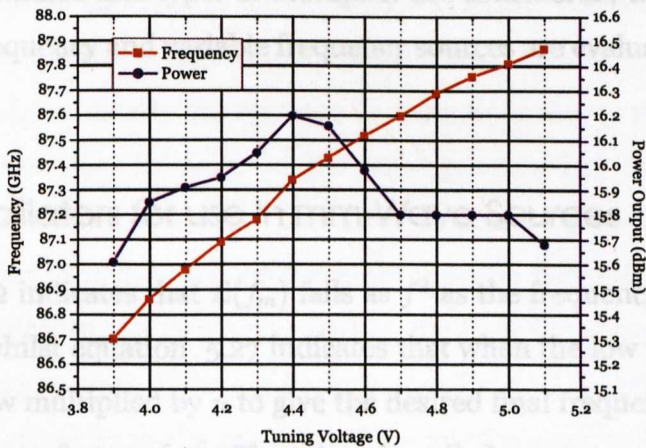
¹The author is indebted to Dr. D. Robertson of the Photonics Innovation Centre, University of St Andrews School of Physics and Astronomy.

²The phase noise data was extracted from [157] using Data Thief.

7.1. DESIGN CONSIDERATIONS



(a) Gunn oscillator phase noise from [157].



(b) Measured Gunn oscillator tuning performance.

Figure 7.1: The key parameters which the new source design is required to be better. Note that the phase noise is for a free running Gunn oscillator.

Both fixed frequency and tunable sources are required. Ideally, the tunable source would provide a higher power output over a wider tuning range with a lower phase noise content over its tuning range than the Gunn oscillator. The fixed frequency oscillator should provide greater power and lower phase noise at the specified spot frequency, in this case 94GHz, than the Gunn source.

7.2 Source Design

Having identified in chapter 5 that a viable method of producing a 94GHz source is to multiply a low frequency oscillator, in this section suitable oscillators are identified and types of multiplier are considered; the options for both fixed frequency and variable frequency sources are evaluated.

7.2.1 Oscillators for use in mm-Wave Sources

Equation 5.2 indicates that $\mathcal{L}(f_m)$ falls as f^2 as the frequency of oscillator is reduced, whilst equation 5.27 indicates that when the low frequency oscillator is now multiplied by n to give the desired final frequency, the noise is degraded by a factor of n^2 . Thus, keeping all else constant the act of reducing the oscillator frequency by a suitable amount, and then employing a frequency multiplication stage, would appear to be noise neutral. This however is not the case.

As has been demonstrated, the interplay between f_b and f_c is crucial in establishing the close to carrier noise performance, however as a guide, provided the increase in cavity Q obtained by reducing the oscillator frequency

7.2. SOURCE DESIGN

is greater than the multiplication factor required to recover the output frequency, close to carrier noise will be improved for a multiplied source.

7.2.1.1 Fixed Frequency Sources

As the frequency of the oscillator is reduced, resonators have lower fractional bandwidths and active devices tend to have lower $1/f$ noise corner frequencies, all of which make it easier to construct a low noise oscillator.

Figure 7.2 shows the calculated phase noise contents of a Gunn oscillator compared to various multiplied sources all producing 94GHz. In all cases the oscillators were constructed from a hypothetical device having a noise figure of 15dB, a $1/f$ corner frequency of 3kHz and a 5dB allowance was made for the noise added by the multiplication circuit. The properties of the various resonators use in this simulation are shown in table 7.1.

Figure 7.2 shows clearly the increase in noise floor due to multiplication. Considering the 'close in' noise i.e. the noise generated by each source inside the Gunn oscillator curve. The SAW oscillators show clearly that it is not sufficient to merely reduce the multiplication factor employed; here the lower multiplication factor required by the high frequency SAW device (which represents state of the art performance for a SAW resonator [172]) is more than off set by the increased Q of the low frequency SAW resonator. The crystal oscillator demonstrates that whilst a high Q low frequency oscillator, even after multiplication, is able to produce very low noise very close to carrier, the high multiplication factor gives rise to a very high noise floor further away from the carrier. In addition, the output of the final multiplier will consist of a comb of the desired 94GHz signal surrounded by a comb of additional frequencies spaced at 94MHz. These comb frequencies poten-

7.2. SOURCE DESIGN

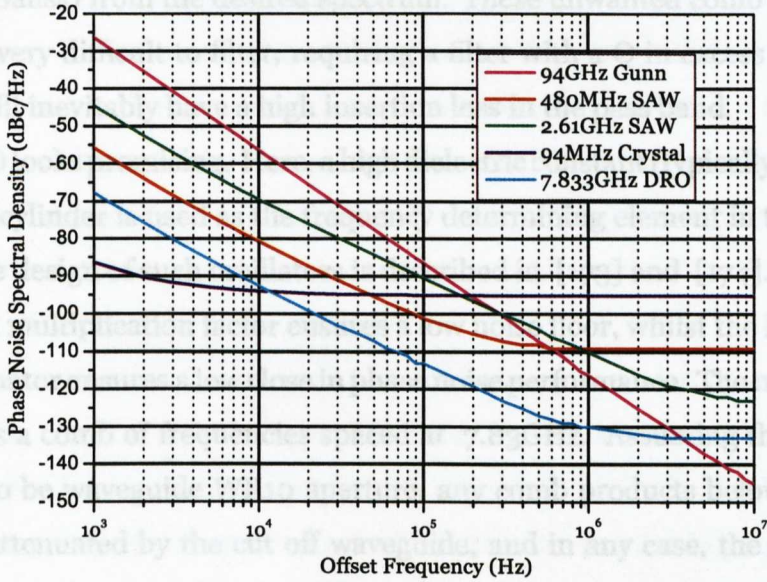


Figure 7.2: A comparison of the calculated phase noise to be expected from various types of oscillator, all have been multiplied to 94GHz with exception of the Gunn source.

Resonator	Frequency	Q	Multiplication Factor
SAW	480MHz	1000	196
SAW	2.61GHz	280	36
Crystal	94MHz	50,000	1000
DRO	7.833GHz	4000	12

Table 7.1: The properties of various resonators used in the simulation of the phase noise of multiplied sources.

7.2. SOURCE DESIGN

tially represent spurious outputs from the spectrometer, and are spaced only 5mT (5 Gauss) from the desired spectrum. These unwanted comb frequencies are very difficult to filter, requiring a filter with a Q in excess of 1000, which will inevitably have a high insertion loss in the pass band.

The DRO looks promising. Here, a high dielectric constant (typically $\epsilon_r \sim 38$) low loss cylinder is used as the frequency determining element in the oscillator, the design of such oscillators is described in [173] and [174]. The low required multiplication factor ensures a low noise floor, whilst the high Q of the resonator ensures a low close in phase noise performance. The multiplier produces a comb of frequencies spaced at 7.83GHz. Assuming the source output to be waveguide WR10 aperture, any comb products below 75GHz will be attenuated by the cut off waveguide, and in any case, the spurious spectra are 270mT (2700 Gauss) from the desired spectrum, which is easily resolved. It was for these reasons that a DRO based source was selected for fixed frequency work.

7.2.1.2 Variable Frequency Sources

Because a polished YIG sphere has a large unloaded Q it is attractive as a low noise tunable source. Using [130], if the unloaded Q of a YIG sphere is 5000 at 10GHz, it is 5500 at 7GHz. The phase noise of an oscillator is related to Q_l^2 (equation 5.2), and therefore a YIG oscillator should not have a phase noise more than 4.1dB worse than a DRO (assuming the YIG sphere to be critically coupled) at the same frequency and employing the same active device. Thus, a 7.83GHz YTO multiplied to 94GHz would be expected to outperform a 94GHz Gunn oscillator.

The YTO is magnetically tuned and in the same way and for the same reasons

7.2. SOURCE DESIGN

that the spectrometer magnetic field is swept and modulated using two coils, the YTO has a main tuning coil and an FM coil. The main coil, having a large inductance, is used to set the nominal centre frequency about which the oscillator may be frequency modulated using the FM coil, which has small inductance. Alternatively, having set the nominal frequency of the oscillator it may be phase locked using the FM coil; phase locking the oscillator on the main coil is not generally viable due to the bandwidth restriction the RL time constant of the main coil would impose.

The main coil typically produces a (slow) frequency variation of order 100's of MHz/mA, and is able to support currents in excess of 1A, whilst the FM coil may produce modulation rates (with a bandwidth of 10's of kHz) of 300 to 400kHz/mA with an upper current limit of order 200mA imposed by the diameter of the wire employed in the construction of the FM coil.

If only a small tuning range (of order ± 70 MHz) about some nominal centre frequency is required, then the main (tuning) coil may be dispensed with, and a permanent magnet may be employed to bias the YIG sphere to produce the desired nominal centre frequency. In this case the oscillator is referred to as a Permanent Magnet YTO or PMYTO.

The magnetic field required to tune the YTO produced by either coil is proportional to the current flowing in the coil, and therefore because most control signals are voltage sources, voltage to current convertors are required to drive the coils.

An FM Coil Driver

The FM coil driver, being required to tune both above and below the nominal centre frequency, must be able to both source and sink current. Such

7.2. SOURCE DESIGN

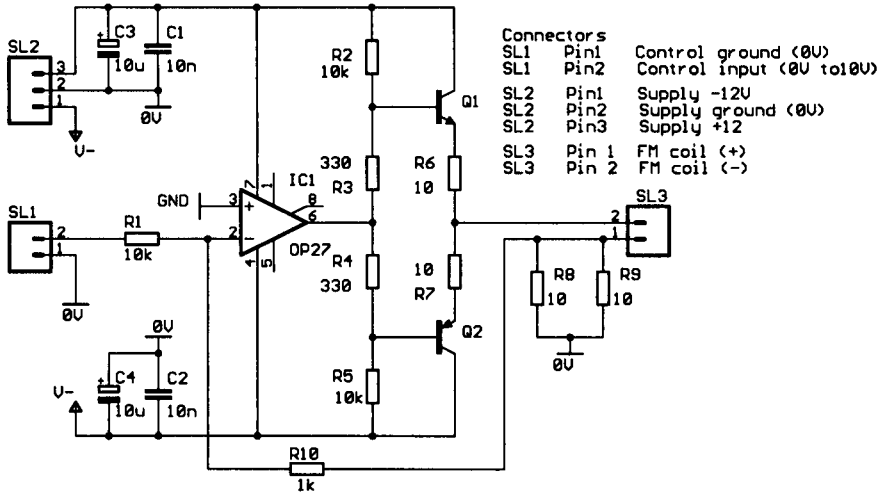


Figure 7.3: An FM coil driver following the oscillator manufacturers recommendations. All resistor values are in Ohms, all capacitor values are in Farads.

a circuit is shown³ in figure 7.3. The circuit is that of a class AB audio amplifier, the output of which drives the 5Ω sensing resistor formed by the parallel combination of R8 and R9. The maximum voltage which needs to be developed across these resistors is 1V. This is scaled by a factor of 0.1 by the op-amp so that the required $\pm 200\text{mA}$ through the coil is given by an input voltage of $\pm 10\text{V}$.

The output transistors are power devices, and should be mounted on a heatsink, in a worst case scenario they might have to dissipate in excess of 2W. Similarly, the output resistors (R6, R7) may be called upon to dissipate 0.4W and should be over rated accordingly (1W).

The driver must be a low noise circuit to prevent circuit noise modulating

³www.microlambdawireless.com gives this circuit in the form used for simulation purposes. Checked June 2005

7.2. SOURCE DESIGN

the oscillator and degrading the oscillator phase noise spectrum. The operational amplifier was selected to be a low noise device. The total input noise voltage is given by [175]

$$E_{ni}^2 = E_{Rin}^2 + E_{na}^2 + I_n^2 R_s^2 \quad (7.1)$$

in which

E_{Rin} is the noise voltage due to R_1 ($V/\sqrt{\text{Hz}}$)

E_{na} is the operational amplifier input noise density ($V/\sqrt{\text{Hz}}$)

I_n is the operational amplifier input current noise density ($A/\sqrt{\text{Hz}}$)

and $R_s = R_1 + R_+$ where R_+ is the input current bias compensation resistor often included on the op-amp non inverting input. For the OP27 used as shown in figure 7.3, the input noise is dominated by the the input noise voltage term ($3\text{nV}/\sqrt{\text{Hz}}$) and the input current term (calculated as $10\text{nV}/\sqrt{\text{Hz}}$). The total output noise voltage V_{no} in the frequency interval f_l to f_u is given by

$$V_{no} = G \sqrt{\int_{f_l}^{f_u} E_{ni}^2 df} \quad (7.2)$$

where G is the amplifier closed loop gain. Assuming E_{Rin} and E_{na} to be flat in the interval 1kHz to 100kHz , this gives an output noise voltage of 329nV RMS, which across the 5Ω sensing resistor is a current of approximately 65nA . The SSB phase noise produced by this noise current is [176]

$$\mathcal{L}(f) = 20 \log \left[\frac{1}{\sqrt{2}} \frac{K_v V_{no}}{f_m} \right] \quad (7.3)$$

where k_v is the tuning sensitivity, and f_m is the carrier offset frequency. Then at 1kHz , and assuming a tuning sensitivity of $400\text{kHz}/\text{mA}$ the driver will produce a noise floor of $-95\text{dBc}/\text{Hz}$. This is insignificant, being 25dB lower than the YIG manufacturers specified noise at 1kHz .

7.3 Phase Locked Sources

At offset frequencies such that $f_m > f_b$ or $f_m > f_c$, whichever is the greater, the oscillator noise is determined by the noise floor of the device used to construct the oscillator, and this depends only upon the device and is not affected by oscillator action. Thus the ultimate noise floor of the multiplied oscillator will be degraded by a factor of n^2 , and therefore, whilst a multiplied source may well have a better close to carrier noise, the noise floor of a multiplied source will, as is demonstrated in figure 7.2, be degraded over a direct generation approach.

It would therefore be useful if a method could be found which multiplied a low noise low frequency oscillator to the desired output (source) frequency, whilst giving the low phase noise close to carrier of a multiplied oscillator with the noise floor of a directly generated source.

The phase locked loop (PLL) is a circuit configuration which achieves this [177, 178] and is outlined in figure 7.4. The output of the 94GHz Gunn

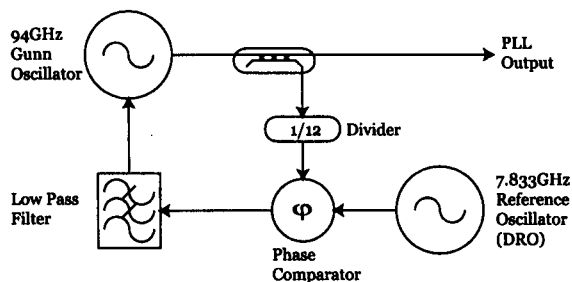


Figure 7.4: The outline of a phase locked source. Here a 94GHz Gunn oscillator has been phase locked to a 7.833GHz DRO.

oscillator is sampled and divided by a factor of 12 to give an output from the divider of 7.833GHz. The divider output is taken as one input of a phase

7.3. PHASE LOCKED SOURCES

comparator, the other input of which is taken directly from a 7.833GHz DRO. The phase comparator produces an output which is proportional to the phase difference between the the divider output and the DRO. After filtering by the low pass filter this becomes a DC signal which may be used to hold the frequency of the Gunn oscillator stable. In effect, the DRO frequency has been multiplied to the Gunn frequency, hence the factor 1/12 indicated in figure 7.4.

The PLL is a feedback system, the closed loop bandwidth of which is determined by the low pass filter the Gunn oscillator tuning sensitivity and the phase comparator phase gain. Inside the loop bandwidth the phase noise of the 94GHz output is that of the multiplied reference (DRO). Outside the loop bandwidth the phase noise of the source is that of the free running Gunn oscillator.

Therefore by placing the closed loop bandwidth with care an optimum phase noise distribution may be obtained. For the Gunn oscillator and DRO shown in figure 7.2, it would appear that a closed loop bandwidth of between 3MHz and 4MHz would give an optimum phase noise distribution.

The PLL (usually) relies on frequency dividers (essentially very fast digital counters) to reduce the Gunn oscillator frequency to a lower frequency at which the phase locking is undertaken. Unfortunately, simple dividers are not available at 94GHz, commercial units have an upper frequency limit of order 40GHz ⁴ with 20GHz being rather more common. The problem may be reduced by using a second harmonic Gunn oscillator and extracting the 47.5GHz fundamental, which may then be used in a mixing system [179], or used in conjunction with a regenerative divider to provide a more manageable frequency.

⁴Centellax part number TD40MCA @ www.centellax.com -checked June 2005

Despite the attraction of an optimal phase noise spectrum, the PLL is not suited to producing the fastest pulses and is not considered further.

7.4 Multipliers

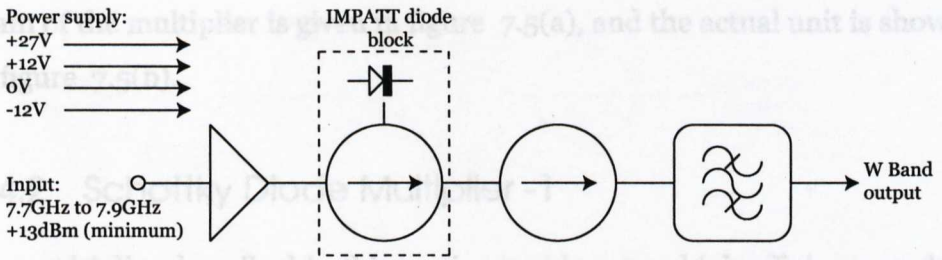
In this section 3 multipliers, all based upon diodes, are described in detail. Two of the diode multipliers use Schottky Barrier devices and in fact, the second Schottky multiplier is a realisation of the first multiplier by the manufacturer of the Schottky diode multipliers. The third multiplier, which employs IMPATT diodes, is projected to give a lower phase noise than the Schottky diode multiplier by virtue of its relative simplicity.

7.4.1 Multiplication using IMPATT Diodes

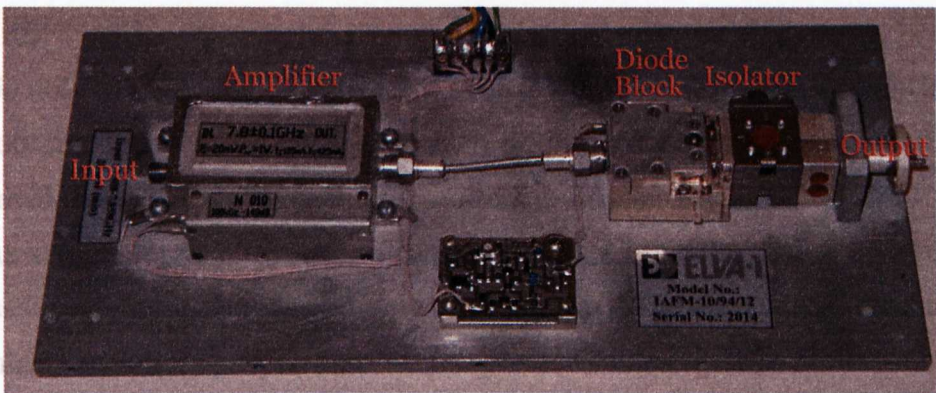
IMPATT diodes, when used as oscillators have a reputation for being able to deliver high powers at mm-wave frequencies, but only with high FM and AM noise content; in fact, both the phase noise and amplitude noise content of a well designed IMPATT oscillator have been demonstrated to be of order 10dB worse than a similar Gunn oscillator [180]. The high noise of the IMPATT oscillator is due to the wide frequency range over which they generate negative resistance, and their subsequent sensitivity to the effects of parasitic components generating spurious oscillations [181].

However, when used as frequency multipliers the IMPATT diode offers some considerable advantages over other diode multipliers. The phase noise added by the IMPATT is lower than might be expected from its oscillator performance [182], and they are intrinsically high power devices. Thus, with

7.4. MULTIPLIERS



(a) Block diagram of an IMPATT multiplier.



(b) Realisation of an IMPATT multiplier.

Figure 7.5: The ELVA IMPATT multiplier. This multiplier realises a x12 multiplication factor in a single stage.

sufficient drive (input power) high multiplication factors may be obtained in a single stage [182]. Therefore, because the multiplier consists of a low noise driver amplifier, and only a single multiplier stage, the phase noise added by an IMPATT multiplier is expected to be closer to the $20 \log(n)$ minimum, than it is for other diode multipliers.

A single stage x12 IMPATT multiplier type IAFM 10/94/12 was obtained from ELVA-1. Details of the multiplier are shown in figure 7.5; a block dia-

7.4. MULTIPLIERS

gram of the multiplier is given in figure 7.5(a), and the actual unit is shown in figure 7.5(b).

7.4.2 Schottky Diode Multiplier -1

The multiplier described in this section employs two high efficiency multiplier stages based on Schottky barrier diodes to obtain multiplication by a factor of 4, and an active x3 stage to give the required multiplication factor of 12.

It is able to accept input at two different frequencies. The first at 23.5GHz is obtained from a DRO with a 23.5GHz output, which must be amplified to provide sufficient drive for the subsequent multiplier stages.

The second input is obtained from a 7.833GHz oscillator (DRO or YTO). These oscillators provide output to drive an active tripler stage the output of which must once again be amplified to provide sufficient drive to the following x4 stages.

The block diagram of the multiplier is shown in figure 7.6, and the realisation is shown in figure 7.7. The Schottky multipliers, M2 and M3, were selected because, compared to other available devices, they produce a high output power for a given drive level.

In this realisation of the x4 multiplier, because the multipliers were purchased as separate blocks, an isolator at 47GHz (I2) was required between the multiplier blocks.

Both M2 and M3 are self biased, using the signal from the previous stage to develop the diode bias. The diode bias is developed across the resistors R1 and R2, which are specified by the manufacturer to be 1M Ω and 5k Ω respectively. The maximum safe continuous bias levels are 30V for M2 and 18V for M3, with absolute maximum values of 35V and 25V; these voltages

7.4. MULTIPLIERS

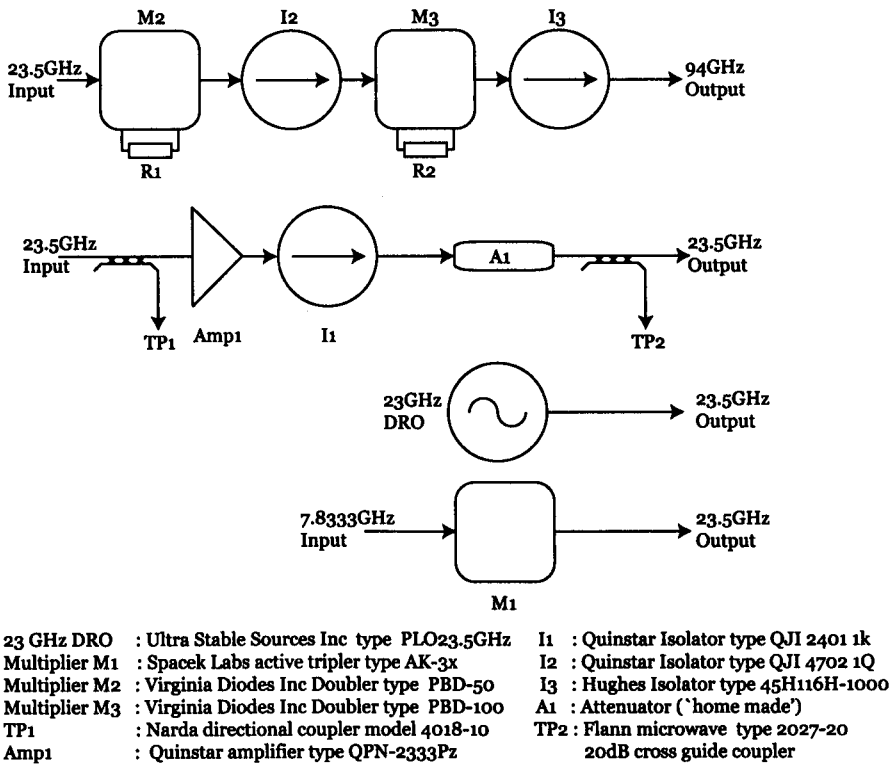


Figure 7.6: Block diagram of a prototype Schottky Diode multiplier

are continuously monitored during operation.

The D46 multiplier block (M2) will achieve its maximum output power for a typical drive level of 1W, which will produce an output power of order 300mW, and which will provide sufficient drive to the second multiplier (M3) which will provide the desired output. The drive for these multipliers is delivered from an amplifier (Amp1) which is capable of delivering 2W at 23.5GHz. The drive to the multipliers is controlled by attenuator A1 which is used to set the safe multiplier voltages. The attenuator is a simple device which inserts a block of metal into the wave guide connecting the amplifier

7.4. MULTIPLIERS



Figure 7.7: Realisation of the prototype Schottky Diode multiplier. It is shown here configured for use with the 23.5GHz DRO.

and the multipliers. The 'unwanted' power is reflected back towards the amplifier output, and therefore isolator I1 is required to protect the amplifier. The multiplier may be driven from either a 23.5GHz DRO (which is actually an 11.75GHz DRO with an internal doubler) which is used for fixed 94GHz spectrometry, or via an additional tripler (M1) from a suitable 7.8333GHz source for either fixed (using a DRO) or variable frequency work using a YTO

7.4. MULTIPLIERS

or PMYTO.

7.4.3 Schottky Diode Multiplier -2

Having demonstrated that significant power could be generated using a Schottky Diode based multiplier, a second unit was ordered from the manufacturer of the Schottky Diode based multipliers, and was specified to be a single unit to perform a x12 multiplication from 7.8333GHz to 94GHz with an output power in excess of 200mW (+23dBm).

The unit was supplied with fan assisted cooling system. Vibration from fans is known to cause amplitude modulation of signals within the spectrometer by changing the alignment of the spectrometer optics, and therefore the multiplier chain was repackaged as shown in figure 7.8 The multiplier is much simpler. The first multiplier (M1) is a x3 stage, Spacek part number A246-3XW-31, which with a drive level of +17dBm between 7.58GHz and 8.08GHz, delivers +30dBm to the following multiplier blocks, M1 and M2 which are VDI multipliers type D50 and D100 respectively.

There are two major differences between this multiplier chain and the chain described in section 7.4.2. Firstly, with the manufacturer assembling the multiplier, it was possible to ensure suitable matching between multiplication stages, and therefore the need for interstage isolators was eliminated. Secondly, rather than the self bias used in the previous multiplier, the diode blocks are biased by an external voltage (30V for D50 block and 18V for the D50 block) and the drive applied to M1 is adjusted to maintain the current in the diode blocks at safe levels, 18mA for the D50 unit and 10mA for the D100 unit.

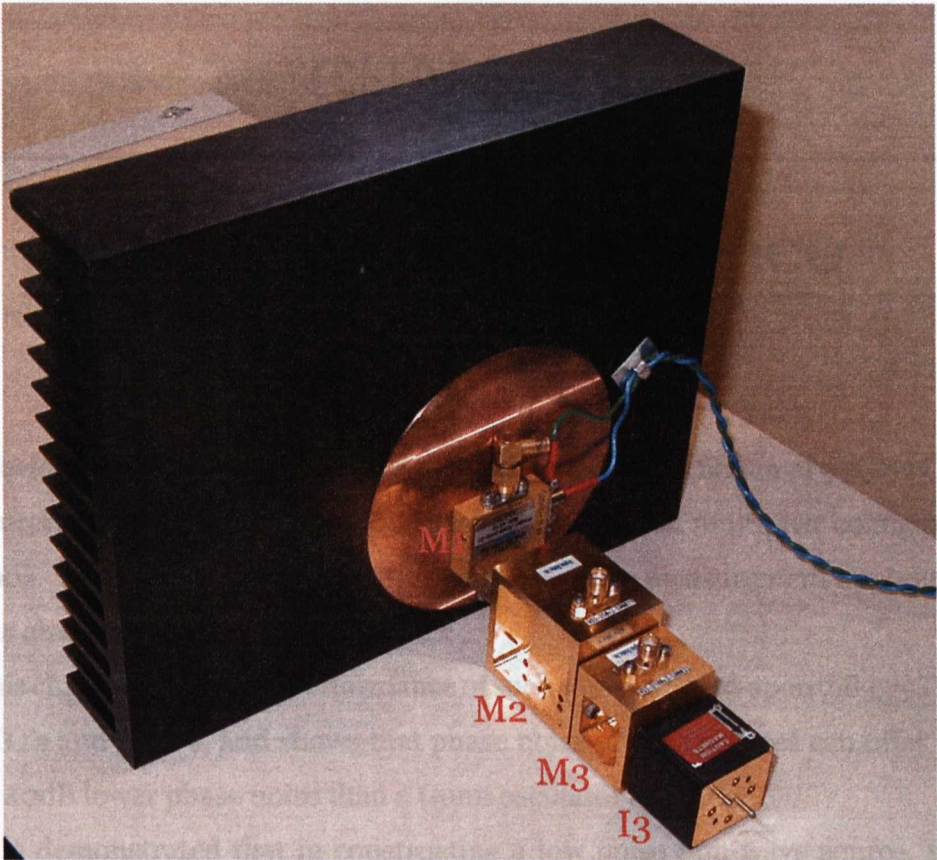


Figure 7.8: The second Schottky Diode multiplier.

CHAPTER 8

CW Source Performance

Previous chapters have described the design and construction of 94GHz CW sources based on a number of different oscillators and multiplier configurations. The design and construction of phase noise measurement apparatus has also been discussed.

This chapter reports the performance of such sources based upon 7.8333GHz YTO's and DRO's, and shows that phase noise of such sources can offer up to 40dB lower phase noise than a Gunn oscillator at 94GHz.

It is demonstrated that in constructing a low noise mm-wave source, not only must the oscillator performance be taken into consideration, the circuit configuration of the multiplier chain must also be considered.

The improvement in the performance of a CW spectrometer which is obtained when a DRO based source rather than a Gunn oscillator is used (in conjunction with an InSb bolometric detector) is demonstrated.

8.1 Measured oscillator Performance

The power output, phase noise spectrum and where applicable, the tuning characteristics, of three oscillators in the 7GHz range were measured. They were a DRO having a nominal frequency of 7.833GHz, a permanent magnet biased YTO (PMYTO) having a nominal frequency of 7.192GHz and a YTO capable of tuning 6.8GHz to 8.8GHz, set to a nominal centre frequency of 7.8333GHz.

The frequency of the PMYTO makes it unsuitable for use in the spectrometer under consideration; it is included however as being representative of an important oscillator option when moderate tuning range and a low phase noise are required.

8.1.1 Measured DRO Performance

A DRO, with a nominal output frequency of 7.833GHz, was obtained from the same company as the 7.192GHz DRO used in section 6.1.

The DRO has a mechanical frequency adjustment and this was adjusted such that the DRO provided an output frequency of 7.833GHz, at which point it produced an output power of +13dBm. The result of a phase noise measurement made on this 7.833GHz DRO, is shown in figure 8.1.

Note the discrete spectral line at approximately 70kHz offset. Such lines are often seen at multiples of 15,625Hz, the television line timebase frequency in the UK, 50Hz and its multiples (if a measurement can be made sufficiently close to the carrier) and at frequencies related to other switching systems in the laboratory. These are spurious responses, the amplitudes which should be measured as strict powers and, whilst part of the oscillator spectral output

8.1. MEASURED OSCILLATOR PERFORMANCE

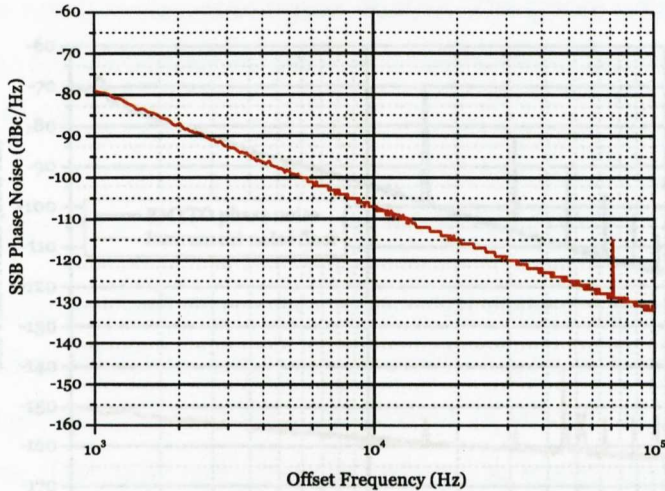


Figure 8.1: 7.833GHz DRO phase noise

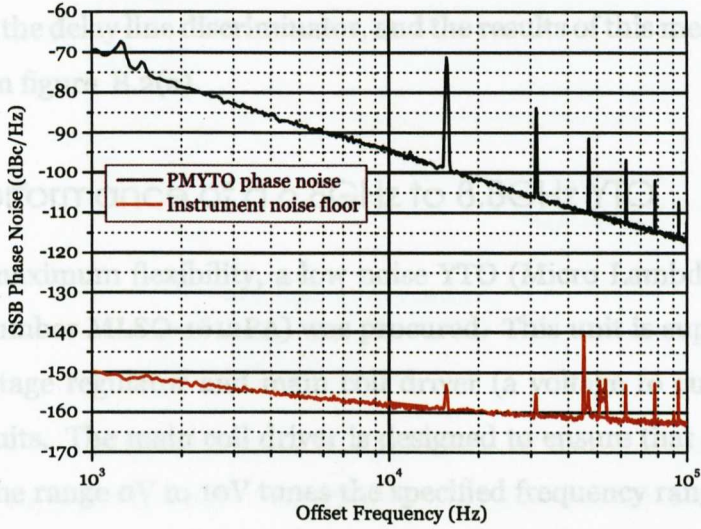
are not part of the phase noise spectrum.

8.1.2 Measured PMYTO Performance

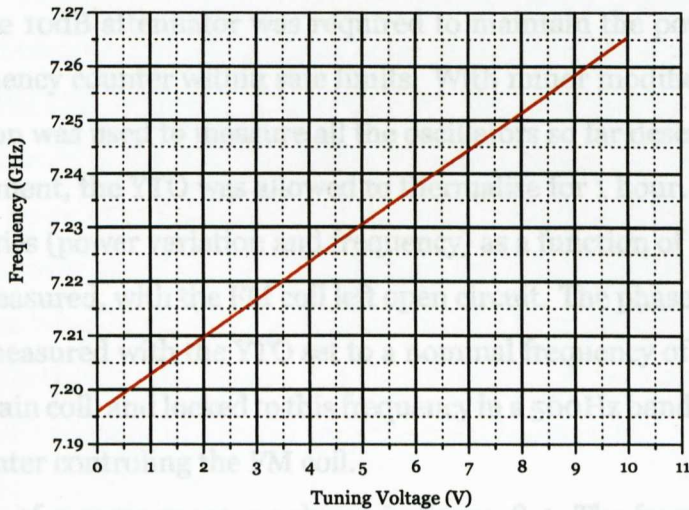
The PMYTO has poor long term stability and was phase locked to an EIP counter whilst performing the phase noise measurement. The locking bandwidth was 500Hz, which minimised distortion of the phase noise spectrum at a 1kHz offset due to the phase locking process. The PMYTO was connected to the discriminator, and with the oscillator and heater supplies applied, locked to 7.2GHz and allowed to thermalise for 1 hour, prior to measurement.

The key parameters for the PMYTO are its tuning range and phase noise spectrum. Using the FM driver described in section 7.2.1.2, the tuning characteristic was measured by varying the input voltage in the range 0-10V. Note that only the positive direction was measured, the negative direction being

8.1. MEASURED OSCILLATOR PERFORMANCE



(a) Phase noise.



(b) Tuning performance.

Figure 8.2: The tuning and phasenoise characteristics of a PMYTO with a centre frequency of 7.23GHz.

8.1. MEASURED OSCILLATOR PERFORMANCE

identical. The result is shown in figure 8.2(b). The phase noise was measured using the delay line discriminator, and the results of this measurement are shown in figure 8.2(a).

8.1.3 Performance of a 6.8GHz to 8.8GHz YTO

To obtain maximum flexibility, a low noise YTO (Micro Lambda Wireless Inc. part number MLSO-1612PA) was procured. This unit is supplied with integral voltage regulator and main coil driver (a voltage to current converter) circuits. The main coil driver is designed to ensure that an applied voltage in the range 0V to 10V tunes the specified frequency range. An FM coil driver was constructed using the circuit shown in figure 7.3.

The oscillator parameters were measured using the test set shown in figure 8.3, the 10dB attenuator was required to maintain the power applied to the frequency counter within safe limits. With minor modifications, this configuration was used to measure all the oscillators so far described. Prior to measurement, the YTO was allowed to thermalise for 1 hour. The tuning characteristics (power variation and frequency) as a function of tuning voltage were measured, with the FM coil left open circuit. The phase noise spectrum was measured with the YTO set to a nominal frequency of 7.8333GHz using the main coil, and locked to this frequency in a 500Hz bandwidth using an EIP counter controlling the FM coil.

The results of measurement are shown in figure 8.4. The frequency range over which measurements were made was restricted to a range imposed by subsequent multiplier stages. The power output has been corrected to allow for the insertion losses of the isolator and directional coupler, 0.4dB (maximum) and 1.0dB (maximum) respectively.

The phase noise is poor, especially when it is considered that the theoretical

8.1. MEASURED OSCILLATOR PERFORMANCE

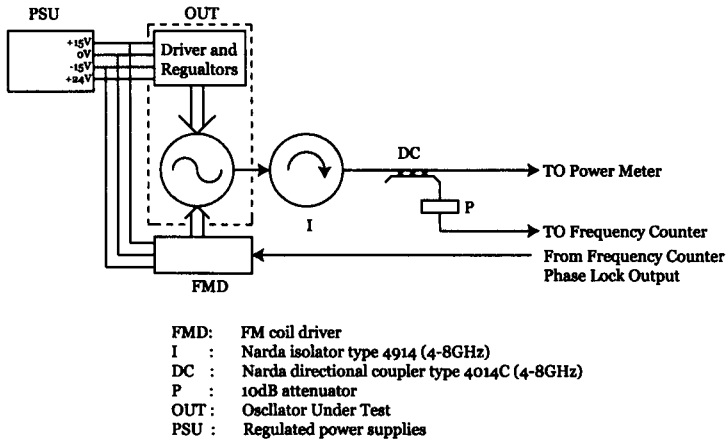


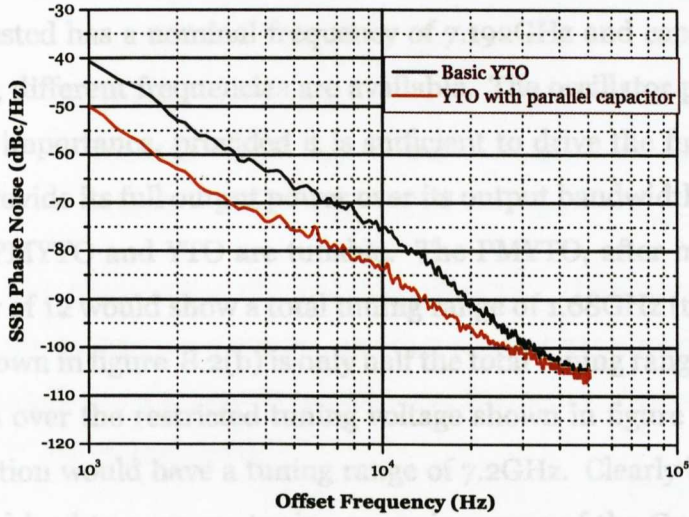
Figure 8.3: YTO test set. Simple modifications of the apparatus (power supply outputs for example) were employed to test all oscillators.

degradation over the DRO due to the YTO having a lower Q is less than 5dB, and the manufacturer quotes a phase noise of -105dBc/Hz at 20kHz offset, which the PMYTO achieves. The reason for this discrepancy is the large tuning sensitivity of the YTO (200MHz/V) which makes the oscillator very sensitive to noise from the driver circuit, which is supported by the fact that the manufacturer specifies the YTO without the driver circuit. The driver noise may be band limited by the application of a large capacitor in parallel with the main tuning coil. Figure 8.4 also shows the phase noise measured with a $350\mu\text{F}$ capacitor in parallel with the main tuning coil.

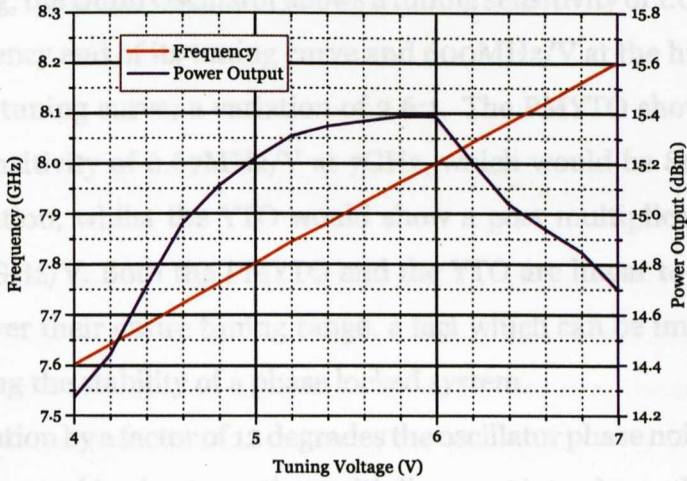
8.1.4 Comparison of oscillator Performances

The key parameters are frequency and power output. It is only necessary that the oscillator has the correct frequency for multiplication to the source output frequency. With a multiplication factor of 12 this results in a required

8.1. MEASURED OSCILLATOR PERFORMANCE



(a) Phase noise.



(b) Tuning performance.

Figure 8.4: The tuning and phasenoise characteristics of a YTO with potential tuning range of 6 to 8GHz, about a centre frequency of 7.8333GHz.

8.1. MEASURED OSCILLATOR PERFORMANCE

oscillator frequency of 7.8333GHz for a source frequency of 94GHz. The PMYTO tested has a nominal frequency of 7.192GHz and cannot be set to 7.833GHz, different frequencies are available. The oscillator power output is of little importance, provided it is sufficient to drive the first multiplier stage to provide its full output power over its output bandwidth.

Only the PMYTO and YTO are tunable. The PMYTO, after multiplication by a factor of 12 would show a total tuning range of 1.68GHz (the frequency change shown in figure 8.2(b) is only half the total tuning range), whilst the YTO, even over the restricted tuning voltage shown in figure 8.4(b), post multiplication would have a tuning range of 7.2GHz. Clearly both types of YTO would lead to a source tuning range in excess of the Gunn Oscillator (1.2GHz) shown in figure 7.1(b). The linearity of the tuning curves is also interesting, the Gunn Oscillator shows a tuning sensitivity of 1.6GHz/V at the low frequency end of its tuning curve and 600MHz/V at the high frequency end of its tuning curve; a variation of 2.6:1. The PMYTO shows a constant tuning sensitivity of 6.67MHz/V at 7GHz, which would be 80MHz/V post multiplication, whilst the YTO would show a post multiplication sensitivity of 2.4GHz/V. Both the PMYTO and the YTO are linear to within 1MHz (0.02% over their entire tuning range, a fact which can be important when considering the stability of a phase locked system.

Multiplication by a factor of 12 degrades the oscillator phase noise by 21.58dB and as discussed in chapter 5 the multiplier must introduce additional noise in its own right. A total degradation (multiplication and circuit factors) of 25dB will be employed for the purposes of estimation. The results of this allowance are shown in table 8.1. Thus, we would expect to find the PMYTO and the DRO as clear favourites as oscillators used to produce mm-wave sources. A source based on a multiplied YTO is expected to never offer worse

8.2. MEASURED SOURCE PERFORMANCE

Offset Frequency	Gunn	YTO	PMYTO	DRO
1kHz	-25*	-25	-45	-55
10kHz	-55	-60	-70	-82
100kHz	-85	-90*	-90	-105
1MHz	-115	-120*	-120*	-132*

Table 8.1: The phase noise of various oscillators. The Gunn diode has a direct mm-wave output, all other sources have been degraded by 25dB to refer them to a mm-wave frequency. Quantities marked “*” are extrapolated.

phase noise than the Gunn oscillator, and indeed may offer considerable advantage when extreme tuning range is required.

8.2 Measured Source Performance

In this section, the performance of three multipliers, in conjunction with the DRO and YTO are described. Two of the multipliers use Schottky Barrier devices, whilst the third uses IMPATT diodes to perform the multiplication. Only one phase noise measurement of the multiplied YTO is reported, the generalised trends may be observed using the DRO.

The multiplier bandwidths are established using the YTO. For all sources, the phase noise of the source is measured at 94GHz using the coaxial discriminator and down conversion system of chapter 6.

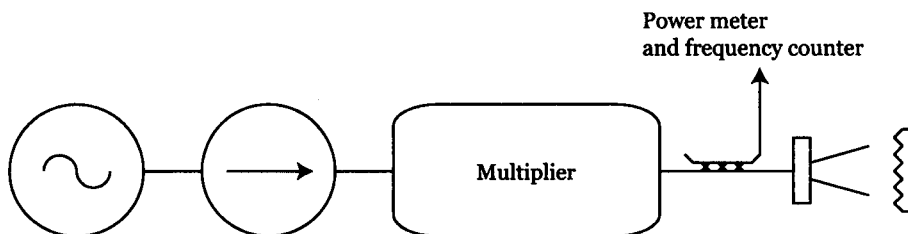


Figure 8.5: The multiplier test method.

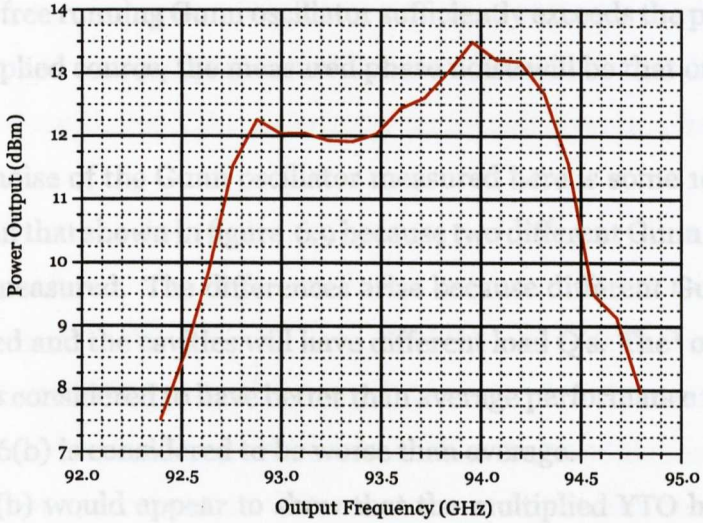
8.2.1 IMPATT MULTIPLIER and YTO

In the interval 7.7GHz to 7.9GHz the YTO produces an output power in excess of +14.8dBm (figure 8.4(b)) which satisfies the minimum input power requirements of the IMPATT multiplier, and the YTO was therefore connected directly to the multiplier input; the remaining test equipment was connected as shown in figure 8.2. The power output of the IMPATT multiplier as a function of output frequency is shown in figure 8.6(a), in which correction has been made for the 10dB coupling and insertion loss of the directional coupler of the coupler.

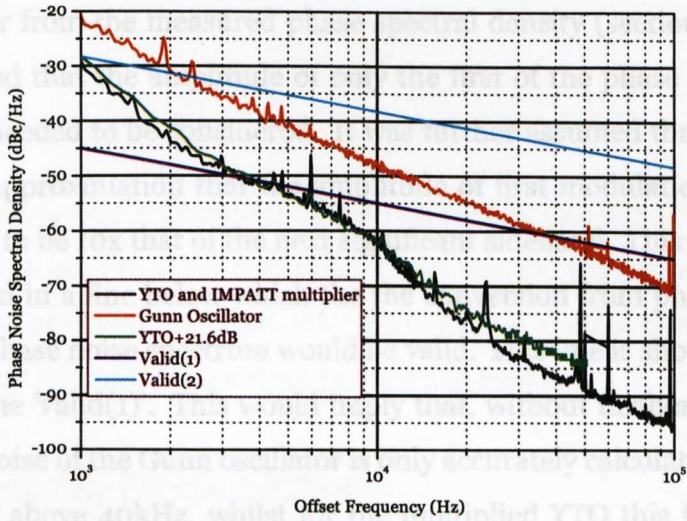
Over a similar tuning range centred at 94GHz, as opposed to the nominal 87.4GHz of the Gunn oscillator, the IMPATT multiplier shows a power variation of 1dB over a ± 600 MHz tuning range, with a peak power of 13.5dBm. The IMPATT multiplier has a higher power variation and a lower output power than the Gunn oscillator, although this power deficiency could be remedied with the use of an output amplifier.

The phase noise performances of the multiplied YTO and for comparison the phase noise of the free running Gunn oscillator, are shown in figure 8.6(b). The phase noise performance of the Gunn oscillator was obtained by 'killing' the external cavity; this may be achieved by placing an RF absorbing material

8.2. MEASURED SOURCE PERFORMANCE



(a) IMPATT power output



(b) IMPATT multiplied YTO phase noise

Figure 8.6: The performance of an IMPATT multiplier driven by a YTO.

*Comments made by Dr. G.Smith during discussion.

8.2. MEASURED SOURCE PERFORMANCE

in front of the concave mirror in the cavity. In this situation, if the phase noise of the free running Gunn oscillator sufficiently exceeds the phase noise of the multiplied source, the measured phase noise will be that of the Gunn oscillator.

The phase noise of the Gunn oscillator measured here is some 10dB worse (higher) than that shown in figure 6.9 because two different Gunn oscillators have been measured. The differences arise because different Gunn diodes are employed and the cavities will have different load Q's. The¹ oscillator of figure 6.9 is considered to have better than average performance whilst that of figure 8.6(b) is considered to be worse than average.

Figure 8.6(b) would appear to show that the multiplied YTO has a lower phase noise than the free running Gunn oscillator, however care must be taken in making this statement. In calculating the phase noise spectrum of an oscillator from the measured phase spectral density (section 6.1.1.4) it was assumed that the amplitude of only the first of the phase modulation sidebands needed to be considered. It was further assumed that for this to be a valid approximation that the amplitude of first modulation sideband would have to be 10x that of the next significant sideband. This approximation resulted in a line below which the the conversion from phase spectral density to phase noise spectrum would be valid. This line is shown in figure 8.6(b) as line 'valid(1)'. This would imply that, without further correction, the phase noise of the Gunn oscillator is only accurately calculated for offset frequencies above 40kHz, whilst for the multiplied YTO this frequency is 3kHz.

Now, the calculated phase noise of the YTO (unmultiplied) is certainly below the 'valid(1)' line (c.f. figure 8.4) if the 350 μ F capacitor is included. If

¹Comments made by Dr. G.Smith during discussions.

8.2. MEASURED SOURCE PERFORMANCE

the approximations considered above are correct then adding 21.6dB to the measured YTO phase noise will produce the effect of the ideal multiplier on the oscillator. If the approximation is correct then the ideal multiplied and the measured multiplied YTO phase noise curves will diverge below an offset of 3kHz.

Figure 8.6(b) shows this not to be the case, and therefore it may be concluded that the factor of 10 requirement was too severe. There would appear to be no appreciable divergence between the YTO curves at an offset of 1kHz. If it is assumed that the conversion is valid at 1kHz, it is found that second modulation sideband has an amplitude of half the first modulation sideband. Under this new approximation the measurement conversion would appear to be valid below line 'valid(2)'. It may now be concluded that the multiplied YTO has a lower phase noise for offsets in excess of 2kHz.

8.2.2 IMPATT and DRO

With the mechanical adjustment of the DRO set to provide a frequency of 7.833GHz, the output of the multiplier chain was indeed 94GHz, having a power output of +13.3dBm at 94GHz. The results of a phase noise measurement made at the multiplier output is shown in figure 8.7.

8.2.3 Schottky Diode Multiplier -1

The performance of the in house constructed multiplier chain was measured using the apparatus shown in figure 8.5. Variable frequency measurements were made using the YTO, whilst phase noise was measured using only DRO based oscillators.

8.2. MEASURED SOURCE PERFORMANCE

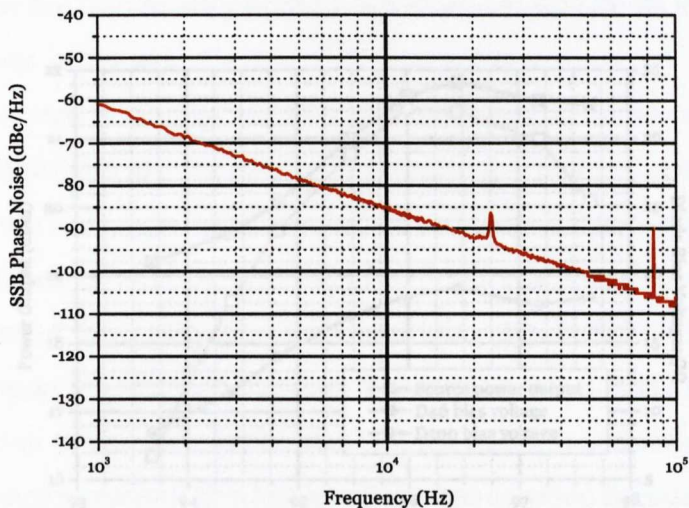
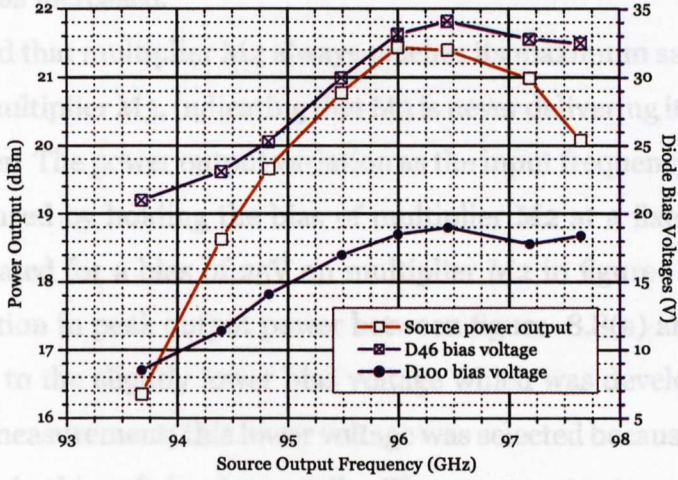


Figure 8.7: Phase noise produced by a $\times 12$ multiplier chain, realised using an IMPATT diode. The multiplier was driven with a 7.833GHz DRO, and this measurement is at 94GHz.

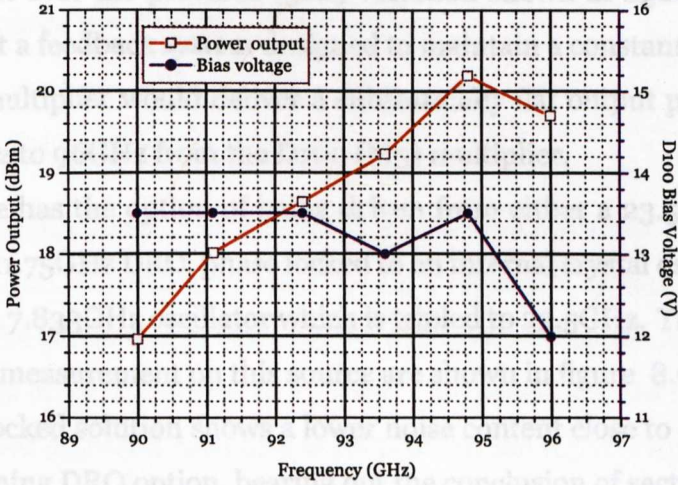
As noted, this multiplier chain allows each multiplier block to develop a bias voltage across fixed resistors. The curves of figure 8.8(a) were obtained by allowing the diode bias voltages to vary as the input frequency was varied. An initial sweep of the input frequency was made whilst monitoring the voltages developed by the multiplier blocks, the input power was adjusted so that the bias voltages developed never exceeded permitted values and the curves of figure 8.8(a) were then measured. Compared to the Gunn source, this source gives a greater power over a wider tuning range, and allowing the same power variation as the Gunn source approximately 8dB more power over the same tuning range.

It is clear however that had the multiplier chain input power been set to maximise the output power at 94GHz (maximum bias voltage), the bias voltage

8.2. MEASURED SOURCE PERFORMANCE



(a) Variable bias.



(b) Fixed bias

Figure 8.8: The power output of the first Schottky diode multiplier under conditions of fixed and variable bias on the D46 diode block.

8.2. MEASURED SOURCE PERFORMANCE

developed by the D46 module would have exceeded safe limits as the output frequency was increased.

It is observed that multiplier M2 always reaches its maximum safe bias voltage before multiplier M3, indicating that M3 is never delivering its maximum output power. The power output variation as the input frequency is changed may be reduced by holding the bias of multiplier M2 at a fixed level, this is demonstrated for a bias of 25V on multiplier M2 in figure 8.8(b). The slight reduction in peak output power between figure 8.8(a) and 8.8(b) is attributable to the slightly lower bias voltage which was developed during the second measurement; this lower voltage was selected because it was easier to maintain this safe level manually. The power output now shows less than 1dB variation in the interval 94GHz to 96GHz, which is a considerable improvement over the previous (5dB) variation shown in figure 8.8, and suggests that a feedback system designed to maintain a constant bias on the D46 (M2) multiplier would deliver a substantially flat output power in the range 92GHz to 96GHz from the D100 (M3) multiplier.

This source has the option of being driven from either a 23.5GHz source which is an 11.75GHz DRO, phase locked to an internal crystal oscillator and doubled or a 7.833GHz oscillator which is tripled to 23.5GHz. The results of phase noise measurement on this source are shown in figure 8.9.

The phase locked solution shows a lower noise content close to carrier than the free running DRO option, bearing out the conclusion of section 7.3.

Figure 8.9 also shows the noise floor of the complete phase noise measurement instrument. Comparison with the phase noise floor results for delay line discriminator at 7GHz show a consistent performance and is sufficiently below the measured source phase noise to be considered negligible.

8.2. MEASURED SOURCE PERFORMANCE

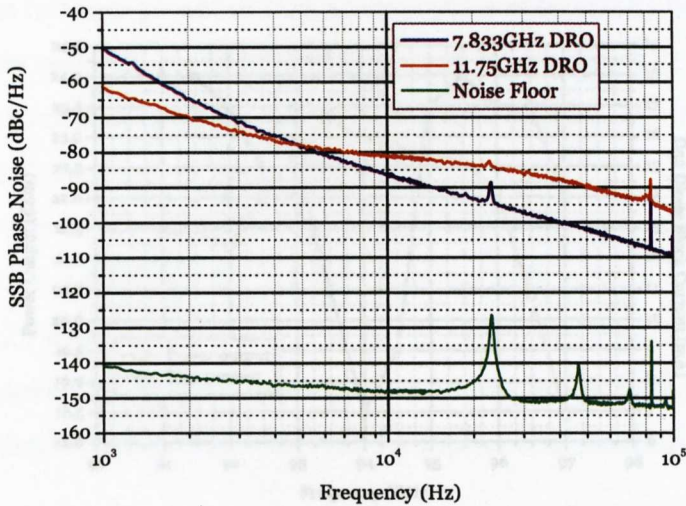
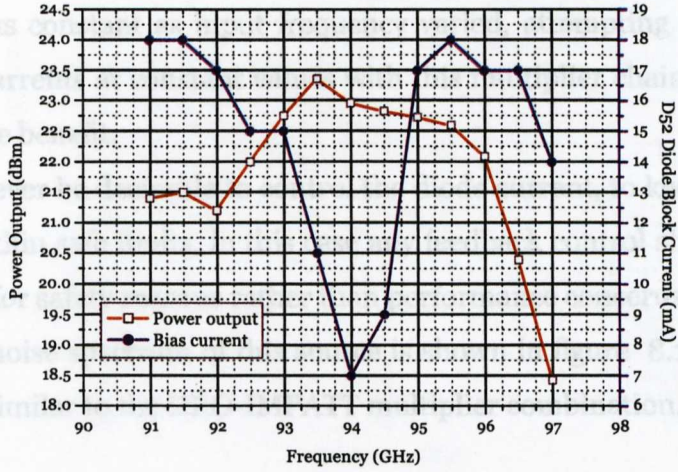


Figure 8.9: Phase noise performance of a 94GHz Sources using Schottky Diode Multiplier -1. Also shown is the noise floor of the 94GHz phase noise measurement system.

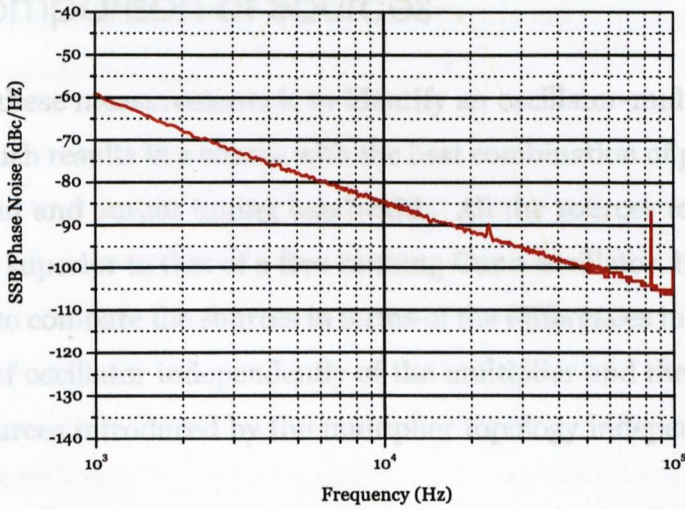
8.2.4 Schottky Diode Multiplier -2

As previously described, this multiplier chain employs fixed bias voltages applied from an external (supplied) voltage regulator system. With this multiplier, the diode stages can only be controlled by adjusting the power applied to the input of the Spacek x3 stage. The power applied to the multiplier chain was adjusted such that at no point in the input frequency range 7.5833GHz to 8.0833GHz did the current drawn by the diode multipliers exceed a safe maximum value. As in the previous Schottky diode based multiplier, it is the first diode block (the D50 block) which reaches its safe maximum condition first, the input power was adjusted to give 18mA maximum. The results of measurement are shown in figure 8.10. Whereas with the previous Schottky diode multiplier chain, there was considerable

8.2. MEASURED SOURCE PERFORMANCE



(a) Power variation



(b) Phase noise

Figure 8.10: The power output, first diode block bias voltage and phase noise of the second Schottky diode multiplier system. Phase noise was measured at 94GHz.

8.3. COMPARISON OF SOURCES

advantage in terms of power output flatness to be obtained by holding diode bias currents constant as input frequency varied, attempting to maintain the diode currents at constant values with this multiplier chain, has no RF performance benefit.

It may however be desirable to control the diode current, to keep the diode currents within safe limits, in this case any feedback control should be implemented for safety reasons rather than performance concerns.

The phase noise spectrum of this source is shown in figure 8.10(a), and is not too dissimilar to the DRO-IMPATT multiplier combination.

8.3 Comparison of Sources

The aim of these measurements is to identify an oscillator-multiplier combination which results in a source with the best combination of phase noise, power output and output tuning bandwidth. All the sources tested have a phase noise superior to that of a free running Gunn oscillator, however it is interesting to compare the sources in terms of the differences introduced by the choice of oscillator independently of the multiplier and the differences between sources introduced by the multiplier topology independent of the source.

8.3.1 The Choice of Oscillator

The comparison of sources in terms of the oscillator, only makes sense in terms of a given multiplier. Figure 8.11 shows the performance of the IMPATT multiplier for all the oscillators considered. The PMYTO, as has been

8.3. COMPARISON OF SOURCES

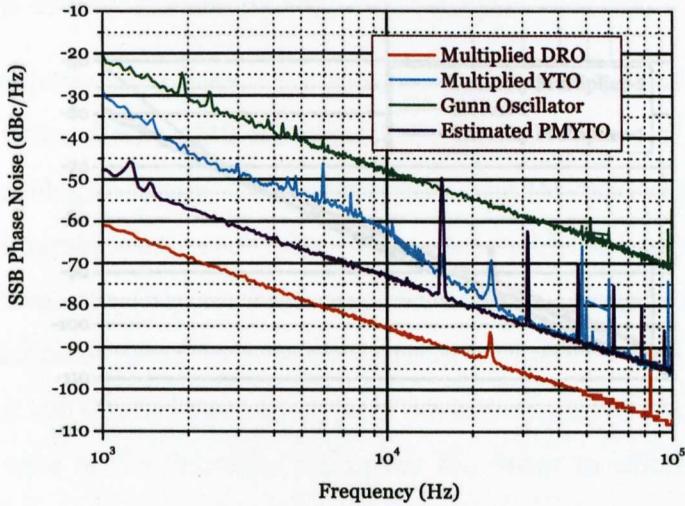


Figure 8.11: Source phase noise performance for the Elva multiplier and various oscillator options. The PMYTO is not a measured 94GHz result, see text.

consistent with obtaining the required tuning range, should be employed. In noted, produces an output frequency which is not suitable for use with any of the multipliers available. This result was estimated by adding 21.6dB to the measured 7GHz data, which makes no allowance for noise added by the multiplier components. However because this estimated curve and the YTO measured phase noise curve converge at high offset frequencies it is probably a reasonable estimate.

The phase noise curve shown for the Gunn oscillator is for the unit measured in section 8.2.1 and is the result of measuring a free running oscillator. There is now a clear trade-off between sources based on fixed frequency oscillators and sources based upon variable frequency oscillators, with fixed frequency (highest Q) oscillators producing the lowest phase noise sources. If a tunable source is desirable the lowest possible tuning sensitivity, con-

8.3. COMPARISON OF SOURCES

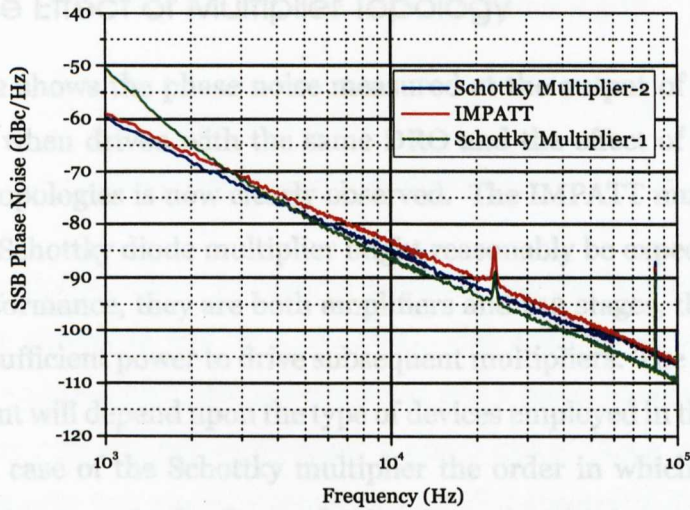


Figure 8.12: Source phase noise performance of three multipliers driven with the same DRO.

sistent with obtaining the required tuning range, should be employed. In this case even the worst performing oscillator (the YTO) shows a multiplied phase noise which betters the free running Gunn oscillator.

These results of order 5dB are better than was expected when the anticipated phase noise performance was calculated for table 8.1. The implication is that the phase noise introduced by the multiplier is very close to the theoretical $20 \log(n)$ for these multipliers, the multiplier components would appear to make a minimal contribution to the source output phase noise spectrum. Whilst this may be true for an IMPATT multiplier, it may not be true for other multiplier topologies.

8.3.2 The Effect of Multiplier Topology

Figure 8.12 shows the phase noise measured at the output of the various multipliers when driven with the same DRO and the effect of the various multiplier topologies is now clearly observed. The IMPATT multiplier and the second Schottky diode multiplier might reasonably be expected to have similar performance, they are both amplifiers and x12 stages, the amplifier delivering sufficient power to drive subsequent multipliers. The exact phase noise content will depend upon the type of devices employed in the amplifier and, in the case of the Schottky multiplier the order in which the amplifier and tripler occur in the first multiplication stage. Without this detailed knowledge it is impossible to say which source should be "quieter".

The first Schottky multiplier on the other hand has an amplifier at 23.5GHz to provide sufficient power to drive the following x4 stages and this is responsible for the increase in noise below approximately 2kHz. Thus it is concluded that away from the $1/f$ corner frequency of the devices employed in the multiplier chain, the phase noise of the amplifier is close to the theoretical $20\log(n)$ value. This is why the predicted phase noise of the PMYTO and the YTO agree with each other in figure 8.11 above approximately 30kHz with only 21.6dB added to the measured PMYTO phase noise.

Whilst the increase in phase noise at low frequencies is a real effect, it is not clear which multiplier has the lower phase noise at high offset frequencies, due to the lack of information regarding the construction of various modules employed in the construction of the multiplier. Therefore it would appear reasonable to take the discrepancy between the multipliers measured above and use this as a first estimate of the uncertainty in the measurement. It is concluded that the uncertainty in the measurement of the phase noise on a 94GHz source, using a cavity stabilised Gunn oscillator as a down conversion

source and a 7GHz delay line discriminator is of order $\pm 3\text{dB}$.

8.4 Spectrometer Performance

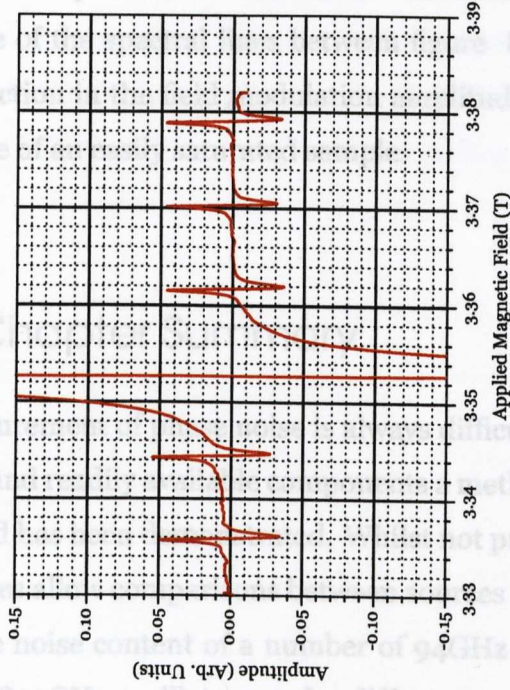
The first multiplied source to become available was the 'home made' multiplier chain driven by the 23.5GHz DRO. This source was incorporated into the St Andrews high field spectrometer and a direct comparison of the spectrometer performance using either a phase locked Gunn source or the multiplied source was made by measuring an ESR spectrum. In both cases the detector was an InSb bolometer.

The results are of measurement on a Manganese based sample are shown in figure 8.13. The spectra show an offset in magnetic field due entirely to the difference in frequency between sources, the Gunn source was locked to 94GHz using an EIP counter, whilst the DRO based source was free running at a frequency of $\sim 93.4\text{GHz}$.

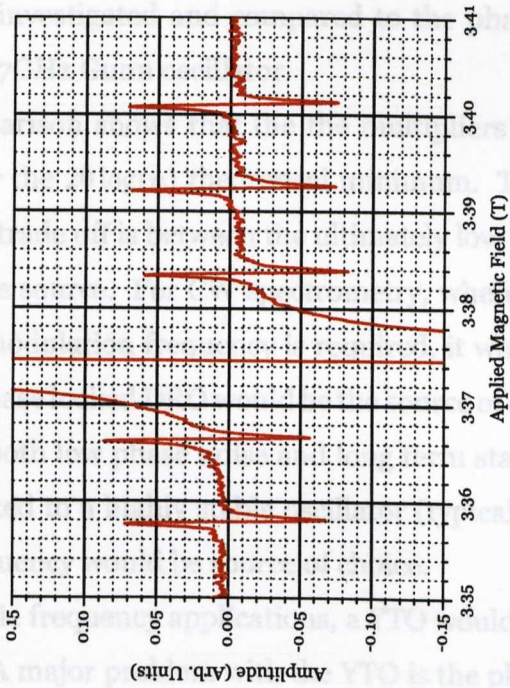
The noise levels of the two measurements are considerably different. It was noted in section 4.4 that the LO signal and the signal returned from the sample, being derived from the same source, are phase coherent. However the signal returning from the sample is delayed relative to the LO signal due to its longer path length. Thus, the spectrometer is a form of delay line discriminator and the noise at the detector output may be minimised by correct phasing of the LO and return signals. If the source has a low phase noise this minimisation, which may be performed by translating the roofing mirror in figure 4.11, is less sensitive to the mirror position and once obtained more stable, than it is using the relatively noisy Gunn oscillator.

Having obtained a low instrument noise floor, the amplitude of the field

8.4. SPECTROMETER PERFORMANCE



(a) Gunn spectrometer spectrum.



(b) DRO spectrometer spectrum.

Figure 8.13: The spectrum of a Manganese sample obtained using both a Gunn source and a DRO-multiplier source.

modulation may be reduced and this is the reason for the reduction in the amplitude of the spectral lines between figure 8.13(a) and figure 8.13(b). This reduction in the field modulation amplitude can be a great advantage in the case of an easily saturated sample.

8.5 Chapter Summary

The measurement of phase noise is always difficult. However, using simple methods and readily available components a method measuring phase noise at W-Band has been demonstrated. Whilst not providing the ultimate accuracy, it does allow comparisons between sources to be made.

The phase noise content of a number of 94GHz sources constructed using various 7.833GHz oscillators and 3 different x12 multiplier configurations has been investigated and compared to the phase noise content of a free running 87GHz Gunn oscillator.

The comparison shows that the the multipliers investigated add minimal noise over the $20 \log(n)$ theoretical minimum. This indicates that the performance trade off is between the ultimately low phase noise and the ability to tune the source. For CW spectrometry, where minimum phase noise at the field modulation frequency is required, it would appear that a DRO, or better a phase locked DRO would be the source of choice. For Pulsed systems in which both low phase noise and long term stability are required, a DRO phase locked to a highly stable oscillator (typically a crystal oscillator) at a lower frequency would be source of choice.

For variable frequency applications, a YTO would appear to be an attractive solution. A major problem with the YTO is the phase noise, introduced due

8.5. CHAPTER SUMMARY

to their extreme tuning sensitivity, by the main coil driver circuit. This has been clearly observed. A solution to this problem has been demonstrated using a PMYTO. Post multiplication the PMYTO offers a slightly worse phase noise than a DRO with a tuning range exceeding that of a Gunn oscillator.

CHAPTER 9

HiPER -a 1kW 1ns pulsed ESR Spectrometer

In chapter 2, the properties of an ESR spectrum were briefly considered in terms of a CW spectrum and an outline of some of the main features of a CW ESR spectrum was given.

It was pointed out that under certain circumstances, for example when a sample becomes saturated, or where the spectral lines are too close together to be separated, one broad line would be detected, and therefore only limited spectral information would be obtained.

These problems have been ameliorated in the context of Nuclear Magnetic Resonance (NMR) spectroscopy, where excited states have relatively long relaxation times, by the use of pulse measurements. Although pulse techniques are becoming widely used in the ESR experiments, the short relaxation times mean that the full potential of pulsed ESR measurements has

not been realised; the difficulty arising due to the high powers and short duration required by the pulses.

HiPER is a large collaborative project between several establishments to solve the problems of implementing very high power, very short pulses in a W-Band (94GHz) ESR system. This chapter outlines the need for pulse experiments, obtains the necessary pulse characteristics, describes some of the problems encountered with such pulses and thus explains why the pulse generating system of chapter 10 and the detector of chapter 11 were conceived.

9.1 A Comparison of Pulse and CW Techniques

A CW experiment (NMR or ESR) is performed by bringing each spectral line into resonance in turn. It was pointed out in section 2.4 that the ability of an instrument to resolve two spectral lines increases with applied field, and therefore frequency. However, it is not always possible to resolve individual spectral lines even at high frequencies, and all that is recorded is a single broad line. There are two generic types of line broadening, and detailed discussions of these may be found in [34], [32] and [33]. They may be summarised as follows:

Homogeneous broadening. In this case, the broadened line arrives as a result of transitions between two ill defined (broad) excited states, and is a manifestation of very short relaxation times. The line shape, being determined by relaxation times, is therefore usually Lorentzian.

Inhomogeneous Broadening. In this case the broad spectral line consists of a large number of narrow, individually homogeneously broadened lines,

9.1. A COMPARISON OF PULSE AND CW TECHNIQUES

each having a slightly different Larmor frequency. The line arises when the net magnetisation at adjacent paramagnetic sites is slightly different. This may be due to inhomogeneities in the applied B_z field over the sample volume, which should be minimised by careful magnet design, but may also arise due to unresolved fine and hyperfine structure due to interaction with the nuclear dipole moment. Such lines are usually Gaussian.

With a suitably selected fixed external field (B_z), a sufficiently short RF pulse may excite the whole ESR spectrum. By performing a Fourier analysis of the relaxation signal, the ESR spectrum of the sample may be obtained and is usually the CW spectrum. The spectrum has been obtained (in principle) as the result of a 'single shot' measurement without the need for time consuming magnetic field sweeping. This is a free induction decay (FID) measurement and is the simplest pulsed ESR experiment which can be performed. It is the direct analog of the way in which NMR spectra are obtained and is unable to resolve broadened lines.

The individual spectral lines of an inhomogeneously broadened line may be resolved using a variety of techniques. Details of hyperfine structure may be resolved in a double resonance technique known as *Electron-Nuclear-Double-Resonance* (ENDOR) which uses an NMR signal to modulate the ESR signal via the hyperfine interaction [33]. Similar information may be obtained from spin-echo measurements, in which a short pulse excites the ESR spectrum and some time later a second (longer) pulse is used to produce the spin-echo in a process known as 'refocusing' [29]. Measuring the spectrum of the echo for various time delays between the two pulses allows the hyperfine spectrum to be resolved [33], [34].

The ability to obtain information from a pulse measurement therefore relies on the ability to excite the entire broadened line, and measure the amplitude

9.2. PULSE REQUIREMENTS

of the decaying relaxation signal whilst it is above the spectrometer noise floor. In liquid state NMR measurements, where line widths are narrow (a few Hz to kHz) and relaxation time constants are long (μs to seconds) relatively long (μs) pulses may be employed. However, in an ESR system, the relaxation times are short (of order ns to μs) and line widths are wide (100's of MHz to GHz) which requires the use of short pulses (ns) [183]. It is the generation of the required ns pulses and the effects the propagation of these pulses has on a spectrometer system which represent the challenge of HiPER project.

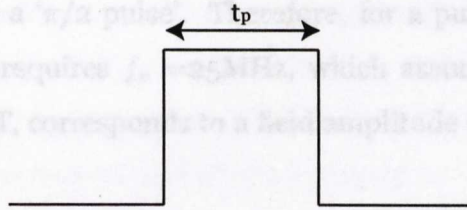
9.2 Pulse Requirements

The pulse used to excite the spins contained within the broadened line, must satisfy a number of conditions. A rectangular pulse envelope formed in the time domain has a sinc ($= \sin(x)/x$) profile in the frequency domain, the central lobe of which has a half power width which is inversely proportional to the original pulse width as shown in figure 9.1. Thus, to excite the spins in a line of width 50MHz ($\pm 25\text{MHz}$ of the line centre) requires a pulse width of 10ns. For a line centred at 10GHz, this pulse will excite spins in the range 9.975GHz to 10.025GHz.

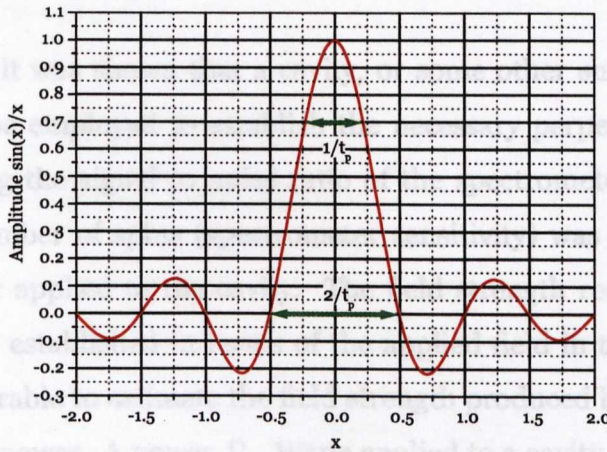
Having obtained the required pulse width, it is now necessary to determine the required pulse amplitude. The probability of forcing a spin flip with an oscillating field (B_x) perpendicular to the large main field (B_z) was shown to be (see equation 2.38)

$$|b(t)|^2 = \frac{1}{2} [1 - \cos \omega_x t] \quad (9.1)$$

9.2. PULSE REQUIREMENTS



(a) Rectangular pulse.



(b) Fourier dual of a rectangular pulse.

Figure 9.1: A rectangular pulse envelope in the time domain produces a sinc envelope in the frequency domain. The pulse width t_p is directly related to the bandwidth of the excitation produced in the frequency domain as shown.

To obtain zero B_z magnetisation (i.e. a 50% population inversion) after a pulse of duration t_p requires

$$\omega_x t_p = 2\pi f_x t_p = \frac{\pi}{2} \quad (9.2)$$

9.3. POWER REQUIREMENTS

which is known as a ' $\pi/2$ pulse'. Therefore, for a pulse of length 10ns to induce a spin flip requires $f_x = 25\text{MHz}$, which assuming a gyromagnetic ratio of 28MHz/mT , corresponds to a field amplitude (B_x) of $\sim 0.89 \times 10^{-3}\text{T}$ or 8.9G.

9.3 Power Requirements

In chapter 4 it was shown that a cavity, or some other suitable resonant circuit, may be employed to establish the necessary perpendicular fields. By considering the signal to noise ratio of the spectrometer, a minimum detectable number of spins (spectrometer sensitivity) was established for a given power applied to the cavity. The field strength required to flip a spin has been established in terms of the applied field in the above. It is therefore desirable to estimate the field strength produced by a cavity for a given applied power. A power P_{av} Watts applied to a cavity will give rise to a maximum field B Tesla in the cavity given by [184]

$$B = \sqrt{k \frac{\mu_o Q_L P_{av}}{V_c \omega}} \quad (9.3)$$

in which

- P_{av} is the power applied to the cavity
- B is the peak magnetic field within the cavity
- V_c is the cavity volume
- ω is the frequency of the signal
- μ_o is the permeability of free space
- Q_L is the cavity loaded Q
- k is a factor depending upon the cavity shape.

9.4. CAVITY REQUIREMENTS

As an example, consider a 10mW excitation applied to the cavity of section 3.8. For a rectangular TE₁₀₂ mode cavity $k = 2$ [184], the cavity has a volume of $9 \times 10^{-6} \text{m}^3$, a Q of 5000 and is resonant at 10GHz. Therefore the 10mW excitation produces a field of order $7.45 \mu\text{T}$.

Then, the same cavity used as the cavity in a 10GHz pulsed spectrometer would require an applied peak power of $\sim 35\text{W}$ for a 10ns $\pi/2$ pulse and 3500W for a 1ns $\pi/2$ pulse.

9.4 Cavity Requirements

The volume and Q of the cavity are now of vital importance. The power required to obtain a given field depends not only on the power applied, but according to equation 9.3

$$B \propto \sqrt{k \frac{QL}{V_c} P_{av}} \quad (9.4)$$

Reducing the cavity volume is therefore advantageous. When equation 9.3 is compared to the expressions obtained by Poole [32], the quantity k is found to be the parameter D introduced into equation 3.68. Without changing the resonant frequency, the best that can be done is to change from a rectangular cavity to a cylindrical or spherical cavity.

Whilst the cylindrical cavity has a slightly increased volume compared to the rectangular cavity, the parameter $D (=k)$ increases more rapidly and therefore a cylindrical cavity will give a better power to field conversion on volume grounds. It will have a higher Q [98] and will therefore produce a better power-magnetic field conversion than the rectangular cavity.

Note that the sphere which will result in a reduced cavity volume for a given resonant frequency, is expected to have approximately the same value of

9.4. CAVITY REQUIREMENTS

D as the cylinder and which has a higher *Q* than either the rectangular or cylindrical cavities [98] might be expected to produce the best power to magnetic field conversion of any of the cavities considered.

However, there are two problems with a pulse system employing a high cavity *Q*: excitation bandwidth and system dead time, both of which are discussed below.

9.4.1 Excitation Bandwidth

If f_o is the centre frequency of the cavity, and Δf is the full width half power (FWHP) bandwidth of the resonator, the *Q* of the resonator is defined to be

$$Q = \frac{f_o}{\Delta f} \quad (9.5)$$

At 10GHz, a *Q* of 5000 would give a FWHP bandwidth of 2MHz, which means that the full excitation bandwidth of the 1ns (500MHz) and 10ns (50MHz) pulses discussed above could not be employed. To use the full excitation bandwidths would require cavity *Q*s of 20 for the 1ns pulse and 200 for the 10ns pulse.

If these revised *Q*s are employed, still using a TE₁₀₂ cavity, the powers needed to excite the spins with a $\pi/2$ pulse at 10GHz are now 890W and 890kW for the 10ns and 1ns pulses respectively. This latter power will almost certainly cause electrical breakdown in the waveguide, and whilst 10GHz systems employing long (10ns) pulses are viable, 10GHz spectrometers employing very short (1ns) pulse 10GHz systems do not appear to be viable.

9.4.2 Cavity Ring Down

It was shown in chapter 3 that provided $1/4Q^2 \ll 1$, the response of a resonator to an impulse may be described (equation 3.11) by

$$i(t) = \frac{V}{\omega_o L} e^{-(\omega_o/2Q)t} \sin \omega_o t \quad (9.6)$$

Where $i(t)$ is the current flowing in the cavity, and V is the amplitude of the voltage excitation. Then power available from the cavity is

$$P_a(t) = \frac{P_{in}}{Q^2} e^{-(\omega_o/Q)t} \sin^2 \omega_o t \quad (9.7)$$

The envelope of this function i.e. the exponential term, determines the length of time for which it is necessary to wait before a measurement can be made; this phenomenon is often referred to as 'cavity ring down'.

The importance of this delay may be seen as follows. Consider a measurement at 10GHz, where the sample is contained in a cavity with a Q of 200, and in which the $\pi/2$ pulse has an amplitude of 890W. Using equation 9.7, immediately after the $\pi/2$ pulse is removed the cavity response envelope has an amplitude of 22.5mW. This must decay to a level which will not obscure the signal under investigation, and must therefore decay to a level close to the noise floor of the detector. In section 3.8.3 it was shown that a noise floor of 10^{-17}WHz^{-1} could be expected¹. In a bandwidth of 50MHz, the detector noise floor will be of order $5 \times 10^{-7} \text{mW}$ and therefore (using equation 9.7) a 56ns delay will be required after the $\pi/2$ pulse to ensure that a reliable spectrum can be measured.

The problem now encountered is that whilst the cavity response has been

¹This assumed field modulation was being employed with a homodyne detector. In a pulse experiment no field modulation is employed, however a heterodyne demodulator will produce a similar noise floor. This is discussed in chapter 11

decaying, so has the desired spectral information, and therefore many averages of repeated measurements may be required to obtain a useful spectrum.

9.5 A 94GHz Pulse Spectrometer

The problems of producing a 10GHz based system are now clear. Any attempt to produce a 1ns pulse requires multi kW power levels, which arises due to the required cavity Q and cavity volume.

Increasing frequency certainly helps. A suitable rectangular cavity at 94GHz has a volume of $5.06 \times 10^{-9} \text{m}^3$, and the excitation bandwidth of a 1ns pulse suggests that a cavity Q of 188 will be required for satisfactory excitation of the spin system. Equation 9.2 gives an oscillating field amplitude of 8.93mT to be required for a 1ns $\pi/2$ pulse, which using equation 9.3 is obtained for a peak pulse power of 2kW. In a 500MHz bandwidth, the detector noise floor is $5 \times 10^{-10} \text{mW}$ and the ring down time is approximately 4ns.

These figures represent a considerable improvement over the 10GHz figures, however considerable improvement is required to satisfy the goals of the Hiper project which require a 1kW, 1ns $\pi/2$ pulse with a ring down time of 1ns.

Assuming a peak pulse power of 1kW, a cavity Q of approximately 30 will be required if a ring down time of 1ns is to be achieved. This in turn implies that the cavity volume will have to be reduced by a factor of 6 to make allowance for the Q reduction, if the required spin flip is to be produced.

The cavities so far considered have been rectangular metallic boxes. If a cylindrical cavity is considered, (see table 4.1) the volume will increase by a factor of approximately 5; the cylindrical cavity produces an improvement

9.5. A 94GHZ PULSE SPECTROMETER

because the factor $k (=D)$ increases by a factor of 10 which leaves the power-field conversion factor unchanged; any increase in this conversion factor is due to the higher Q of the cylindrical cavity.

However, if the cavity is constructed from a high dielectric constant (ϵ_r) material, the volume may be reduced by a factor of $\epsilon_r^{3/2}$. Using Silicon (for which $\epsilon_r=11.9$), would reduce the cavity volume by a factor of 41. Such a cavity would have a volume of $1.23 \times 10^{-10} \text{m}^3$, which, using a Q of 30, would result in a peak power requirement of 160W for a 1ns $\pi/2$ pulse at 94GHz.

Such cavities have been constructed using non-radiative dielectric resonators (NRDRs) [101]. Here a dielectric cylinder is held between two conductive plates which are cut-off at the cavity resonant frequency. The plates containing the dielectric cylinder are then placed at the end of a length of waveguide. Practical results from these cavities at 190GHz [102] indicate that based on Quartz ($\epsilon_r=5.6$), cavity conversion factors (applied power to magnetic field) of $49\text{G}/\sqrt{\text{W}}$ ($4.9\text{mT}/\sqrt{\text{W}}$) are attainable. The figures given in [102] allow a check of the validity of the approximations made to obtain the power levels required by a 94GHz system.

The starting point for the estimation is to estimate the volume of a rectangular metallic box; for 190GHz this is of order $6 \times 10^{-10} \text{m}^3$. A metallic cavity is estimated to have a Q of 700, which using equation 9.3 gives a conversion factor of $1.2 \times 10^5 \text{W}/\text{T}^2$. This is now scaled down by $\epsilon_r^{3/2}$ (13.25), and up by a factor of 4 to allow for the reduction in Q encountered in going from a metallic to NRDR structure. This gives a conversion factor of $3.53 \times 10^4 \text{W}/\text{T}^2$ or $58\text{G}/\sqrt{\text{W}}$, which is in remarkable agreement considering the approximations made for the cavity and Q; it indicates that the estimates made are of the correct order of magnitude.

9.6 Spectrometer Dead Time

Because the transients introduced by the excitation pulse must decay before a measurement can be made, the instrument is said to be 'dead', and this enforced delay after the end of the excitation pulse is known as the spectrometer dead time.

The major contributions to dead time are cavity ring down, standing waves in the spectrometer and detector recovery from the excitation pulse.

Cavity ring down was discussed in section 9.4.2, and it has been shown that this can only be controlled by manipulating the cavity Q. To obtain a 1ns ring down a loaded cavity Q of 30 is required. This low cavity Q has consequences for the rest of the spectrometer.

9.6.1 The Effect of Low Cavity Q

Whilst a low Q cavity could be constructed by using a lossy material for the cavity, such a structure would be difficult to reproduce. Rather than try and construct a low Q cavity, the loaded Q may be controlled using the coupling coefficient between the cavity and its external circuit. Assuming a reflection cavity, using equations 3.32 3.36 and 3.37 we have

$$\beta = \frac{Q_o}{Q_L} - 1 \quad (9.8)$$

The Q of 30 required is the loaded cavity Q, and a typical NRDR constructed of Silicon might be expected to have an un-loaded Q of 4000, the exact value depending upon the NRDR geometry and the conductivity of the supporting plates, which suggests that we require a β of 65, i.e. the cavity must be over coupled. Then equation 3.38, assuming resonance, gives $S_{11}=0.97$, and

9.6. SPECTROMETER DEAD TIME

therefore when a 1kW pulse is applied to the cavity, 940W will be reflected. This reflected power will be divided between the detector input and the source output. The circulator employed to couple power into the resonator will offer some protection to the source; assuming 20dB isolation between the circulator common port approximately 10W will arrive at the source output, which may be controlled with an isolator on the source output. More importantly approximately 930W will be delivered to the detector input, which unless considerable care is taken will destroy the detector.

9.6.2 Receiver Requirements

An induction mode spectrometer, be it implemented using degenerate cavity modes or polarisation coding, with careful adjustment is able to offer 30dB to 60dB isolation and will thus reduce the power applied to the detector input to safe levels. However, even with 60dB isolation this will result in ~ 0 dBm being applied to the detector input which will cause the detector to ring in its own right and it is likely that the detector will saturate. If the spectrometer is to be usable within 1ns of the end of the applied pulse, the detector must recover from this input pulse inside 1ns.

In discussing Bolometric and homodyne detectors in chapter 3, it was pointed out that whilst InSb detectors are available which will respond to ns pulses, they show a considerable reduction in sensitivity compared to those employed in many homodyne systems CW spectrometers.

The wide bandwidth required to process the pulse information makes a Heterodyne detector very attractive, and such a detector is discussed in detail in chapter 11.

The wide bandwidth nature of the pulse signals and the necessity of avoiding

9.7. CHAPTER SUMMARY

mixer $1/f$ noise, forces the use of a relatively high intermediate frequency (IF). The necessary amplifiers with suitable bandwidths and noise figures are available, however not only must the mixer recover from saturation, the complete post mixer signal processing system must similarly recover.

9.6.3 Standing waves

Any impedance mismatch in the system will result in a reflection, and all elements in the system are potential sources of mismatch. Once a reflection has occurred, the reflected signal may itself be reflected by other spectrometer components forming standing waves and this way the spectrometer optics may ring in their own right.

As with all other transient responses, standing wave effects with the spectrometer decay in under 1ns. Controlling these standing waves is a major challenge within the HiPER project, and will require high quality quasi optical components.

9.7 Chapter Summary

This chapter has described parameters desirable for an ESR spectrometer capable of recovering the information required to perform an FID spectral measurement.

It has been shown that it is possible to design a 94GHz system, which when driven with 1kW will produce the required $\pi/2$ pulse, and it has been suggested that a heterodyne detector will be required to demodulate the spectrum. The remainder of this thesis describes the design, construction and

9.7. CHAPTER SUMMARY

testing of these key components.

In parallel with this work, colleagues have been investigating the problems of protecting the detector, obtaining 1kW at 94GHz, and preventing the spectrometer ringing [185].

CHAPTER 10

Pulsed Sources

The need for pulsed sources has been described in chapter 9. In this chapter, a new pulse modulator is described which is able to generate 110ps Gaussian and 1ns 200mW (+23dBm) rectangular pulses suitable for amplification to 1kW as required by the HiPER project.

The method developed is capable of generating sub nanosecond pulses by controlling the modulation port of a bi-phase modulator and using the non-linearity of the multiplier chain. This technique is shown to produce pulses with rise and fall times of order 76ps, thus producing ‘nearly’ rectangular pulses of 250ps, and Gaussian pulses of 157ps at the FWHP point, all having full output power. Moreover, the extinction ratio of the new pulsed source is infinite, and is able to produce pulses at repetition rates solely determined by the pulse generator used to control the pulsed source.

In comparison, using the fastest available PIN switches as On-Off Keying (OOK) modulators, by considering the switch rise time, it is expected that

10.1. OOK MODULATION

full amplitude non rectangular pulses of order 2nS at the full width half power (FWHP) point with an extinction of 60dB, should be viable.

10.1 Pulse Generation by On-Off Keying

OOK may be regarded as a 100% amplitude modulation of a carrier. Perhaps the most obvious approach to the problem is to directly generate (using a Gunn or IMPATT oscillator) the required carrier frequency and simply switch the diode power supply. Using an IMPATT diode, a 100ns pulse with a 5W output power has been obtained [186]. However, such oscillators are undesirable due to their previously noted phase noise problems.

Alternatively, the carrier may be turned on and off (gated) by employing a suitable switching element at the source output; this is the simplest method of pulse generation, and is shown figure 10.1. For the purposes of discussion,

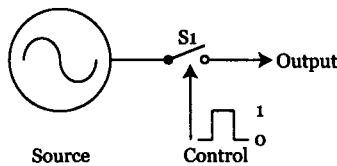


Figure 10.1: OOK of a carrier using an output switch

a switch in the *on* state will be regarded as being transmissive (i.e. closed), whilst a switch in the *off* state (i.e. open) will be regarded as being in an attenuating state. Key parameters are the time for transition between the on and off states (rise and fall times), the ultimate attenuation (isolation) in the off state, and the insertion loss of the switch.

10.1. OOK MODULATION

Mechanical solutions, whilst available, are slow; typical figures for a W-band waveguide switch ¹ are switching times of order 20ms, with isolations (on-off power ratios) of 30dB.

Electronic switches based upon PIN diodes are well known. However, as frequency increases, the power handling capability, bandwidth and isolation of simple PIN switches decreases. In waveguide, one solution is to employ multiple diodes [187] which in its logical conclusion results in a 'window' of PIN diodes (reminiscent of a grid array multiplier) which restores the power handling capability, and results in isolations of in excess of 20dB, insertion losses of order 0.5dB and switching times of 60ns or less over a frequency range of 26 to 40GHz (ka Band) [188].

Rather faster switches may be produced in waveguide in a finline [189] construction. By placing the PIN diode(s) in the E-Field plane of the waveguide, with multiple diodes extending in the direction of propagation, depending upon the number and type of diodes employed, such constructions are able to offer power handling of up to 10W with 75dB isolation and switching times of order 35ns at ka Band, or switching times of 0.6ns and 20dB isolation over a frequency range of 50 to 75GHz (V Band) [190].

10.1.1 OOK Pulse Properties.

A commercially available fast PIN switch, type FPS-SPST-10/94/2/1, was obtained from ELVA-1. This switch is advertised as having a maximum insertion loss of <2dB, a rise time of <5nS and an isolation of 30dB at W Band(75 to 110GHz); the actual switch obtained was selected by the manu-

¹Flann Microwave W-Band waveguide switch part number 27334. Data available at www.flann.com -checked 25 July 2005

10.1. OOK MODULATION

facturer to have a rise time of 1ns.

The switch was tested using the previously described IMPATT multiplier, with an input frequency of 7.8333GHz obtained from a YTO, to give the required 94GHz drive. The 94GHz source was connected as shown in figure 10.2. The required control pulses were obtained from an Agilent PARBERT

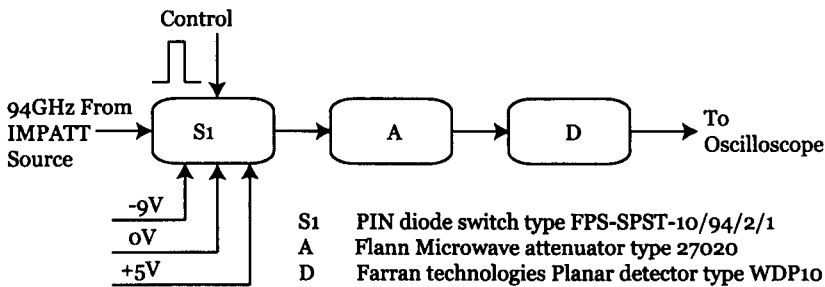


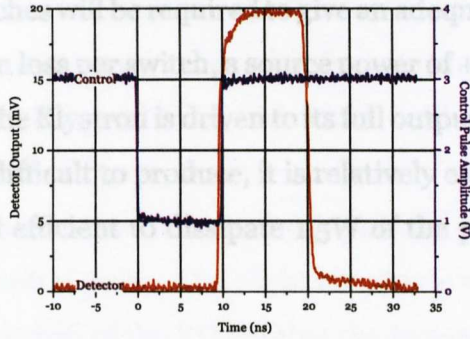
Figure 10.2: Method of PIN switch testing.

generator, which is capable of generating sub ns pulses, and the pulse envelope produced by the detector was measured using a Lecroy 'Wavemaster' 8620 6GHz oscilloscope. The attenuator was adjusted to produce a known safe power for the detector.

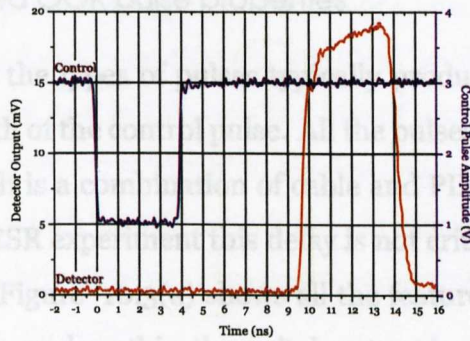
The insertion loss and isolation of the switch were measured by setting the control pulse to be permanently high (switch closed) or a permanently low (switch open) state as required, and were found to be 2.1dB and 32.3dB respectively. The slightly higher than expected insertion loss may be due to the waveguide extensions with which the switch was supplied.

Here we encounter the first disadvantage of PIN switches. To obtain a final peak pulse power of 1kW (60dBm), the basic source is used to drive a Klystron amplifier with a gain of 33dB. A single switch will therefore only reduce the Klystron output power to 27dBm, and therefore at least two, and

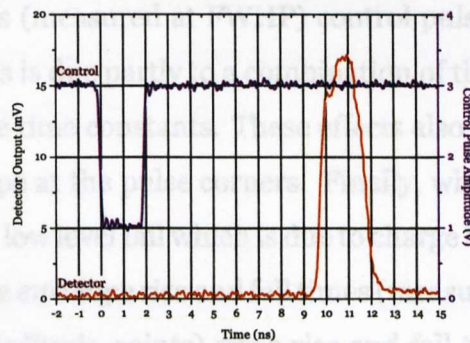
10.1. OOK MODULATION



(a) PIN diode 10ns pulse.



(b) PIN diode 3.9ns pulse



(c) PIN diode 2ns pulse

Figure 10.3: The pulse envelopes of a 94GHz carrier produced using a PIN switch.

10.1. OOK MODULATION

probably three switches will be required to give an adequate overall isolation. With a 2dB insertion loss per switch, a source power of +33dBm (2W) will be required to ensure the Klystron is driven to its full output power. Whilst such a drive level is not difficult to produce, it is relatively expensive to generate; it is not considered efficient to dissipate 1.5W of the power applied to the switch as heat.

10.1.1.1 Measured OOK pulse properties

Figure 10.3 shows the types of pulses typically produced. The pulses are denoted by the width of the control pulse. All the pulses show a propagation delay of 10ns, which is a combination of cable and PIN driver propagation times; in a pulsed ESR experiment this delay is not critical providing that it remains constant. Figure 10.3(a) shows all the features of a typical pulse; even for a long pulse such as this, the switch output is not rectangular.

Two distortions are evident. The pulse is stretched, off screen measurement shows that the 10ns (measured at FWHP) control pulse produces a 10.5ns pulse at 94GHz; this is due partly to a combination of the finite driver bandwidth and the diode time constants. These effects also lead to the rounding of the pulse envelope at the pulse corners. Finally, when switching off, the pulse shows a slow, low level tail which is due to charge storage in the diodes. Consideration of the envelope rise and fall times (measured between the 10% and 90% of full amplitude points) gives rise and fall times of 1ns for both the 10ns pulse and the 3.9ns pulses, which might suggest that 2ns full power pulses should be attainable. The leading edge distortion prevents this.

Figure 10.3(a) shows that the pulse leading edge has two components. The first is a fast transition from the off state to a point which is within 7mV of the

final detector output level which is outside the 90% rise time measurement point. Beyond this, pulse requires of order 5ns to achieve complete turn on, and thus the shortest full amplitude pulse which can be produced should be of order 5ns. The pulse of figure 10.3(b) was obtained after some experimentation, and shows the shortest full amplitude pulse to have a 4.4ns envelope width for a 3.9ns control pulse. The slight amplitude reduction here is due entirely to frequency drift of the YTO during the measurement.

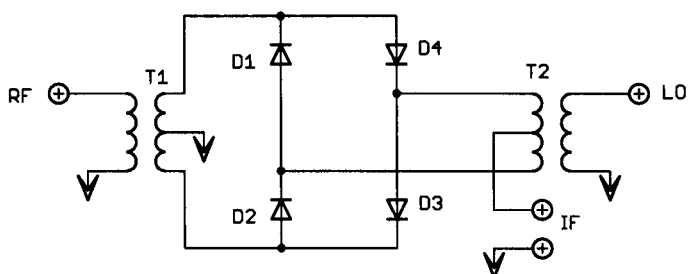
The effect of applying a 2ns control pulse to the system is shown in figure 10.3(c); the output pulse envelope has a width of 2.1ns, and the reduction in amplitude is self evident. Note that the YTO had been reset to 7.8333GHz for this measurement, and in this case the loss of peak power is due to the leading edge distortion. The 'glitch' in the leading edge, shown clearly in figure 10.3(c) and which may just be visible in figure 10.3(b), is thought to be due to the slightly different charge storage properties of the two PIN diodes employed in the switch.

The PIN switch certainly generates usable pulses. However, the insertion loss and finite isolation are potentially problematic, and it would appear not to be possible to obtain sub ns pulses from them. An alternative method of pulse generation was therefore sought.

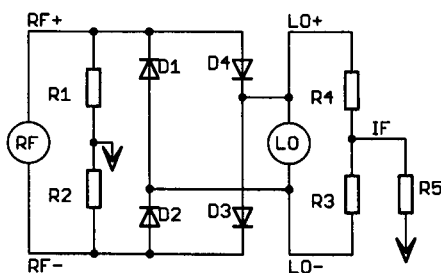
10.2 Pulse Generation Using Diode Ring Mixers

The circuit diagram of a diode ring mixer (also known as a double balanced mixer or DBM) is shown in figure 10.4(a). T1 provides anti-phase signals at the junctions of D1-D4 and D2-D3 from the RF port, and similarly, T2 provides anti-phase signals to the junctions of D1-D2 and D3-D4. If T2 is

10.2. THE USE OF DIODE RING MIXERS



(a) Physical circuit of a DBM



(b) Simulation circuit of a DBM

Figure 10.4: Representations of a diode ring mixer.

perfectly balanced, there can be no LO frequency current flowing in the IF port, the only current which flows in the IF port is the result of multiplying the RF and LO currents in the diodes.

The multiplication action of the DBM may be simulated by using the circuit of figure 10.4(b), and performing a non-linear simulation of this circuit. The non-linear simulation was performed using a SPICE ² derivative.

In SPICE, voltage sources provide anti-phase signals at their terminals, which allows a simple emulation of transformer action, whilst R1 and R2

²The simulator employed was LTSPICE, which may be down loaded from www.Linear.com -checked 28 July 2005

10.2. THE USE OF DIODE RING MIXERS

provide the required loads for the RF source. The load required by the LO source is provided by R3, R4 and R5, in addition these resistors provide the summing action required to obtain the IF voltages. Node labels have been added to figure 10.4(b), and for the purposes of demonstration all diodes are 1N4148 types, all resistors are $1k\Omega$ and the simulation is performed at 1MHz.

The IF waveform shown in figure 10.5 was obtained by applying a rising

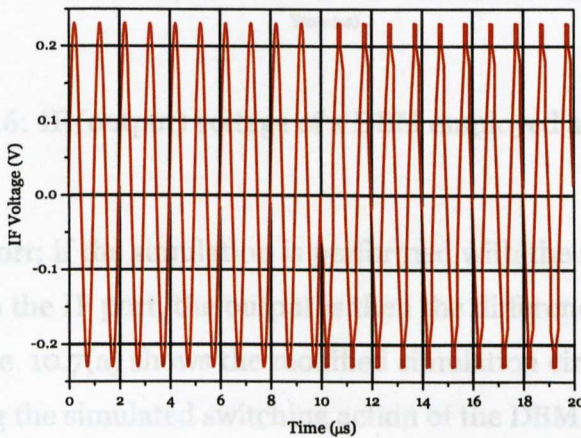


Figure 10.5: IF (output) voltage of a DBM employed as a biphase modulator.

edge between levels of $-1V$ and $+1V$ to the LO port of the simulation circuit $10\mu s$ into the simulation, with a sinewave of peak amplitude $1V$ applied to the RF port. The 180° phase change at $10\mu s$ is clearly visible, which demonstrates the multiplier action of the DBM, and its use as a biphase modulator. Clearly therefore, applying a rising $0V$ to $+1V$ at the LO port should result in a gated waveform at the LO port, and this is seen in figure 10.6. These simulations demonstrate the multiplicative action of the DBM only because the circuit as simulated responds to DC levels. In reality the only DC coupled

10.2. THE USE OF DIODE RING MIXERS

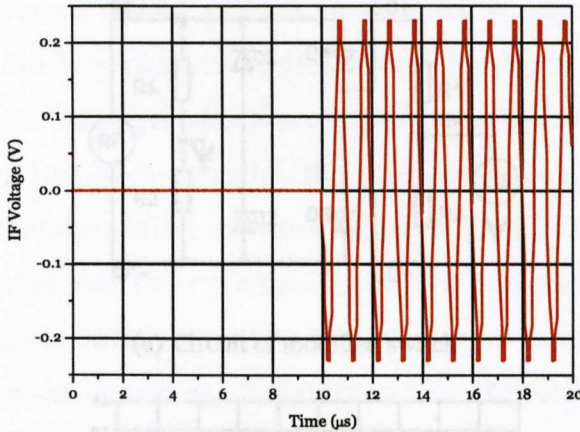


Figure 10.6: IF (output) voltage of a DBM employed as a switch.

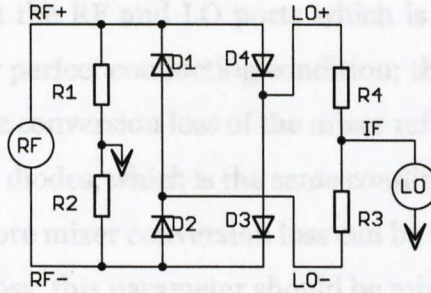
port is the IF port; if the simulation is performed with the switching waveform applied to the IF port, the output is then the difference between LO+ and LO-. Figure 10.7(a) shows the modified simulation circuit, with figure 10.7(b) showing the simulated switching action of the DBM.

Figure 10.7: The circuit diagram and simulated switch response of a DBM based switch, modified to show the effect of applying the DC

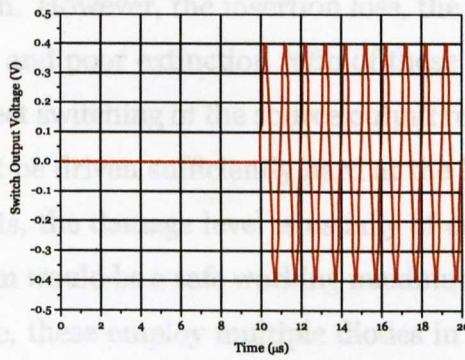
10.2.1 Selecting a DBM for Switch Applications.

The above simulations of the DBM based switch indicate that a good switching action should be available. With the switch open (the control voltage is 'low'), there would appear to be perfect isolation. Indeed, because the diode ring (for simulation purposes) consists of identical diodes and the transformers have been simulated as perfectly centre tapped, there can be no output in this condition because the DBM has the form of a balanced AC bridge. In reality, the diodes are not identical and the transformers are not perfectly centre tapped and therefore there is a finite leakage between the LO and RF

10.2. THE USE OF DIODE RING MIXERS



(a) Circuit of modified switch



(b) Output of modified switch

Figure 10.7: The circuit diagram and simulated switch response of a DBM based switch, modified to show the effect of applying the DC switch control to the DBM LO port.

ports. When used as mixers, real DBMs show an LO-RF isolation in excess of 20dB, which reflects the isolation of the switch in the off condition, and in selecting a DBM for use as a switch this parameter should be maximised. The insertion loss when the switch is closed (the control voltage is 'high') reflects the losses associated with the transformer construction and diode losses. When used as a mixer, the conversion loss of the DBM is specified between the RF and IF ports. When used as a switch as described above,

10.2. THE USE OF DIODE RING MIXERS

it is the loss between the RF and LO ports which is important, with two diodes in a nominally perfect conducting condition; this is not specified for a mixer. However, the conversion loss of the mixer reflects the losses of two transformers and two diodes, which is the same condition as encountered in the switch and therefore mixer conversion loss can be taken as a measure of the switch insertion loss; this parameter should be minimised.

Diode ring mixers are available with RF-LO frequency capabilities well into the mm-wave region. However, the insertion loss, the relatively low power handling capability and poor extinction ratio of these devices makes them unattractive for direct switching of the source output frequency.

The mixer must not be driven sufficiently hard at the RF to cause damage. For 'standard' DBMs, the damage level is usually of order +13dBm, which suggests that +9dBm would be a safe working maximum. Whilst 'high level' mixers are available, these employ multiple diodes in the ring and exhibit rather high conversion losses.

Assuming a mixer which has been optimised for operation at the frequency of interest, the rise time of the switch (the time taken for an open to closed or closed to open transition) is determined by the bandwidth of the signal ports. Mixers with large RF and LO bandwidths are readily available at 7GHz, and 5GHz bandwidths on these ports are not hard to identify. The IF bandwidth is a little more troublesome, although 4GHz bandwidths are available. These bandwidths ensure that pulses of order 500ps (equivalent to half the IF bandwidth) should be viable.

10.3 Pulses and Multipliers

Whilst the DBM switch is not attractive for direct switching of the source output frequency, there remains the possibility of using a DBM based switch to gate the drive to a multiplier chain. It is now demonstrated that using the DBM based switch to drive a diode based multiplier results in very short pulses with infinite extinction ratios.

Figure 10.8 shows a DBM based switch inserted between a source and

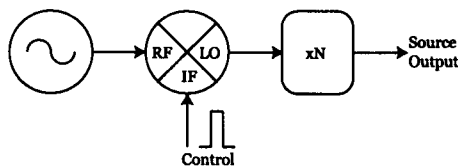


Figure 10.8: The use of a DBM based switch in a multiplier chain.

a multiplier chain and the way in which the various ports of the DBM are employed. If an amplifier is required to overcome the DBM loss, it is inserted in the LO arm of the multiplier.

The properties of both varistor and varactor diode frequency multipliers were presented in section 5.4 in terms of their harmonic content and efficiency. In the following sections the effect such multipliers upon a pulse modulated sinusoid is investigated.

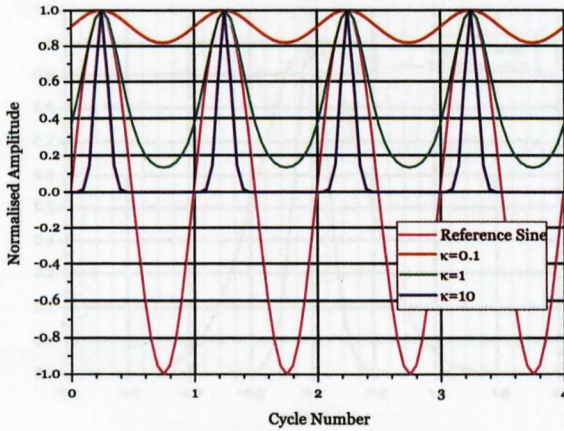


Figure 10.9: Diode current for various values of applied sinusoidal (voltage) drive, the sinusoid is included for reference.

10.3.1 Varistor multipliers

For voltage $V = f(t)$ applied to a diode, the current is of the form (chapter 5)

$$I_D = I_Q e^{\kappa f(t)} \tag{10.1}$$

where $\kappa = V/\gamma V_T$, and all terms are defined in chapter 5. Figure 10.9 shows the (normalised) diode current for various sinusoidal ($f(t) = \sin(\omega t)$) drive levels. As the drive level increases the distortion becomes greater i.e. the current pulse narrows. It is this distortion which is responsible for harmonic generation.

From the point of view of pulse generation it is the variation of the pulse shape with κ which is important. With a sufficiently small applied voltage, $\kappa = 0.1$ for example, the output current is still sinusoidal and no multiplication occurs. Thus, with the multiplier output tuned to the N^{th} harmonic there is no output from the multiplier. It is apparent therefore that there is a

10.3. PULSES AND MULTIPLIERS

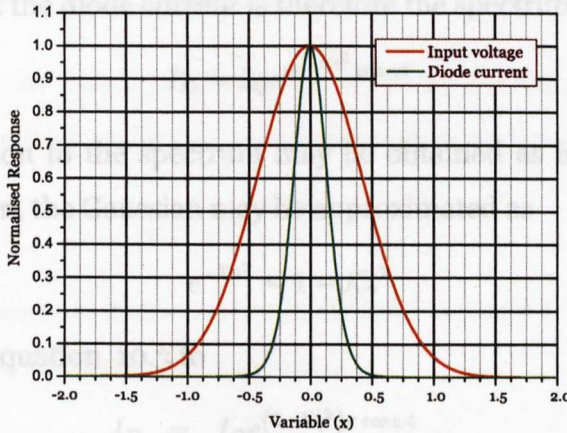


Figure 10.10: Diode response to a Gaussian voltage pulse, showing the pulse compression expected from a varistor multiplier

threshold below which there is no output from the multiplier, and it is not necessary for the switch element to offer 100% isolation, the switch need only take the input amplitude above and below the threshold at which multiplication occurs. Thus a switching element with a finite isolation, when used with a multiplier, is expected to produce an infinite extinction ratio at the multiplier output.

Figure 10.10 shows the diode current for an applied voltage of the form $f(t) = \exp[-2.7726t^2]$ with $\kappa = 10$, which shows clearly that the diode non linearity is able to introduce considerable sharpening of the leading and trailing edges on the diode current pulse.

Now consider the case in which the voltage applied to the multiplier diode is a sinusoid modulated by a Gaussian; it is of the form

$$f(t) = e^{-\kappa t^2} \cos \omega t \quad (10.2)$$

10.3. PULSES AND MULTIPLIERS

The spectrum of the diode current is therefore the spectrum of

$$I_D = I_Q e^{\kappa e^{-\kappa t^2} \cos \omega t} \quad (10.3)$$

An approximation to the spectrum may be obtained as follows. Using a Taylor expansion, the Gaussian may be approximated as

$$e^{-\kappa t^2} \sim 1 - \kappa t^2 \quad (10.4)$$

which reduces equation 10.3 to

$$I_D = I_Q e^{(1-\kappa t^2)\kappa \cos \omega t} \quad (10.5)$$

$$= I_Q e^{\kappa \cos \omega t} e^{-\kappa \kappa t^2 \cos \omega t} \quad (10.6)$$

Using the 'slow envelope' approximation' we have

$$e^{-\kappa \kappa t^2 \cos \omega t} \sim e^{-\kappa \kappa t^2} \quad (10.7)$$

and equation 10.6 reduces to

$$I_D = I_Q e^{\kappa \cos \omega t} e^{-\kappa \kappa t^2} \quad (10.8)$$

Thus, the diode current spectrum is the convolution of the spectra of the two exponential terms. The spectrum of the first exponential ($\exp[\kappa \cos \omega t]$) is given by equation 5.9. The second term is a Gaussian, and its spectrum is another (narrower) Gaussian. Therefore the spectrum of the multiplier output, is a series of Gaussian envelopes centred on harmonics of the input frequency, i.e. there will be a gaussian envelope pulse containing each harmonic waveform.

Whilst equation 10.4 is a gross approximation, the neglected higher order terms only change the steepness of the transition, and the analysis confirms that the multiplication of a pulse results in a narrower pulse at the desired harmonic.

10.3.2 Varactor multipliers

If a semiconductor junction is reverse biased by a voltage V , the charge stored in the resulting depletion layer is given by equation 5.13 as

$$Q(V) = Q_o \left[1 - \frac{V}{V_b} \right]^{1/2} \quad (10.9)$$

in which all terms have been previously defined in section 5.4.1.2. Then the diode current due a varying reverse bias is

$$I(V) = \frac{d}{dt} Q(V) = \frac{dQ}{dV} \frac{dV}{dt} \quad (10.10)$$

If the applied reverse bias is a Gaussian modulated sinusoid of the form

$$V(t) = e^{-kt^2} \sin \omega t \quad (10.11)$$

then the diode current is given by

$$I = C_{jo} \left[1 - \frac{e^{-kt^2} \sin \omega t}{V_b} \right]^{-1/2} [\omega \cos \omega t - 2kt \sin \omega t] e^{-kt^2} \quad (10.12)$$

in which all quantities have been previously defined. Applying a Taylor expansion to the first term of this, retaining only the first two terms of the expansion and the use of standard trigonometric identities yields

$$I = C_{jo} (\omega \cos \omega t - 2kt \sin \omega t) e^{-kt^2} + \frac{C_{jo}}{V_b} (\omega \sin 2\omega t - 2kt \cos 2\omega t) e^{-2kt^2} \quad (10.13)$$

The analysis of section 5.4.1.2 shows that when driven with a single tone, the varactor multiplier produces only the driving frequency and the second harmonic of the driving signal. This is demonstrated again in equation 10.13. However, in this case the fundamental component is modulated by the original Gaussian envelope, whilst the second harmonic component of the diode current is modulated by a Gaussian which is narrower than initial

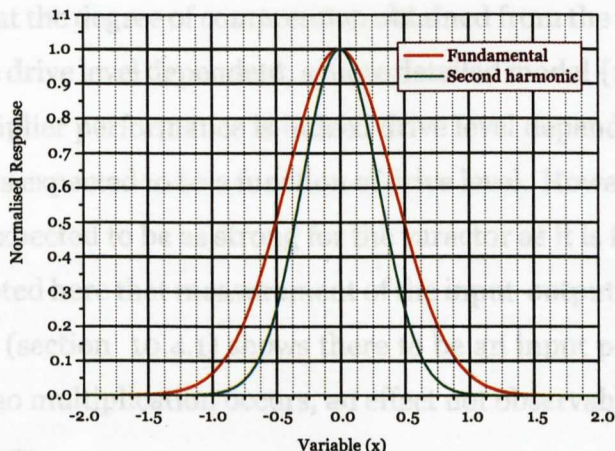


Figure 10.11: The response of a varactor diode to a Gaussian envelope voltage pulse, showing the pulse compression expected from a varactor multiplier.

modulating Gaussian.

Once again it should be noted that the truncation of the Taylor expansion is an over simplification. The neglected terms introduce additional pulse steepening.

A comparison between the applied Gaussian envelope and the Gaussian envelope modulating the second harmonic component of the diode current is shown in figure 10.11. This shows clearly the pulse compression produced by the varactor multiplier. Comparing figures 10.10 and 10.11 indicates that the varistor multiplier might be expected to produce a higher level of pulse compression than the varactor multiplier. This is not necessarily so. The pulse compression shown for the varistor multiplier was obtained for a relatively high drive level, and the level of compression obtained from the varistor multiplier is highly dependant upon the peak power applied to the multiplier. Whilst the simple model of the varactor diode used above does

10.4. THE PROPERTIES OF MULTIPLIED PULSES

not predict that the degree of compression obtained from the varactor multiplier would be drive level dependent, a more detailed model [143] shows that varactor multiplier performance is indeed drive level dependent. Therefore compression is expected to be a function of drive level. However, the dependency is not expected to be as strong for the varactor as it is for the varistor. Finally it is noted here that measurement of the input-output power transfer characteristic (section 10.4.1) shows there to be an input power threshold below which no multiplication occurs, an effect not observable in the simple model used here.

Section summary

The high insertion loss and poor isolation of the DBM switch are not now important. If the RF input to the DBM is maintained at a safe level, any loss may be overcome with a suitable amplifier at the LO port; it is only necessary to ensure that the amplifier has sufficient bandwidth that the pulses generated are not distorted. Further, provided the switch-amplifier combination is able to produce sufficient power variation at the multiplier input to induce the required nonlinearity, significant pulse compression occurs and it is possible to generate very narrow pulses with an infinite extinction ratio.

10.4 The Properties of Multiplied Pulses

The DBM selected was the Hittite HMC220SM8 which has RF and LO port frequency ranges of 5-12GHz, and an IF frequency range of DC to 4GHz. This device is specified to have an LO-RF isolation of 25dB at 7GHz, and a

10.4. THE PROPERTIES OF MULTIPLIED PULSES

conversion loss of 8dB.

10.4.1 DBM Attenuation Characteristics.

The attenuation characteristics of the HMC220 were measured by applying +6dBm to the RF port, a variable DC level to the IF port and monitoring the power delivered to the LO port as a function of IF port voltage. The results are shown in figure 10.12.

The insertion loss, measured at 4.5dB, is considerably better than the

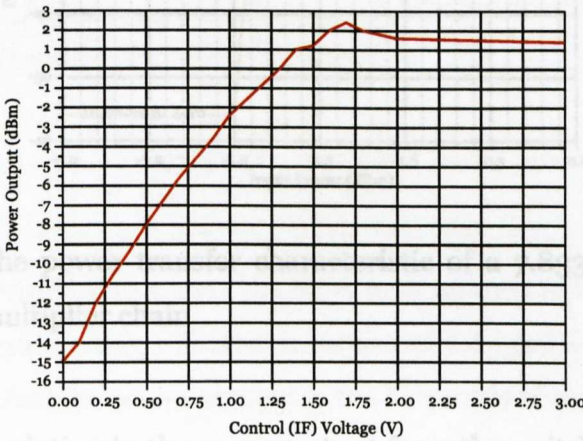


Figure 10.12: The transfer characteristic of an HMC220 (RF-LO port) as a function of IF port DC level.

expected 8dB, whilst the isolation, measured at 16dB, is rather worse than expected. An attempt to improve the isolation by driving the LO port through a 50Ω 3dB pad did not improve matters, and there is as yet no explanation of this effect.

The question therefore is will this change in attenuation be sufficient to drive

10.4. THE PROPERTIES OF MULTIPLIED PULSES

the subsequent diode multipliers between no output and full output?

The power change required to take the complete multiplier chain from zero to full output was investigated by driving the multiplier of section 7.4.2 from a 7.8333GHz source, and monitoring the 94GHz output power.

The results of this measurement are shown in figure 10.13. It is now clear

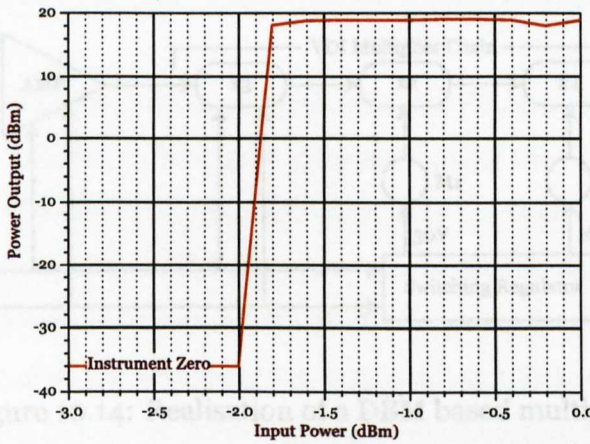


Figure 10.13: The power transfer characteristic of a 7.833GHz to 94GHz multiplier chain.

that the 16dB variation in the power output from the switch is sufficient to drive the multiplier chain from no output to full output.

10.4.2 Pulse Parameters.

A pulse system, based upon the multiplier of section 7.4.3, and using a DBM as the switching element, was constructed and tested. The block diagram is shown in figure 10.14.

The 7.8333GHz oscillator may be any of the previously discussed types. At-

10.4. THE PROPERTIES OF MULTIPLIED PULSES

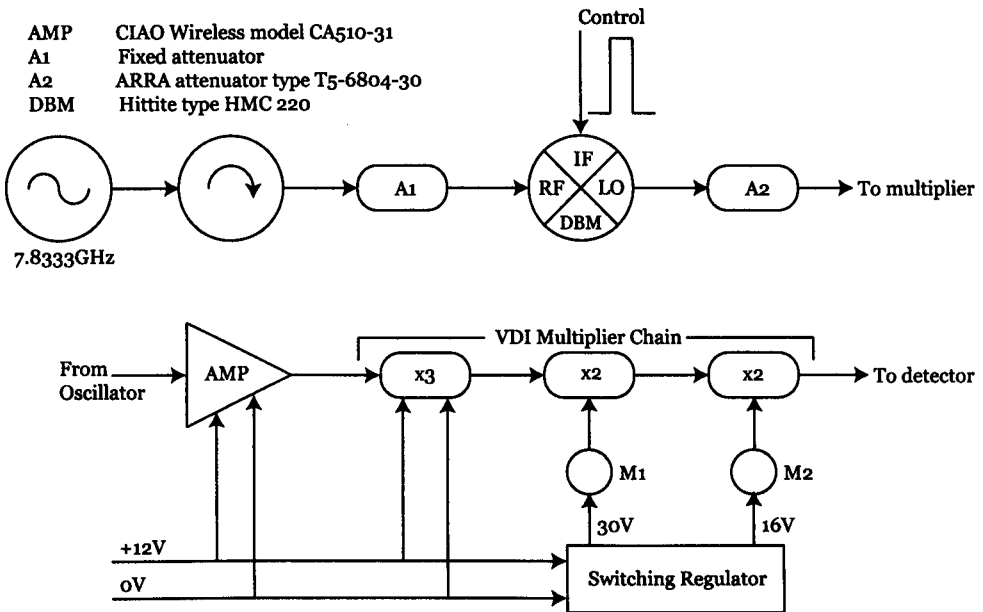


Figure 10.14: Realisation of a DBM based multiplier

tenuator A1 is required to ensure the drive level applied to the DBM RF port is within safe limits; using a YTO as the source of 7.8333GHz, an attenuation of 6dB ensures that the power applied to the RF port is of order 9dBm, which is 6dB less than the maximum specified safe level.

Although some measured parameters are available, the power distribution was calculated on a 'worst case' basis. The minimum LO-RF loss is 8dB, which with the switch closed and based on 6dBm at the RF port gives -2dBm at the LO port. Therefore, because the first multiplier stage might require +17dBm to give full output, AMP1 requires a gain of 19dB. The amplifier specified is a custom derivative of a standard part, and offers 28dB +1.2dB/-0.45dB over the 5GHz to 10GHz octave. In reality, the first multiplier requires considerably less than +17dBm to produce an output which

will damage the following mixer stages, and therefore attenuator A2 is provided to allow the multiplier to be adjusted to a safe operating condition.

The system was set up by monitoring (using M1 and M2) the current drawn by the final diode multiplier blocks. With attenuator A2 set to maximum attenuation, the switch was closed (a 3V signal applied to the IF port) and the attenuator adjusted to give safe currents in both multipliers as previously described.

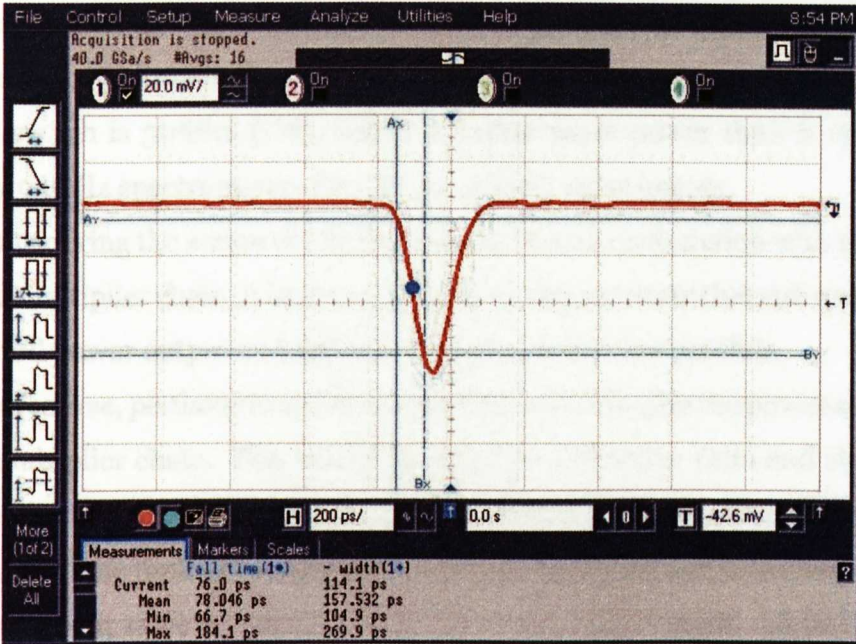
The output of the source was measured using the Flann planar diode detector type WPD10. However, the pulses generated using the HMC220 proved to be so fast that the Lecroy oscilloscope perviously employed was found to have insufficient bandwidth to show the true pulse shape; an Agilent DSO81204A oscilloscope, which has a bandwidth of 12GHz was employed for these measurements. Typical pulses are shown in figures 10.15(a) and 10.15(b). Both these pulses are full power pulses; note the negative going pulse envelope is obtained because the detector produces an increasingly negative voltage for higher powers.

The rise times of the pulses are remarkably consistent at 70ps to 80ps (which is the rise time of the oscilloscope), therefore a 1ns pulse would show essentially vertical edges and would appear as a rectangular pulse.

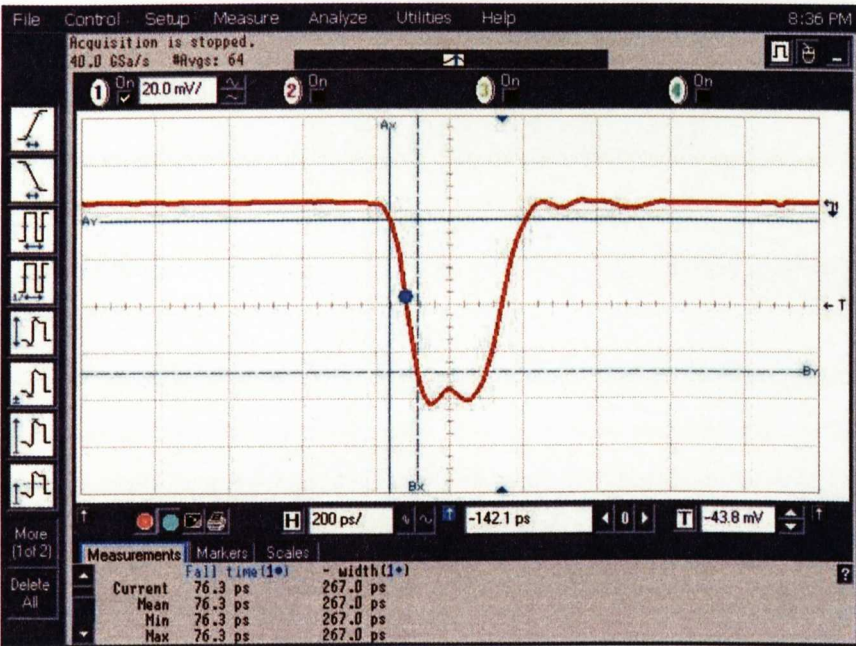
10.5 Chapter summary

It has been demonstrated that PIN diodes have considerable limitations when used as OOK modulators at 94GHz. They are able to generate distorted full power pulses of a few ns width, whilst shorter pulses may only be generated at the expense of output power; i.e. the PIN switch never fully

10.5. CHAPTER SUMMARY



(a) DBM 115ps pulse envelope.



(b) DBM 250ps pulse envelope.

Figure 10.15: The pulse envelopes of a 94GHz carrier produced using a DBM based switch to gate the input to a multiplier chain

closes. Whilst an extinction ratio of 30dB may be acceptable for low power systems, for pulse powers of 1kW (+60dBm), the leakage power through the open switch is 30dBm (1W), which is rather more power than is used by many 94GHz spectrometers for CW (or pulse!) experiments.

By considering the action of a biphase modulator in conjunction with a diode based multiplier chain, it has been possible to demonstrate that sub ns pulses with full power output and infinite extinction ratios are possible.

It is, of course, perfectly in order to use a PIN switch to gate the power applied to a multiplier chain. This would increase the extinction ratio and sharpen the edges of the pulse envelope. As a further benefit, provided the switch modulated the multiplier input power across the multiplier threshold, there would appear to be no reason that a PIN based switch would not be able to generate sub ns second pulses.

CHAPTER 11

A 94GHz Heterodyne Demodulator

Having excited the sample spin system by applying a series of mm-wave pulses, it is now necessary to detect the signal radiated by the sample as it relaxes. This chapter is concerned with the design and realisation of a heterodyne demodulator suitable for use in both a 94GHz CW spectrometer, and a 94GHz 1ns pulsed instrument.

A word of caution is needed here. In the following sections the detector will be described as responding to a 1ns pulse. This is *not* the 1ns pulse used to excite the spin system, indeed considerable effort must be expended to prevent such a response. Rather, because the relaxation of the excited spin system can occur on a ns time scale the detector must have sufficient bandwidth to respond to a ns timescale pulse.

11.1 The Heterodyne Demodulator

It has been demonstrated in previous chapters that, for a CW spectrometer, a simple homodyne detector can offer excellent performance and a sensitive high frequency quasi-optical spectrometer has been discussed in chapter 3. It should be noted that the homodyne detector has a high sensitivity because the field modulation produces a signal at the mixer output removed from the low frequency (LF) $1/f$ noise content of the InSb mixer.

The homodyne detector, requiring only one source, is a relatively simple system to engineer. It has the additional property that the main spectrometer signal and the signal used in the demodulation process are coherent and therefore the effect of source phase noise may be minimised by ensuring that both the main spectrometer and detector signals have the same path length. For a 94GHz pulse spectrometer, typical InSb detector elements are too slow to respond on the required ns timescales. A solution to this is the heterodyne demodulator, the outline of which is shown in figure 11.1.

Here, the source S_1 at frequency F_1 provides the signal to excite the sample spin system. The signal returning from the cavity at frequency F_1 is now mixed with a second frequency F_2 provided by source S_2 ; in the special case in which $F_1=F_2$, the detector is a Homodyne system. However if $F_1 \neq F_2$, the mixer IF output is a signal with a carrier frequency of $|F_1-F_2|$, the sum frequency being neglected.

It is now seen that the heterodyne scheme, requiring two sources, is rather more complex than the homodyne scheme and that minimising the effects of source phase noise are rather more complicated.

11.1. THE HETERODYNE DEMODULATOR

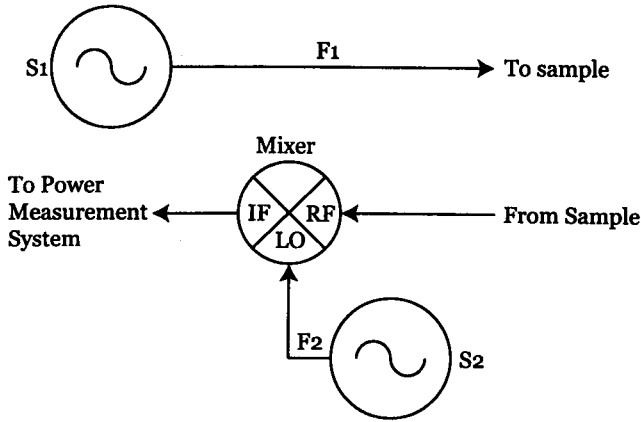


Figure 11.1: The block diagram of a Heterodyne detector.

11.1.1 Choice of IF Frequency

In the case of the homodyne detector, which may be regarded as a heterodyne detector with a very low, (essentially zero) IF frequency, for a CW system the frequency of demodulation is the field modulation frequency and this may be regarded as the 'true' homodyne IF frequency. In the case of the heterodyne scheme, the IF frequency is independent of the field modulation frequency, being determined entirely by the relative frequencies of the sources. However, if the heterodyne demodulator is used in conjunction with field modulation, the detection frequency is the IF frequency plus or minus the field modulation frequency.

In a communications system the choice of IF frequency is determined primarily by the requirements of adjacent channel and image rejection [191]. In a CW ESR spectrometer, the requirements are set by the need to avoid LF mixer noise, whilst in a pulsed spectrometer, the IF frequency is determined by the need to avoid LF noise and the pulse width.

11.1. THE HETERODYNE DEMODULATOR

The effect of LF noise on spectrometer sensitivity was considered in section 3.8. The LF noise generated by the mixer diodes is highly dependent upon the materials used in and the construction of the diodes. For example InP diodes for use in a 94GHz mixer show excess noise for IF frequencies extending to approximately 10MHz [192], whilst silicon diodes at 75GHz show no excess noise at IF frequencies above approximately 200kHz [193]. Thus, it would appear reasonable to require an IF frequency in excess of 10MHz for a 94GHz CW spectrometer.

Figure 11.2 shows the spectrum of the mixing process for a signal with an extended RF bandwidth; the frequencies F_1 and F_2 are referred to in figure 11.1. The LO signal (F_2) is mixed with the signal frequency (F_1), and taking

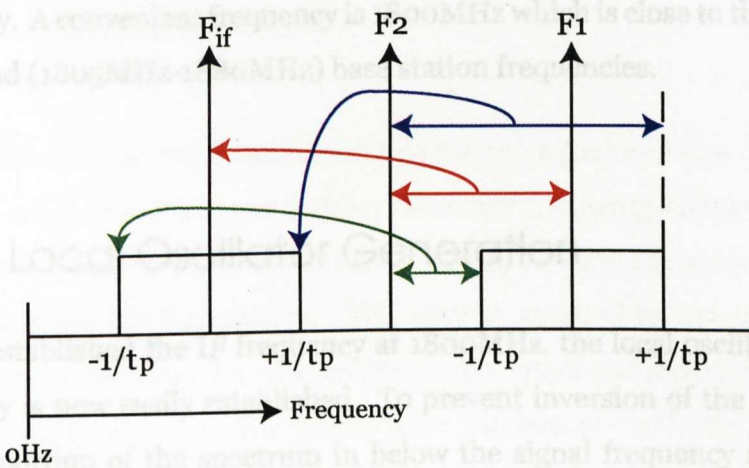


Figure 11.2: The spectrum of the mixing process for a pulsed signal, having a pulse width t_p , showing the way in which various components of the spectrum are converted to the IF frequency.

the difference frequency results in the IF frequency F_{if} . Energy contained in frequencies extending below the signal frequency mixes with the LO signal and extends below the IF frequency (only the limit is shown in figure 11.2),

11.2. LOCAL OSCILLATOR GENERATION

and similarly energy contained in frequencies above the signal frequency mixes with the LO signal and extends above the IF frequency. In this way, the information is simply translated to the IF frequency by the mixer.

For a rectangular pulse of width t_p , the first zero of the RF spectrum (and therefore the IF spectrum) does not occur until a frequency of $\pm 1/t_p$ centered on the IF frequency. The low frequency component of the IF signal should not extend into the mixer diode $1/f$ region, which for a 1ns pulse suggests a minimum IF frequency of 1.1GHz.

Beyond these considerations, the choice of IF frequency is one of convenience. The availability of filters amplifiers and other components for the cellular telephone market make these frequencies very attractive for the IF frequency. A convenient frequency is 1800MHz which is close to the cellular GSM band (1805MHz-1880MHz) base station frequencies.

11.2 Local Oscillator Generation

Having established the IF frequency at 1800MHz, the local oscillator (LO) frequency is now easily established. To prevent inversion of the spectrum (i.e. the portion of the spectrum in below the signal frequency appearing on the high frequency side of the IF centre frequency and visa-versa) which would occur if the LO signal were placed above the signal frequency (high side injection), the LO is placed below the signal frequency (low side injection). With an IF of 1800MHz this gives an LO frequency of 92.2GHz.

Methods of generating such frequencies have been discussed in the context of generating the main spectrometer signal and a multiplier technique is employed to generate the required LO frequency.

11.2. LOCAL OSCILLATOR GENERATION

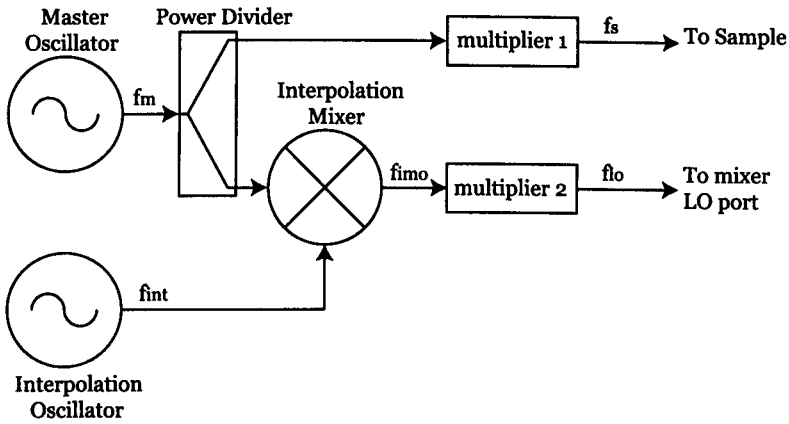


Figure 11.3: Generation of the spectrometer LO signal using an interpolation oscillator. Port allocation on the interpolation mixer is discussed in the text.

Clearly, two independent oscillators, one for the signal and one for the LO could be employed. However if either oscillator frequency changes relative to the other, the IF frequency changes, and any IF signal processing would have to account for this change. This may be avoided by using a master oscillator to derive both the main spectrometer signal and the LO frequency, as shown in figure 11.3. The power from the master oscillator is divided into two, not necessarily equal amplitude, components. One output of the power divider is applied to a multiplier (multiplier 1) and generates the main spectrometer signal as previously discussed. The second output is applied to the RF port of a suitable mixer (the interpolation mixer) and is mixed with a fixed, highly stable frequency, provided by the interpolation oscillator. The output of the interpolation mixer is now multiplied using multiplier 2, to obtain the required LO frequency.

Let multiplier 1 multiply by a factor n and multiplier 2 multiply by a factor

11.2. LOCAL OSCILLATOR GENERATION

m. Then

$$F_{if} = F_s - F_{lo} \quad (11.1)$$

$$= nF_m - mF_{imo} \quad (11.2)$$

Now, the demodulator uses low side injection, and therefore $F_{lo} < F_s$, and thus $F_{imo} = F_m - F_{int}$ giving

$$F_{if} = nF_m - m(F_m - F_{int}) \quad (11.3)$$

$$= nF_m - mF_m + mF_{int} \quad (11.4)$$

Then if $m = n$ the IF frequency is independent of the master oscillator frequency (F_m) and depends only upon the frequency of the interpolation oscillator. It would appear logical to select $m = n = 12$ because this factor was selected as the multiplication factor to produce the main spectrometer signal. This then fixes the frequency plan for the spectrometer, and this is shown in figure 11.4.

11.2.1 The Interpolation Mixer

As was noted previously when discussing pulse generation (section 10.2.1), mixers with suitable frequency responses to beyond 7GHz for all ports are not easy to identify. However, the symmetry of the diode ring mixer means that the functions of the LO and IF ports may be exchanged and the Hittite mixer type HMC220MS8 used for both the pulse generator and phase noise measurement may be used as the interpolation mixer.

The mixer must however be driven with care. The maximum powers which may be applied to the HMC220MS8 RF and IF ports is +13dBm. A 150MHz drive level of +10dBm applied to the IF port keeps the IF port within safe dissipation limits. When driven normally, the mixer 1dB compression point

11.2. LOCAL OSCILLATOR GENERATION

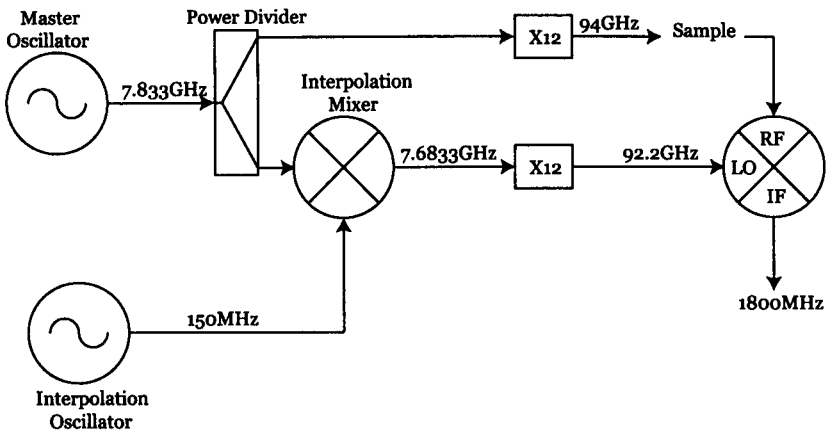


Figure 11.4: Frequency plan of a 94GHz spectrometer based on two x12 multiplier chains and an 1800MHz IF frequency.

is at best +8dBm and at worst +4dBm with +13dBm of local oscillator drive. With the mixer LO and IF ports exchanged, it is not clear how the mixer will perform in terms of compression, conversion loss and output distortion. The performance of the mixer has considerable bearing upon the design of the interpolation oscillator in terms of the required power output. The HMC220MS8 was therefore investigated to determine optimum drive levels. A power division scheme, which delivers sufficient power to the main signal multiplier and a low level signal to the interpolation mixer is shown in figure 11.5, which also shows typical measured powers at each point.

11.2.2 Mixer saturation

The mixer saturation performance was investigated by applying the -0.8dBm 7.833GHz signal from the power distribution system to the RF port of the HMC220MS8 and a variable amplitude 150MHz signal to the IF port.

11.2. LOCAL OSCILLATOR GENERATION

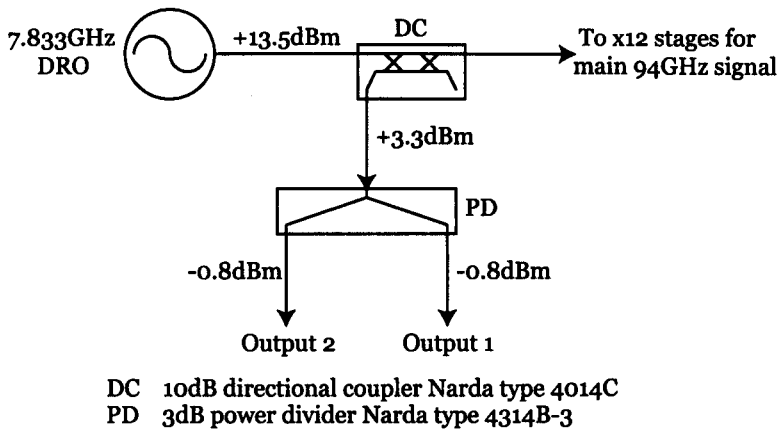


Figure 11.5: Power distribution for the interpolation chain.

The mixer performance was determined by measuring the amplitude of the 7.683GHz mixer product on the LO port as a function of the 150MHz power. The result is shown in figure 11.6. With -0.8dBm applied to the RF port the mixer is 1dB compressed with +2dBm of 150MHz applied to the IF port. This then indicates the region in which the mixer may be operated. Noting that the conversion loss (RF to LO) is highly dependent upon the 150MHz drive level, it is concluded that the highest possible 150MHz drive level should be employed.

It would appear that with -0.8dBm at 7.833GHz applied to the RF port and 0dBm at 150MHz applied to the IF port, the mixer is not significantly compressed and the conversion gain (7.833GHz to 7.683GHz) is expected to be of order -15dB. These were the drive levels selected for the interpolation mixer.

11.2. LOCAL OSCILLATOR GENERATION

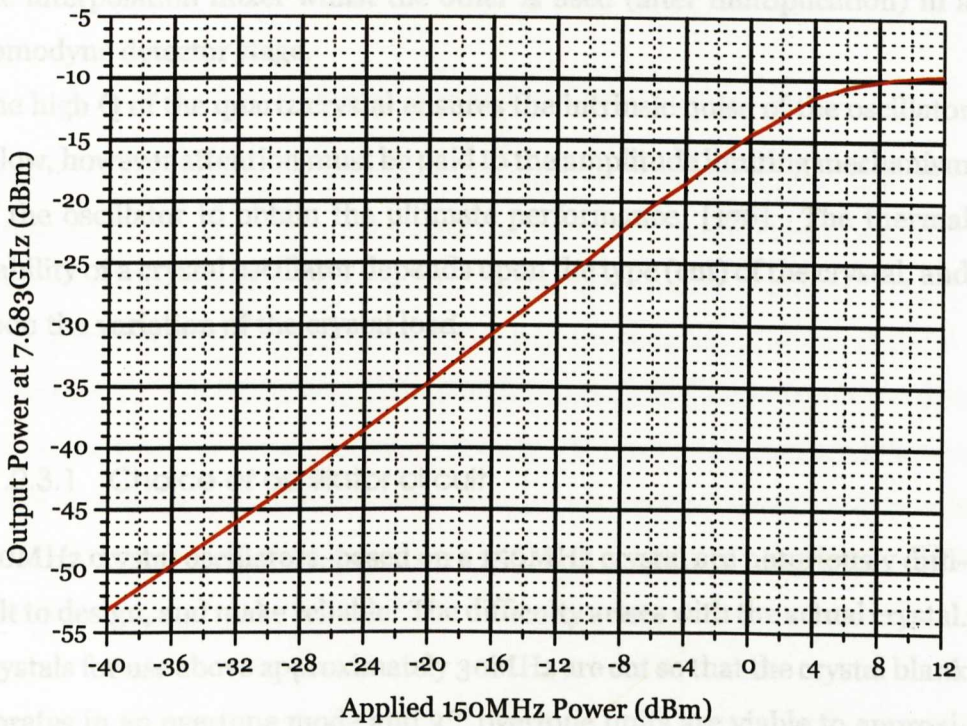


Figure 11.6: The power handling of the HMSC220MS8 when driven with 0dBm applied to the RF port, a variable 150MHz signal applied to the IF port and power is extracted from the LO port.

11.2.3 The Interpolation Oscillator

The interpolation oscillator must be low noise and thermally stable. The low noise requirement ensures that the LO noise is dominated by only one source, the master oscillator, whilst the stability ensures that, because the only source of drift is the interpolation oscillator, drift is minimised.

A crystal oscillator will achieve both these goals. It must produce a frequency of 150MHz and provide two outputs each of +10dBm. One of these drives

11.2. LOCAL OSCILLATOR GENERATION

the interpolation mixer whilst the other is used (after multiplication) in a homodyne detector stage.

The high Q of the quartz crystal ensures the intrinsic noise of the oscillator is low, however attention must be paid to the amplitude limiting mechanism of the oscillator to obtain the ultimate performance [176]. The thermal stability of a crystal oscillator depends upon the type (cut) of the crystal, and upon the variation of the crystal load.

11.2.3.1 Choice of oscillator circuit

150MHz crystal oscillators, based on a 150MHz crystal are notoriously difficult to design, and make reliable. The difficulty arises with the actual crystal. Crystals for use above approximately 30MHz are cut so that the crystal blank vibrates in an overtone mode and 3rd overtone units are viable to approximately 140MHz. Beyond this, 5th and even higher overtones are required. The problem with high overtone crystals is that they become more difficult to excite, having a high equivalent series resistance and they show a remarkable ability to oscillate preferentially at lower overtones and unwanted crystal modes. Thus whilst simple circuits can be made to function, considerable care must be taken to ensure that the oscillator loop gain is reduced to prevent oscillation at unwanted crystal modes and overtones [194].

Using a third overtone crystal at 75MHz and doubling to the desired 150MHz output is viable. However, the oscillator must generate a comb of frequencies spaced at 75MHz and the filter required to ensure even moderate spectral purity is difficult to design with reasonable insertion loss. To avoid some of the problems of filtering a 150MHz oscillator was constructed using a two transistor Butler configuration and a 5th overtone 150MHz crystal.

11.2. LOCAL OSCILLATOR GENERATION

11.2.3.2 Realisation of the interpolation Oscillator

The circuit diagram of the complete oscillator is shown in figure 11.7. This configuration is recommended for series resonant crystals, and is stated to have 'good' frequency stability [195]. Q1 and Q2 form the oscillator proper. Q1 is a common base configuration, the input resistance of which is dominated by $r_e (= 1/g_m)$ where g_m is the device transconductance and is therefore determined by the device collector current. Q2 forms an emitter follower which provides a low source resistance to drive the crystal network. Power is extracted from the oscillator via the directional coupler DC1, which couples minimum energy out of the feedback loop and thus maintains the oscillator Q.

The design follows the recommendations of [195], although without exact crystal and transistor parameters, the component values obtained must represent a 'best guess' and some experimentation must be expected.

A 150MHz 5th overtone crystal is expected to have an effective series resistance of order 100Ω, which according to [195] suggests an input resistance of order 33.3Ω for Q1. The input resistance of the common base stage¹ is

$$r_e = \frac{26}{I_E} \quad (11.5)$$

where r_e is in Ohms and I_E , the device emitter current, is in mA; thus Q1 requires a collector current of order 1.3mA. Resistor values are now obtained by assuming the bases of Q1 and Q2 to be at approximately 6V, half the regulated supply voltage. Q1 is biased as described, whilst Q2 is biased to approximately maximise the device current gain.

¹The relationships used for transistor biasing and gain calculation are contained in [196].

11.2. LOCAL OSCILLATOR GENERATION

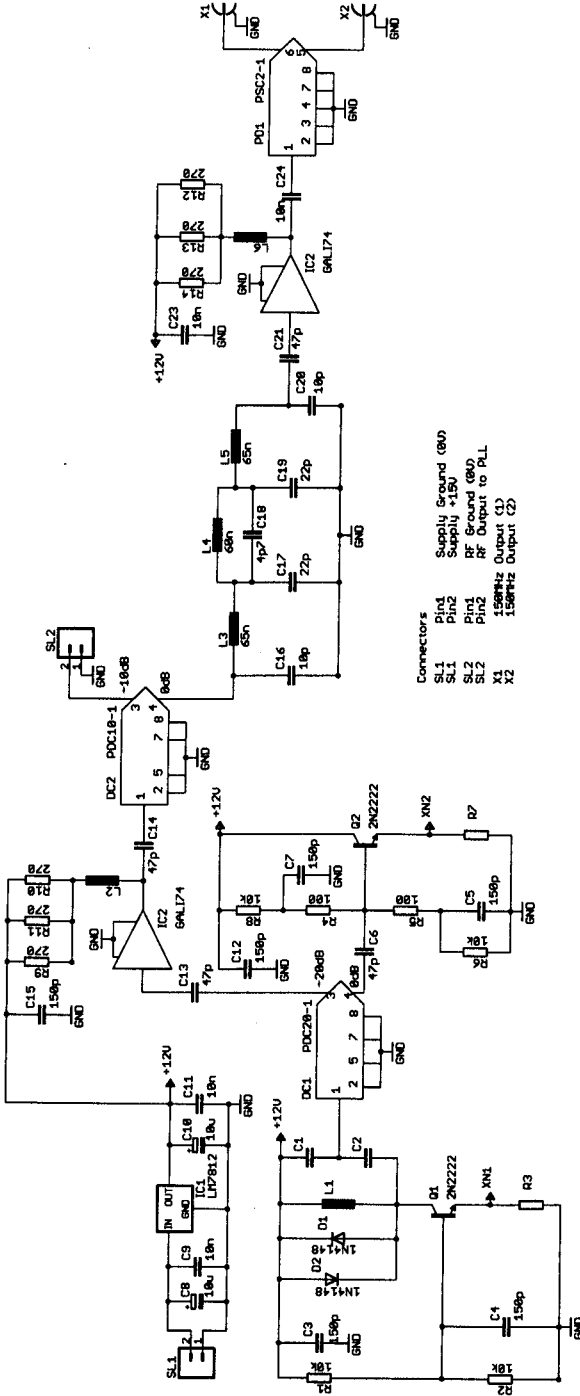


Figure 11.7: The 150MHz crystal oscillator. The points XN1 and XN2 connect to the one or other of the crystal networks shown in figure 11.8. Resistor values are in Ohms, all capacitor values are in Farads, all inductor values in Henrys.

11.2. LOCAL OSCILLATOR GENERATION

Assuming the crystal network sufficiently bypasses R_3 , the stage gain of Q1 is given by

$$A_v = \frac{R_L}{r_e} \quad (11.6)$$

where R_L is the collector load of Q1 and this must be sufficient to overcome the losses associated with the crystal network, the directional coupler and the emitter follower. The directional coupler has a gain of 0.87x, the emitter follower has a gain of order 0.8x and the crystal network has a gain of 0.25x, a total loss of 0.174x which gives a stage gain of 5.7x for Q1 for a total loop gain of unity. At start up the loop gain must exceed this value, and a gain of 20x is selected, the collector load must therefore be of order 666 Ω .

The collector load of Q1 is the parallel combination of the equivalent parallel resistance of L1 and the input resistance of the emitter follower (50 Ω by virtue of R4 and R5) transformed by the action of L1, C1 and C2 which must resonate at 150MHz.

An inductance of 78nH is assumed, which is provided by a Coilcraft inductor type 146-02j08 which will be brought to resonance at 150MHz by a total collector capacitance of order 14pF. Assuming circuit stray capacitances of 10pF, the total capacitance of C1 and C2 needs to be of order 4pF. The selected inductor has a Q of 100 at 50MHz, and thus an effective parallel resistance of 8k Ω . Hence the collector network must transform the 50 Ω load to approximately 700 Ω . At resonance, the impedance transformation ratio of the collector network is

$$\frac{R_p}{R_L} = \frac{700}{50} = \sqrt{\left[1 + \frac{C1}{C2}\right]} \quad (11.7)$$

which gives initial component values shown in table 11.1.

The limiting action of the oscillator must now be considered. Without D1 and D2 the amplitude of the oscillations will increase until either Q1 or Q2

11.2. LOCAL OSCILLATOR GENERATION

R3	3k9	R7	680 Ω
C1	15pF	C2	5p6
L1	78nH		

Table 11.1: Initial component values for the 150MHz oscillator

saturates, which will result in a drive level of several volts being applied to the crystal network; this drive level is too high. According to [195] a drive level of 600mV (peak) is about optimum. Diodes D1 and D2 clamp the output of Q1 to approximately this value without reducing the stage gain.

The remainder of the oscillator circuit is associated with raising the output power to a suitable level and providing some harmonic filtering.

Although the reasons are not discussed here, it is sometimes desirable to maintain a known phase relationship between the main spectrometer signal and the local oscillator. In such cases it is desirable to provide for the voltage control of the main and interpolation oscillator frequencies so that it may be phase locked to a low frequency master oscillator. The output available on connector SL2 is provided to drive the required phase locking circuitry. Outputs X1 and X2 are provided as the oscillator outputs, and are used to drive the interpolation mixer, and additional circuitry required for processing of the 1800MHz IF signal of the spectrometer.

The LC network between DC2 and IC2 forms a lowpass filter. Initial component values were obtained using an approach based on m-derived sections, with $m=0.6$ and assuming 50 Ω load impedances for each section. The transmission zero of the centre section was placed at 300MHz, and all sections were designed to have a cut-off frequency of 240MHz. The filter component values were then optimised to use standard capacitor values and realistic

11.2. LOCAL OSCILLATOR GENERATION

inductances. This filter is set up by observing the oscillator harmonic content and adjusting the inductors for lowest loss at 150MHz and maximum harmonic rejection.

Crystal networks

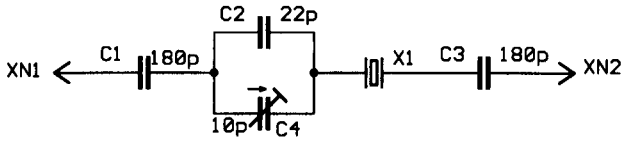
As indicated in figure 11.7, the crystal is placed between the points XN1 and XN2. Three networks are required, one for fixed frequency operation with fundamental mode crystals, one for fixed frequency operation with overtone crystals and one for voltage controlled operation. These are shown in figure 11.8. The exact frequency of the oscillator is set by adjusting the crystal loading. In the case of the oscillator employing fundamental mode crystals (figure 11.8(a)) the frequency is set by adjusting the total capacitive loading using C4. In the case of overtone oscillators (figures 11.8(b) and 11.8(c)), the loading is required to be inductive and the frequency is set using LA.

In both overtone oscillators, the inductor LX is included to remove the effect of the crystal static capacitance (C_0), a parasitic capacitance introduced by the metallisation of the crystal blank during manufacture. At low frequencies, C_0 presents a relatively high impedance and it is not a problem. However as frequency increases the impedance of C_0 may fall to a point at which the crystal is effectively bypassed, and the oscillator will not 'lock' to the crystal frequency. LX is employed to resonate C_0 at the crystal frequency.

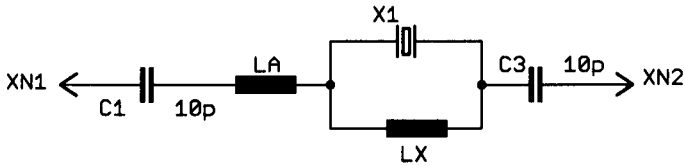
11.2.3.3 Crystal Oscillator Performance

In setting up the 150MHz oscillator, considerable experimentation was required to ensure reliable starting of the oscillator. Particular attention had

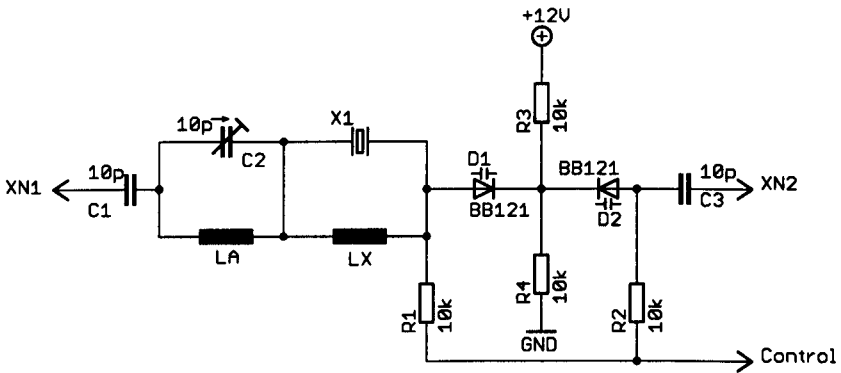
11.2. LOCAL OSCILLATOR GENERATION



(a) Fixed frequency fundamental usage. Note that C2 may not be required.



(b) Fixed frequency overtone usage.



(c) Voltage controlled after [177].

Figure 11.8: Crystal networks employed with the Butler crystal oscillator.

to be paid to the value of R_3 , and reliable starting could not be guaranteed until this value had been reduced to 390Ω .

The initial value of L_1 (a nominal $78nH$) was satisfactory, but was always set

11.2. LOCAL OSCILLATOR GENERATION

R3	390 Ω	R7	680 Ω		
C1	15pF	C2	5p6		
L1	90nH	LA	108nH	LX	165nH

Table 11.2: Final component values for the 150MHz oscillator. Inductor values are nominal, mid adjustment values.

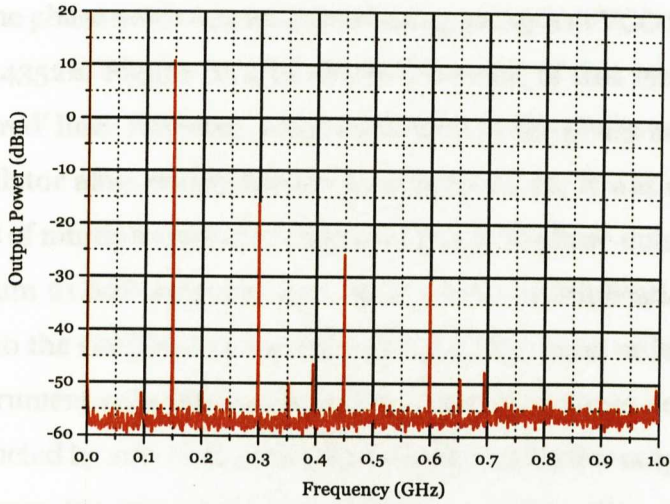
to its maximum inductance. A change to a nominal 90nH (Coilcraft inductor type 146-03j08), indicating rather less than 10pF stray capacitance in the collector circuit of Q1, provided a rather more satisfactory adjustment range. The final component values are shown in table 11.2

The fixed frequency oscillator (XCO)

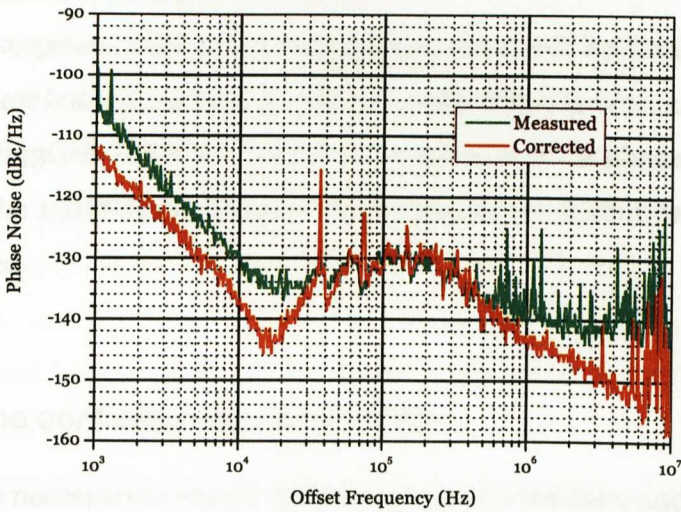
The fixed frequency 150MHz oscillator is constructed using the crystal network of figure 11.8(b) and is set up as follows. The crystal and LA are temporarily replaced with a short and L1 is adjusted to give a frequency of oscillation of approximately 150MHz. Removing the short across the crystal, a 5p6 capacitor (this value is close to the typical value of Co) is used in place of the crystal and LX is adjusted so that oscillation stops. The short across LA is removed, the 5p6 is replaced with the crystal and LA is adjusted to give the desired crystal locked frequency.

Figure 11.9(a) shows the spectrum of the oscillator at X1 (or X2). The harmonic rejection is rather worse than might have been expected. The spectrum at SL2 shows the 2nd harmonic to be less than 10dB below the fundamental, so the filter is improving matters. The reason for the poor rejection is that there is sufficient drive from the amplifier IC2 to drive the second stage of amplification into saturation.

11.2. LOCAL OSCILLATOR GENERATION



(a) Harmonic spectrum



(b) Phase noise spectrum

Figure 11.9: The harmonic and phase noise spectra of the fixed frequency 150MHz crystal oscillator.

11.2. LOCAL OSCILLATOR GENERATION

The 150MHz crystal oscillator was powered from an 18V lead-acid battery pack and the phase noise was measured using an Agilent VCO test set equipment type 4352B. Figure 11.9(b) shows the result of this measurement as the 'measured' line. However, when compared to the phase noise spectrum of the oscillator after multiplication by a factor of 12, it was observed that the process of multiplication had degraded the XCO phase noise by less than the minimum 21.6dB expected as a result of the multiplication. This was attributed to the oscillator phase noise being of the same order as the measuring instrument noise floor. Therefore a corrected phase noise spectrum was constructed by subtracting 21.6dB from the multiplier output spectrum, and this forms the 'corrected' line of figure 11.9(b). The validity of this correction is demonstrated by the agreement between the 'humps' between offset frequencies of 20kHz and 1MHz.

With the exception of the phase noise hump, which will be discussed shortly, this oscillator has a phase noise which is 20dB better (lower, c.f. figure 8.1) than the 7.833GHz DRO. It is therefore expected that the phase noise contribution of the 150MHz oscillator to the interpolation chain phase noise may be neglected.

The Voltage controlled oscillator (VCXO)

Should it be necessary to ensure that the 7.833GHz oscillator and the 150MHz oscillator maintain a fixed phase relationship, the DRO may be replaced with a PMYTO, the 150MHz XCO with a Voltage Controlled Crystal Oscillator (VCXO) and both may then be phase locked to a common reference oscillator.

A 150MHz VCXO may be constructed using the oscillator circuit of figure 11.7

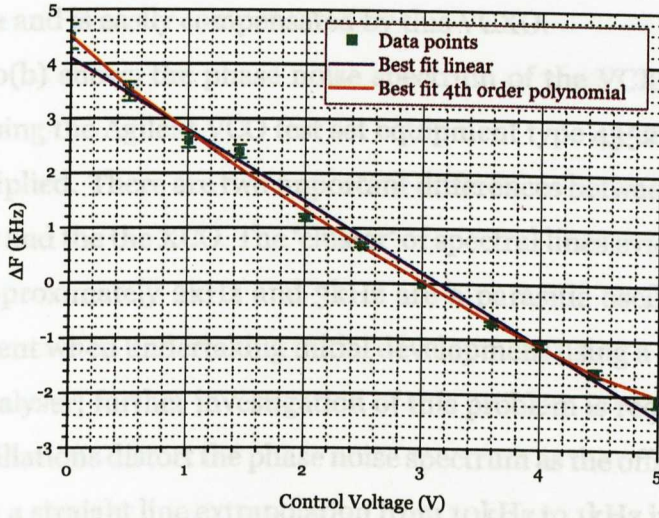
11.2. LOCAL OSCILLATOR GENERATION

by replacing the network of figure 11.8(b) with that of figure 11.8(c). It is important to note that the oscillator will tune 'backwards' i.e. high frequency will correspond to 0V applied to the control line, and this must be considered when phase locking the VCXO. The 6V bias applied to the common cathode of the varactor diodes means that in this case, because the diode must always be reverse biased, the maximum control voltage must not exceed 6V.

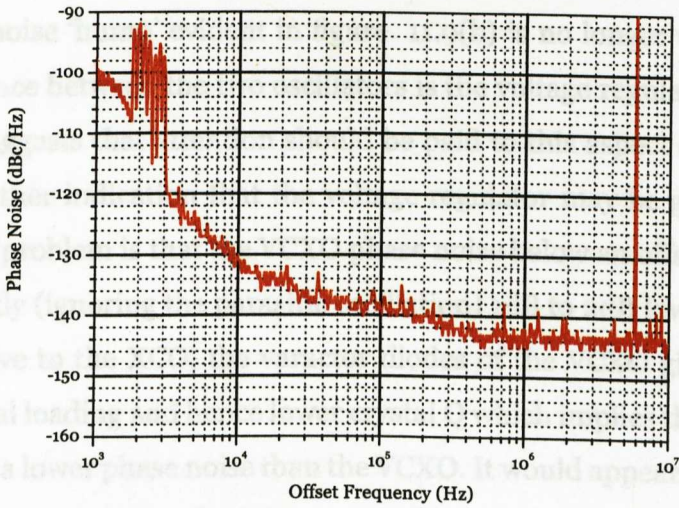
This VCXO is rather difficult to align correctly because all the adjustments interact. The oscillator is aligned by individually shorting the various sections of the crystal network, and removing the short circuits as the alignment proceeds. With all shorts in place, once L1 has been set to give a nominal frequency of 150MHz, the short across the crystal is removed and with a 5p6 capacitor in place of the crystal, LX is adjusted as above. With a crystal inserted, the shorts across LA and the diode network are now removed, the control voltage is set to the mid point of the control range (3V for the network as shown) and the frequency is set by adjusting LA. C4 sets the tuning linearity of the VCXO, but in reality the combination of C4 and LA is set to give satisfactory oscillation over the VCXO tuning range.

The VCXO was constructed without the voltage regulator, but is otherwise identical to the fixed frequency oscillator. The oscillator was tested using a 12V lead-acid battery pack. The harmonic content of the VCXO is similar to that of the fixed frequency oscillator, the VCXO tuning and phase noise performances are shown in figure 11.10. The tuning curve for this VCXO is shown in figure 11.10(a). The object of producing a VCXO is to allow phase locking such that the 7.833GHz and 7.683GHz signal bear a fixed phase relationship to each other and one of the major contributions to a relative phase change between the oscillators is thermal drift. The crystal has a thermal stability of $\pm 30\text{ppm}$ over the temperature range -20°C to 70°C which over

11.2. LOCAL OSCILLATOR GENERATION



(a) 150MHz VCXO tuning curve



(b) VCXO phase noise

Figure 11.10: The tuning curve and phase noise spectrum of the 150MHz voltage controlled crystal oscillator.

11.2. LOCAL OSCILLATOR GENERATION

the expected operating temperature range of 10°C to 30°C amounts to less than ± 4 ppm and is easily compensated by this VCXO.

Figure 11.10(b) shows the phase noise spectrum of the VCXO which was measured using the Agilent VCO test set equipment type 4352B at 150MHz i.e. *not* multiplied. There are two important differences between the spectra of the VCXO and the XCO. The 'cluster' of spectral lines evident between offsets of approximately 2kHz and 3kHz are a parasitic oscillation which was not evident when undertaking initial development using a conventional spectrum analyser; further investigation of this problem is required. These parasitic oscillations distort the phase noise spectrum as the offset frequency falls to 1kHz; a straight line extrapolation from 10kHz to 1kHz indicates that in the absence of these parasitic effects the VCXO would have an 'uncorrected' 1kHz phase noise of -110dBc/Hz.

The phase noise 'hump' evident in figure 11.9(b) is no longer visible. The only difference between the two oscillators is the voltage regulator and this therefore suggests that attention should be paid to this aspect of the oscillator. A further indication that the voltage regulator may be generating a phase noise problem is that the VCXO phase noise below an offset of 10kHz is consistently (ignoring the parasitic oscillation) 1dB to 2dB lower than the XCO. Relative to the XCO, the varactor diodes of the VCXO give rise to a higher crystal loading and hence lower crystal Q which implies that the XCO should have a lower phase noise than the VCXO. It would appear that supply noise is phase modulating the XCO over a wide bandwidth.

11.2.4 Interpolation mixer output

The ideal balanced mixer would produce only a difference frequency (which, in this case, is the required frequency) and a sum frequency, which is un-

11.2. LOCAL OSCILLATOR GENERATION

wanted. However, a real balanced mixer is not perfectly balanced and there is always some leakage of the 7.833GHz signal onto the mixer output, this too being an unwanted signal. These unwanted sum and leakage signals must be removed by filtering.

Figure 11.11 shows typical spectra at the mixer output (LO port). The RF frequency has been shifted to 7.5GHz for the purposes of demonstration, there is no difference in the spectra obtained if the RF signal is at 7.8333GHz. The 150MHz was obtained from the interpolation oscillator described above, with the output being reduced to 0dBm by use of a (commercially available) 10dB attenuator.

The suppression of the 7.5GHz signal relative to the two (7.5 ± 0.15) GHz products at the mixer output is 19dB to 22dB, which satisfies the manufacturers specification of >17dB when driven 'normally'.

The conversion loss for the high drive level (figure 11.11(a)) is estimated as 10dB, which lies within the normally driven mixer specification. The conversion loss for the low level drive (figure 11.11(b)) is noted to be of order 15dB. However the degree of compression in the high power case is indicated by the approximately 5dB drop in mixer output as the RF port drive is reduced by 10dB; the conversion loss is higher in this mode than in normal usage.

The more important result however is the spurious content of the mixer output. As noted, the perfect mixer would produce only the (7.5 ± 0.15) GHz outputs, whilst the imperfect balance of the mixer would result in leakage of the 7.5GHz signal.

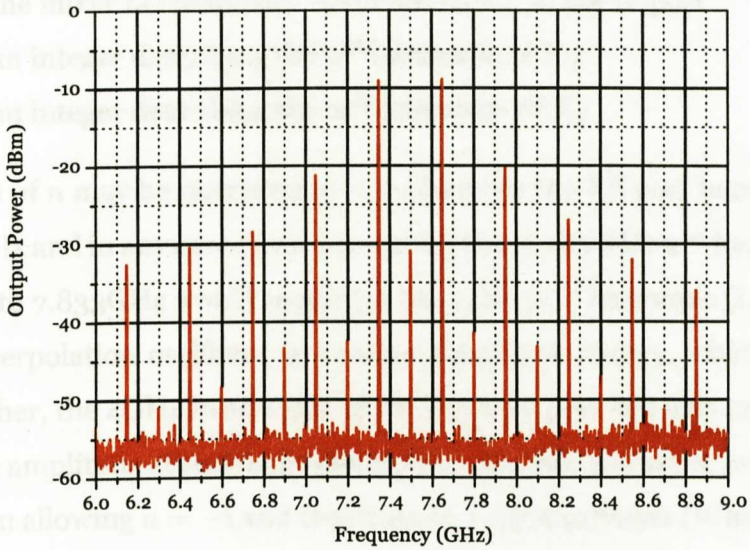
The mixer output is given by

$$F_{if} = |\pm n F_{rf} \pm m F_{lo}| \quad (11.8)$$

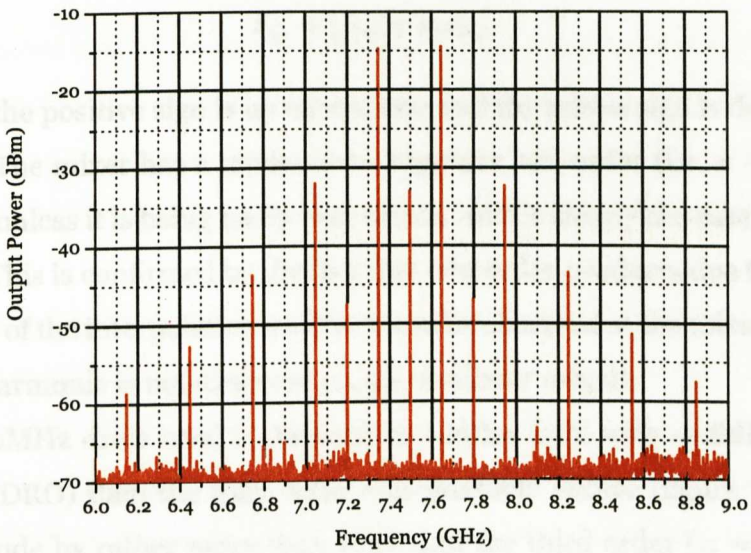
F_{if} is the mixer output frequency -here the signal on the LO port

F_{rf} is the mixer RF frequency -here the signal on the RF port

11.2. LOCAL OSCILLATOR GENERATION



(a) 150MHz drive +10dBm.



(b) 150MHz drive +1dBm.

Figure 11.11: The output (LO port) spectra obtained from the interpolation mixer. In both cases the RF port drive level was -0.8dBm , the 150MHz drive applied to the IF port were as indicated.

11.2. LOCAL OSCILLATOR GENERATION

F_{lo} is the mixer LO frequency -here the signal on the IF port

n is an integer describing the n^{th} harmonic of F_{rf}

m is an integer describing the m^{th} harmonic of F_{if}

The value of n may be restricted to $n = 1$ because the RF port bandwidth is only 12GHz and in any case down converting the 15.667GHz 2^{nd} harmonic of the DRO to 7.833GHz would require at least the 52^{nd} harmonic (i.e. $m=52$) of the interpolation oscillator to contain significant energy, which it does not. Further, the 4GHz bandwidth of the mixer IF port will also restrict the harmonic amplitude at such high values of m . Further n must be positive because even allowing $n = -1$ and requiring an output between DC and 12GHz on the mixer LO port requires $52 \leq m \leq 132$ which is clearly unreasonable. Thus equation 11.8 reduces to

$$F_{if} = |F_{rf} \pm mF_{lo}| \quad (11.9)$$

in which the positive sign is up conversion and the minus sign is down conversion. The mixer has a tendency to suppress odd order (i.e. $n + m$ odd) products unless it is being badly over driven -this is clearly the case in figure 11.11(a). This is confirmed by the fact that odd order products due to the 8^{th} harmonic of the interpolation oscillator can be observed at the mixer output, but this harmonic is not observed on the oscillator output.

If the 150MHz drive level is reduced to +1dBm (still with -0.8dBm drive from the DRO) then the high order odd products reduce (figure 11.11(b)) in amplitude by rather more than 10dB and the third order ($n = 1, m = 2$) product shows a small improvement. The presence of unwanted even order product also indicates an over driven mixer and the reduction in the 150MHz drive level also helps reduce the level of the unwanted even order product.

Any attempt to reach the ideal mixer output will result in desired products

11.2. LOCAL OSCILLATOR GENERATION

with such low amplitudes that the degree of amplification required post mixer to give a signal which will satisfactorily drive the following multiplier stages is prohibitive, both in terms of cost and potential stability.

In any case, the presence of the unwanted sum and leakage signals on the mixer LO port means that filtering of the mixer output will be required. The drive levels applied to the mixer to obtain figure 11.11(b) are safe and imply a post mixer gain of order 25dB, which is readily attainable, will be required to satisfactorily drive the subsequent multiplier stage . Therefore the drive levels were fixed at -0.8dBm at 7.833GHz and +1dBm at 150MHz, and a suitable filter was sought.

11.2.5 Mixer output filter

If it is assumed that the mixer products at ± 150 MHz of the desired 7.683GHz output were required to be at a level of -90dBc, the mixer output filter would have to offer a rejection of 60dB at the ± 150 MHz points. Further more, the filter must not rise back within at least 2GHz of the 7.683GHz desired mixer output.

Such a fixed frequency filter may be constructed using shortened resonant lines with capacitive loading to set the exact resonant frequency of each filter element [197]. To obtain the required stop band attenuation, this filter must have a narrow pass band. Therefore if it is required to change (tune) the mixer output frequency, these filters would prohibit all but the smallest frequency changes if system performance is to be maintained.

By using varactor diodes to provide the capacitive loading these filters may be made tunable [198]. However such filters show not only a variable centre frequency, but bandwidth and insertion loss also vary with tuning. Further,

11.2. LOCAL OSCILLATOR GENERATION

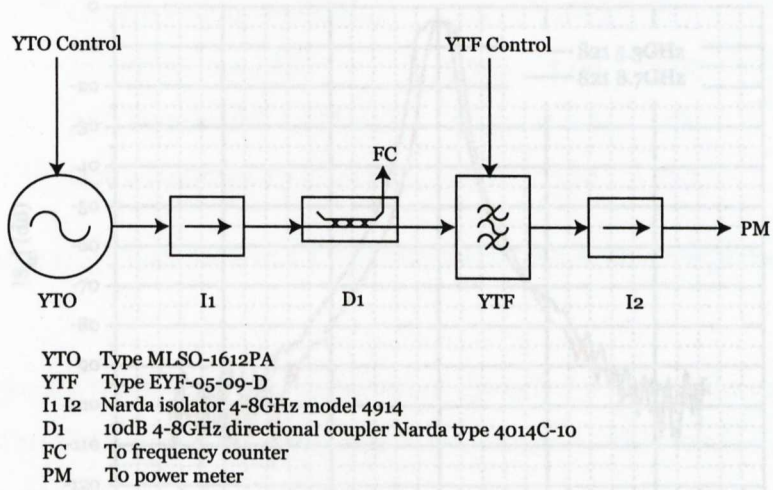
as noted for VCOs, the tuning range is restricted by the capacitance ratio of the varactor diodes. A YIG tuned filter (YTF) on the other hand is able to offer the required rejection, is tunable over a considerable range and shows a remarkably consistent bandwidth over its tuning range. The construction of such a filter is outlined in [199].

If the 7.833GHz source for experiments requiring frequency variation is chosen to be a YTO, both the YTO and YTF have extremely linear tuning characteristics and therefore any offset between the YTF center frequency and the YTO output frequency remain constant and may be electronically compensated. Thus, it may be arranged that the centre frequencies of the YTO and YTF track each other. A caveat here is that the YTO and YTF will probably have quite different thermal coefficients and it is therefore necessary to ensure that they are in good thermal contact and are allowed to thermalise prior to calibration and use.

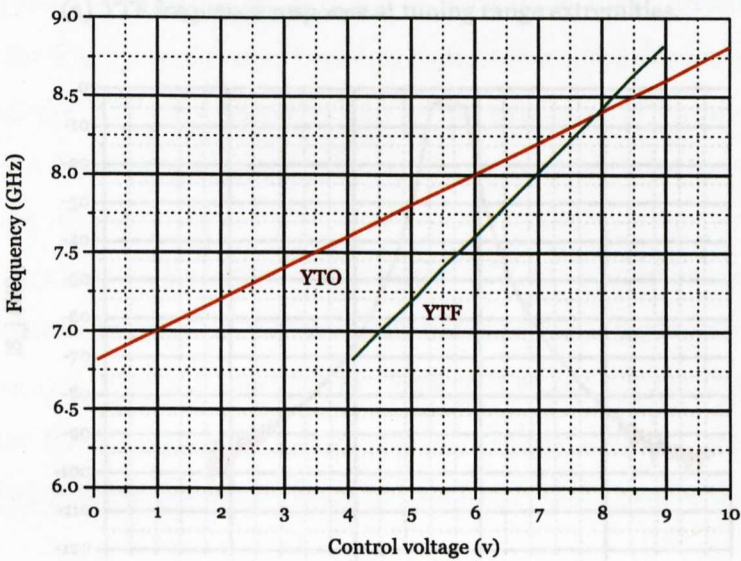
11.2.5.1 YTF performance

A four section YTF type EYF-05-09-D was obtained from ELVA, which has an integral driver for the tuning coil. The voltage range required to set the YTF centre frequency to a given frequency was determined using the apparatus shown in figure 11.12. The tuning curves were obtained by first setting the YTO control voltage and noting the frequency produced by the YTO. The YTF control voltage was then adjusted to maximise the power output. It is noted that indeed the YTO and YTF both show linear tuning performance and that they show tuning sensitivities of 200MHz/V and 400MHz/V respectively. Thus, scaling the YTO control voltage by a factor of 0.5 and then adding an offset of 4V would produce a voltage suitable for the control of the YTF and

11.2. LOCAL OSCILLATOR GENERATION



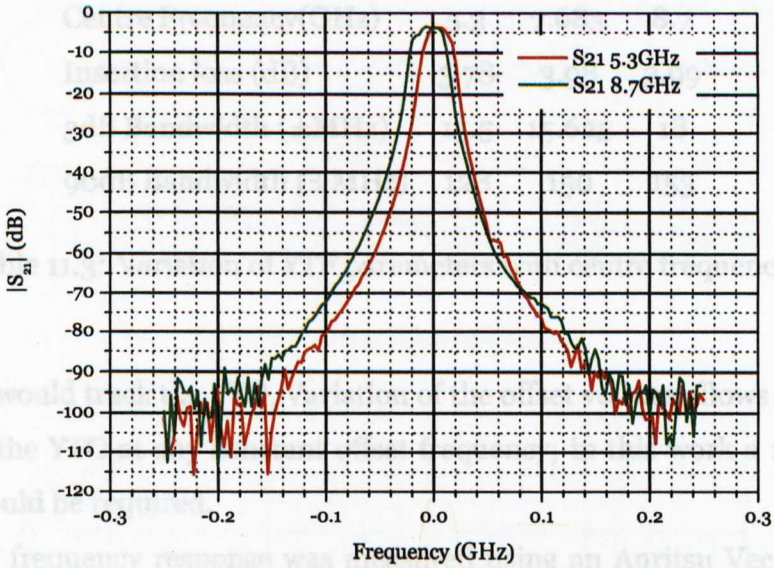
(a) YTF test set.



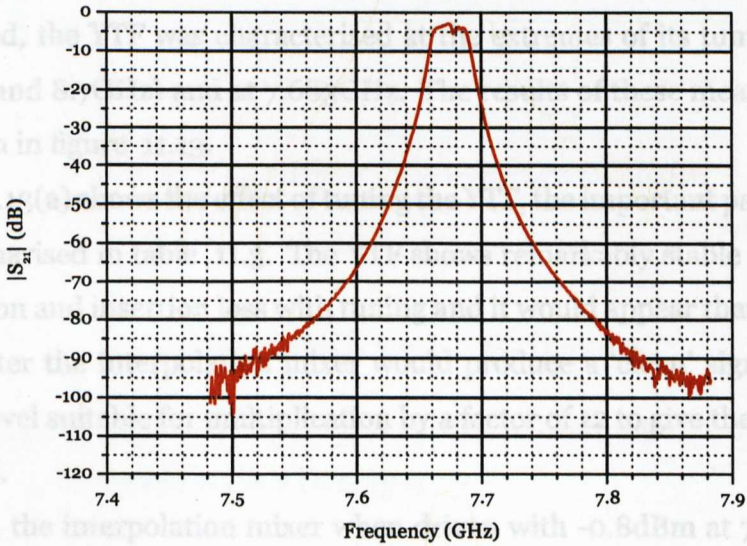
(b) Comparison of YTO and YTF tuning performance.

Figure 11.12: The test method and the results of measuring the control voltage required to set the YTF center frequency in the range.

11.2. LOCAL OSCILLATOR GENERATION



(a) YTF frequency response at tuning range extremities.



(b) YTF frequency response at 7.683GHz.

Figure 11.13: Frequency response of a YTF at its frequency extremes and at 7.683GHz, which is the particular frequency of interest.

11.2. LOCAL OSCILLATOR GENERATION

Centre Frequency(GHz)	5.3	7.683	8.7
Insertion loss (dB)	3.78	3.98	3.99
3dB Bandwidth (\pm MHz)	15.5	15.625	18
90dB Bandwidth (\pm MHz)	128	150	153

Table 11.3: Variation of YTF parameters with centre frequency.

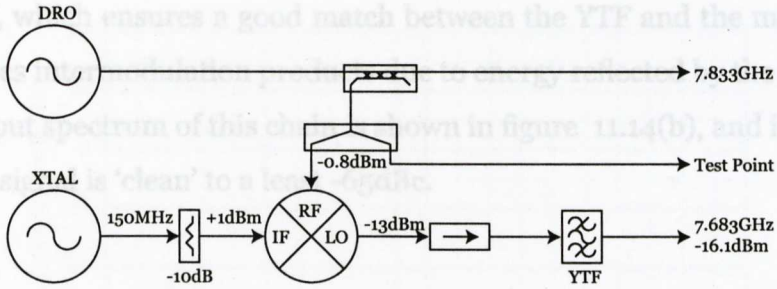
the YTF would track the YTO. Variation of the offset voltage allows the YTF to track the YTO at any constant offset frequency; in this work a 150MHz offset would be required.

The YTF frequency response was measured using an Anritsu Vector Network Analyser type MS4624B, which was loaned for these measurements. Although for the system under construction only a fixed frequency output is required, the YTF was characterised at the extremes of its tuning range (5.3GHz and 8.7GHz) and at 7.683GHz. The results of these measurement are shown in figure 11.13.

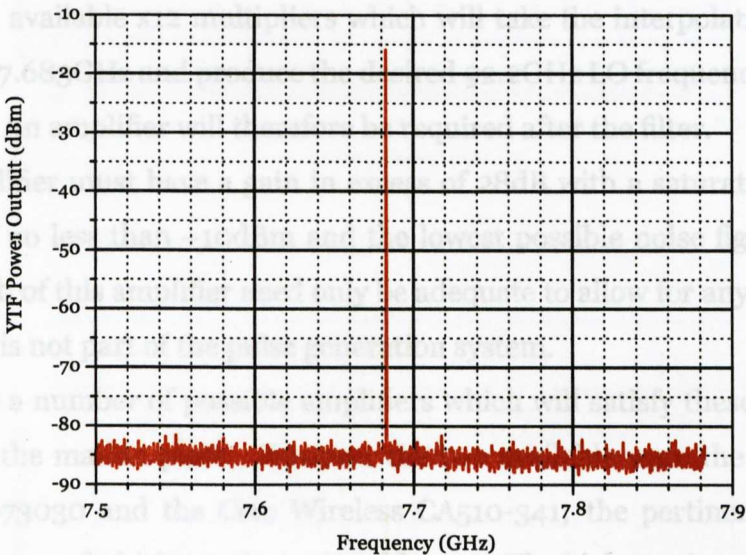
Figure 11.13(a) shows the effect of tuning the YTF, the important parameters are summarised in table 11.3. The YTF shows remarkably stable stopband attenuation and insertion loss with tuning and it would appear that this unit placed after the interpolation mixer would produce a 'clean' signal at the -90dBc level suitable for multiplication by a factor of 12 to give the required LO signal.

However, the interpolation mixer when driven with -0.8dBm at 7.833GHz and 0dBm at 150MHz is expected to produce -14dBm, which suggests that the interpolation chain power output post filter will be of order -18dBm.

11.2. LOCAL OSCILLATOR GENERATION



(a) Interpolation chain realisation.



(b) Interpolation chain spectrum at YTF output.

Figure 11.14: Realisation and spectral content of the interpolation chain measured at the YTF output.

11.2.5.2 Interpolation chain low level output

The block diagram of the interpolation chain so far described is shown in figure 11.14(a). Note the inclusion of an isolator between the mixer and which is sufficient to drive any of the available multiplier chains, and in fact

11.2. LOCAL OSCILLATOR GENERATION

the YTF, which ensures a good match between the YTF and the mixer and minimises intermodulation products due to energy reflected by the YTF.

The output spectrum of this chain is shown in figure 11.14(b), and indicates that the signal is 'clean' to a least -65dBc.

11.2.6 Post filter amplification

Typically, available x12 multipliers which will take the interpolation chain output at 7.683GHz and produce the desired 92.2GHz LO frequency require +10dBm. An amplifier will therefore be required after the filter.

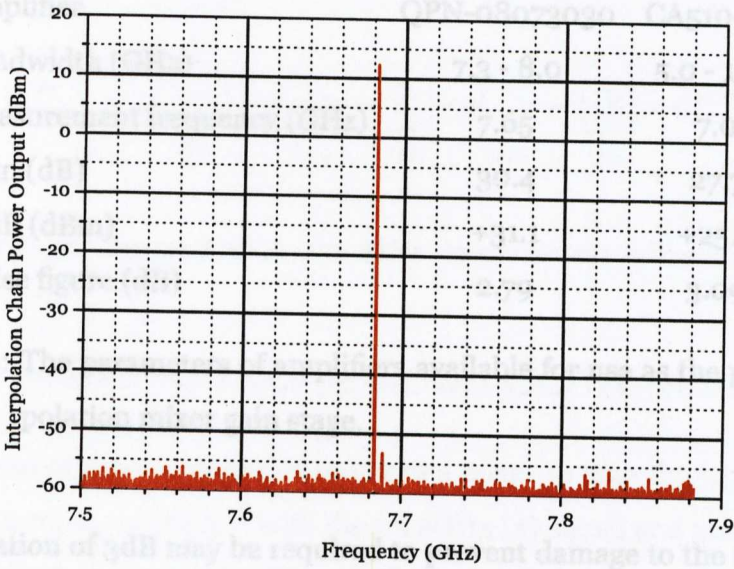
This amplifier must have a gain in excess of 28dB with a saturated power output of no less than +10dBm and the lowest possible noise figure. The bandwidth of this amplifier need only be adequate to allow for any required tuning, it is not part of the pulse generation system.

There are a number of possible amplifiers which will satisfy these requirements in the market place. However the two available were the Quinstar QPN-08073030 and the Ciao Wireless CA510-341; the pertinent performance figures of which are shown in table 11.4. The higher gain and saturation power output (P_{1dB}) combined with the marginally lower noise figure make the QPN-08073030 the amplifier of choice. Note that the lower bandwidth of the chosen amplifier encompasses the tuning range of the PMYTO.

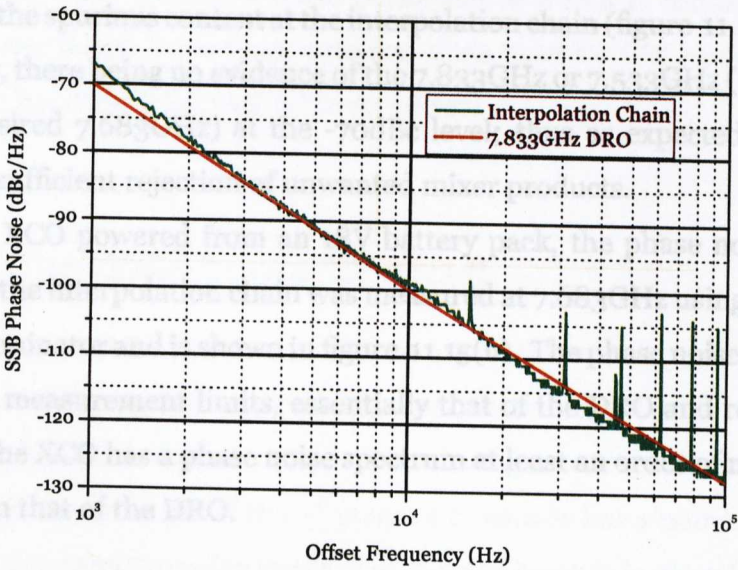
11.2.6.1 Interpolation chain performance.

The key parameters for the complete interpolation chain are power output and spectral purity. Power output is measured to be +13dBm at 7.683GHz, which is sufficient to drive any of the available multiplier chains, and in fact

11.2. LOCAL OSCILLATOR GENERATION



(a) Interpolation chain spectrum at amplifier output.



(b) Interpolation chain phase noise spectrum at amplifier output.

Figure 11.15: The output spectra of the interpolation chain at the amplifier output. A straight line approximation to the 7.833GHz DRO has been added for comparison.

11.2. LOCAL OSCILLATOR GENERATION

Amplifier	QPN-08073030	CA510-341
Bandwidth (GHz)	7.3 - 8.0	5.0 - 10.0
Measurement frequency (GHz)	7.65	7.0
Gain (dB)	30.4	27.7
P ₁ dB (dBm)	+31.1	+25.9
Noise figure (dB)	2.79	3.09

Table 11.4: The parameters of amplifiers available for use as the post interpolation mixer gain stage.

an attenuation of 3dB may be required to prevent damage to the multiplier chain.

The spectral purity of the interpolation chain is shown in figure 11.15. As expected the spurious content at the interpolation chain (figure 11.15(a)) output is low, there being no evidence of the 7.833GHz or 7.533GHz (± 150 MHz of the desired 7.683GHz) at the -70dBc level; thus as expected, the YTF provides sufficient rejection of unwanted mixer products.

With the XCO powered from an 18V battery pack, the phase noise at the output of the interpolation chain was measured at 7.683GHz using the delay line discriminator and is shown in figure 11.15(b). The phase noise spectrum is, within measurement limits, essentially that of the DRO and reflects the fact that the XCO has a phase noise spectrum at least an order of magnitude lower than that of the DRO.

11.3. 94GHZ TO 1.8GHZ DOWN CONVERSION

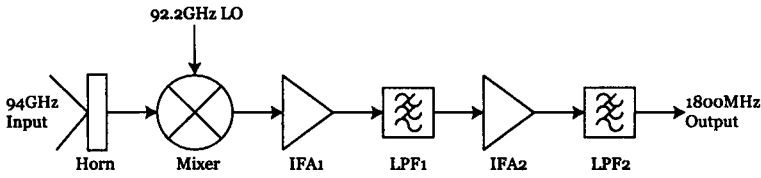


Figure 11.16: The 94GHz to 1800MHz down convertor block diagram

11.3 94GHz to 1.8GHz Down Conversion

The process of down conversion employs a mixer to take the 94GHz signal from the sample, multiply it with the 92.2GHz LO signal and produce an IF signal centred at 1800MHz. The sum frequency being in excess of 180GHz is outside the mixer IF pass band and is ignored.

The system must provide a noise performance which is comparable with a Bolometer based Homodyne detector when used for CW work, and have sufficient bandwidth to respond to ns pulses.

11.3.1 The down convertor circuit.

The down convertor consists of all the components which appear in the signal path between the 94GHz input and the 1800MHz output which is applied to the homodyne demodulator stage. A block diagram of the down convertor is shown in figure 11.16. If the i^{th} stage of a cascade has a noise factor of F_i and a gain G_i then the noise factor of an n-stage cascade is given by the Friss equation [191]

$$F_{cas} = F_1 + \sum_{i=2}^n \frac{F_i - 1}{\prod_{j=1}^{i-1} G_j} \quad (11.10)$$

11.3. 94GHZ TO 1.8GHZ DOWN CONVERSION

The input horn is a standard corrugated horn and has a loss (measured) of 0.1dB; as with all passive components, the loss may be treated as the device noise figure and thus the horn has a noise figure of 0.1dB.

The first IF amplifier (IFA1) now plays an important role in determining the system noise temperature. Provided the gain of IFA1 is large, equation 11.10 shows that the noise contributions of the stages following the first IF amplifier may be neglected to a good first approximation.

The amplifier must have a high gain and a low noise figure with frequency response of at least 800MHz to 2.8GHz. The selected amplifier is the Miteq AFS4-001004-13-3-4 which has a frequency response of 100MHz to 4GHz, a gain of 36dB and a noise figure (NF) of 1.3dB.

The mixer has been selected to be a Farran Technology BMC10. For an RF input of 94GHz with an LO drive of +13dBm at 92.2GHz, this device has a conversion loss of 7dB.

The mixer noise factor must, however, be calculated with care. In the absence of input filtering, the mixer must respond to an image frequency 1.8GHz *below* the 92.2GHz LO signal i.e. a frequency of 90.4GHz. Whilst this frequency contains no useful spectral information, it contains noise which will appear in the IF output of the mixer, and therefore a Double Sideband (DSB) mixer noise figure must be employed [200].

The mixer DSB noise figure is defined as

$$F_{DSB} = \frac{T_D}{T_O} \left[\frac{L_s L_i}{L_s + L_i} - 1 \right] + 1 \quad (11.11)$$

where

- T_D is the effective diode temperature
- T_O is the reference temperature (290K)
- L_s is the signal-IF path conversion loss

11.3. 94GHZ TO 1.8GHZ DOWN CONVERSION

	Horn	Mixer	IF Amplifier	
gain	-0.1	-6.4	35	dB
	0.9772	0.2291	3981	
NF	0.1		1.3	dB
F	1.0233	2.8175	1.35	

Table 11.5: Summary of down convertor parameters

L_i is the image-IF path conversion loss

The effective diode temperature is included to account for intrinsic thermal effects within the mixer diodes, it is usually taken to be 350K [200]. The conversion losses (L_s and L_i) are, in this case equal and are the mixer loss. For a loss of 7dB this is a loss factor of 5.0119. Then using equation 11.11 the mixer noise factor is

$$F_{DSB} = \frac{350}{290} \left[\frac{5.0119}{2} - 1 \right] + 1 = 2.8175 \quad (11.12)$$

The parameters of the various components are summarised in table 11.5. These figures may now be used in equation 11.10 to estimate the noise factor of the down convertor; the result is $F_{cas} = 4.6733$ or 6.7dB. This may be converted to a noise temperature using

$$T_{cas} = T_O [F_{cas} - 1]$$

where T_O has been previously defined. The mixer is expected to have a noise temperature of 1065K.

11.3. 94GHZ TO 1.8GHZ DOWN CONVERSION

11.3.1.1 Measured results

The cascade noise temperature of the first three stages of the down convertor (horn, mixer and first IF amplifier) was measured using a hot/cold load technique [200], in which the down convertor is employed as a radiometer. The output of the IF amplifier was connected to a power meter via a 2.4GHz lowpass filter; the maximum insertion loss of which is 1dB and adds 6mK to the predicted system noise temperature. The input horn was allowed to look at either a warm (TK RAM at 295K) load, or a cold (Eccosorb CV3 immersed in boiling liquid Nitrogen at 77K) load and the change in IF power output was recorded.

The ratio of the hot and cold powers is known as the 'Y-factor' which is defined to be [200]

$$Y = \frac{P_{HOT}}{P_{COLD}} = \frac{T_{HOT} + T_{SYS}}{T_{COLD} + T_{SYS}} \quad (11.13)$$

and therefore

$$T_{SYS} = \frac{T_{HOT} - YT_{COLD}}{Y - 1} \quad (11.14)$$

where

T_{HOT} is the 'hot' laboratory temperature

T_{COLD} is the 'cold' liquid Nitrogen temperature (77K)

T_{SYS} is the system noise temperature

Tables converting between Y-factors and system noise temperature (based on a warm temperature of 295K and a cold temperature of 77k) are readily available [201].

Unfortunately, with the 92.2GHz LO signal derived from the interpolation chain, the front end noise temperature could not be measured, there was no

11.3. 94GHZ TO 1.8GHZ DOWN CONVERSION

measurable power change at the down convertor output between the hot and the cold loads indicating an excessively high system noise temperature.

The interpolation chain was removed and the LO signal derived directly from the 7.833GHz DRO, giving an LO frequency of 94GHz. Under these conditions the measured power ratio at the down convertor output was 0.6dB, which gives a measured system noise temperature of 1394K, which is in broad agreement with theory.

The system noise temperature is particularly sensitive to Horn insertion loss and the mixer conversion loss and a calculation of the effects of uncertainty in these values may be performed. Keeping all else constant, if the Horn insertion loss is 0.2dB rather than 0.1dB the system noise temperature rises from 1065K to 1096K whilst a mixer conversion loss of 7.5dB results in a system noise temperature of 1238K. Further, if the Y factor is held constant at 0.6dB and T_{HOT} is allowed to vary by ± 1 K the measured system temperature will vary by ± 6.7 K. If all these factors are taken into consideration, the agreement between the calculated and measured noise temperatures is considered good and the detector noise temperature of the down convertor compares favourably with the noise temperature of the Helium cooled Bolometer (of order 2000K) currently employed on the St Andrews spectrometer.

An additional factor to be considered is that the IF port on the BMC10 mixer is DC coupled, and therefore the IF passband extends from DC to 2.4GHz, the upper limit being set by the lowpass filter. This measurement therefore includes the region dominated by the rising mixer diode $1/f$ noise. Further, the IF amplifier has a rising noise figure below 300MHz and may have in excess of 10dB gain at 10MHz. There is therefore considerable room for low frequency effects to significantly contribute to the system noise temperature. The low frequency response of the down convertor was restricted by insert-

11.3. 94GHZ TO 1.8GHZ DOWN CONVERSION

ing a 250MHz high pass filter at the IF amplifier output. Repeating the Y-factor measurement using a DRO as the local oscillator source now gives a power variation of 1.03dB, which corresponds to a noise temperature of 737K, which is a considerable improvement over the current Bolometer.

If the same IF filtering regime is used with an LO derived from the interpolation chain, a power change of 0.1dB is just measurable which corresponds to a noise temperature of 9282K, confirming that the origin of the excess noise is the interpolation network.

11.3.1.2 Reduction of the excess noise

The high noise floor encountered with the interpolation was unexpected. Certainly, the close in phase noise of the interpolation chain is not the problem because both the DRO based and the interpolation chain have the same close to carrier phase noise. Neither can it be due to the multiplier chain since both the DRO and interpolation chain measurements were made with the same multiplier chain. Suspicion must fall on the mixer, the post mixer amplifier, or the YIG filter.

The HMC220MS8 mixer used as the mixer uses GaAs technology and therefore has the potential to have a considerable $1/f$ noise close to carrier, although it will have a low ultimate noise floor. The potential contribution of the interpolation mixer was investigated by changing the mixer. The interpolation chain mixer was changed to a Mini-Circuits mixer type ZMX-10G which employs Silicon diodes. As with the HMC220MS8, the port bandwidths of the ZMX-10G require that the ports of the ZMX-10G be driven in exactly the same way as those of the HMC220MS8. With this substitution, the noise temperature was once again measured as 9282K. The excess noise is either so high that any effect due to the mixer is masked or there is no

11.3. 94GHZ TO 1.8GHZ DOWN CONVERSION

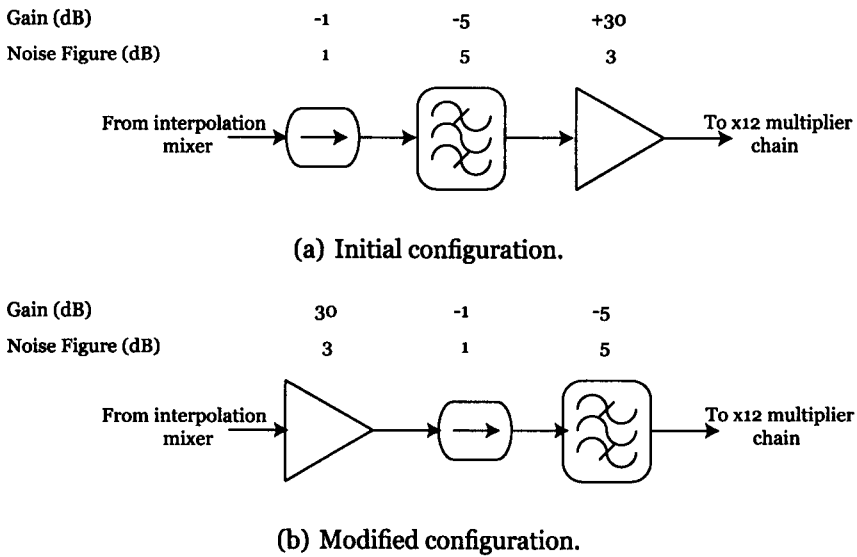


Figure 11.17: Two possible configurations of the post interpolation mixer components.

effect due to the mixer.

Suspicion must therefore fall on the post mixer amplifier-filter combination. Figure 11.17 shows two possible combinations of these components. Figure 11.17(a) shows the basic post filter components in the configuration employed above, whilst figure 11.17(b) shows an alternative configuration in which basically the order of the filter and amplifier has been reversed.

The noise temperature of the interpolation chain shown in figure 11.17(b) was measured using the Y factor approach; a power variation of 0.6dB between hot and cold loads was measured corresponding to a noise temperature of 1394K.

The noise figure of the cascades shown in figure 11.17 may be calculated using equation 11.10. It is found that for figure 11.17(a) the estimated cascade noise figure is $f_{cas}=7.948$ (~ 9 dB) whilst for figure 11.17(b) a value of

11.4. AN 1800MHZ DEMODULATOR

$f_{cas}=1.998$ ($\sim 3\text{dB}$) is estimated. The results are not unexpected, the amplifier gain ensures that the contribution to the cascade noise figure of components after the filter may be neglected.

The noise figures have a ratio of 4:1. If the excess down convertor noise is due to the post mixer components we would expect a noise temperature of $(9282/4)\text{K}$ or 2300K . Because the measurement exceeds this improvement it is concluded that the filter has either a 2dB higher insertion loss than expected or has a 3dB higher than expected noise figure.

11.4 An 1800MHz Demodulator

In the introduction to this chapter, it was indicated that having down converted the 94GHz signal to 1.8GHz , a homodyne demodulator would be employed to produce a baseband signal which would be suitable for further processing to obtain the spectrum borne by the 1.8GHz IF signal.

11.4.1 The 1800MHz source

Homodyne demodulation requires that the signal to be demodulated being carried by a signal, in this case at the IF frequency, be mixed with an unmodulated signal at the IF frequency. Equation 11.4 shows that the carrier (IF) frequency at the output of the down convertor is simply $12\times$ the interpolation oscillator frequency.

The circuit used to perform this multiplication is shown in figure 11.18. The network involving IC1 is a simple voltage regulator. Q1 and Q2 are respectively a doubling stage and a tripling stage, which take the 150MHz input to

11.4. AN 1800MHZ DEMODULATOR

900MHz. Doubling this to 1800MHz in a bipolar stage would be possible. However this requires very careful layout and would have been an iterative process. The approach taken was to employ a commercially available balanced doubler, in this case the HMC187SM8 (IC2). Amplifier IC5 takes the 900MHz available at the collector of Q2 and produces sufficient drive for IC2. The output of this doubler is then filtered (using Helical filters FL1 and FL2) and further amplified to produce +10dBm, which is sufficient to drive a diode ring mixer.

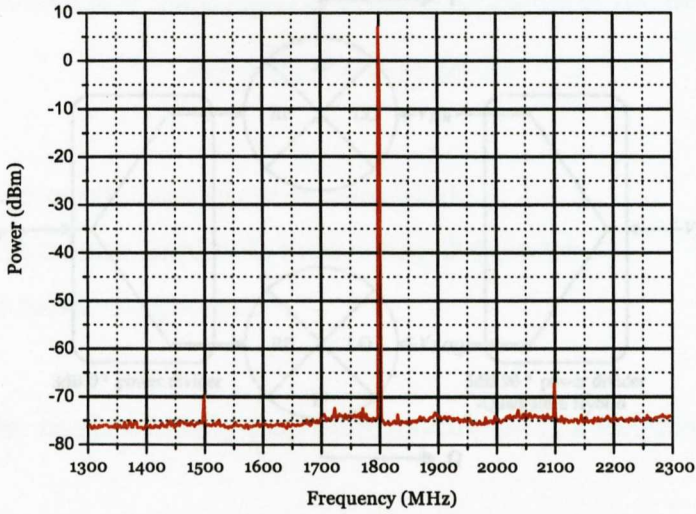
The output spectrum of the multiplied source when driven with the 150MHz crystal oscillator (XCO) is shown in figure 11.19. The harmonic purity of the multiplied output with no spuri greater than -70dBc, reflects the use of helical filters in the multiplier chain output.

The phase noise content of the multiplied XCO reflects the phase noise of the driving XCO degraded by $20 \log(n)$ dB. This phase noise result was used to obtain the 'corrected' phase noise spectrum of the XCO shown in figure 11.9(b). The multiplier must degrade the phase noise spectrum of the XCO by a minimum of 21.6dB; the fact that the phase noise agreement between the corrected and measured phase noise curves in the 'hump' of figure 11.9 is so good indicates that there is minimal additional phase noise introduced by the multiplier chain circuitry.

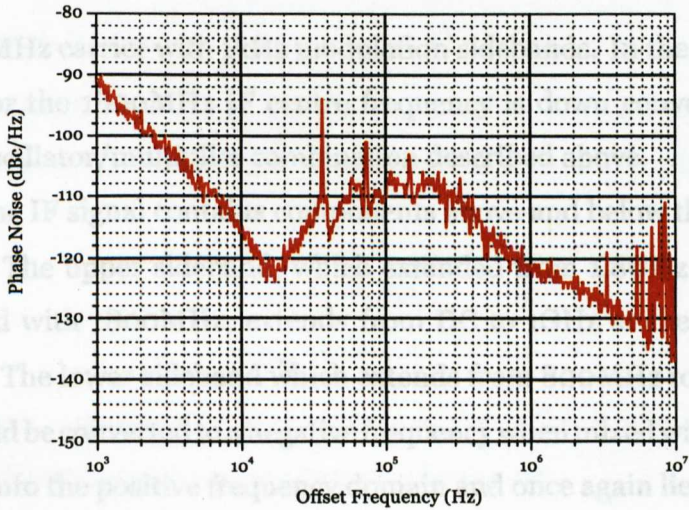
11.4.2 The homodyne stage

The IF signal is a frequency translated copy of the 94GHz signal returned from the sample and therefore for a 1ns pulse the demodulator input should ideally extend from 800MHz to 2.8GHz. This will also accommodate a CW experiment with a 1kHz field modulation for which the IF signal will consist

11.4. AN 1800MHZ DEMODULATOR



(a) Harmonic spectrum



(b) Phase noise spectrum

Figure 11.19: The harmonic and phase noise spectra of the x12 (150MHz to 1800MHz) multiplier when driven with the 150MHz XCO. The actual power output is in excess of +10dBm.

11.4. AN 1800MHZ DEMODULATOR

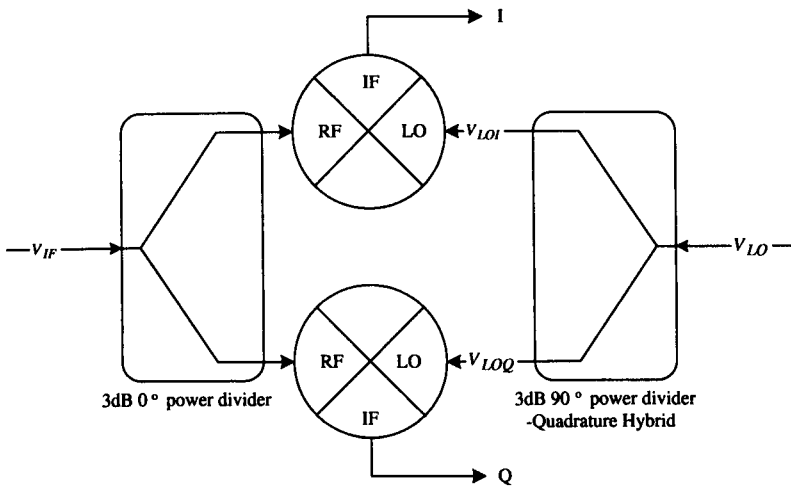


Figure 11.20: A two channel Homodyne demodulator.

of an 1800MHz carrier with 1kHz modulation sidebands. In the Homodyne demodulator the 1800MHz IF centre frequency is down converted to DC using the oscillator/multiplier combination described above.

However, the IF signal contains components above and below the IF centre frequency. The upper sideband, which extended from 1.8GHz to 2.8GHz, when mixed with 1800MHz, extends from DC to 1GHz at the demodulator output. The lower sideband which extends from 800MHz to 1800MHz, which should be converted to a negative frequency when mixed with 1800MHz, folds back into the positive frequency domain and once again lies in a bandwidth of DC to 1GHz. Thus the 2GHz wide signal at the demodulator input has a 1GHz bandwidth at the demodulator output.

The sideband ambiguity is resolved using an I-Q demodulator. Consider figure 11.20. The input signal, centered at 1800MHz is divided into two equal amplitude signals which are applied to individual mixers. The input

11.4. AN 1800MHZ DEMODULATOR

signal is assumed to be an amplitude modulated signal of the form

$$V_{IF} = A_o [1 + \alpha(t)] \sin \omega_c t \quad (11.15)$$

where

A_o is the unmodulated IF carrier amplitude

$\alpha(t)$ is the function amplitude modulating the carrier

ω_c is the carrier frequency

let the carrier be sinusoidally amplitude modulated at a frequency ω_m , such that

$$\alpha(t) = A_m \sin \omega_m t \quad (11.16)$$

In which case the input signal has the form

$$V_{IF} = A_o A_m \sin \omega_c + \frac{A_o}{2} [\cos (\omega_c - \omega_m) t - \cos (\omega_c + \omega_m)] \quad (11.17)$$

The two LO signals V_{LOI} and V_{LOQ} are in quadrature. They are derived from a single LO source (V_{LO}) using a 3dB Quadrature Hybrid and may be expressed as

$$V_{LOI} = \sin \omega_c t \quad (11.18)$$

$$V_{LOQ} = \cos \omega_c t \quad (11.19)$$

In which case, assuming mixer products at twice the applied carrier frequency are filtered out, the mixer output voltages are

$$V_I = \frac{A_m A_o}{4} \sin \omega_m t \quad (11.20)$$

$$V_Q = \frac{A_m A_o}{4} \cos \omega_m t \quad (11.21)$$

Now clearly, either of the output signals could be simply power detected using a diode detector for example. However combining these signals gives

$$\sqrt{V_I^2 + V_Q^2} = \frac{A_m A_o}{\sqrt{8}} \quad (11.22)$$

11.4. AN 1800MHZ DEMODULATOR

which is proportional to the amplitude of the signal returned from the cavity. Now consider the case in which the input signal acquires a small phase shift. By writing

$$V_{IF} = A_o \sin(\omega_c + \varphi) t \quad (11.23)$$

and following an exactly analogous route to that outlined above, it is shown that

$$V_I = \frac{A_o}{4} \sin(\varphi) \quad (11.24)$$

$$V_Q = \frac{A_o}{4} \cos(\varphi) \quad (11.25)$$

which may be combined to give

$$\varphi = \arctan \frac{V_I}{V_Q} \quad (11.26)$$

which may be used to correct for errors introduced by dispersive loading of the cavity. It should be noted that the amplitude result of equation 11.22 is independent of phase and that the phase result of equation 11.26 is independent of amplitude. This method of demodulation is known as IQ demodulation. The quadrature I and Q signals are now post processed to obtain the required ESR spectrum.

11.4.2.1 Demodulator realisation

The circuit of the demodulator is shown in figure 11.21.

The above analysis was carried out with the quadrature signal at the fixed LO frequency. Using microstrip techniques it is reasonably easy to obtain accurate quadrature over a narrow bandwidth [202], it would be very difficult to obtain an exact quadrature over the full IF bandwidth from a single component. On the other hand, an accurate zero degree power division may

11.4. AN 1800MHZ DEMODULATOR

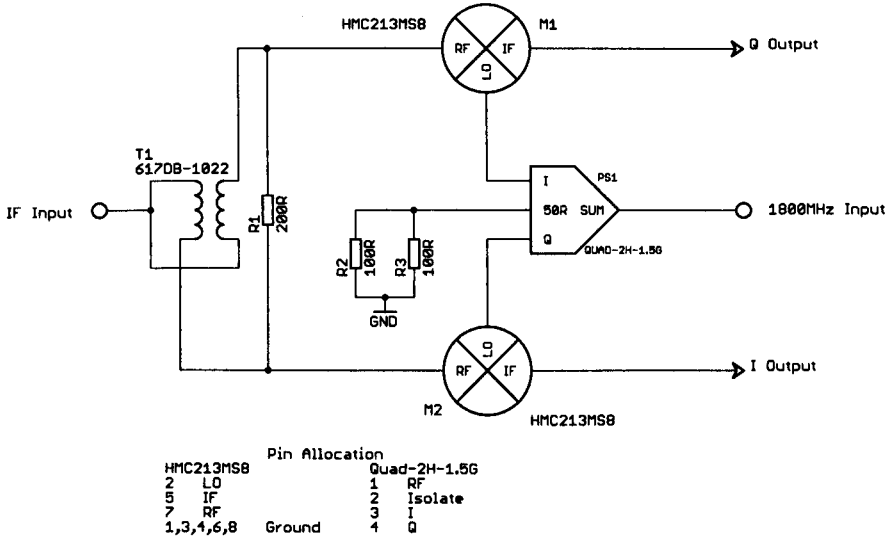


Figure 11.21: Circuit diagram of the IQ demodulator.

be obtained with relative ease over the full IF bandwidth using transformers. The IQ demodulator was implemented using available components. The bandwidths required by the mixer ports were established above. In an attempt to keep the IF bandwidth as wide as possible it was necessary to employ a mixer with a less than optimum RF bandwidth: the Hittite HMC213MS8 has an IF bandwidth of 1.5GHz with an RF bandwidth of 1.5GHz to 4.5GHz. The input power division is provided by transformer T1, which is more appropriately considered as a transmission line system and has a bandwidth of 4.5MHz to 3.3GHz. The required quadrature signals are provided by the 'hybrid quad' PS1, which is a component intended for use in cellular applications and which is centred at 1.8GHz.

11.4. AN 1800MHZ DEMODULATOR

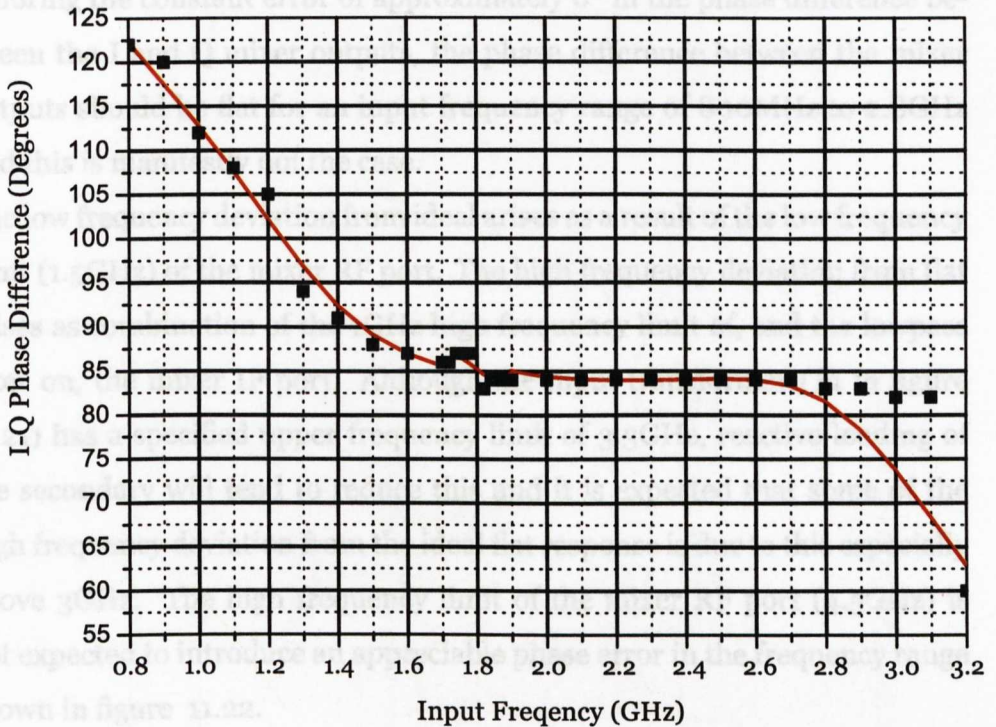


Figure 11.22: The phase balance of the initial IQ demodulator

Demodulator performance

The key parameters for successful operation of the IQ demodulator are the phase difference between, and the amplitude balance of the I and Q outputs. The deficiencies imposed on the demodulator as realised in figure 11.21 may be observed in the phase difference between the I and Q channels shown in figure 11.22. This measurement was made with the IF outputs terminated in 1650MHz lowpass filters to reduce the distortion on the measurements introduced by the leakage of 1800MHz between the LO and IF ports of the mixers.

11.5. THE COMPLETE HETERODYNE DEMODULATOR

Ignoring the constant error of approximately 6° in the phase difference between the I and Q mixer outputs, the phase difference between the mixer outputs should be flat for an input frequency range of 800MHz to 2.8GHz and this is manifestly not the case.

The low frequency deviation from ideal arises as a result of the low frequency limit (1.5GHz) of the mixer RF port. The high frequency deviation from flat arises as combination of the 1GHz high frequency limit of, and the lowpass filter on, the mixer IF port. Although the input transformer (T₁ in figure 11.21) has a specified upper frequency limit of 3.3GHz, reactive loading of the secondary will tend to reduce this and it is expected that some of the high frequency deviation from the ideal flat response is due to this especially above 3GHz. The high frequency limit of the mixer RF port (4.5GHz) is not expected to introduce an appreciable phase error in the frequency range shown in figure 11.22.

The permanent off set from 90° , probably arises due to a phase error in the 1800MHz quadrature hybrid, which in this case is compounded by unequal trace lengths in the PCB layout. This is not of its self a problem because it may be compensated for in the post demodulator processing.

11.5 The Complete Heterodyne Demodulator

The complete heterodyne spectrometer capable of generating and detecting pulses on a ns pulse capability may now be constructed. The complete block diagram of such an instrument is shown in figure 11.23 in which all the previously described components may be identified.

Due to the high noise floor of the heterodyne detector when driven from

11.5. THE COMPLETE HETERODYNE DEMODULATOR

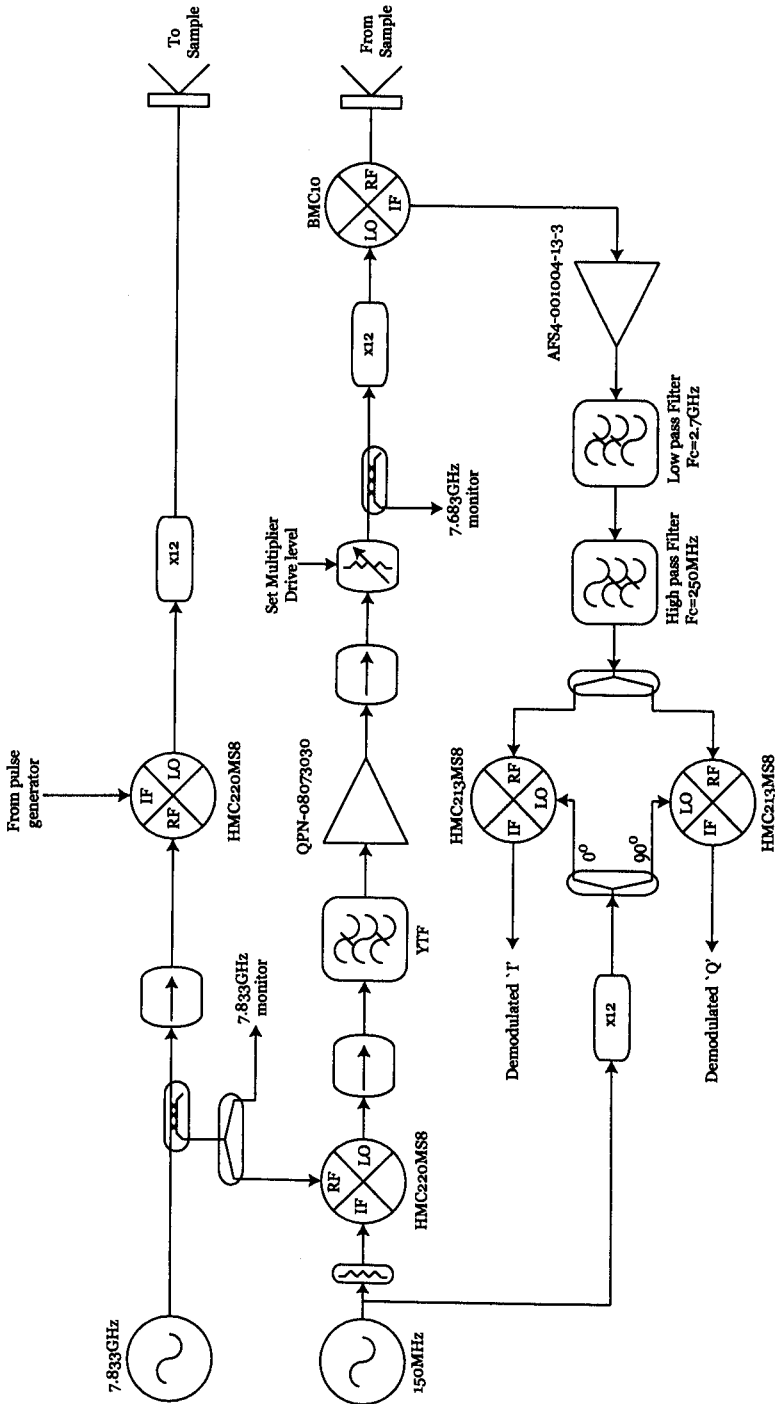


Figure 11.23: The complete heterodyne spectrometer.

11.5. THE COMPLETE HETERODYNE DEMODULATOR

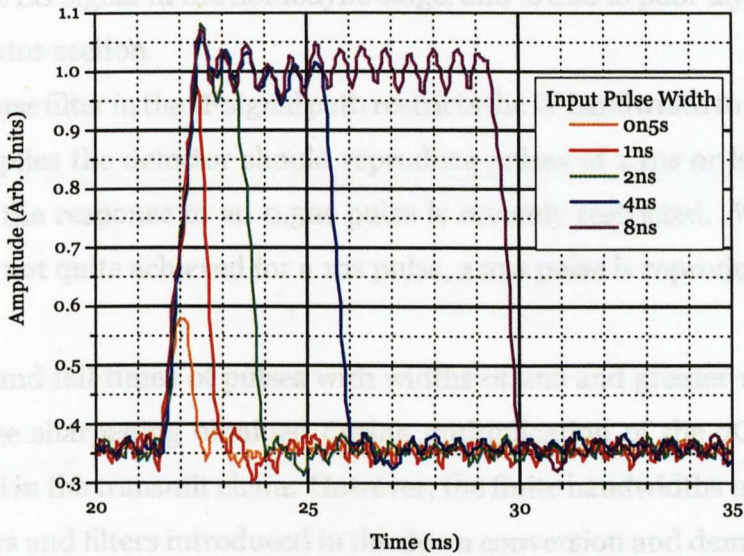


Figure 11.24: The pulse response of the complete Heterodyne demodulator.

Pulse widths are defined at the pulse generator output.

the interpolation chain, the system is not able to produce an ESR spectrum, however it is possible to demonstrate that the system will respond to pulses on a ns timescale.

The pulse response of the system is demonstrated by coupling the transmit chain ('to sample') output to the detector ('from sample') input by allowing the apertures of the two horns shown in figure 11.23 to face each other. By inserting an attenuator between the transmit chain multiplier output and the transmit (to sample) horn, the power in the system could be adjusted to prevent saturation of the demodulator. The required pulse output may be observed on either the I or the Q output and is shown for various pulse widths in figure 11.24. The pulse response was observed using only the 'Q' channel. The large ripple observed on the pulse output is leakage of the

11.5. THE COMPLETE HETERODYNE DEMODULATOR

1800MHz LO signal in the homodyne stage, and is due to poor layout of the demodulator section.

The low pass filter in the IF signal path restricts the IF bandwidth to 900MHz, which implies the detector should reproduce pulses of 1.1ns or longer. As expected the response to an 0.5ns pulse is severely restricted. Whilst full fidelity is not quite achieved for a 1ns pulse, a 2ns pulse is reproduced accurately.

The rise and fall times of pulses with widths of 2ns and greater reflect the pulse edge sharpening obtained during multiplication of the 7GHz pulse generated in the transmit chain. However, the finite bandwidths of the various mixers and filters introduced in the down conversion and demodulation processes have increased the rise time from 76ps to approximately 500ps.

There are also distortions within the pulse. Both the rising and trailing edges shows some overshoot and this is a consequence of the IF shaping filters having a Butterworth response, in practice these filters need to be Gaussian to prevent such overshoot.

CHAPTER 12

Conclusions and Further Work

This thesis has described the design and construction of components for a new state of the art high field ESR spectrometer operating at 94GHz which is capable of both CW and pulse operation.

The challenges of measuring the phase noise spectrum of oscillators at 7GHz and sources at 94GHz have been addressed and a low phase noise source, which provides both the main spectrometer and demodulator local oscillator signals, has been described. The oscillator configuration allows fast (sub ns) phase coherent pulses to be produced at 94GHz.

A heterodyne detector consisting of a 94GHz to 1.8GHz down convertor followed by a 1.8GHz IQ demodulator has been constructed. This detector has an IF bandwidth of 2GHz and a bandwidth of 1GHz at the IQ demodulator output which allows the detector to respond to pulses on a ns time scale. The detector also demonstrates a noise temperature of 740K which compares favourably with the 2000K noise temperature of the Helium cooled bolome-

ter currently used at 94GHz.

Whilst it has been shown that the basic components designed have the required performance for use in a CW spectrometer it is necessary to integrate the complete system into a spectrometer. This will be completed in the next few months.

There are several areas in which further work is required to optimise the performance of these circuits. Perhaps most importantly, the noise temperature of the interpolation chain based down convertor must be reduced from the current 1400K towards the 740K obtained when driven from the DRO. This will optimise the sensitivity of the spectrometer.

The use of a multiplier chain to obtain the 1800MHz signal required in the homodyne demodulator requires investigation. Multiplication produces a low phase noise close to carrier and is suitable for CW work. However, the multiplier raises the far-out noise floor at the output of the multiplier which potentially reduces the sensitivity of the spectrometer in pulsed mode. This is expected to be solved by using an 1800MHz oscillator phase locked to the 150MHz interpolation oscillator. This will not change the CW sensitivity, but will reduce the influence of the 1800MHz noise floor on the pulse spectrometer sensitivity.

The long term stability of the master oscillator must be sufficient to ensure that the source frequency does not change significantly during a measurement. This may be ensured by placing the DRO in a thermally stable environment. If some degree of tunability is required, the DRO may be replaced by a PMYTO. The long term stability of the PMYTO has not been investigated since it was assumed that it could be phase locked to an available EIP counter. However, the EIP counter produces close to carrier discrete spuri which detract from the desired spectral purity of the source. It may well

be necessary to ensure the long term stability and tunability of the PMYTO by phase locking to a DDS signal derived from the 150MHz interpolation oscillator.

Finally, simple modifications allow the techniques described in this thesis to be employed at higher frequencies. Essentially, only the multiplication factors employed to obtain the final main spectrometer and LO signals and the frequency of the interpolation oscillator need to be changed.

Assuming a starting frequency of 7.833GHz for a 188GHz instrument, the required multiplication factor for both signals is 24. High efficiency doublers for the main spectrometer signal are available which are able to deliver in excess of 50mW (+17dBm) at 188GHz. The down conversion mixer could be changed to a suitable sub-harmonic mixer. Then, assuming an 1800MHz IF frequency, the interpolation oscillator frequency changes to 75MHz and the 1800MHz generation scheme changes accordingly. This series of changes would produce a state of the art CW and a pulsed spectrometer at 188GHz. For higher frequencies, a higher IF frequency should be considered thus allowing a reasonable rejection of the unwanted interpolation mixer outputs by the YTF.

APPENDIX A

Evaluation of Modified Bessel Functions

McLachlan [152] gives the integral form of the generating function of modified Bessel functions of order p and argument x as

$$I_p(x) = \frac{1}{\pi} \int_0^\pi e^{x \cos \theta} \cos p\theta d\theta \quad (\text{A.1})$$

This equation is not (easily) hand integrable, it is evaluated numerically. It will be evaluated for $0 \leq p \leq 5$ and $x = 0.1, 0.3, 0.5, 1, 3, 5, 10$. These values are then used directly in equation (5.9) to calculate the normalized amplitude of the p^{th} harmonic of an exponential sine function.

There are various ways in which this integration may be performed numerically. Gaussian Quadrature is the method of choice because it has computational simplicity and a high degree polynomial fit with few calculations. The disadvantage of this scheme is that some mathematical effort is required to place the integrand in a form suitable for this type of quadrature.

The process of performing the quadrature is to transform the integral according to

$$\int_a^b f(\theta)d\theta = \int_{-1}^{+1} g(\phi)d\phi \quad (\text{A.2})$$

using the linear transformation

$$\theta = m\phi + c \quad (\text{A.3})$$

and forcing $\phi = 1$ at $\theta = b$ and $\phi = -1$ at $\theta = a$. Under this transformation the integral may be stated as

$$\int_{-1}^{+1} g(\phi)d\phi = \sum_{i=1}^n w_i g(\phi_i) \quad (\text{A.4})$$

where ϕ_i are the points at which the quadrature is performed (the abscissas), and w_i are weighting functions. We are now able to transform, and thus solve (A.1).

$$f(\theta) = e^{x \cos(\theta)} \cos(p\theta) d\theta \quad (\text{A.5})$$

Then using (A.3) and forcing limits we obtain $c = \frac{\pi}{2}$ and $m = \frac{\pi}{2}$. Then (A.1) becomes

$$I_p(x) = \frac{1}{2} \int_{-1}^{+1} e^{x \cos(\frac{\pi}{2}\phi + \frac{\pi}{2})} \cos(\frac{p\pi}{2}\phi + \frac{p\pi}{2}) d\phi \quad (\text{A.6})$$

Note the change in multiplicative constant, which reflects the change in limits of integration. This slightly simplifies to

$$I_p(x) = \frac{1}{2} \int_{-1}^{+1} e^{x \sin(\frac{\pi}{2}\phi)} \cos(\frac{p\pi}{2}\phi + \frac{p\pi}{2}) d\phi \quad (\text{A.7})$$

We may now write

$$g(\phi_i) = e^{x \sin(\frac{\pi}{2}\phi_i)} \cos(\frac{p\pi}{2}\phi_i + \frac{p\pi}{2}) \quad (\text{A.8})$$

For an n^{th} Quadrature scheme, the abscissas are the zeros of a Legendre polynomial of order n . The weighting factors are related to the abscissas

and derivatives of Legendre polynomials. The abscissas and weights for a selection of Quadrature orders are tabulated in [89]. Should tables not contain the required coefficients it will be necessary to calculate them.

The zeros of a high order Legendre polynomial are somewhat difficult to calculate by hand. Evaluation of the required derivatives is a source of additional work and error. It would appear that Gaussian Quadrature is not an attractive proposition, despite it's polynomial fitting advantage over other methods.

However, the evaluation of polynomials, and their zeros is trivial in algebraic manipulation packages. Thus the abscissas require little effort. This still leaves the weights. Hildebrand [203] gives the weights as

$$w_i = \frac{2(1 - \phi_i^2)}{(n + 1)^2 [P_{n+1}(\phi_i)]^2} \quad (\text{A.9})$$

Which requires the evaluation of the $(n + 1)^{th}$ degree Legendre polynomial at the i^{th} abscissa, a task which is trivial in an algebraic manipulation package. The package of choice is Maple. The following Maple work sheet calculates the abscissas and weighting functions. The abscissas are evaluated using the `RootsOf()` statement, whilst the weights are evaluated using the `evalf(P(m,x))` where P inside the "orthopoly" package is the Legendre polynomial.

```

> restart;
> Digits:=15:
> with(orthopoly):
> n:=8:
> m:=n+1:
> t:=[evalf(allvalues(RootOf(P(n,x))))]:
> for i from 1 to n do
> t[i]:=Re(t[i])
> end do:
> for i from 1 to n do
> w[i]:=2*(1-t[i]^2)/(m*eval(P(m,x),x=t[i]))^2;
> end do:
> printf("Abcissa      Weight\n"):for i from 1 to n do
> printf("%18.15f      %18.15f\n",t[i],w[i])
> end do;

```

Abcissa	Weight
.960289856497533	.101228536290644
-.960289856497533	.101228536290644
.796666477413627	.222381034453368
-.796666477413627	.222381034453368
.525532409916331	.313706645877898
-.525532409916331	.313706645877898
.183434642495645	.362683783378358
-.183434642495645	.362683783378358

This worksheet produces the parameters required for a 8 point Quadrature; to obtain the parameters for other orders it is necessary to change the "n:=8:" statement.

The values of abscissas and weights obtained from this worksheet have been used in a FORTRAN program to calculate modified Bessel functions using both 8 and 16 point quadrature. The values are shown at the end of this appendix.

As with any numerical scheme, errors are important. In the case of the Maple routine, the errors are outside our control. By specifying "Digits:=15" the worksheet is calculating in a double precision mode. The real problem arises in the worksheet with the definition of zero. The roots of $P(n,x)$ are real; however, occasionally Maple returns a complex number. The complex part is invariably small, of order 10^{-10} (or smaller) which is small in comparison to the real part. Thus to all intents and purposes the real part and magnitude are the same. However, unless steps are taken, the worksheet will fail because the evaluation of the weighting factors requires a real number. The statement "t[i]=Re(t[i])" solves this problem. The question of zero in computational algebra schemes is discussed in Heck [204], which also gives additional references.

In an iterative scheme the usual technique for establishing error is to continue iteration until some required arbitrary accuracy has been arrived at. This scheme is closed, and agreeing an accuracy requires repeated determination of abscissas and weights and comparison of tabular results. In evaluating the integral there are a number of potential sources of error. These may be broadly characterized as truncation and numerical errors. Truncation errors arise because the polynomial fit is only approximate; in effect we truncate an infinite expansion of the function. The truncation error for a 16 point Quadrature is small, being of order 10^{-34} . Clearly however, we have a bigger problem than this. In this case the error arises because of the speed with which $I_p(x)$ varies at high values of x . In this case it would appear likely that

as the order of Quadrature is increased the values of the modified Bessels function will oscillate about the true value showing a slow convergence to the true value.

The acceptable accuracy of a numerical solution depends upon application. Here, the error between 10 and 16 point Quadrature is less than 15% which is sufficient for the intended application.

Modified Bessel Functions Using 8 Point Quadrature						
x	n=0	n=1	n=2	n=3	n=4	n=5
0.10	1.0025	0.0501	0.0013	0.0000	0.0000	0.0001
0.30	1.0226	0.1517	0.0113	0.0006	0.0000	0.0002
0.50	1.0635	0.2579	0.0319	0.0026	0.0002	0.0002
1.00	1.2661	0.5652	0.1357	0.0222	0.0028	0.0001
3.00	4.8808	3.9533	2.2450	0.9585	0.3215	0.0831
5.00	27.2383	24.3330	17.5001	10.3252	5.1273	2.2925
10.00	2.8173e3	2.6736e3	2.2875e3	1.7707e3	1.2469e3	801.743

Modified Bessel Functions Using 16 Point Quadrature						
x	n=0	n=1	n=2	n=3	n=4	n=5
0.10	1.0025	0.0501	0.0013	0.0000	0.0000	0.0000
0.30	1.0226	0.1517	0.0113	0.0006	0.0000	0.0000
0.50	1.0635	0.2579	0.0319	0.0026	0.0002	0.0000
1.00	1.2661	0.5652	0.1357	0.0222	0.0027	0.0003
3.00	4.8808	3.9534	2.2452	0.9598	0.3257	0.0912
5.00	27.2399	24.3356	17.5056	10.3311	5.1082	2.1580
10.00	2.8157e3	2.6709e3	2.2815e3	1.7584e3	1.2265e3	777.189

BIBLIOGRAPHY

- [1] Robert C. Weast, editor. *Handbook of Chemistry and Physics*. CRC Press, 57 edition, 1976.
- [2] P. Zeeman. The Effect of Magnetisation on the Nature of Light Emitted by a Substance. *Nature (Translation from Proc. Phys. Soc. Berlin by A. Stanton; see <http://dbhs.wvusd.k12.ca.us/webdocs/Chem-History/Zee-man-effect.htm>- checked 04-10-05)*, 55:347, 1897.
- [3] H. Okamura M. Ohta, M. Yashuda. Susceptibility of Calcium Deficient Hydroxapatite Collagen Composite to Irradiation. *Radiation Protection Dosimetry*, 94(4):385–388, 2001.
- [4] P.S Rao J.K Dash, S. Balakrishman. A Preliminary Study on Application of EPR in Dating Marine Shells Along the Podicherry Coast India. *Advances in ESR Applications*, 18:41–46, 2002.
- [5] Tadashi Yoshida Masao Ikeda-Saito, Hiroshi Fujii. Heme Oxygenase Active Site Structure Studied by EPR of Cobalt(ii) Porphrin-Enzyme Complex. *RIKEN Review*, pages 53–55, 1999.

BIBLIOGRAPHY

- [6] T.Yonetani. Structural and functional regulation of hemoglobin by nitric oxide as studied by EPR spectroscopy. *RIKEN Review*, 24:51–52, 1999.
- [7] Wolfgang Lubitz. *Electron Paramagnetic Resonance Volume 19*, chapter 5: EPR in Photosynthesis. The Royal Society of Chemistry, 2000.
- [8] Thomas P. Sakmar Steven O. Smith Ted Shieh, May Han. The Steric Trigger in Rhodopsin Activation. *Journal of Molecular Biology*, 269:373–384, 1997.
- [9] G.R. Buettner V.G.J. Rodgers S.F. Oppenheim, J.O. Rich. Protein Structure Change on Adherence to Ultra-filtration Membranes: An Examination by Electron Paramagnetic Spectroscopy. *Journal of Colloid and Interface Science*, 183:274–279, 1996.
- [10] Harold J. Swartz. The use of nitroxides in biable biological systems: an opportunity and challenge for chemists and biochemists. *Pure and Applied Chemistry*, 62:235–239, 1990.
- [11] Victoria J. DeRose Nak-Kyoon Kim, Ayaluru Murali. A Distance Ruler for RNA using EPR and Site-Directed Spin Labeling. *Chemistry and Biology*, 11:939–948, 2004.
- [12] G.V Martinez R.G Griffin D.J Singel G.L Millhauser M. Bennati, G.J Gerfen. Nitroxide Side Chain Dynamics in Spin-Labeled Helix Forming Peptide Revealed by High Frequency (193.5GHz) EPR. *Journal of Magnetic Resonance*, 139:281–286, 1999.

BIBLIOGRAPHY

- [13] Sanhyuk Lee Injae Shin, Hyuk Jun Jung. Synthesis of Doubly Labeled Mono- and Disaccharides and their EPR Spectra in Different Solvents. *Bulltin Korean Chemical Society*, 21(11):1067–1068, 2000.
- [14] Murali C. Krishna Periannan Kuppusamy. EPR Imaging of Tissue Redox Status. *Current Topics in Biophysics*, 26(1):29–34, 2002.
- [15] Kai Pan Chi-Wei Hsu Tong-Ing Ho, Chiou-Rong Lin. Spin Trapping Studies on Radical Cations of Styrene. *Journal of the Chinese Chemical Society*, 48:983–986, 2001.
- [16] D.G Blair A.N Luiten, A.G Mann. Paramagnetic Susceptibility and Permittivity Measurements at Microwave Frequencies in Cryogenic Sapphire Resonators. *Journal of Physics D:Applied Physics*, 29:2082–2090, 1996.
- [17] R. Clerac R. Moret P. Launois J. Hone C. Coulson, A. Penicaud. Metal-Insulator and Structural Phase Transitions Observed by ESR Spectroscopy and X-Ray Diffraction in KC_{60} . *Physical Review Letters*, 86(19):4346–4394, 2001.
- [18] Ferec Muranyi Titusz Feher Hideo Shimoda Yoshihiro Iwasa Laszlo Forro Ferenc Simon, Andreas Janossy. Magnetic Resonance in the Antiferromagnetic State and Normal State of $NH_3K_3C_{60}$. *Physical Review B*, 61(6):3826–3829, 2000.
- [19] Anna-Lisa Maniero Louis C. Brunel Dennis Arcon, Kosmas Prassides. Low temperature Magnetic Instabilities in Triply Charged Fulleride Polymers. *Physical review Letters*, 84(3):562–565, 2000.
- [20] Wolfgang Harneit. A fullerene-based electron spin quantum computer. *Physical Review A*, 65:032322, 2002.

BIBLIOGRAPHY

- [21] W.C. Holton, H. Sierzputowska-Gracz, E.O. Stejskal, David Collins, K.W. Kim. NMR quantum computation with directly coupled gates. *Physical Review A*, 62:022304, 2000.
- [22] S. Gasiorowicz. *Quantum Physics*. John Wiley, 2 edition, 1996. ISBN 0-471-85737-1.
- [23] P.C. Mathews. *Vector Calculus*. Springer-Verlag, 2002. ISBN 3-540-76180-2.
- [24] S. Flugge. *Practical Quantum Mechanics*, volume 2. Springer-Verlag, 1974. ISBN 0-387-07050-8.
- [25] F. Bloch. Nuclear Induction. *Physical Review*, 70(7 and 8):460–474, October 1946.
- [26] Gerald Gabrielse, Lowell S. Brown. Geonium theory: Physics of a single electron or ion in a Penning trap. *Reviews of Modern Physics*, 58(1):233–311, January 1986.
- [27] Hans Dehmelt. Less is more: Experiments with an individual atomic particle at rest in free space. *American Journal of Physics*, 58(1):17–27, January 1990.
- [28] H.G. Dehmelt, P.B. Schwinberg, R.S. Van Dyck. New comparison of the Positron and Electron g Factors. *Physical Review Letters*, 47(24):1679–1682, December 1981.
- [29] N.M. Atherton. *Principles of Electron Spin Resonance*. Prentice Hall, 1993.

BIBLIOGRAPHY

- [30] Li Gu Xuebo Cao. Spindly cobalt ferrite nanocrystals: preparation, characterization and magnetic properties. *Nanotechnology*, 16:180–185, 2005.
- [31] W.W.Ruhle M. Oestreich. Temperature Dependence of the Electron Lande g Factor in GaAs. *Physical Review Letters*, 74(12):2315–2328, March 1995.
- [32] Charles P. Poole JR. *Electron Spin Resonance*. Dover, 1996.
- [33] John E. Wertz John A. Weil, James R. Bolton. *Electron Paramagnetic Resonance Elementry Theory and Practice*. John Wiley and Sons, 1994.
- [34] Gunnar Jeschke Arthur Schweiger. *Principles of pulse electron paramagnetic resonance*. Oxford University Press, 2001.
- [35] P.C.M Christianen U. Zietler J.C Maan J.A.A.J Perenboom, S.A.J Wiegers. Research in High Magnetic Fields: The Installation at the University of Nijmegenr. *Journal of Low Temperature Physics*, 133(1-2):181–201, October 2003.
- [36] W.S Marshall C.A Swenson A. Gavrilin H.J Scneider-Muntau. Development of ‘Fast Cool’ pulse magnet coil technology a NHMFL. *Physica B*, 346-347:594–598, 2004.
- [37] J.H. Van Vleck. The Dipolar Broadening of Magnetic Resonance Lines in Crystals. *Physical Review*, 74(9):191168–1183, November 1948.
- [38] K.W.H Stevens B. Bleaney. Paramagnetic Resonance. *Reports on Progress in Physics*, 16:108–159, 1953.

BIBLIOGRAPHY

- [39] G. Feher. Sensitivity Considerations in Microwave Paramagnetic Resonance Absorption Techniques. *The Bell System Technical Journal*, 36:449–484, March 1957.
- [40] P.C. Riedi G.M. Smith. *Electron paramagnetic resonance*, volume 17. The Royal Society of Chemistry, 2000.
- [41] J. Berliner Oleg Y. Grinberg, editor. *Very High Frequency (VHF) ESR/EPR*, volume Biological Magnetic Resonance 22. Kluwer Academic/Plenum Publishers, 2004.
- [42] J.R. Barker. *Mechanical and Electrical Vibrations*. Methuen & Co Ltd, 1964.
- [43] G.Weber J. Grambow. Measurement of the magnetic ac susceptibility at frequencies between 2MHz and 1GHz: zero field spin-spin relaxation of cerium- and neodymium- magnesium nitrate at 4.2K. *Journal of Physics E: Scientific Instruments*, 4:865–867, 1971.
- [44] C. Starr. Paramagnetic Dispersion Measurements at 77.3K. *Physical Review*, 60:241–249, August 1941.
- [45] Robert E. Collin. *Foundations For Microwave Engineering*. McGraw-Hill, 1992.
- [46] Guillermo Gonzalez. *Microwave Transistor Amplifiers*. Prentice Hall, 1 edition, 1984. ISBN 0-13-581646-7.
- [47] George G. Vendelin. *Design Of Amplifiers And Oscillators By The S-Parameter Method*. John Wiley and Sons, 1 edition, 1982. ISBN 0-471-09226-6.

BIBLIOGRAPHY

- [48] Greg R. Smith-Keith Earle David E. Budil, Zhebo Ding. Jones Matrix Formalism for Quasioptical EPR. *Journal of Magnetic Resonance*, 144:20–34, 2000.
- [49] Michael D. Janezic Kevin J. Coakley, Jolene D. Splett. Estimation of Q-Factors and Resonant Frequencies. *IEEE Trans. Microwave Theory and Techniques*, 51(3):862–868, March 2003.
- [50] A.J. Baden Fuller. *Ferrites at microwave frequencies*. Electromagnetic waves. Peter Peregrinus Ltd., 1987.
- [51] M. Packard F.Bloch, W. W. Hansen. The Nuclear Induction Experiment. *Physical Review*, 70(7 and 8):474–489, October 1946.
- [52] W.G. Proctor. On the Magnetic Moments of Tl^{203} , Tl^{205} , Sn^{117} , Sn^{119} , Cd^{111} , Cd^{113} , Pb^{207} . *Physical Review*, 79(1):35–44, 1950.
- [53] H.E. Weaver Jr. Magnetic Moments of Si^{29} , S^{33} , Zn^{67} , As^{75} , Se^{77} , Te^{123} , Te^{125} . *Physical Review*, 89(5):923–930, 1953.
- [54] W.K. Campe E.A. Richards, G. Philips. A sensitive and stable nuclear induction head. *Journal of Scientific Instruments*, 33:260–262, July 1956.
- [55] Cafiero Franconi. Microwave Cavity Analogs of Bloch Inductors. *Review of Scientific Instruments*, 41:148–149, 1970.
- [56] M. Puglisi G. Conciauro. Bimodal Inductors for EPR Spectroscopy. *Journal of Magnetic Resonance*, 9:363–377, 1973.
- [57] R.I. Hunter. *Characterisation of Ferrite and Dielectric Materials and their use in Millimetre-Wave Quasi-Optical Devices*. Ph.D. thesis, School of Physics and Astronomy University of St. Andrews, 2004.

BIBLIOGRAPHY

- [58] Jack H. Freed. New Technologies in Electron Spin Resonance. *Annual Review of Physical Chemistry*, 51:655–89, 2000.
- [59] R. Clark Jones. A New Calculus for the Treatment of Optical Systems. *J. Optical Society of America*, 31:488–493, 1941.
- [60] J.C.G. Lesutf. *Millimetre-wave Optics, Devices and Systems*. Adam Hilger, 1990.
- [61] C.D.H. Williams. An appraisal of the noise performance of constant temperature bolometric detector systems. *Measurement Science Technology*, 1:322–328, 1990.
- [62] G. chulkova A. Lipatov A Dzardavov K. Smirnov S. semenov B. Voronov C. Williams R. Soblewski G. Gol'tsman, O. Okunev. Hot-Electron Effect in Superconductors and Its Applications for Radiation Sensors. *LLE Review*, 87:134–152, 2001.
- [63] B. Bumble H.G. LeDuc P.J. Burke A.A. Verheijen R.J. Schoelkopf D.E. Prober A. Skalare, W.R. McGrath. Large bandwidth and low noise in a diffusion-cooled hot-electron bolometer mixer. *Applied Physics Letters*, 69(11):1558–1560, March 1996.
- [64] G.J. White H.M.Araujo, E.F.Pupplet. Optimising phonon cooled Nb hot-electron bolometers. *Journal of Applied Physics*, 88(11):6801–6807, November 2000.
- [65] C.A. Burrus. Backward Diodes for Low-Level Millimeter-wave Detection. *IEEE Trans. Microwave Theory and Techniques*, 11(5):357, September 1963.

BIBLIOGRAPHY

- [66] Radivoje Popovic Giovanni Boero, Pierre-Andre Besse. Hall detection of magnetic resonance. *Applied Physics Letters*, 79:1498–1500, 2001.
- [67] N. Ramesh Rao Y. Manassen, I. Mukhopadhyay. Electron-spin-resonance STM on iron atoms in silicon. *Physical Review B*, 61:16223–16228, 2000.
- [68] C.J. Gorter. Paramagnetism at Radiofrequencies. *Physics Review*, 51:778, 1937.
- [69] L.W.Rupp Jr W.M. Walsh Jr. A Self-Detecting Microwave Marginal Oscillator. *The Review of Scientific Instruments*, 42:468–470, 1971.
- [70] R.D. Hogg. Applications of IMPATT Diodes as rf Sources for Microwave EPR Spectroscopy. *Review Scientific Instruments*, 44:582–587, 1973.
- [71] A. Sotgiu F. Momo. Cavity stabilised Impatt oscillator for ESR spectroscopy. *Journal of Physics E: Scientific Instruments*, 14:339–344, 1981.
- [72] Harry R. Crowe Ira B. Goldberg. Effect of Cavity Loading on Analytical Electron Spin Resonance Spectrometry. *Analytical Chemistry*, 49(9):1353–1357, August 1977.
- [73] B.E. Prewer E.J. Becklake, C.D. Payne. Submillimetre performance of diode detectors using Ge, Si and GaAs. *Journal of Applied Physics*, 3(4):473–481, 1970.
- [74] J.R. Gao T.M. Klapwijk P.A.J. de Korte B. Voronov G. Gol'tsman M. Hajenius, J.J.A. Baselmans. Low noise NbN superconducting hot

BIBLIOGRAPHY

- electron bolometer mixers at 1.9 and 2.5THz. *Superconductor Science and Technology*, 17:224–228, 2004.
- [75] Kenneth K. Clarke and Donald T. Hess. *Communication Circuits: Analysis And Design*. Addison-Wesley, 2 edition, 1978. ISBN 0-201-01040-2.
- [76] K. Michelakis K.-H. Hieber J. Muller H. Schumacher I. Kallfass. F. Gruson, P. Abele. A SiGe HEMT Mixer IC with Low Conversion Loss. *Proc. 11th GAAS Symposium*, pages 513–516, 2003.
- [77] Robert V. Pound. *Microwave Mixers*. Mc-Graw Hill, 1948.
- [78] Sverre T. Eng. Low Noise Properties of Microwave Backward Diodes. *IRE Trans. Microwave Theory and Techniques*, 9:419–425, September 1961.
- [79] K.B. Jefferts T.G. Phillips. A Low Temperature Bolometer Heterodyne Receiver for Millimeter Wave Astronomy. *Review of Scientific Instrumentation*, 44(8):1009–1014, August 1973.
- [80] David Halliday Robert L. Cumberow. Paramagnetic Losses in Two Manganous Salts. *Physics Review*, 70(5):433, September 1946.
- [81] R.H. Mitchell P.C. Reidi G.M. Smth, J.C.G. Lesurf. Quasi-Optical CW MM-Wave Electron Spin Resonance Spectrometer. *Review of Scientific Instruments*, 69(11):3924–3937, 1998.
- [82] P. Sclottmann M.D. Bird, J.E. Crow. The National High Magnetic Field Laboratory: Condensed Matter in Continuous Magnetic Fields. *Journal of Low Temperature Physics*, 133(1-2):203–225, October 2003.

BIBLIOGRAPHY

- [83] D. Collison F.E. Mabbs. *Electron Paramagnetic Resonance of d Transition Metal Compounds*, volume 16 of *Studies in Inorganic Chemistry*. Elsevier, 1992.
- [84] M.E. Newton J.M. Baker J.A. van Wyk, J.H.N. Loubserf. ENDOR and high-temperature EPR of the N₃ centre in natural type 1b diamonds. *J. Phys. Condens. Matter*, 4:2651–2662, 1992.
- [85] Paval Kubacek Jan Jurik. The Temperature Dependant HFS EPR and Conformation of 9-Substituted Octahydrocarbazole Cation Radical. *Molecules*, 1:134–136, 1996.
- [86] J. Maier K. Sasaki. In situ EPR studies of chemical diffusion in oxides. *Phys. Chem. Chem. Phys.*, 2:3055–3061, 2000.
- [87] D. Haneman R.P. Lemke. Low-Temperature EPR Measurements on in situ Vacuum Cleaved Silicon. *Physical Review Letters*, 35(20):1379–1382, 17 November 1975.
- [88] Theodore Van Duzer Simon Ramo, John R. Whinnery. *Fields and Waves in Communication Electronics*. John Wiley & Sons, Inc, 1965.
- [89] Milton Abramowitz and Irene A. Stegun. *Handbook Of Mathematical Functions*. Dover Publications Inc, 9 edition, 1979.
- [90] Kenneth J. Button, editor. *Infrared and Millimeter Waves*, volume 13. Academic Press Inc., 1985.
- [91] R.J Wylde. Millimeter-wave Gaussian beam-mode optics and corrugated feed horns. *IEE Proceedings*, 131:258–262, 1984.
- [92] T. Li H. Kogelnik. Laser Beams and Resonators. *Applied Optics*, 5(10):1550–1567, October 1966.

BIBLIOGRAPHY

- [93] Lee W. Casperson. Synthesis of Gaussian beam optical systems. *Applied Optics*, 20(10):2243–2249, October 1981.
- [94] Jack H. Freed. *Very High Frequency (VHF)ESR/EPR*, volume 22 of *Biological Magnetic Resonance*, chapter Chapter 2, pages 19–43. Kluwer Academic/Plenum Publishers, 2004.
- [95] N. Marcuvitz. *Waveguide Handbook*. Peter Peregrinus, 1986.
- [96] M.R. Webb. A MM-Wave Four-Port Quasi-Optical Circulator. *International Journal of Infrared and Millimeter Waves*, 12(1):45–63, January 1991.
- [97] S. Kang D. Franklin J.C.G. Lesurf G.M. Smith, C.P. Unsworth. Design and Applications of high frequency quasi-optical Faraday rotators. In *Int. Conf. IR and Microwaves*. 1996.
- [98] H.R.L. Lamont. *Wave Guides*. Methuen, 1950.
- [99] V Williams L-C Brunel M Rohrer, J Kryzstek. Fabry-Perot resonator for high-field multi-frequency ESR at millimetre and submillimetre wavelengths. *Measurement Science Technology*, 10:275–284, 1999.
- [100] Jack H. Freed Jeff P. Barnes. A “shunt” Fabry-Perot resonator for high-frequency electron spin resonance utilizing a variable coupling scheme. *Review of Scientific Instruments*, 69:3022–3027, 1998.
- [101] M. Martinelli P.J.M. van Bentum G. Annino, M. Cassettari. A Non Radiative Approach to Single-Mode Dielectric Resonators. *Applied Magnetic Resonance*, 24:157–175, 2003.

BIBLIOGRAPHY

- [102] M. Martinelli G. Annino, M. Cassettari. High-Frequency Investigations on Non-Radiative Single Mode Dielectric Resonators. *Applied Magnetic Resonance*, 26:447–456, 2004.
- [103] Perry Miles. High efficiency optical diplexers. *Applied Optics*, 21(8):1367–1372, April 1982.
- [104] P.C.Riedi G.M.Smith. Progress in High Field ESR. In *Electron Paramagnetic Resonance*, volume 17 of *Specialist Periodical Reports*. Royal Society of Chemistry, 2000.
- [105] Harold Sobol. Microwave Communications-An Historical Perspective. *IEEE Trans. Microwave Theory and Techniques*, MTT-32(9):1170–1181, September 1984.
- [106] Darrel.T Emerson. The Work Of Jagadis Chandra Bose: 100 Years Of Millimeter-Wave Research. *IEEE Trans. Microwave Theory and Techniques*, 45(12):2267–2273, December 1997.
- [107] Ulrich L. Rohde. Oscillator Basics and Low-Noise Techniques for Microwave Oscillators and VCOs. In *Proc. GaAs 2000*. October 2000.
- [108] A. E. Ruehli. Inductance Calculations In a Complex Integrated Circuit Environment. *IBM J. Res.Dev*, 16(5):470–481, Sept 1972.
- [109] M. Schott M.Thiel H.-O. Ruoss W. Heinrich M. Steinhauer, H. Irion. SiGe Based Circuits for Sensor Applications beyond 100 GHz. In *2004 IEEE MTT-S Digest*, pages 223–226. 2004.
- [110] Axel Tessmann Wolfgang Bronner Michael Schlechtweg Steffen Kudzus, William H. Haydl. Push-Push Oscillators for 94 and 140GHz

BIBLIOGRAPHY

- Applications Using Standard Pseudomorphic GaAs Hemts. In *2001 IEEE MTT-S Digest*, volume 3, pages 1571–1574. 2001.
- [111] Fanz X. Sinnesbilcher. Hybrid Millimeter-Wave Push-Push Oscillators Using Silicon-Germanium HBT's. *IEEE Trans. Microwave Theory and Techniques*, 51(2):422–430, February 2003.
- [112] Huei Wang Yu-Long Tang. A Novel Triple-Push Oscillator Approach. In *2000 IEEE MTT-S Digest*, volume 2, pages 1201–1204. June 2000.
- [113] Huei Wang Yu-Lung Tang. A 24.6-GHz MMIC HBT Triple-Push Oscillator. In *Proc. Gallium Arsenide Application Symposium GAAS 2001*, pages 24–28. September 2001.
- [114] Gabriel M. Rebeiz Laurent Dussopt, Denis Guillois. A Low Noise Silicon 9GHz VCO and an 18GHz Push Push Oscillator. In *2002 IEEE MTT-S Digest*, volume 2, pages 695–698. 2002.
- [115] J.A. Bryant S.J. Inati V. Eies G.J. Gerfen M. Bennati, C.T. Farrar. Pulsed Electron-Nuclear Double Resonance (ENDOR) at 140GHz. *Journal of Magnetic Resonance*, 138:232–243, 1999.
- [116] Mitsutoshi Tanimoto Toshiaki Okabayashita, Yoshiko Sakai. Millimeter-Wave Spectrum of Fluorodiacetylene. *Journal of Molecular Spectroscopy*, 193:273–276, 1999.
- [117] G.S. Hobson. *The Gunn Effect*. Clarendon Press, 1974.
- [118] H. Barth K. Solbach, F. Sickling. Harmonic Gunn Oscillators Allow Frequency Growth. *Microwaves and RF*, 22(4):75, April 1983.
- [119] George I. Haddad Herbert Eisele, Andrew Rydberg. Recent Advances in the Performance of InP Gunn Devices and GaAs TUNNET Diodes

BIBLIOGRAPHY

- for the 100-300-GHz Frequency Range and Above. *IEEE Trans. Microwave Theory and Techniques*, 4(4):626–631, April 2000.
- [120] Dimitris Pavlidis Egor Alekseev. GaN Gunn Diodes For THz Signal Generation. *IEEE MTT-S Digest*, 3:1905–1908, 2000.
- [121] Jochen Hilsenbech Wolfgang Heinrich Friedrich Lenk, Matthias Schott. Low Phase-Noise GaAs-HBT Monolithic W-Band Oscillator. In *Proc. 34th European Microwave Conference*. 2004.
- [122] J.C.G. Lesurf G.M. Smith. Quasi-Optical Stabilisation Of Millimeter Wave Sources. In *IEEE MTT-S Digest*. 1992.
- [123] S.M. Sze. *Physics of Semiconductor Devices*. John Wiley and Sons, 2 edition, 1981.
- [124] Richard M. Beach. Hyperabrupt Varactor Tuned Oscillators. *Watkins Johnson Compant Tech-notes*, 5(4):2–15, July/August 1978.
- [125] Edward C. Niehenke. A Microstrip Low-Noise X-Band Voltage Controlled Oscillator. *IEEE Trans Microwave Theory and Techniques*, 27(12):December, 1979.
- [126] Robert J. Trew. Design Theory for Braod-Band YIG-Tuned FET Oscillators. *IEEE Trans. Microwave Theory and Techniques*, 27(1):8–14, January 1979.
- [127] Yoshiomi Koyano James C. Papp. An 8-18 GHz YI-Tuned FET Oscillator. *IEEE Trans. Microwave Theory and Techniques*, 28(7):762–767, July 1980.

BIBLIOGRAPHY

- [128] R. Funck S. Barvet J. Obregon, Y. Le Tron. Decade Bandwidth FET Functions. *MTT-S Digest*, pages 141–142, 1981.
- [129] J. Buenrostro A.P.S. Khanna. 2-22GHz Low Noise Silicon Bipolar YIG Tuned Oscillator Using Composite Feedback. *MTT-S Digest*, pages 1297–1299, 1992.
- [130] Gerald F. Dionne Ernst F. Schloemann Steven N. Stitzer J. Douglas Adam, Lionell E. Davies. Ferrite Devices and Materials. *IEEE Trans. Microwave Theory and Techniques*, 50(3):721–737, March 2002.
- [131] Asad A. Abidi. *Analog Circuit Design-RF Analog-to-Digital Converters; Sensor and Actuator Interfaces; Low-Noise Oscillators PLLs and Synthesizers*, chapter How Phase Noise Appears in Oscillators, pages 428–449. Kluwer Academic Publishers, 1997. ISBN 0-7923-9968-4.
- [132] J.W. Palmour S.L. Rumyantsev N.V. Dyakonova, M.E. Levinshtein. Broadening of noise spectra in semiconductors and the $1/f^{1.5}$ problem. *Semiconductor Science and Technology*, 10:1126–1130, 1995.
- [133] David M. Boulin Micheal Frei Kwok K. Ng Ran-Hong Yan Samuel Martin, Vance D. Archer. Device Noise in Silicon RF Technologies. *Bell Labs Technical Journal*, Summer:30–45, 1997.
- [134] john D. Cressler Rao Rapeta Alvin J. Joseph David Haramé Guofu Nui, Zhenrong Jin. Transistor Noise in SiGe HBT RF Technology. *IEEE Journal Solid-State Circuits*, 36(9):1424–1427, 2001.
- [135] Zdzislaw Wolosiak Lech Dobrzanski. On the origin of low frequency noise in GaAs metal-semiconductor field-effect transistors. *Journal of Applied Physics*, 87:517–521, 2000.

BIBLIOGRAPHY

- [136] D.B. Leeson. Simple Model of a Feedback Oscillator Noise Spectrum. *Proc. IEE*, 103, 1956. Part B.
- [137] Ali Hajimiri Thomas H. Lee. Oscillator Phase Noise: A Tutorial. *IEEE Journal of Solid-State Circuits*, 35(3):326–336, March 2000.
- [138] Marc Camiade Jaun Obregon Jean-Christophe Nallatamby, Michel Prigent. Phase Noise in Oscillators-Leeson Formula Revisited. *IEEE Trans. Microwave Theory and Techniques*, 51(4):1386–1394, April 2003.
- [139] Jochen Hilsenbeck WolfgangHeinrich Friedrich Lenk, Matthias Schott. A New Design Approach for Low Phase-Noise Reflection-Type MMIC Oscillators. *IEEE Trans. Microwave Theory and Techniques*, 52(12):2725–2731, December 2004.
- [140] S.A. Maas. *Nonlinear Microwave Circuits*. Artech House, 1988.
- [141] Brendon Lyons Eoin O’Ciardha, Sverre U. Lidholm. Generic-Device Frequency Multiplier Analysis-A Unified Approach. *IEEE Trans. Microwave Theory and Techniques*, 48(7):1134–1141, July 2000.
- [142] Chester H. Page. Frequency Conversion With Positive Nonlinear Resistors. *Journal of Reasearch of the National Bureau of Standards*, 56(4):179–182, April 1956.
- [143] C.B. Burckhardt. Analysis of Varactor Frequency Multipliers for Arbitrary Capacitance Variation and Drive Level. *The Bell System Technical Journal*, pages 675–692, April 1965.
- [144] R.P. Rafuse P. Penfield. *Varactor Applications*. M.I.T Press, Cambridge MA., 1962.

BIBLIOGRAPHY

- [145] H.E. Rowe J.M. Manley. Some General Properties of Nonlinear Elements -Part1. General Energy Relations. *Proc. IRE*, pages 904–913, July 1956.
- [146] Mirosław E. Adamski Marek T. Faber, Jerzy Chramiec. *Microwave and Millimeter-Wave Diode Frequency Multipliers*. Artech House, 1995. ISBN 0-89006-611-6.
- [147] Alain Maestrini Goutam Chattopadhyay John Pearson David Pukala Imran Mehdi Frank Maiwald, Erich Schlecht. THz frequency multiplier chains based on planar Schottky diodes. In *Proc. SPIE: Int. Conf. Astronomical Telescopes and Instrumentation*, pages 435–446. August 2002.
- [148] J. Ovey M. Sawan M. Missous Ali Rahal, R.G. Rogers. A W-Band Medium Power Multi-Stack Quantum Barrier Varactor Frequency Tripler. *IEEE Microwave and Guided Wave Letters*, 5(11):368–370, November 1995.
- [149] Howard Z. Chen K. Jell S. Stolt Christina F. Jou, Wayne M. Lam. Millimeter-Wave Diode-Grid Frequency Doubler. *IEEE Trans. Microwave Theory and Techniques*, 36(11):1507–1514, November 1998.
- [150] Wolfgang Menzel Werner Thiel. Full-Wave Design and Optimization of mm-Wave Diode-Based Circuits in Finline Technique. *IEEE Trans. Microwave Theory and Techniques*, 47(12):2460–2466, December 1999.
- [151] A. Maestrini A. Fung S. Martin D. Pukala J. Bruston-I. Mehdi E. Schlecht, G Chattopadhyay. 200,400 and 800GHz Schottky

BIBLIOGRAPHY

- Diode "Substrateless" Multipliers: Design and Results. In *IEEE MTT-S Digest*, pages 1649–1652. May 2001.
- [152] N W. McClachlan. *Bessel Functions For Engineers*. Clarendon Press, 2 edition, 1955.
- [153] Wendell D. Seal Algie L. Lance and Frederik Labaar. Phase Noise And AM Noise Measurements In The Frequency Domain. Tech Note TN-1337, NIST, March 1980. Section D2. Reprinted in *Infrared and Millimeter Waves Vol.11* ed. Kenneth J. Button.
- [154] Warren F. Walls. Practical Problems Involving Phase Noise Measurements. In *33rd Annual Precise Time and Interval (PTTI) Meeting*.
- [155] *RF & Microwave Phase Noise Measurement Seminar*. Hewlett Packard, 1988.
- [156] John G. Ondria. A Microwave System for Measurements of AM and FM Spectra. *IEEE. Trans. Microwave Theory and Techniques*, 16:767–781, 1968.
- [157] Jim C.G. Lesurf Graham M. Smith. A Highly Sensitive Millimeter Wave Quasi-Optical FM Noise measurement System. *IEEE Trans. Microwave Theory and Techniques*, 39:2229–2236, 1991.
- [158] J.C.G. Lesurf A.R. Harvey, G.M. Smith. Phase Noise Measurements of a D-Band Backward Wave Oscillator. *IEEE Microwave and Guided Wave Letters*, 4:271–273, 1994.
- [159] Dieter Scherer. The 'Art' Of Phase Noise Measurement. *Proc. RF and Microwave Measurement Symposium*, May 1983.

BIBLIOGRAPHY

- [160] Aeroflex Inc. PN9500 And PN9000 Test Set. [Www.aeroflex.com](http://www.aeroflex.com).
- [161] Agilent. E5052A Signal Source Test Set. [Www.agilent.com](http://www.agilent.com).
- [162] Christopher Sceibold. Theory And Design Of The Delay Line discriminator For Phase Noise Measurement. *Microwave Journal*, 26(12):103–112, December 1983.
- [163] C. John Grebenkemper. Local Oscillator Phase Noise And Its Effect On Receiver Performance. *Watkins Johnson Company Tech-notes*, 8(6), November/December 1981.
- [164] Stephen R. Kurtz. Mixers As Phase Detectors. *Watkins Johnson Company Tech-notes*, 5(1), January/February 1978.
- [165] Thomas A. Barley J. Robert Ashley and JR Gustav J Randt. The Measurement of Noise in Microwave Transmitters. *IEEE. Trans. Microwave Theory and Techniques*, MTT-25(4):294–318, April 1977.
- [166] Yves Rolain Wendy Van Moer and Alain Geens. Measurement Based Nonlinear Modeling Of Spectral Regrowth. *IEEE MTT-S Digest*, 3:1467–1469, 2000.
- [167] Fredric J. Harris. On The Use Of Windows For Harmonic Analysis With Discrete Fourier Transform. *Proc. IEEE*, 66(1):51–83, January 1978.
- [168] J-D. Buchs R. Knochel, K. Schunemann. Theory and performance of cavity stabilised microwave oscillators. *Microwaves Optics and Acoustics*, 1(4):143–155, July 1977.

BIBLIOGRAPHY

- [169] B. Schiek. Comparison Between Transission and Reaction-Cavity-Stabilised Oscillators. *Electronics Letters*, 7(20):618–620, October 1971.
- [170] Andrew R. Harvey. *A Millimeter Wave, Quasi Optical, Complex Impedance Bridge*. Ph.D. thesis, University of St Andrews, 1990.
- [171] Graham M. Smith. *Transferred Electron Oscillators At MM Wave Frequencies And Their Characterisation Using Quasi-Optical Techniques*. Ph.D. thesis, University of St Andrews, 1990.
- [172] W. Steichen M.M. Salomaa T. Makkonen, V.P. Plessky. Surface-acoustic-wave devices for the 2.5-5GHz frequency range based on logitudinal leaky waves. *Applied Physics Letters*, 82(19):3351–3353, May 2003.
- [173] Pierre Guillon Darko Kajfez, editor. *Dielectric Resonators*. Noble, 1998.
- [174] Asamitsu Higasisaka Hideo Takamizawa Hiroyuki Abe, Yoichiro Takayama. A Highly Stabilized Low-Noise GaAs FET Integrated Oscillator with a Dielectric Resonator in the C Band. *IEEE Trans. Mictrowave Theory and Techniques*, 26(3):156–162, March 1978.
- [175] J.A. Connelly C.D. Motcnenbacher. *Low-Noise Electronic System Design*. Wiley Interscience, 1993.
- [176] Randall W. Rhea. *Oscillator Design and Computer Simulation*. Noble Publishing, 2nd edition, 1995.

BIBLIOGRAPHY

- [177] Ulrich L. Rohde. *Microwave And Wireless Synthesizers Theory And Design*. John Wiley and Sons Inc., 1997.
- [178] Floyd M. Gardner. *Phaselock Techniques*. Wiley Interscience, 1979.
- [179] Howard D.G. Lennon Max J. Lazarus Robert G. Davis, J. Leeson. Phase Locked Millimeter-Wave Two Port Second-Harmonic Oscillators. *IEEE Trans. Microwave Theory and Techniques*, 39(10):1746–1753, December 1991.
- [180] John Ondria. Noise Measurements of W-Band (75-100GHz) CW GaAs Gunn and Silicon IMPATT Oscillators. *IEEE MTT-S Digest*, pages 24–26, 1980.
- [181] P. Thomas Lewin Anders Rydberg. An Investigation of Parametric Noise in Millimeter-Wave IMPATT Oscillators. *IEEE Trans. Microwave Theory and Techniques*, 35(7):663–671, July 1987.
- [182] P.A. Rolland J Michel. G. Salmer, M. Chive. A comparison between direct generation and frequency multiplication using avalanche diodes. *Journal of Applied Physics*, 6:L41–L43, 1973.
- [183] James B. Mitchell Murali C. Krishna Sankaran Subramanian, Ken-ichiro Matsumoto. Radio frequency continuous-wave and time-domain EPR imaging and Overhauser-enhanced magnetic resonance imaging of small animals: instrumental developments and comparison of relative merits for functional imaging. *NMR in Biomedicine*, 17:263–294, 2004.
- [184] Jack H. Freed Petr P. Borbat, Richard H. Crepeau. Multifrequency Two-Dimensional Fourier Transform ESR: An X/Ku-Band Spectrometer. *Journal of Magnetic Resonance*, 127:155–167, 1997.

BIBLIOGRAPHY

- [185] D.A. Robertson D.J. Keeble G.M. Smith P.A.S. Cruikshank, D.R. Bolton. The HIPER Project -sub-nanosecond pulse ESR. *Conference digest 29th International conference on Infrared and Millimeter Waves*, pages 171–172, 2004.
- [186] Dab Englisg Albert Grote Thang Pham Cheng Sun George Hayashibara-Percy Yen Wes Piotrowski Kai Chang, Raghbir Tahim. W-Band (75 To 110GHz) Microstrip Components. *IEEE MTT-S Digest*, pages 371–374, 1985.
- [187] Nikolai Drozdovski. SPST Switches for Satellite Communication Systems. *Proc. 2nd IEEE Symposium on Computers and Communication*, pages 360–363, 1997.
- [188] William Moroney Dana Wheeler Albert Armstrong, Joel Goodrich. Monolithic Control Components For High Power mm-Waves. *Microwave Journal*, 28(9):197–201, September 1985.
- [189] Inder Bahl Prakash Bhartia K.C. Gupta, Ramesh Garg. *Microstrip Lines and Slotlines*. Artech House, 1996.
- [190] Wolfgang G. Hoefler Heinrich Callsen, Holger H. Meinel. p-i-n Diode Control Devices in E-Plane Technique. *IEEE Trans. Microwave Theory and Techniques*, 37(2):307–316, February 1989.
- [191] Sephen J. Erst. *Receiving Systems Design*. Artech House, 1984.
- [192] C.W. Chen E.W. Lin P.C. Grossman L.T. Tran J. Cowles-H. Wang A.K. Oki K. Najita M.P. De Lisio Y.H. Chung, K.F. Sato. $1/f$ Noise Modeling of InP HBT-Based Schottky Diodes For Monolithic Millimeter-Wave Mixers. *IEEE MTT-S Digest*, pages 841–844, June 1997.

BIBLIOGRAPHY

- [193] Ralph H. Rasshofer Erwin M. Biebel Martin M. Kaleja, Arnold J. Herb. An I-Q Mixer at 76.5GHz Using Flip-Chip Mounted Silicon Schottky Diodes. *IEEE MTT-S Digest*, 2001.
- [194] Benjamin Parzen. *Design of Crystal and Other Harmonic Oscillators*. John Wiley & Sons, 1983.
- [195] Rober J. Matthys. *Crystal Oscillator Circuits*. Krieger Publishing Company, 1983.
- [196] Paul R. Gray and Robert G. Meyer. *Analysis And Design Of Analog Integrated Circuits*. john Wiley and Son, 3 edition, 1993. ISBN 0-471-57495-3.
- [197] E.M.T Jones G. Matthaei, L. Younge. *Microwave Filters, Impedance-Matching and Coupling Structures*. Artec House, 1980.
- [198] Gabriel M. Rebeiz Andrew R. Brown. A Varactor-Tuned RF Filter. *IEEE Trans. Microwave Theory and Techniques*, 48(7):1157–1160, July 2000.
- [199] Marins Korber. Six-Stage YIG Filters. *Watkins Johnson Company Tech-Notes*, 15(5):2–9, Sepember/October 1988.
- [200] Stephen A. Maas. *Microwave Mixers*. Artech House, 1986.
- [201] *1995 Millimeter Wave Product Catalog*. Millitech Corporation, 1995.
- [202] Shiban K. Koul Bharathi Bhat. *Stripline-Like Transmission Lines for Microwave Integrated Circuits*. John Wiley & Sons, 1989.
- [203] F.B Hidebrand. *Introduction To Numerical Analysis*. McGraw-Hill Book Company Inc, 1956.

BIBLIOGRAPHY

- [204] Andre Heck. *Introduction To Maple*. Springer-Verlag, 1993. ISBN 0-387-97662-0.